AN ANALYSIS OF PION-NUCLEON SCATTERING

by

John Marshall Ford

Dissertation submitted to the Faculty of the
Virginia Polytechnic Institute and State University
in partial fulfillment of the requirements for the degree of

DOCTOR OF PHILOSOPHY

in

Physics

APPROVED:

L. D. Roper, Chairman

R. A. Arndt

M. Blecher

D. A. Jenkins

T. Mizutani

April 1988

Blacksburg, Virginia

AN ANALYSIS OF PION-NUCLEON SCATTERING

by

John Marshall Ford

Committee Chairman: L. David Roper
Physics

(ABSTRACT)

A phase-shift analysis of elastic pion-nucleon scattering data from threshold to a pion kinetic energy of 1100 MeV was performed. The resulting partial-wave amplitudes were investigated in the complex energy plane, and the resonance states with their associated zeros and poles were determined. Particular emphasis was given on elucidating the nature of the P_{11} partial wave.

The phase-shift analysis consisted of both energy-independent and energy-dependent analyses. The energy-dependent partial waves were parametrized as a coupled channel K-matrix whose elements are polynomials in energy plus an explicit pole term.

A complete description of the investigation and the experimental data used are included as is a description of the theoretical models used for interpretation of the results.

ACKNOWLEDGEMENTS

Little of worth is accomplished in life without the help of others, and there are many good people to whom I hold a debt. I would like to express my thanks to some of those who have been a major help to me in my efforts to complete this project. First, I would like to thank the two gentlemen with whom much of this research was performed, Dr. R. Arndt and my graduate committee chairman and advisor, Dr. L. D. Roper. Their patient instruction and continuing guidance were invaluable, and I appreciate their assistance.

I would like to express special thanks to the people at Teledyne Brown Engineering, where I have been employed since 1979, for their support during my studies. I want to thank , who was my supervisor when I began this research, for his personal concern and encouragement to my decision to return to my studies. Thanks are also extended to Technical Publications Department personnel, especially and , for their excellent preparation of this manuscript and their painstaking care. To the management of Teledyne Brown, particularly , , , and , I want to acknowledge my gratitude for their assistance in allowing me three separate leaves of absence, for providing computer time on company-owned machines, and for their continual support.

In any extended project, there are inevitably periods of discouragement. For their loving support and unending encouragement, I would like to thank my parents, , and my brother and sister, . Without the help of all of these individuals, this research could not have been completed.

TABLE OF CONTENTS

TABLE OF CONTENTS (Continued)

TABLE OF CONTENTS (Concluded)

1. INTRODUCTION

The pion-nucleon scattering problem has long been recognized as an important arena for the study of the strong nuclear force because it is the simplest example of the strong interaction easily accessible to experimentation. The nucleon is the lowest mass nucleus and has the simplest quark structure of all the baryons, being composed primarily of up and down quarks. Correspondingly, the pion is the lowest mass and simplest of the mesons. The pion-nucleon interaction is, therefore, responsible for the most important longest range part of the nucleon-nucleon interaction, the force that holds the nucleus together. Although the pion-nucleon interaction is obviously important to our understanding of the hadronic force, explicit first principle calculations of the physical observables: masses, cross sections, etc., are not yet possible. The theory of the strong interaction, quantum chromodynamics (QCD) is not amenable to exact or even perturbative calculations because of its complexity and the large magnitude of its coupling constant. Theoretical models can, however, be developed based on QCD, but a means of relating the model predictions to the experimental results must be established. Historically, that means has been the phenomenological approach of partial-wave, phase-shift analysis of the experimental data. Such an approach results in the description of the data set in terms of a relatively small number of energy-dependent, partial-wave amplitudes that can be directly related to model predictions in terms of both

statics (masses and widths of states) and dynamics (cross sections, lifetimes, etc).

Phase-shift analyses of pion-nucleon scattering data have been performed since the days of Fermi[1] in the early 1950's. Since then the analyses have become much larger and more sophisticated, and much understanding of the physics of the interaction has been gained. In particular, a rich spectroscopy of resonant states responsible for most of the structure in pion-nucleon data has been identified, including the two earliest and among the most dominant resonances, the Delta and Roper resonances. Even with the great amount of effort that has been and continues to be directed at the pion-nucleon problem, the problem is not completely solved and work remains to be done. Evidence for several resonances: P_{13} at 1540 MeV, P_{31} at 1550 MeV, and P_{33} at 1600 in standard spectroscopic notation, is weak and their existence needs to be verified. In addition, the resonance parameters (masses, widths, and residues) for most of the confirmed states need a more reliable determination for better comparison with model predictions. The above uncertainties, by themselves, provide sufficient motivation for pursuing the investigation being presented here, but they are not the only reasons. In the mid-1970's, the Saclay[2] group performed a phase-shift analysis of elastic pion-nucleon scattering data that identified a splitting of the Roper resonance into two states at 1413 and 1532 MeV, respectively. It is this intriguing possibility that served as the initial catalyst for this investigation. In addition to verifying or rejecting, as appropriate,

the proposed resonant states and providing a precise determination of their parameters, the objective of this research has been to clarify the situation with the Roper resonance and the P_{11} partial wave as a whole. Is the Roper actually split, and, if so, what impact does that splitting have on the validity of several popular theoretical models?

The approach needed to address these questions begins with the development of a complete and up-to-date data base of elastic pion-nucleon scattering results. That development and the description of the resulting data base are presented in Chapter 2 with the references for the many experiments given in Appendix A. A detailed explanation of the phase-shift analysis is provided in Chapter 3. Both the energy-dependent and energy-independent parametrizations of the partial amplitudes are described, as is the methodology used to couple these two distinct approaches. The formalism used to compute the physical observables from the partial waves is given in Appendix B. Also described in Chapter 3 is the chi-squared minimization technique employed to determine the partial waves from the large data base and the assumed parametrization. The fitting program used in this process is documented in Appendix C. After the fitting process is completed and a proposed solution is obtained, the resulting partial waves are described and interpreted in Chapter 4. Additional details of the partial-wave amplitudes are shown in Appendix E. Many resonant states are observed that are then described and their resonance parameters presented. In addition, an exploration of the topology of the partial amplitudes in the complex energy plane is undertaken to better

understand the complex zeros and poles in the amplitudes associated with the resonances. Much emphasis is given to the particularly interesting P_{11} wave. Once this description of pion-nucleon scattering is obtained from the experimental data and the phase-shift analysis, the results are compared to three popular and successful models of hadron spectroscopy: the constituent quark models, the bag models, and the Skyrmion model. Chapter 5 presents a description and discussion of the relevance of these three models to the pion-nucleon problem, providing further insight into the physics of the important pion-nucleon interaction. A summary of the progress made by this research toward a better understanding of the pion-nucleon interaction and, hence, of the strong interaction is given in the conclusions of Chapter 5 as the final results are all tied together. Recommendations for future research are also made here as a final and appropriate end to this dissertation.

1.1 REFERENCES

1. H. L. Anderson, E. Fermi, R. Martin, D. E. Nagle, *Physical Review*, Vol. 91, 1953, p. 155

2. Ayed, Unpublished Thesis from the Saclay Group as reported in Particle Data Group, *Reviews of Modern Physics*, Vol. 48, 1976, p. S147

2. THE PION-NUCLEON DATA BASE

Obviously, a phase-shift analysis can be no better than the data on which it is based. Therefore, an attempt has been made to assemble as complete a collection as possible of elastic pion-nucleon data, particularly those results published in refereed journals. Although the analysis extends only to 1100 MeV, experiments have been included with incident pion kinetic energy up to 1200 MeV in the laboratory frame. The extension of the data base beyond the analysis limit allows one to investigate extrapolations of the present analysis. A chronological summary of the experiments in the data base as of September 1986 is presented in Table 2-1 with the numbered references given in Appendix A. Under the status column, the notation "A" identifies active experiments included in the analysis, and "X" labels those experiments excluded from the analysis. The "Short ID" consists of an abbreviation of the principal author's name and the year in which the data were published. For an example, the Measday *et al.* 1984 publication of charge exchange total elastic cross section is given the ID of ME(84). Reaction types for positive pion, negative pion, and charge exchange scattering off of protons are labeled PI+P, PI-P, and CXS, respectively. Differential cross sections and polarization data are labeled with DSG and P, while total and total-elastic cross sections are labeled with SGT and SGTE. Because older experiments are generally associated with larger errors, no data published before 1964 have been included in the data base. This date was chosen somewhat arbitrarily but is based on the principle that deleted data be

TABLE 2-1. PION-NUCLEON DATA BASE (0 to 1200 MeV)* (Sheet 1 of 4)

SHORT ID	REFERENCE	ENERGY*	REACTION	OBSERVABLE	STATUS
BO(64)	40	756 to 1165	CXS	DSG	A
BU(64)	50	545 to 1000	CXS	SGTE	X
EA(64)	82	520 to 990	PI+P	P	A
EA(64)	82	520 to 990	PI-P	P	A
HE(64)	94	530 to 900	PI+P	DSG	A
HE(64)	95	530 to 900	PI-P	DSG	A
MU(64)**	114	595 to 800	CXS	DSG	A
VI(64)	137	604	PI-P	DSG	A
BA(65)	19	410, 492	PI+P	P	A
BA(65)	20	410, 492	PI-P	P	A
BU(65)	52	558	PI-P	DSG	A
CU(65)	63	35	CXS	DSG	A
DE(65)	65	500	PI+P	DSG	A
DE(65)	65	500	PI+P	SGTE	A
DE(65)	65	500	PI+P	SGTR	X
DE(65)	72	495 to 1195	PI+P	SGT	X
DE(65)	72	415 to 1195	PI-P	SGT	X
LI(65)	108	313, 371	CXS	DSG	A
OG(65)	117	310 to 650	PI+P	DSG	A
OG(65)	117	370 to 650	PI-P	DSG	A
BE(66)	30	775	PI-P	DSG	A
BI(66)	35	310 to 700	PI+P	SGT	X
BI(66)	35	310 to 700	PI-P	SGT	X
CA(66)	57	790 to 870	PI-P	SGTE	X
DI(66)	73	365	PI-P	P	A
DO(66)	76	39	CXS	DSG	A
DU(66)**	80	745 to 850	PI+P	DSG	A
DU(66)**	80	745 to 850	PI-P	DSG	A
OL(66)	118	646	PI-P	DSG	A
RI(66)	122	450 to 685	CXS	DSG	A
ST(66)	131	525 to 1170	PI+P	SGT	X
ST(66)	131	540 to 1170	PI-P	SGT	X
TI(66)	132	781	PI+P	SGTE	A
TR(66)	133	248	PI+P	DSG	A
TR(66)	133	248	PI+P	SGT	A
VA(66)	135	300	PI-P	P	A
BA(67)	17	410, 490	PI+P	DSG	A
BA(67)	17	410, 490	PI-P	DSG	A
BC(67)	13	949, 1098	PI-P	SGTE	A
BE(67)	32	900	PI+P	SGTE	A
CH(67)	59	500 to 1120	CXS	DSG	A
DE(69)	70	810	PI+P	DSG	A
ED(67)	83	98	PI+P	DSG	A

*Kinetic energy of incident pion in laboratory frame (MeV)

**More data available, but only in plotted form

TABLE 2-1. PION-NUCLEON DATA BASE (0 to 1200 MeV)* (Sheet 2 of 4)

SHORT ID	REFERENCE	ENERGY*	REACTION	OBSERVABLE	STATUS
FE(67)	84	650	PI-P	DSG	A
GO(67)	89	245 to 410	PI+P	P	A
GO(67)	89	245 to 410	PI-P	P	A
HA(67)	92	470 to 770	PI-P	P	A
JO(67)	103	615 to 770	PI+P	P	A
ME(67)	112	900	PI+P	DSG	A
AR(68)	11	225 to 390	PI-P	P	A
BE(68)	31	595 to 675	PI-P	DSG	A
BI(68)**	36	765	PI+P	P	A
BI(68)**	36	564, 650	PI-P	P	A
CA(68)	54	345 to 1170	PI+P	SGT	A
CA(68)	54	350 to 1200	PI-P	SGT	A
CR(68)	62	60	PI+P	DSG	A
CR(68)	62	60	PI-P	DSG	A
DE(68)	66	722	PI+P	DSG	A
DE(68)	66	722	PI+P	SGTE	A
DU(68)**	81	745 to 800	PI-P	P	A
HY(68)	99	590 to 680	CXS	DSG	A
RI(68)	123	435 to 1005	CXS	DSG	A
VA(68)	134	720	PI-P	DSG	A
BU(69)	51	525 to 1115	CXS	SGTE	A
CO(69)	61	515 to 1185	PI-P	P	A
DE(69)	67	710 to 880	PI+P	SGTE	A
DE(69)	68	405 to 635	PI-P	SGTE	A
DE(69)	71	407, 493	PI-P	DSG	A
AB(70)	2	745 to 1150	PI-P	DSG	A
AL(70)	4	685 to 1170	PI+P	DSG	A
AL(70)	4	685 to 1170	PI+P	P	A
BA(70)	15	765 to 910	PI+P	DSG	A
BA(70)	15	765 to 910	PI+P	SGT	A
BI(70)	37	560 to 1185	PI-P	SGT	A
BO(70)	41	465 to 685	PI+P	SGTE	A
BO(70)	41	465 to 685	PI+P	SGTR	A
HI(70)	96	868	PI+P	DSG	A
HI(70)	96	868	PI+P	P	A
HL(70)	97	310	CXS	P	A
AP(71)	10	1075 to 1170	PI-P	DSG	A
BL(71)	38	551, 592	CXS	DSG	A
BR(71)	43,44	430 to 1195	PI-P	DSG	A
BU(71)	49	90 to 295	CXS	SGTE	A
CA(71)	55	70 to 285	PI+P	SGT	A
CA(71)	55	75 to 295	PI-P	SGT	A

*Kinetic energy of incident pion in laboratory frame (MeV)

**More data available, but only in plotted form

TABLE 2-1. PION-NUCLEON DATA BASE (0 to 1200 MeV)* (Sheet 3 of 4)

SHORT ID	REFERENCE	ENERGY*	REACTION	OBSERVABLE	STATUS
HA(71)	93	200 to 450	CXS	DSG	A
KA(71)	104	1148	PI+P	DSG	A
SL(71)	130	595 to 850	PI+P	P	X
AB(72)	3	745 to 1150	PI-P	DSG	A
AL(72)	5	735 to 1120	PI-P	DSG	A
AL(72)	5	735 to 1120	PI-P	P	A
BA(72)	16	765 to 910	PI+P	SGTE	A
BE(72)	29	205 to 375	CXS	DSG	A
BO(72)	42	465 to 680	PI+P	DSG	A
DA(72)	64	295 to 745	PI+P	SGT	X
DA(72)	64	295 to 745	PI-P	SGT	X
RO(72)	125	445 to 1440	PI+P	DSG	X
RO(72)	125	445 to 1140	PI-P	SGT	X
BU(73)	53	85 to 295	PI+P	DSG	A
BU(73)	53	85 to 295	PI-P	DSG	A
CA(73)	56	20 to 1198	PI+P	REF	X
CA(73)	56	20 to 1198	PI-P	REF	X
DO(73)	74	585 to 815	PI-P	DSG	A
DU(73)	79	20 to 45	CXS	DSG	A
GO(73)	90	240 to 400	PI+P	P	A
GO(73)	90	240 to 400	PI-P	P	A
GR(73)	91	401, 545	PI-P	DSG	A
MA(73)	109	670 to 825	PI+P	DSG	A
NE(73)**	116	900	CXS	SGTE	A
AB(74)	1	1075	PI+P	DSG	A
BE(74)	33	1064	PI+P	DSG	X
CH(74)	58	356, 428	CXS	DSG	A
DO(74)	75	855 to 995	PI-P	SGTE	A
JE(74)	101	110 to 230	CXS	DSG	A
RI(74)	121	475 to 1150	PI-P	DSG	A
SH(74)	129	900,1113	CXS	P	A
AM(75)	8	236	PI+P	P	A
BA(75)**	18	865 to 1185	PI-P	DSG	A
CO(75)	60	135 to 260	CXS	DSG	A
DE(75)	69	475 to 870	PI-P	DSG	A
DE(75)	69	475 to 870	CXS	DSG	A
MA(75)	110	475 to 1195	PI+P	P	A
AM(75)	9	90 to 195	PI+P	P	A
BA(76)	14	495, 879	PI+P	SGT	A
BA(76)	14	885	PI-P	SGT	A
BK(76)	23	450	PI+P	P	A
BK(76)	23	450	PI-P	P	A

*Kinetic energy of incident pion in laboratory frame (MeV)

**More data available, but only in plotted form

TABLE 2-1. PION-NUCLEON DATA BASE (0 to 1200 MeV)* (Sheet 4 of 4)

SHORT ID	REFERENCE	ENERGY*	REACTION	OBSERVABLE	STATUS
BE(76)	34	20 to 100	PI+P	DSG	A
BR(76)	45,48	490 to 1145	CXS	DSG	X
BY(76)	22	140 to 275	CXS	DSG	A
BA(77)	21	1049, 1118	PI-P	P	A
BR(77)	46	650, 746	PI+P	P	X
DU(77)	77,78	290 to 310	PI+P	P	A
JE(77)	102	125 to 245	CXS	DSG	A
OT(77)	119	1115 to 1185	PI+P	DSG	A
VA(77)	136	1145 to 1185	PI-P	DSG	A
AL(78)	6	292, 308	PI-P	P	A
BL(78)	39	40, 50	PI+P	DSG	A
BR(78)	47	490 to 1145	CXS	P	X
KR(78)	107	400 to 600	CXS	DSG	A
NE(78)	115	265 to 325	PI+P	DSG	A
NE(78)	115	260 to 330	PI-P	DSG	A
PE(78)	120	70 to 370	PI+P	SGT	A
PE(78)	120	70 to 370	PI-P	SGT	A
AU(79)	12	48	PI+P	DSG	A
HO(79)	98	20 to 1100	PI+P	REF	A
HO(79)	98	20 to 1100	PI-P	REF	A
KA(79)	105	885 to 1045	PI-P	DSG	A
SA(79)	128	540 to 590	PI-P	DSG	A
BE(81)	24,25	450 to 600	PI-P	P	A
GO(81)	88	275 to 600	PI+P	DSG	A
GO(81)	88	285 to 600	PI-P	DSG	A
RI(82)	124	65 to 140	PI+P	DSG	A
SA(82)	126	260 to 565	PI+P	DSG	A
SA(82)	126	260 to 565	PI-P	DSG	A
AL(83)	7	95 to 295	PI-P	P	A
AL(83)	7	235 to 310	CXS	P	A
BE(83)	26,27,28	335 to 580	PI+P	P	A
FR(83)	86	25 to 90	PI+P	DSG	A
FR(83)	86	25 to 90	PI-P	DSG	A
GA(84)	87	401	CXS	DSG	A
ME(84)	111	27, 39	CXS	SGTE	A
FI(85)	85	30 to 65	CXS	DSG	A
IR(86)	100	65 to 230	CXS	DSG	A
KI(86)	106	190 to 505	CXS	P	A
MO(86)	113	350 to 565	PI+P	P	A
MO(86)	113	350 to 565	PI+P	P	A
SA(86)	127	290 to 565	PI+P	DSG	A
SA(86)	127	290 to 565	PI-P	DSG	A
WI(86)	138	425 to 535	CXS	P	A

*Kinetic energy of incident pion in laboratory frame (MeV)

supplanted by more recent and accurate results covering the same kinematic (energy, angle) range. Also excluded from the data base are those total-elastic cross sections that are not measured independently of differential cross sections that have been included. There are also several references[1-6] that are not in Table 2-1 or in the data base because the published data are in plotted form only. Any reader knowing how to obtain these or any additional data is requested to notify the author.

When this work was begun, the data base was considerably smaller and consisted largely of data from experiments with energy less than 800 MeV. Since that time, the data base has been greatly increased with the addition of many new experiments and the expansion of the energy range to the present 1200 MeV. Even with the removal of the old pre-1964 experiments, the data base has been approximately doubled. With this rapid change in the data base, a computer-based Data Log was developed to keep track of its evolution. The Data Log enables comments about each reference -- such as why a particular experiment is not included in the analysis -- to be recorded for future reference.

2.1 ACTIVE EXPERIMENTS

Because of the large number of experiments in the data base, no attempt has been made to describe it in detail. Instead, the extent of the data base is shown via the kinematic distribution plots in Figures 2-1 through 2-6. The distributions in angle and energy for differential cross sections and polarization data are shown for each

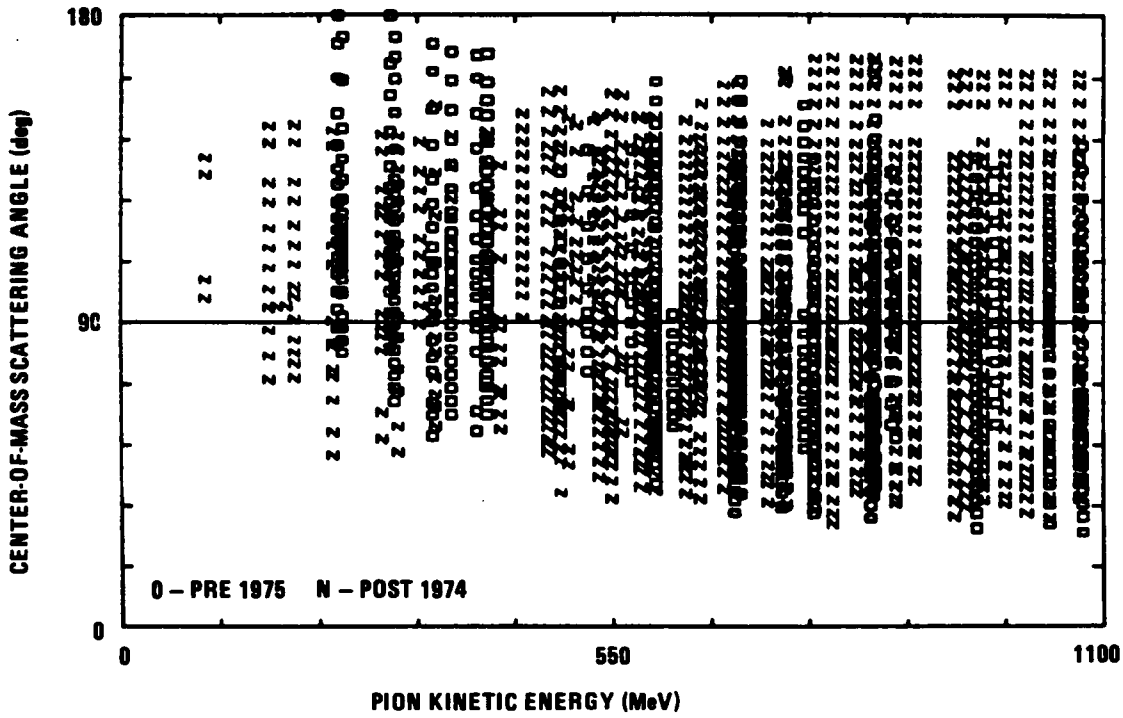

FIGURE 2-1. KINEMATIC VARIABLE SCATTER PLOT OF POSITIVE PION ELASTIC POLARIZATION

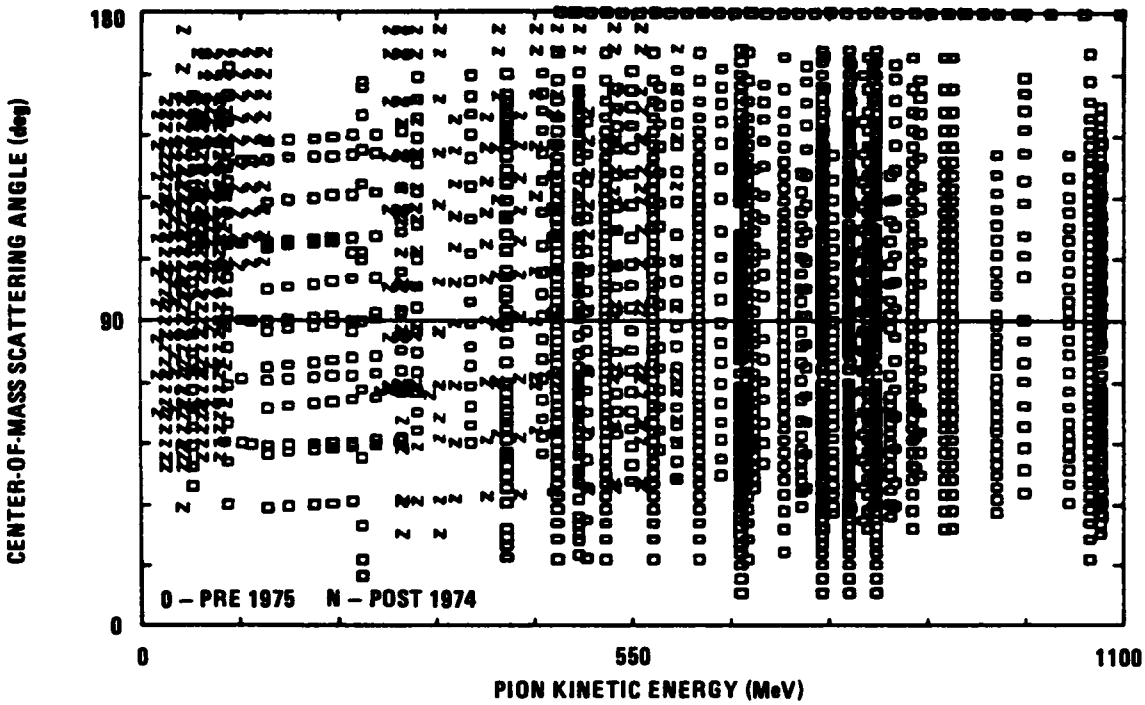

FIGURE 2-2. KINEMATIC VARIABLE SCATTER PLOT OF POSITIVE PION ELASTIC DIFFERENTIAL CROSS-SECTION DATA

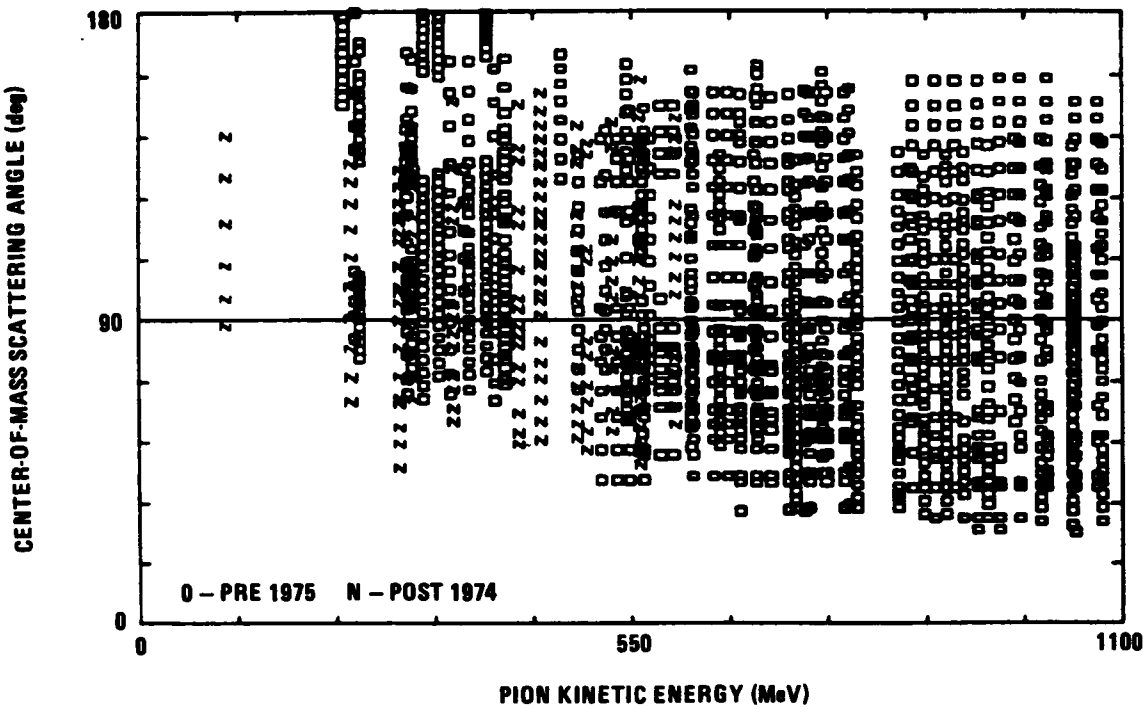

FIGURE 2-3. KINEMATIC VARIABLE SCATTER PLOT OF NEGATIVE PION ELASTIC POLARIZATION DATA

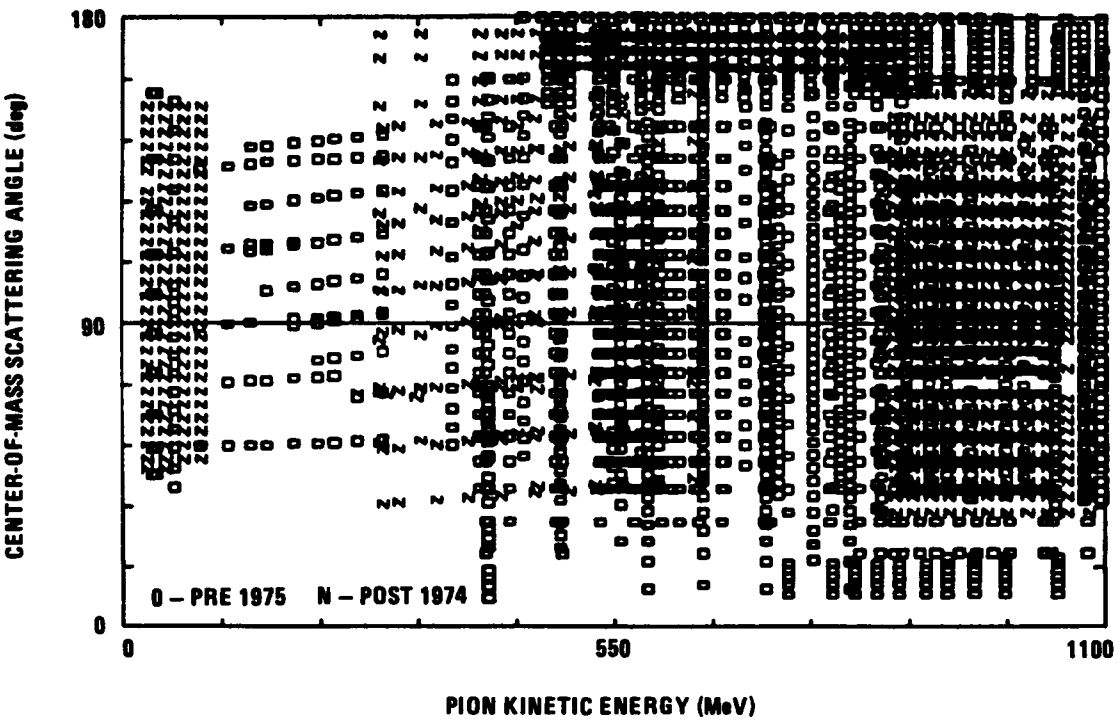

FIGURE 2-4. KINEMATIC VARIABLE SCATTER PLOT OF NEGATIVE PION ELASTIC DIFFERENTIAL CROSS-SECTION DATA

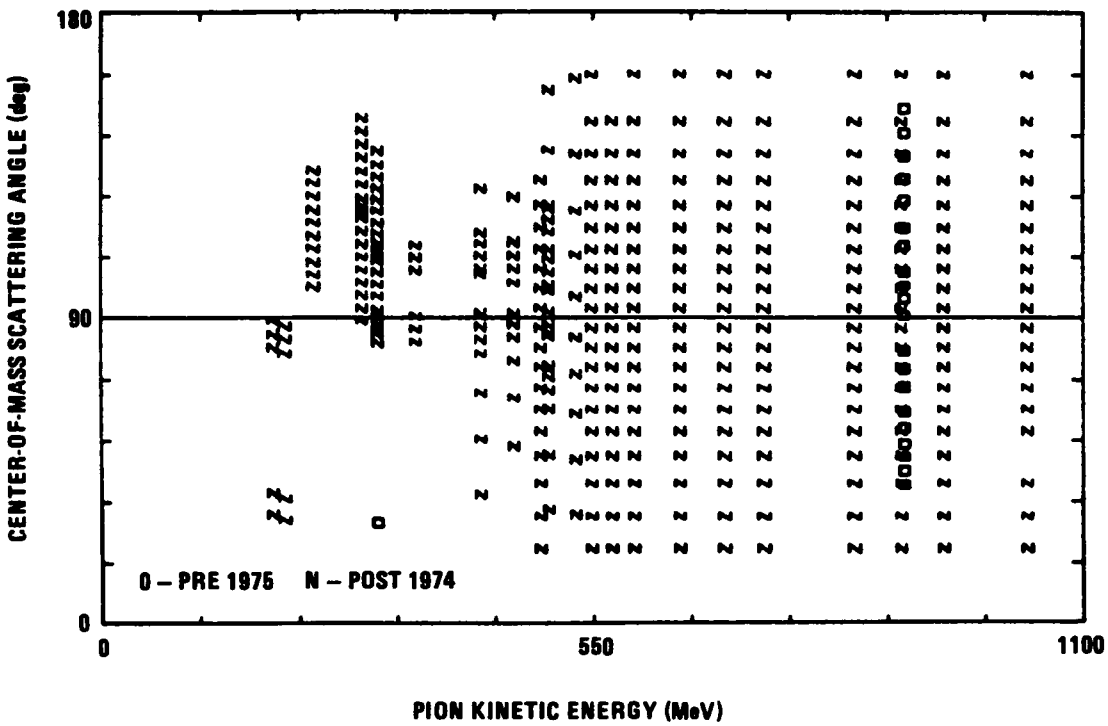

FIGURE 2-5. KINEMATIC VARIABLE SCATTER PLOT OF CHARGE EXCHANGE POLARIZATION DATA

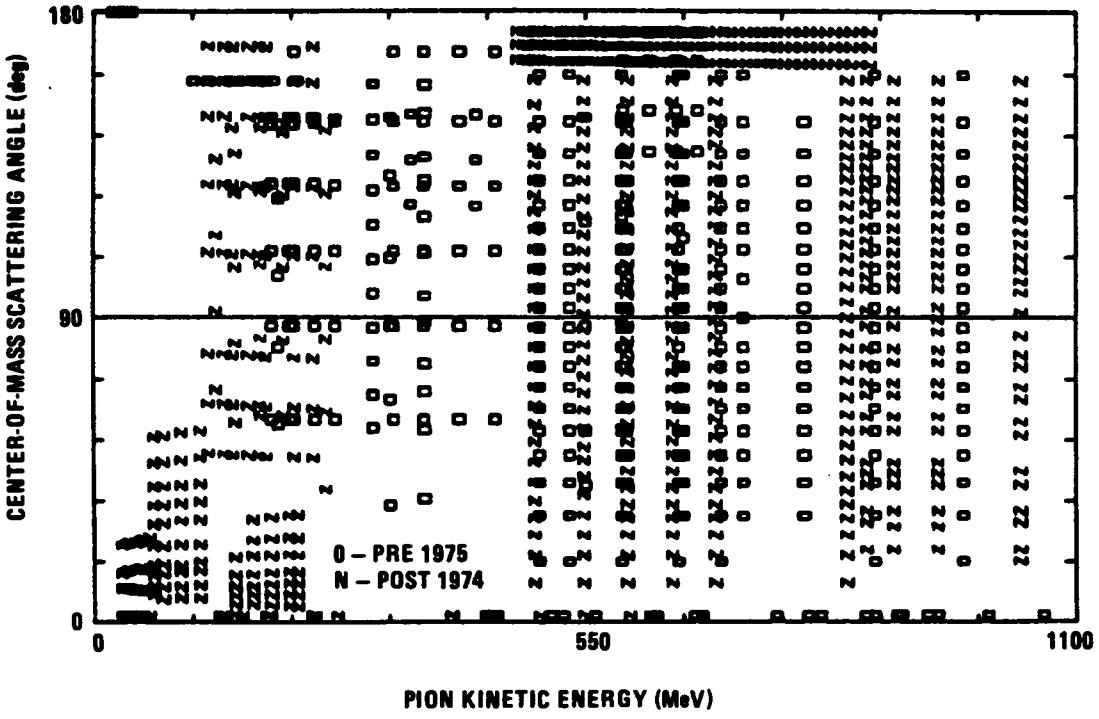

FIGURE 2-6. KINEMATIC VARIABLE SCATTER PLOT OF CHARGE EXCHANGE DIFFERENTIAL CROSS-SECTION DATA

of the three charge channels. In these plots each data point is indicated as being pre-1975 data with the label O for old data or as being post-1974 data with the label N for new data. The positive pion scattering is seen to cover the entire energy range relatively well except for a large 100-MeV gap in the low-energy polarization data and some much smaller gaps in the high-energy end of the differential cross-section data. There is also a lack of data in the far forward and backward directions, especially for polarization. The distribution of negative pion scattering data is similar to that of the positive. The negative pion polarization data also have a low-energy gap of about 200 MeV, with a dearth of data at the extreme angles. The negative pion cross sections are in better shape than the positive pion cross sections, with no significant gaps in angle or energy in the medium- and high-energy sections of the data base. More data at the low-energy end, especially at the extreme angles, would again be helpful. There are far fewer charge exchange data, although most of them are from recent (post-1974) experiments. The polarization data have major gaps in the low-energy end, while the low-energy, cross-section gap is smaller. Except for the low-energy, differential cross sections, the angle range does tend to be fairly well-covered. The *PI-N Newsletter*[7] describes an experiment planned by the SIN group to measure low-energy, differential cross sections of high quality. These results would remove many of the deficiencies in the low-energy part of the data base.

The total cross sections in the data base are dominated by the experiments of Carter-CA(68) and CA(71), Pedroni-PE(78), and Bulos-BU(69). New high-precision measurements of total cross sections over the entire energy range to verify these results would be very helpful. As alluded to in the next subsection, particular care would be needed to be taken in the determination of the pion's beam energy.

There are currently no measurements available in the energy range of this analysis for any of the spin observables other than polarization. To date, no experiments have been performed to measure the low-energy, spin rotation parameters, R and A, or the spin rotation angle, β. The *PI-N Newsletter* describes an experiment planned by the Leningrad group to make such a measurement. Such measurements would be very valuable for eliminating ambiguities.[8]

Originally included in the data base were values of the real part of the forward elastic scattering amplitude, Re[f(0)], determined by Carter and Carter-CA(73).[9] These quasi-data were calculated from forward dispersion relations using total cross sections and provided the only dispersion-theoretic constraint in the early stages of this analysis. This set of values has been supplanted by the newer set of real parts of the forward amplitude HO(79), obtained from Dr. G. Höhler of the Karlsruhe group.[10] Their results come from a dispersion-theory-based, partial-wave analysis. They are expected to be of greater validity than the older Carter values alone, at least partially, because they are based on a larger, newer, and better data

set. The Karlsruhe values provide the dispersion-theoretic constraint in all the results presented in this report.

2.2 EXCLUDED EXPERIMENTS

In addition to those data described above that have been omitted from the data base, there are other data that are in the data compilation but have been excluded from the analysis. Because data with large errors do little to constrain the analysis, polarization data with absolute errors greater than 0.2 have been excluded from the analysis. Most of these data come from source CO(69). Table 2-2 shows the χ^2 obtained from solution FP86 of those experiments in Table 2-1 that have a status of "X" and are excluded from the analysis. Of these, the total cross sections of Bizard-BI(66), Devlin-DE(65), and Sterling-ST(66) are all older experiments with relatively large errors and are inconsistent with the more precise measurements of CA(68), CA(71), and PE(78). The total elastic cross sections of Cason-CA(66) are inconsistent with other nearby data. The Davidson-DA(72) total cross sections have known problems,[11,12] particularly in the determination of the beam energy. From the same group as the Davidson experiment came the backward differential cross sections of Rothschild-RO(72). This experiment also has an apparent difficulty with its beam energy determination[12,13] but not in the same direction as DA(72). In addition, the data of both DA(72) and RO(72) are inconsistent with the remainder of the data base, as seen by their high χ^2, shown in Table 2-2. The Brown differential cross sections and polarization data, BR(76), BR(77), and BR(78), have also been excluded

TABLE 2-2. DATA EXCLUDED FROM ANALYSIS

SHORT ID	REACTION	OBSERVABLE	ENERGY*	χ^2	NO. OF DATA	$\chi 2$/ NDATA
BU(64)	CXS	SGTE	545 to 999	92.0	7	13.1
DE(65)	PI+P	SGT	497 to 1100	37.9	15	2.5
DE(65)	PI-P	SGT	418 to 1100	155.7	29	5.4
BI(66)	PI+P	SGT	310 to 698	145.7	20	7.3
BI(66)	PI-P	SGT	310 to 698	385.0	32	12.0
CA(66)	PI-P	SGTE	790 to 870	48.1	3	16.0
ST(66)	PI+P	SGT	525 to 1100	68.5	14	4.9
ST(66)	PI-P	SGT	540 to 1100	209.2	21	10.0
SL(71)	PI+P	P	598 to 846	709.0	130	5.5
DA(72)	PI+P	SGT	298 to 742	1483.0	25	59.3
DA(72)	PI-P	SGT	298 to 742	2902.0	25	116.1
RO(72)	PI+P	DSG	468 to 1100	2888.0	33	87.5
RO(72)	PI-P	DSG	449 to 1100	3066.0	34	90.2
CA(73)	PI+P	REF	21 to 1100	417.8	102	4.1
CA(73)	PI-P	REF	21 to 1100	301.9	102	3.0
BE(74)	PI+P	DSG	1064	1419.0	49	29.0
BR(76)	CXS	DSG	494 to 1100	4197.0	310	13.5
BR(77)	PI+P	P	649 to 747	270.0	48	5.6
BR(78)	CXS	P	493 to 1100	4857.0	215	22.5

*Kinetic energy of incident pion in laboratory frame (MeV)

from the analysis. The positive pion data of BR(77) have never been published in a refereed journal, and the scatter in the data appears unreasonable. The charge exchange data of BR(76) and BR(78) are described in the *PI-N Newsletter* as being controversial,[11] with the polarization data earning only one star out of three in the newsletter's quality rating scale. Bulos's charge exchange data, BU(64), have been supplanted by more recent and accurate data from the same group, BU(69). The differential cross sections of Berthon-BE(74) and the polarizations of Sleeman-SL(71) each have unreasonably small errors as compared with the considerable scatter in those data.

2.3 REFERENCES

1. P. Baillon *et al.*, *Physics Letters*, Vol. 50B, 1974, p. 387

2. O. Chamberlain, University of California Research Laboratory Report No. UCRL-17186, 1966

3. S. G. F. Frank, *Proceedings of the Physical Society of London*, Vol. 92, 1967, p. 609

4. R. Frascaria *et al.*, *Physics Letters*, Vol. 91B, 1980, p. 345

5. M. A. R. Kemp *et al.*, *Physics Letters*, Vol. 31B, 1970, p. 613

6. V. Z. Peterson, University of California Research Laboratory Report No. UCRL-11576, 1964

7. B. M. K. Nefkens and G. Höhler, *PI-N Newsletter*, No. 1, 1984, Sections 5 and 6

8. R. L. Kelly J. C. Sandusky, and R. E. Cutkosky, *Physical Review D*, Vol. 10, 1974, p. 2309

9. A. A. Carter and J. R. Carter, Rutherford Laboratory Report No. RL-73-024, 1973

10. R. Koch and E. Pietarinen, *Nuclear Physics*, Vol. A336, 1980, p. 331

11. B. M. K. Nefkens and G. Höhler, *PI-N Newsletter*, No. 1, 1984, p. 22

12. B. M. K. Nefkens, Personal Communication

13. B. M. K. Nefkens and G. Höhler, *ibid.*, p. 2.6, 2.7, and Table 14

3. THE PHASE-SHIFT ANALYSIS

The phase-shift analysis consisted of both an energy-dependent fit and 23 separate single-energy fits covering the pion laboratory kinetic energy range of 0 to 1100 MeV. The two types of analyses complement each other, with the energy-dependent solution permitting an investigation of the analytic structure of the amplitudes and a determination of resonance parameters. The single-energy analysis ensures that all structure in the amplitudes demanded by the data is encoded. The coupling of these two types of analyses results in mutually consistent solutions and hence the best of both approaches.

The objective of these analyses was primarily to obtain a precise and economical encoding of the data and was not to test dispersion theories. Consequently, a minimum amount of theoretical constraint is included. The only explicit dispersion theory constraint was the use of the forward dispersion relation derived real part of the forward scattering amplitude, quasi-data of the Karlsruhe group.[1] The approach being presented here is unlike other works, such as the Karlsruhe analysis,[2] which includes much dispersion theory.

The amplitudes used in this work are the usual spin-no-flip and spin-flip amplitudes, f and g. These amplitudes and their relation to the experimental observables are described in Appendix B. The amplitudes, f and g, are obtained from the parametrized, partial-wave T-matrices after applying the coulomb corrections to be discussed in Subsection 3.3. The partial waves were fitted with the standard approach of minimizing χ^2 where

$$\chi^2(p) = \sum_{i=1}^{N_D} \left[\frac{a^n \cdot \theta^i(p) - \theta^i_{exp}}{\sigma^i_{exp}} \right]^2 + \sum_{i=1}^{N_a} \left[\frac{a^i - 1}{\Delta a^i_{exp}} \right]^2 \qquad (3\text{-}1)$$

$\theta^i(p)$ = value of observable "i" determined from parameters [p]

θ^i_{exp} = experimental value of observable "i"

σ^i_{exp} = experimental standard deviation (error) of ith data point

a^n = normalization parameter for experiment n = n(i)

N_D = number of data points being fit

N_a = number of normalization parameters

Δa_{exp} = standard deviation of normalization parameter a^i.

In particular, the square error-matrix search method[3] was employed using the SHSZSA (Spin-Half Spin-Zero Scattering Analysis) code developed over the last 20 years by Dr. R. A. Arndt. SHSZSA is described in further detail in Appendix C.

3.1 THE ENERGY-DEPENDENT ANALYSIS

3.1.1 Parametrization of Energy-Dependent Partial Waves

The energy-dependent solution is parametrized by a multiple-channel Chew-Mandelstam K-matrix[4] whose elements are analytic functions of energy. For each partial wave, the K-matrix includes both the elastic π-N channel and the inelastic π-Δ channel of lowest orbital angular momentum to which the elastic channel can couple. In addition, because the S_{11} wave is known to couple strongly to the η-N channel,[5] this channel has been chosen as a second inelastic channel for the S_{11} wave. The π-Δ and η-N states of lowest orbital angular momentum to which the various π-N states can couple conserving total

momentum and parity are given in Table 3-1. Thus the S_{11} wave is modeled via a three-channel K-matrix and the other partial waves via two-channel K-matrices. The η-N channel is responsible for the S-wave eta production, clearly seen in Figure 4-1(c) as a cusp.

Because this is a phase-shift analysis of elastic scattering and covers a relatively low-energy range (0 to 1100 MeV), all the inelasticity was assumed to proceed only through the two (π-Δ or η-N) described two-particle intermediate states. That such an assumption does not detract from the analysis is obvious by the efficient encoding of the data resulting from this parametrization.

The real symmetric K-matrix for a given partial wave is of the form:

$$K = \begin{pmatrix} K_{ee} & K_{e1} & K_{e2} \\ K_{e1} & K_{11} & 0 \\ K_{e2} & 0 & K_{22} \end{pmatrix} \qquad (3\text{-}2)$$

where K_{e2} and K_{22} are zero except for the S_{11} wave. Each K-matrix element is parametrized as a polynomial in the barycentric energy, W, with an optional explicit pole term and is given by:

$$K_{ee} = p_1 + p_2 z + p_3 z^2 + p_4 z^3 + p_5 z^4 + \left[\frac{(p_{17}^2 + p_{19}^2)}{d} \right]$$

$$K_{ei} = p_{1+5i} + p_{2+5i} z + p_{3+5i} z^2 + \left[\frac{(p_{15+2i}) \cdot (p_{16+2i})}{d} \right] \qquad (3\text{-}3a)$$

TABLE 3-1. STATES (L_{2J}) OF LOWEST ORBITAL ANGULAR MOMENTUM THAT CAN COUPLE TO π-N

π-N STATE	π-Δ STATE I = 1/2, 3/2	η-N STATE I = 1/2
S_1	D_1	S_1
P_1	P_1	P_1
P_3	P_3	P_3
D_3	S_3	D_3
D_5	D_5	D_5
F_5	P_5	F_5
F_7	F_7	F_7
G_7	D_7	G_7
G_9	G_9	G_9
H_9	F_9	H_9
H_{11}	H_{11}	H_{11}
I_{11}	G_{11}	I_{11}
I_{13}	I_{13}	I_{13}

$$K_{ii} = p_{4+5i} + p_{5+5i}\, z + \left(\frac{p_{16+2i}^2}{d}\right), i = 1 \text{ or } 2$$

$$\text{with } z = \left[\frac{W - (M_\pi + M_N + 140\ MeV)}{1000\ MeV}\right], \text{ and } d = \left(\frac{p_{16} - W}{1000\ MeV}\right) \qquad (3\text{-}3b)$$

where W is the total barycentric energy and M_Π and M_N are the charged pion and proton masses, respectively. The parameters p_1 through p_{20} are those that are varied in the χ^2 minimization process. Parameters p_{17} and p_{18} serve as elastic and inelastic coupling constants, respectively, for the resonance pole given by the explicit K-matrix pole at $z = p_{16}$. In this analysis, only the first 18 parameters were actually used. Parameters p_{19} and p_{20} were always zero.

This Chew-Mandlestam K-matrix is related to the elastic element of the nuclear T-matrix for the same partial wave by:

$$\left(T_\ell\right)_n = \left[Im\,(C_\ell) * K_\ell\ (I - C_\ell * K_\ell)^{-1}\right]_{11} \qquad (3\text{-}4)$$

where I is the identity matrix and C is a diagonal matrix whose elements are dispersion integrals of phase space factors over the appropriate unitarity cuts:

$$\left(C_\ell\right)_{jk} = \delta_{jk}\ \frac{1}{\pi}\ \int_0^1 dx\ \frac{x^{\ell+1/2}}{x - \left(\frac{W - W_t}{W - W_s}\right)} \qquad (3\text{-}5)$$

ℓ = orbital angular momentum index

W = total barycentric energy

W_t = channel threshold energy

= $M_N + M_\pi$, for j = k = 1, the elastic channel

= $M_\Delta + M_\pi$, for j = k = 2, the inelastic π-Δ channel

= $M_N + M_\eta$, for j = k = 3, the inelastic η-N channel

W_s = subtraction point

= $M_N + M_\pi$ - 150 MeV, for the elastic channel

= $M_N + M_\pi$ + 140 MeV, for either inelastic channel

and

M_π = 139.5 MeV

M_N = 938.256 Mev

M_Δ = 1232.0 - i * 51.0 MeV

M_η = 549.0 - i * 2.5 MeV.

The imaginary components in the delta and eta masses reflect the short lifetimes of these two particles but are not meant to be identified with their true widths. The given values were chosen largely for the convenience of aiding the fitting process. The analytic structure of the C_ℓ's is discussed in detail in Appendix D. There, it is shown that the usual space factor (ρ in Reference 4) is just the imaginary part of C. That this choice of C gives the proper threshold dependence for the partial waves is also demonstrated in the appendix.

With the K-matrix parametrized as described above, the T-matrix is manifestly analytic in the barycentric energy variable, W, with much of the analytic structure provided by the C_ℓ's It is also necessary

for the T-matrix to obey unitarity. For $S = 1 + 2iT$, the generalized unitarity condition, $SS^{\dagger} \leq 1$, gives:

$$T^{\dagger}T \leq 1/2\ i\ (T^{\dagger} - T) \qquad (3\text{-}6)$$

with the equal signs holding for elastic unitarity. One can check this condition for those states that can be described by a two-channel K-matrix (all but the S_{11} wave in this analysis), by first making the following definitions:

$$\begin{aligned} \alpha &= K_e - C_i\ (K_{ee}\ K_{ii} - K_{ei}^2) \\ \beta &= 1 - C_i\ K_{ii} \\ \rho_e &= \mathrm{Im}\ \{C_e\} \\ \rho_i &= \mathrm{Im}\ \{C_i\}\ . \end{aligned} \qquad (3\text{-}7)$$

Simple algebraic manipulation then gives:

$$T = \rho_e\ \alpha/(\beta - C_e\alpha) \qquad (3\text{-}8)$$

from which it is straightforward to derive:

$$T^* T + \frac{\rho_e\ \rho_i K_{ei}^2}{|\beta - C_e\alpha|^2} = \frac{1}{2}\, i(T^* - T) \quad . \qquad (3\text{-}9)$$

Therefore, the nuclear T-matrix given by equation 3-4 will violate elastic unitarity for $\rho_e\rho_i \neq 0$ and will violate generalized unitarity for $\rho_e\rho_i < 0$. Similar conclusions can be reached for the S_{11} state whose partial T-matrix is derived from a three-channel K-matrix. Appendix D shows that, above the elastic threshold, ρ_e is strictly positive. Above the pion production threshold, ρ_i is also nonnegative and generalized unitarity is satisfied. It is below the pion

production threshold that a negative phase space factor in an inelastic channel can arise and result in a small violation of unitarity. The prescription used to correct this problem and to ensure unitarity everywhere is to take the real part of the effective one-dimensional K-matrix:

$$K_{eff} = \mathrm{Re}\,[T_n/(1 + i\,T_n)] \qquad (3\text{-}10)$$

with T_n defined by equation 3-4. Below the pion production threshold, K_{eff} is used to generate a new elastic unitary T-matrix:

$$T_{elastic} = K_{eff}/(1 - i\,K_{eff}). \qquad (3\text{-}11)$$

Because K_{eff} is explicitly real, the proof that $T_{elastic}$ satisfies elastic unitarity is now trivial.

3.1.2 Methodology for Energy-Dependent Analysis

With the T-matrix parametrized as described above, the search program, SHSZSA, was used to determine the values of the 13 parameters (18 for the S_{11} wave) available for fitting in each partial wave. S-waves through I-waves were fitted with higher peripheral waves being assumed to be negligible. The S-, P-, D-, and F-waves are the most important, with G, H, and I being smaller, peripheral waves. Because this analysis did not start in a vacuum but has been able to benefit from earlier analysis,[6] it was not necessary to start with completely unknown parameters. The present analysis began with an initial set of parameters obtained by the CAPS (Center for Analysis of Particle Scattering, VPI&SU) group during an older analysis based on an older,

incomplete data base and with a parametrization that did not allow for explicit poles in the expansion of the K-matrix elements. Those partial waves known to have prominent resonances in the energy range of this analysis were reinitialized, introducing the explicit poles described above by specifically fitting the waves to either the results of preliminary single-energy fits or to the Karlsruhe[7] partial waves. The analysis consisted of a great many iterations of the search program, and the energy-dependent solutions were regularly compared with the results of the single-energy analysis. Occasionally, specific partial waves were reparametrized with a different subset of the 13 (or 18) parameters being selected for fitting and the other parameters fixed at zero. During this iteration process, it became obvious that the experiments described in Subsection 2.2 were "bad," and the decision was made to omit them from further analysis. The energy-dependent solution obtained in this manner has been designated FA86 for "Fall 1986."

3.1.3 The Energy-Dependent Solution

Solution FA86 and six other energy-dependent solutions are summarized in Table 3-2. For each of the solutions, the breakdown of χ^2, number of data, and number of parameters are given.

After developing FA86, the effects of pruning the data were investigated. A number of individual data points had been found to give very large contributions to FA86's total χ^2. By pruning these data with χ^2 contributions greater than 16, overall χ^2 was reduced by slightly over 20 percent with less than 2 percent of the data being

TABLE 3-2. SUMMARY OF ENERGY-DEPENDENT SOLUTIONS

	FP86	FA86	HP86	JP86	PLUS	MNUS	SPLT
Total χ^2	15,645	19,776	15,878	15,572	5,593	9,819	9,812
Total Data (N_d)	9,493	9,630	9,493	9,493	3,739	5,754	5,754
Total Parameters (N_p)	131	131	119	139	61	131	131
$\chi 2/(N_d - N_p)$	1.67	2.08	1.69	1.66	1.52	1.75	1.74
PI + P Data	3,739	3,782	3,739	3,739	3,739	0	0
$\chi 2$ for PI + P Data	5,699	7,233	5,780	5,692	5,593	--	--
PI - P Data	4,881	4,957	4,881	4,881	0	4,881	4,881
$\chi 2$ for PI - P Data	8,155	10,099	8,296	8,085	--	8,131	8,064
CXS Data	873	891	873	873	0	873	873
$\chi 2$ for CXS Data	1,790	2,443	1,801	1,795	--	1,688	1,747
I = 3/2 Parameters	61	61	55	65	61	61	8 + (53)*
I = 1/2 Parameters	70	70	64	74	0	(70)*	70

*These parameters were not varied from their solution FP86 values.

eliminated. The χ^2 per data point limit of 16 is equivalent to 4 standard deviations and certainly is a reasonable cutoff to prune single-data points obviously inconsistent with the rest of the data. The pruned data are in addition to those experiments specifically excluded from the analysis. In addition to inflating χ^2, these data were also frustrating the χ^2 minimization search algorithm. Much cleaner searches resulted after a prune. By applying the above-described pruning procedure iteratively, prune, search, reprune, search, etc., solution FP86 was developed. For the details of the χ^2 comparison between FP86 and FA86, see Table 3-2. With so few data pruned, the two solutions would be expected to be similar, and, as it turns out, they are very close to each other. One comparison between the two solutions is that of parameter 16, the position of the explicit K-matrix pole encoded in most of the major waves. This comparison is made in Table 3-3, and in only one case, P_{31}, does the difference exceed 1 percent. The P_{31} difference is about 1.2 percent, but the K-matrix pole position (2500 MeV) is at an energy considerably greater than that for which the analysis is valid and hence is not expected to be well-determined.

The approach used in this analysis of fitting individual waves necessitates the use of a finite number of waves in the summation defining amplitudes f and g. The usual arguments against such a cutoff include partial-wave indeterminancy caused by the continuum ambiguity. Such arguments are not entirely valid for this analysis because a number of peripheral waves, up through I-waves, are

TABLE 3-3. SENSITIVITY OF K-MATRIX EXPLICIT POLE POSITION TO PRUNING OF DATA AND TO THE NUMBER OF PERIPHERAL WAVES IN SOLUTION

WAVES	SOLUTION			
	HP86 (H-WAVES)	FA86 (I-WAVES)	FP86 (I-WAVES)	JP86 (J-WAVES)
S_{11}	1678.7	1673.3	1677.4	1677.5
S_{31}	1644.8	1639.5	1644.5	1643.9
P_{11}	1576.3	1574.6	1576.4	1575.9
P_{13}	1688.3	1704.9	1693.5	1696.2
P_{31}	2583.9	2473.8	2504.4	2504.5
P_{33}	1283.2	1283.4	1283.3	1283.3
D_{13}	1578.4	1586.1	1577.9	1581.0
D_{15}	1699.7	1700.0	1699.7	1699.6
D_{33}	1668.6	1655.4	1666.1	1666.3
D_{35}	2571.1	2593.2	2610.7	2569.7
F_{15}	1702.5	1700.4	1701.4	1701.8
F_{35}	1856.4	1879.7	1867.7	1879.4
F_{37}	1935.6	1934.0	1934.6	1932.6
G_{17}	1789.9	1791.1	1797.2	1791.2

included. Also, the constraint of fitting such a large number of data over a wide-energy range limits the sensitivity of the major waves to the precise number of partial waves included. Solutions HP86 and JP86 are a test of this sensitivity. HP86 is an energy-dependent solution for which only waves through ℓ = H are included. Those partial waves with $\ell > 5$ have been set equal to zero. Solution JP86 includes, in addition, both the I- and J-waves. Solutions HP86 and JP86 are based on the same pruned data set as solution FP86. If HP86 and JP86 are compared with FP86 in Table 3-2, it is obvious that χ^2 changes minimally with the number of peripheral waves. Certainly, given that JP86 has more parameters (139 vs. 131) than FP86, the essentially identical χ^2 per degree of freedom (1.66 vs. 1.67) does not justify the inclusion of the J- and higher waves. The accuracy and extent of the currently available data do not require additional peripheral waves. Table 3-3, which shows the values of the K-matrix explicit pole positions for the three solutions, also justifies this conclusion.

The three other solutions in Table 3-2 are PLUS, MNUS, and SPLT. They constitute a test of isospin invariance in the energy-dependent solution. Solution PLUS began with FP86 and resulted from an analysis of only the positive pion scattering data. Solution MNUS also began with FP86, but only the negative pion elastic and charge exchange scattering data are analyzed. For solution MNUS, the values of the I = 1/2 parameters are fixed at the FP86 values. The I = 3/2 parameters alone were varied in arriving at solutions PLUS and MNUS. By allowing the I = 3/2 parameters to differ in the analysis of the positive and

negative pion data, a check is made of the dependence of the I = 3/2 partial waves on charge channel beyond the coulomb corrections discussed in Subsection 3.3. Although the χ^2 for the positive pion data is 1.9 percent less in PLUS than in FP86 (5699 vs. 5593) and the χ^2 for negative pion and charge exchange scattering is 1.3 percent less in MNUS than in FP86 (9819 vs. 9,945), the decrease is not significant considering that solutions PLUS and MNUS together have effectively more parameters to fit the same data than does solution FP86. In fact, combining the results of solutions PLUS and MNUS results in a chi-squared per degree of freedom negligibly better (1.66 vs. 1.67) than solution FP86. Solution SPLT is a further check on charge independence. As with MNUS, the negative pion scattering data alone are analyzed, but it is the I = 1/2 waves along with the single I = 3/2 wave, P_{33} that are varied. By distinguishing between the P_{33} wave in positive and negative pion scattering, Tromberg *et al.*[8] claim a check is made for short-range electromagnetic effects not accounted for by the charge corrections (Subsection 3.3) of this analysis. The reduction in chi-squared per degree of freedom of the negative pion data from 1.67 for FP84 to 1.65 for SPLT, less than 2 percent, is again not conclusive evidence for charge splitting in the current world data base of pion-nucleon scattering.

FP86 is the solution on which most of the results in this paper are based. The pruned data base upon which FP86 is based provides a clearly superior representation of elastic pion-nucleon scattering below 1100 MeV over that of the unpruned data. The author believes

solution FP86 to be the best energy-dependent fit to date in this energy range. Almost 9,500 data have been fitted to a χ^2 of 15,645 with only 131 variable parameters. The values of all parameters for solution FP86 are given in Table 3-4.

3.2 THE ENERGY-INDEPENDENT ANALYSES

3.2.1 Parametrization of Energy-Independent Partial Waves

Phase-shift analyses at specific energies serve to test the data for any structure that may not be properly encoded by an inherently smooth energy-dependent analysis. Because it is desirable to employ a form-independent parametrization to avoid unwanted biases in the solution, the phase shift, δ, and the inverse cosine of the inelasticity, ρ, have been chosen as the parameters to be fitted at each energy for which an analysis is performed. The phase shift and inelasticity are related to partial wave S- and T-matrices by:

$$S_\ell = \cos(\rho_\ell)\, e^{2i\delta_\ell} = 1 + 2iT_\ell \qquad (3\text{-}12)$$

where ℓ labels the partial waves' orbital angular momentum. In an energy bin for which a single-energy analysis is being performed, only the actual values of the partial wave parameters, δ and ρ, are fitted. Such a natural parametrization obviously obeys elastic unitarity.

3.2.2 Methodology For Single-Energy Analyses

To cover the energy range of the energy-dependent analysis, data were binned at 23 energies from 30 to 1100 MeV. For the final iterations of the single-energy solutions, the data base was first

TABLE 3-4. SOLUTION FP86 PARAMETERS (Sheet 1 of 4)

PARAMETER NUMBER	PARTIAL WAVE						
	S_{11}	S_{31}	P_{11}	P_{13}	P_{31}	P_{33}	D_{13}
1	0.052256	-0.47980	-0.20830	-0.10350	-1.6766	-0.095203	0.099873
2	-0.36185	-1.7135	2.1852	-0.29587	-2.4550	0.98283	0.42203
3	0	1.0743	0	0	0	0	0
4	0	0	0	0	0	0	0
5	0	0	0	0	0	0	0
6	0	0	0	0	0.42247	-0.25703	0
7	-0.81779	-0.55943	9.1881	-1.1138	0	2.4367	2.3506
8	0	-0.73341	-20.416	0	0	0	-4.089
9	0	0	-2.3856	0	0	-3.3640	-7.2918
10	0	0	10.786	0	0	9.7021	18.019
11	0.37750	0	0	0	0	0	0
12	1.2015	0	0	0	0	0	0
13	0	0	0	0	0	0	0
14	-1.5539	0	0	0	0	0	0
15	8.8897	0	0	0	0	0	0
16	1677.4	1644.5	1576.4	1693.5	2504.4	1283.3	1577.9
17	0.27938	0.18872	0.32447	0.032178	1.3504	0.39864	0.2663
18	0.15061	0.40032	0.35693	0.24062	-0.053512	0.025217	0.33671

TABLE 3-4. SOLUTION FP86 PARAMETERS (Sheet 2 of 4)

PARAMETER NUMBER	PARTIAL WAVE						
	D_{15}	D_{33}	D_{35}	F_{15}	F_{17}	F_{35}	F_{37}
1	0.053329	-0.11008	-0.35603	-0.11193	-0.07128	-0.10657	-0.097120
2	-0.033254	0	-0.76566	-0.16042	0	0	0
3	0	0	0	0	0	0	0
4	0	0	0	0	0	0	0
5	0	0	0	0	-0.47441	0	0
6	0	0	0	-0.2572	0	0	-0.17739
7	-0.22326	-0.073011	-2.1816	0	0	0	0
8	0	0	0	0	0	0	0
9	0	0	0	0	63.577	0	0
10	0	0	0	0	-110.87	0	0
11	0	0	0	0	0	0	0
12	0	0	0	0	0	0	0
13	0	0	0	0	0	0	0
14	0	0	0	0	0	0	0
15	0	0	0	0	0	0	0
16	1699.7	1666.1	2610.7	1701.4	0	1867.7	1934.6
17	0.23648	0.1661	0.71615	0.27060	0	0.16848	0.31664
18	0.32785	0.39112	1.0518	0.23284	0	0.36163	0.38133

TABLE 3-4. SOLUTION FP86 PARAMETERS (Sheet 3 of 4)

PARAMETER NUMBER	PARTIAL WAVE						
	G_{17}	G_{19}	G_{37}	G_{39}	H_{19}	H_{111}	H_{39}
1	0.018682	-0.061615	-0.011323	0.021847	0.000040	-0.045007	-0.001175
2	0	0.21022	0.034969	-0.098811	0.043586	0.14019	0.022797
3	0	0	0	0	0	0	0
4	0	0	0	0	0	0	0
5	0	0	0	0	0	0	0
6	0	0	0	0	0	0	0
7	-1.1550	0.86854	0.001186	0.59278	0.24801	0.96707	0.097090
8	0	0	0	0	0	0	0
9	0	0	0	0	0	0	0
10	0	0	0	0	0	0	
11	0	0	0	0	0	0	0
12	0	0	0	0	0	0	0
13	0	0	0	0	0	0	0
14	0	0	0	0	0	0	0
15	0	0	0	0	0	0	0
16	1797.2	0	0	0	0	0	0
17	0.09205	0	0	0	0	0	0
18	0.43774	0	0	0	0	0	0

TABLE 3-4. SOLUTION FP86 PARAMETERS (Sheet 4 of 4)

PARAMETER NUMBER	PARTIAL WAVE				
	H_{311}	I_{111}	I_{113}	I_{311}	I_{313}
1	-0.031151	0.023162	-0.056285	-0.012116	-0.007283
2	-0.10886	-0.069667	0.21357	0.034167	-0.023404
3	0	0	0	0	0
4	0	0	0	0	0
5	0	0	0	0	0
6	0	0	0	0	0
7	0.77580	-0.12027	0.036197	-0.31877	0.15036
8	0	0	0	0	0
9	0	0	0	0	0
10	0	0	0	0	0
11	0	0	0	0	0
12	0	0	0	0	0
13	0	0	0	0	0
14	0	0	0	0	0
15	0	0	0	0	0
16	0	0	0	0	0
17	0	0	0	0	0
18	0	0	0	0	0

pruned with solution FP86. In each bin, the partial-wave parameters were assumed to be linearly dependent on energy with:

$$\delta(E) = \delta_0 + D * (E - E_0)$$
$$\rho(E) = \rho_0 + R * (E - E_0) \quad . \tag{3-13}$$

For an analysis energy, E_0, the initial values of the parameters for the bin given by $EL < E_0 < EU$ were extracted from solution FP86 by an inversion of equation 3-12 to yield:

$$\rho(E) = \cos^{-1}\left[|1 + 2iT(E)|^2\right]$$
$$\delta(E) = 1/2 \sin^{-1}\left[Im\left\{\frac{2T(E)}{\cos[\rho(T)]}\right\}\right] \tag{3-14}$$

with

$$\delta_0 = \delta(E_0)$$
$$\rho_0 = \rho(E_0)$$
$$D = [\delta(EL) - \delta(EU)]/(EL - EU)$$
$$R = [\rho(EL) - \rho(EU)]/(EL - EU). \tag{3-15}$$

A check on the assumption of linearity was made by comparing the χ^2 in each bin obtained directly from solution FP86 with that resulting from linearization. An excessive (>30 percent) increase in χ^2 upon linearization indicated a need to narrow the bin size. Bin sizes were ultimately decided upon by the tradeoff between maximizing the number of data in the bin and minimizing any increase in χ^2 caused by linearization. For each partial wave, only δ_0 and ρ_0 were varied during an analysis. Slopes D and R were kept fixed at their FP86 derived values. At each analysis energy, not every partial wave was fitted.

The decision to search a particular wave in the single-energy analyses was based on the criteria of requiring that either $0.5 * (2J+1) * \text{Im}\{T_\ell\}$ or $0.5 * (2J+1) * [\text{Im}\{T_\ell\} - |T|^2]$ as obtained from the energy-dependent solution FP86 exceed a minimum value, typically 0.014. The values of these two expressions are proportional to the partial total and partial inelastic cross sections, respectively. Once a wave was searched at any one energy, it was then searched at each higher energy. The number of searched parameters went from a low of 4 at 30 MeV to a high of 35 at 1100 MeV. The unsearched waves were not set to zero but were fixed at their FP86 values. The contributions from unsearched waves were most important at the lower energies where the data base is too sparse to support the direct determination of the smaller waves.

3.2.3 The Energy-Independent Solutions

The results of the single-energy analyses are given in Table 3-5 The real and imaginary parts of the T-matrix for each searched partial wave are given with the associated error as determined from the chi-squared error matrix. Plots of these results with the energy-dependent partial waves are given in Figure 3-1. The high degree of consistency between the single-energy and energy-dependent solutions evident in these plots reinforces our confidence that all the structure in the amplitudes demanded by the data is encoded. The error bars shown are those obtained from the error matrix (see Appendix C). For some of the partial waves, such as P_{13}, the errors appear precipitously large near 650 MeV with irregular behavior

TABLE 3-5. SINGLE-ENERGY ANALYSES SOLUTIONS (Sheet 1 of 3)

C 3 Tlab= 30 MeV(20- 40 Ndata=127
Npar= 4 Chi2= 143 Chi2(ed)=(199, 230)

Wave	Delta (Err)	Rho (Err)
S11	5.502(0.077)	0.000(0.010)
S31	-3.855(0.125)	0.000(0.010)
P11	-0.651(0.068)	0.000(0.010)
P33	2.543(0.040)	0.000(0.010)

C 5 Tlab= 50 MeV(35- 65 Ndata=152
Npar= 5 Chi2= 225 Chi2(ed)=(286, 316)

Wave	Delta (Err)	Rho (Err)
S11	6.942(0.113)	0.000(0.010)
S31	-5.522(0.123)	0.000(0.010)
P11	-1.110(0.068)	0.000(0.010)
P31	-0.886(0.042)	0.000(0.010)
P33	6.483(0.043)	0.000(0.010)

C 10 Tlab= 100 MeV(88- 110 Ndata=137
Npar= 6 Chi2= 162 Chi2(ed)=(181, 307)

Wave	Delta (Err)	Rho (Err)
S11	8.717(0.184)	0.000(0.010)
S31	-9.431(0.130)	0.000(0.010)
P11	-1.039(0.196)	0.000(0.010)
P13	-1.010(0.165)	0.000(0.010)
P31	-2.093(0.085)	0.000(0.010)
P33	22.203(0.053)	0.000(0.010)

C 15 Tlab= 150 MeV(140- 160 Ndata= 70
Npar= 6 Chi2= 118 Chi2(ed)=(139, 147)

Wave	Delta (Err)	Rho (Err)
S11	8.669(0.203)	0.000(0.010)
S31	-12.685(0.650)	0.000(0.010)
P11	-0.635(0.343)	0.000(0.010)
P13	-1.949(0.216)	0.000(0.010)
P31	-3.812(0.335)	0.000(0.010)
P33	55.915(0.162)	0.000(0.010)

C 20 Tlab= 200 MeV(190- 210 Ndata= 91
Npar= 6 Chi2= 117 Chi2(ed)=(141, 145)

Wave	Delta (Err)	Rho (Err)
S11	11.399(0.504)	0.000(0.010)
S31	-15.511(0.277)	0.000(0.010)
P11	0.208(1.241)	0.004(0.010)
P13	-1.367(0.665)	0.000(0.010)
P31	-6.184(0.367)	0.001(0.010)
P33	97.622(0.288)	0.000(0.010)

C 25 Tlab= 250 MeV(240- 265 Ndata=150
Npar= 6 Chi2= 259 Chi2(ed)=(280, 292)

Wave	Delta (Err)	Rho (Err)
S11	11.306(0.317)	0.000(0.010)
S31	-18.463(0.137)	0.001(0.010)
P11	8.743(0.273)	0.033(0.019)
P13	-2.694(0.158)	0.000(0.010)
P31	-7.837(0.167)	0.005(0.010)
P33	121.810(0.103)	0.000(0.010)

C 30 Tlab= 300 MeV(285- 315 Ndata=341
Npar= 8 Chi2= 424 Chi2(ed)=(487, 487)

Wave	Delta (Err)	Rho (Err)
S11	10.905(0.152)	0.001(0.010)
S31	-21.501(0.093)	0.002(0.010)
P11	15.464(0.153)	0.086(0.010)
P13	-3.932(0.117)	0.001(0.010)
P31	-9.434(0.096)	0.010(0.010)
P33	134.230(0.101)	0.001(0.010)
D13	4.338(0.079)	0.010(0.011)

C 35 Tlab= 350 MeV(330- 370 Ndata=275
Npar= 8 Chi2= 400 Chi2(ed)=(422, 424)

Wave	Delta (Err)	Rho (Err)
S11	12.828(0.293)	0.001(0.010)
S31	-23.668(0.105)	0.004(0.010)
P11	26.589(0.266)	0.274(0.012)
P13	-4.749(0.252)	0.003(0.010)
P31	-10.706(0.130)	0.018(0.014)
P33	142.340(0.089)	0.000(0.010)
D13	6.807(0.120)	0.026(0.017)

C 40 Tlab= 400 MeV(375- 425 Ndata=399
Npar= 9 Chi2= 720 Chi2(ed)=(727, 730)

Wave	Delta (Err)	Rho (Err)
S11	14.582(0.412)	0.003(0.010)
S31	-25.308(0.148)	0.007(0.010)
P11	39.916(0.570)	0.564(0.012)
P13	-4.413(0.246)	0.007(0.010)
P31	-12.146(0.106)	0.029(0.018)
P33	148.310(0.151)	0.000(0.010)
D13	10.050(0.113)	0.068(0.010)

C 45 Tlab= 450 MeV(425- 475 Ndata=322
Npar=12 Chi2= 540 Chi2(ed)=(585, 610)

Wave	Delta (Err)	Rho (Err)
S11	16.685(0.443)	0.005(0.010)
S31	-26.790(0.153)	0.013(0.012)
P11	50.656(0.704)	0.746(0.010)
P13	-5.730(0.309)	0.016(0.013)
P31	-13.458(0.133)	0.042(0.021)
P33	153.000(0.137)	0.003(0.010)
D13	15.272(0.154)	0.176(0.017)
D15	3.865(0.143)	0.011(0.011)
D33	-0.126(0.103)	0.024(0.010)

C 50 Tlab= 500 MeV(485- 515 Ndata=370
Npar=15 Chi2= 658 Chi2(ed)=(710, 719)

Wave	Delta (Err)	Rho (Err)
S11	20.840(0.704)	0.013(0.012)
S31	-27.747(0.204)	0.024(0.016)
P11	60.095(1.733)	0.851(0.013)
P13	-6.376(0.507)	0.027(0.042)
P31	-14.522(0.195)	0.055(0.024)
P33	157.360(0.153)	0.015(0.013)
D13	23.556(0.482)	0.264(0.026)
D15	4.101(0.276)	0.087(0.024)
D33	0.562(0.114)	0.079(0.010)
F15	4.107(0.182)	0.000(0.010)

C 55 Tlab= 550 MeV(535- 565 Ndata=413
Npar=18 Chi2= 682 Chi2(ed)=(740, 849)

Wave	Delta (Err)	Rho (Err)
S11	30.547(0.844)	0.195(0.028)
S31	-28.894(0.238)	0.046(0.022)
P11	84.529(2.821)	0.939(0.015)
P13	-5.781(0.686)	0.051(0.061)
P31	-15.747(0.276)	0.048(0.010)
P33	161.050(0.161)	0.032(0.010)
D13	37.664(1.126)	0.661(0.021)
D15	6.194(0.328)	0.080(0.021)
D33	0.751(0.118)	0.139(0.010)
F15	6.085(0.380)	0.000(0.010)

*Each solution is characterized by a binning range (in brackets), by the number of searched parameters (Npar), chi-squared (chi2), and the number of data (Ndata) used for analysis. The two numbers listed for chi2(ed) are the chi-squared for FP86 for the selected data set, and the chi-squared after linearization and before searching.

- TABLE 3-5. SINGLE-ENERGY ANALYSES SOLUTIONS (Sheet 2 of 3)

C 60 Tlab= 600 MeV(585- 615 Ndata=321
Npar=19 Chi2= 465 Chi2(ed)=(532, 548)

Wave	Delta (Err)	Rho (Err)
S11	34.834(2.854)	0.753(0.029)
S31	-28.883(0.278)	0.100(0.024)
P11	97.663(5.721)	0.950(0.017)
P13	-6.282(0.706)	0.156(0.052)
P31	-17.402(0.556)	0.044(0.013)
P33	164.960(0.300)	0.066(0.011)
D13	78.688(3.333)	0.953(0.015)
D15	8.332(0.525)	0.035(0.028)
D33	0.811(0.259)	0.171(0.013)
F15	6.803(0.580)	0.004(0.010)

C 70 Tlab= 700 MeV(685- 715 Ndata=243
Npar=28 Chi2= 314 Chi2(ed)=(416, 423)

Wave	Delta (Err)	Rho (Err)
S11	22.951(1.939)	0.601(0.056)
S31	-23.685(0.838)	0.518(0.034)
P11	121.840(4.911)	0.948(0.018)
P13	-9.432(0.977)	0.227(0.088)
P31	-24.134(0.837)	0.041(0.044)
P33	170.940(0.616)	0.220(0.019)
D13	147.270(1.867)	0.732(0.037)
D15	13.133(0.561)	0.084(0.044)
D33	0.671(0.516)	0.273(0.021)
D35	-2.906(0.439)	0.002(0.010)
F15	12.179(0.631)	0.033(0.075)
F35	-0.431(0.233)	0.041(0.018)
F37	3.941(0.222)	0.009(0.010)
G17	2.000(0.433)	0.000(0.010)
G19	0.583(0.292)	0.013(0.010)

C 80 Tlab= 800 MeV(785- 815 Ndata=418
Npar=31 Chi2= 607 Chi2(ed)=(728, 723)

Wave	Delta (Err)	Rho (Err)
S11	46.427(1.222)	0.246(0.052)
S31	-45.995(1.156)	0.763(0.033)
P11	136.020(2.091)	0.897(0.016)
P13	-6.407(0.757)	0.099(0.042)
P31	-21.952(0.923)	0.064(0.045)
P33	172.200(0.551)	0.503(0.027)
D13	161.210(0.978)	0.651(0.029)
D15	23.502(0.401)	0.633(0.026)
D33	-0.102(0.470)	0.391(0.019)
D35	-4.675(0.391)	0.014(0.012)
F15	29.856(0.546)	0.396(0.036)
F35	0.480(0.204)	0.087(0.016)
F37	6.855(0.185)	0.038(0.020)
G17	0.106(0.505)	0.025(0.029)
G19	0.461(0.197)	0.000(0.011)
G39	-0.457(0.163)	0.011(0.010)

C 65 Tlab= 650 MeV(635- 665 Ndata=281
Npar=22 Chi2= 471 Chi2(ed)=(569, 559)

Wave	Delta (Err)	Rho (Err)
S11	35.619(3.794)	0.867(0.026)
S31	-26.779(0.443)	0.128(0.050)
P11	109.300(7.030)	0.955(0.014)
P13	-8.190(0.736)	0.062(0.029)
P31	-19.924(0.759)	0.028(0.027)
P33	168.090(0.564)	0.150(0.021)
D13	135.650(3.191)	0.878(0.019)
D15	8.931(0.389)	0.087(0.022)
D33	1.866(0.487)	0.253(0.025)
F15	9.650(0.517)	0.015(0.013)
F35	0.033(0.263)	0.003(0.014)
F37	3.516(0.243)	0.005(0.010)

C 75 Tlab= 750 MeV(730- 770 Ndata=443
Npar=29 Chi2= 593 Chi2(ed)=(685, 667)

Wave	Delta (Err)	Rho (Err)
S11	33.702(1.722)	0.455(0.050)
S31	-31.350(0.514)	0.759(0.030)
P11	128.730(3.767)	0.921(0.016)
P13	-6.544(0.642)	0.024(0.053)
P31	-19.463(0.591)	0.105(0.040)
P33	171.530(0.424)	0.424(0.019)
D13	156.690(1.249)	0.634(0.040)
D15	16.985(0.385)	0.346(0.044)
D33	1.260(0.243)	0.297(0.014)
D35	-4.571(0.299)	0.006(0.010)
F15	19.944(0.484)	0.215(0.045)
F35	0.012(0.159)	0.044(0.015)
F37	5.254(0.171)	0.013(0.016)
G17	0.853(0.469)	0.020(0.039)
G19	0.291(0.194)	0.020(0.015)

C 85 Tlab= 850 MeV(830- 870 Ndata=443
Npar=32 Chi2= 648 Chi2(ed)=(729, 783)

Wave	Delta (Err)	Rho (Err)
S11	65.270(1.226)	0.349(0.052)
S31	-51.078(1.112)	0.708(0.038)
P11	150.120(1.605)	0.818(0.026)
P13	-7.133(0.852)	0.021(0.041)
P31	-22.691(1.022)	0.111(0.041)
P33	173.310(0.581)	0.538(0.028)
D13	160.600(0.824)	0.573(0.044)
D15	23.529(0.952)	0.908(0.012)
D33	-1.948(0.516)	0.458(0.015)
D35	-4.399(0.403)	0.000(0.010)
F15	48.881(1.051)	0.778(0.015)
F35	0.329(0.202)	0.113(0.014)
F37	7.941(0.152)	0.036(0.023)
G17	0.581(0.535)	0.034(0.029)
G19	1.612(0.319)	0.058(0.018)
G39	-0.731(0.186)	0.008(0.012)

*Each solution is characterized by a binning range (in brackets), by the number of searched parameters (Npar), chi-squared (chi2), and the number of data (Ndata) used for analysis. The two numbers listed for chi2(ed) are the chi-squared for FP86 for the selected data set, and the chi-squared after linearization and before searching.

TABLE 3-5. SINGLE-ENERGY ANALYSES SOLUTIONS (Sheet 3 of 3)

C 90 Tlab= 900 MeV(880- 920 Ndata=489
Npar=32 Chi2= 620 Chi2(ed)=(717,1054)

Wave	Delta (Err)	Rho (Err)
S11	87.422(0.798)	0.334(0.041)
S31	-50.446(1.102)	0.436(0.047)
P11	161.360(1.020)	0.647(0.037)
P13	-5.864(0.832)	0.032(0.015)
P31	-20.503(0.847)	0.070(0.052)
P33	173.650(0.886)	0.582(0.026)
D13	163.690(0.747)	0.460(0.041)
D15	-20.238(1.183)	0.968(0.010)
D33	-5.545(0.763)	0.508(0.017)
D35	-3.092(0.465)	0.001(0.010)
F15	106.320(1.937)	0.970(0.010)
F35	0.180(0.346)	0.148(0.018)
F37	8.673(0.252)	0.105(0.023)
G17	1.990(0.307)	0.028(0.021)
G19	1.288(0.352)	0.060(0.014)
G39	0.117(0.252)	0.015(0.018)

C 95 Tlab= 950 MeV(925- 975 Ndata=610
Npar=38 Chi2= 708 Chi2(ed)=(830, 904)

Wave	Delta (Err)	Rho (Err)
S11	105.840(1.795)	0.488(0.048)
S31	-55.554(1.827)	0.584(0.052)
P11	168.670(2.361)	0.730(0.044)
P13	-5.003(1.294)	0.345(0.035)
P31	-23.181(1.345)	0.107(0.064)
P33	171.540(1.177)	0.531(0.031)
D13	167.120(0.878)	0.266(0.065)
D15	-23.049(1.149)	0.838(0.019)
D33	-6.462(0.927)	0.372(0.037)
D35	-5.603(0.698)	0.098(0.036)
F15	139.320(1.104)	0.807(0.018)
F17	-0.568(0.550)	0.005(0.022)
F35	1.806(0.464)	0.135(0.026)
F37	10.788(0.349)	0.043(0.029)
G17	2.206(0.422)	0.003(0.021)
G19	1.685(0.412)	0.078(0.017)
G39	0.019(0.326)	0.043(0.015)
H111	1.125(0.384)	0.050(0.014)
H311	1.187(0.286)	0.010(0.013)

C 99 Tlab= 999 MeV(975-1025 Ndata=513
Npar=38 Chi2= 691 Chi2(ed)=(856, 888)

Wave	Delta (Err)	Rho (Err)
S11	114.820(1.786)	0.549(0.052)
S31	-55.796(2.186)	0.515(0.054)
P11	168.220(2.407)	0.734(0.042)
P13	-5.241(1.333)	0.526(0.032)
P31	-23.022(1.220)	0.093(0.065)
P33	171.810(1.187)	0.559(0.036)
D13	169.770(0.867)	0.171(0.058)
D15	-17.454(1.091)	0.656(0.025)
D33	-7.155(0.997)	0.414(0.036)
D35	-6.330(0.654)	0.186(0.043)
F15	149.330(1.179)	0.648(0.033)
F17	-0.912(0.400)	0.027(0.024)
F35	2.582(0.404)	0.167(0.028)
F37	13.785(0.355)	0.049(0.036)
G17	3.622(0.506)	0.004(0.012)
G19	1.438(0.341)	0.058(0.022)
G39	-0.381(0.326)	0.049(0.025)
H111	0.711(0.327)	0.060(0.017)
H311	1.353(0.307)	0.007(0.012)

C105 Tlab=1050 MeV(1025-1075 Ndata=456
Npar=38 Chi2= 587 Chi2(ed)=(705, 699)

Wave	Delta (Err)	Rho (Err)
S11	120.330(2.917)	0.689(0.071)
S31	-55.558(2.399)	0.565(0.068)
P11	169.850(3.355)	0.809(0.064)
P13	-9.975(1.738)	0.518(0.051)
P31	-21.575(1.749)	0.185(0.076)
P33	172.680(1.388)	0.546(0.052)
D13	173.090(1.102)	0.070(0.075)
D15	-19.512(1.473)	0.523(0.040)
D33	-8.619(0.951)	0.263(0.044)
D35	-7.471(1.096)	0.132(0.063)
F15	161.910(1.511)	0.584(0.035)
F17	-0.988(0.750)	0.175(0.042)
F35	1.715(0.511)	0.211(0.034)
F37	16.709(0.620)	0.225(0.067)
G17	6.583(0.468)	0.089(0.043)
G19	2.568(0.404)	0.053(0.037)
G39	-0.922(0.478)	0.050(0.038)
H111	0.587(0.338)	0.048(0.019)
H311	2.259(0.422)	0.082(0.017)

C110 Tlab=1100 MeV(1075-1125 Ndata=347
Npar=38 Chi2= 439 Chi2(ed)=(556, 558)

Wave	Delta (Err)	Rho (Err)
S11	126.910(3.140)	0.583(0.092)
S31	-56.797(2.416)	0.643(0.075)
P11	158.530(6.943)	0.834(0.091)
P13	-9.220(2.529)	0.595(0.070)
P31	-22.557(1.838)	0.160(0.114)
P33	173.550(2.089)	0.512(0.071)
D13	173.420(1.997)	0.087(0.097)
D15	-15.408(1.872)	0.322(0.059)
D33	-9.647(1.488)	0.304(0.063)
D35	-4.459(1.294)	0.128(0.098)
F15	161.590(2.131)	0.524(0.089)
F17	0.202(1.160)	0.118(0.061)
F35	1.100(0.733)	0.380(0.039)
F37	19.353(0.452)	0.362(0.064)
G17	8.965(1.004)	0.183(0.113)
G19	3.134(0.499)	0.060(0.074)
G39	-0.424(0.557)	0.055(0.061)
H111	1.242(0.448)	0.097(0.031)
H311	0.776(0.473)	0.080(0.025)

*Each solution is characterized by a binning range (in brackets), by the number of searched parameters (Npar), chi-squared (chi2), and the number of data (Ndata) used for analysis. The two numbers listed for chi2(ed) are the chi-squared for FP86 for the selected data set, and the chi-squared after linearization and before searching.

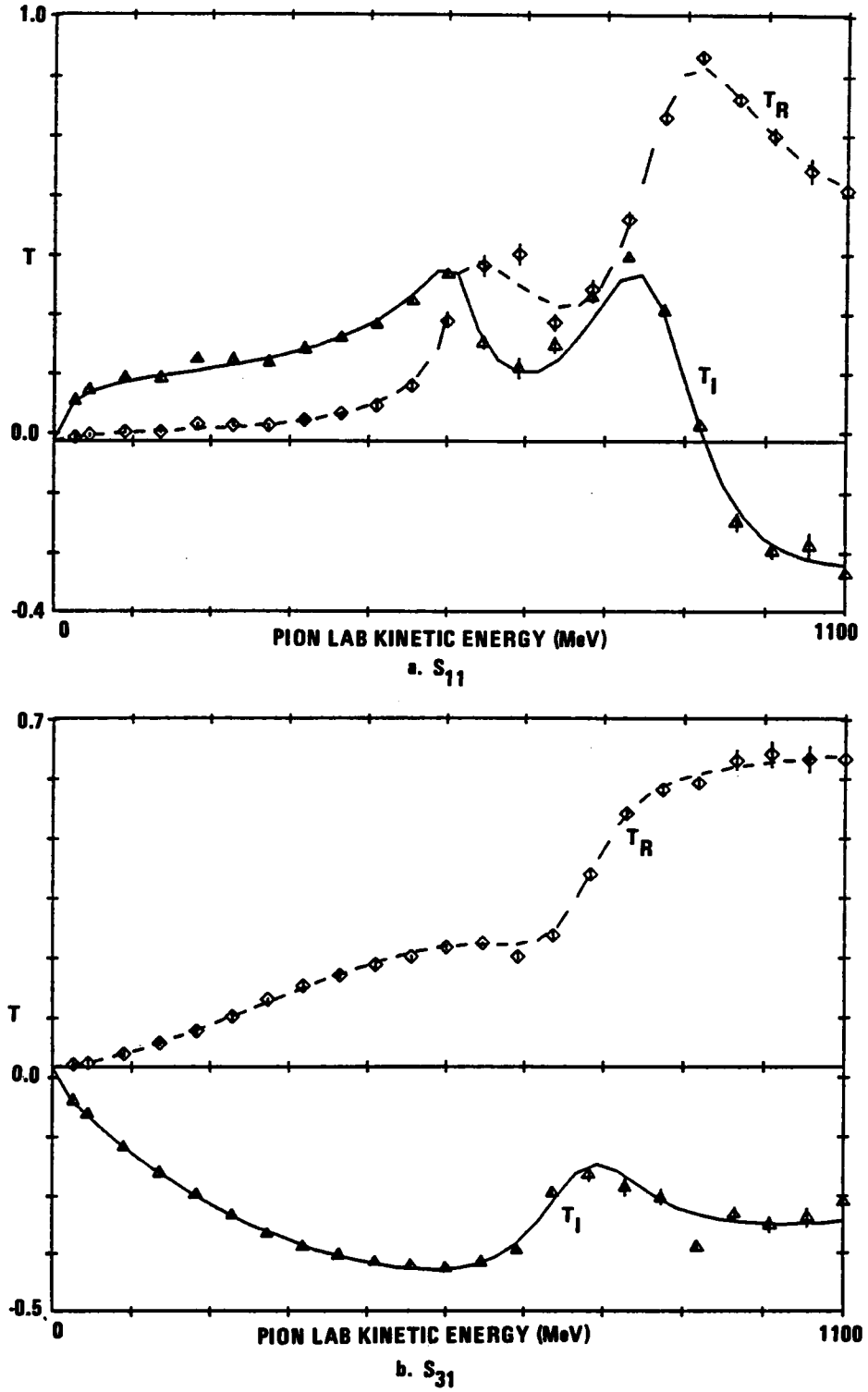

FIGURE 3-1. THE ENERGY-DEPENDENT SOLUTION COMPARED WITH THE ENERGY-INDEPENDENT SOLUTION. The imaginary part of the T-matrix is shown with triangles, the real part with diamonds. (Sheet 1 of 7)

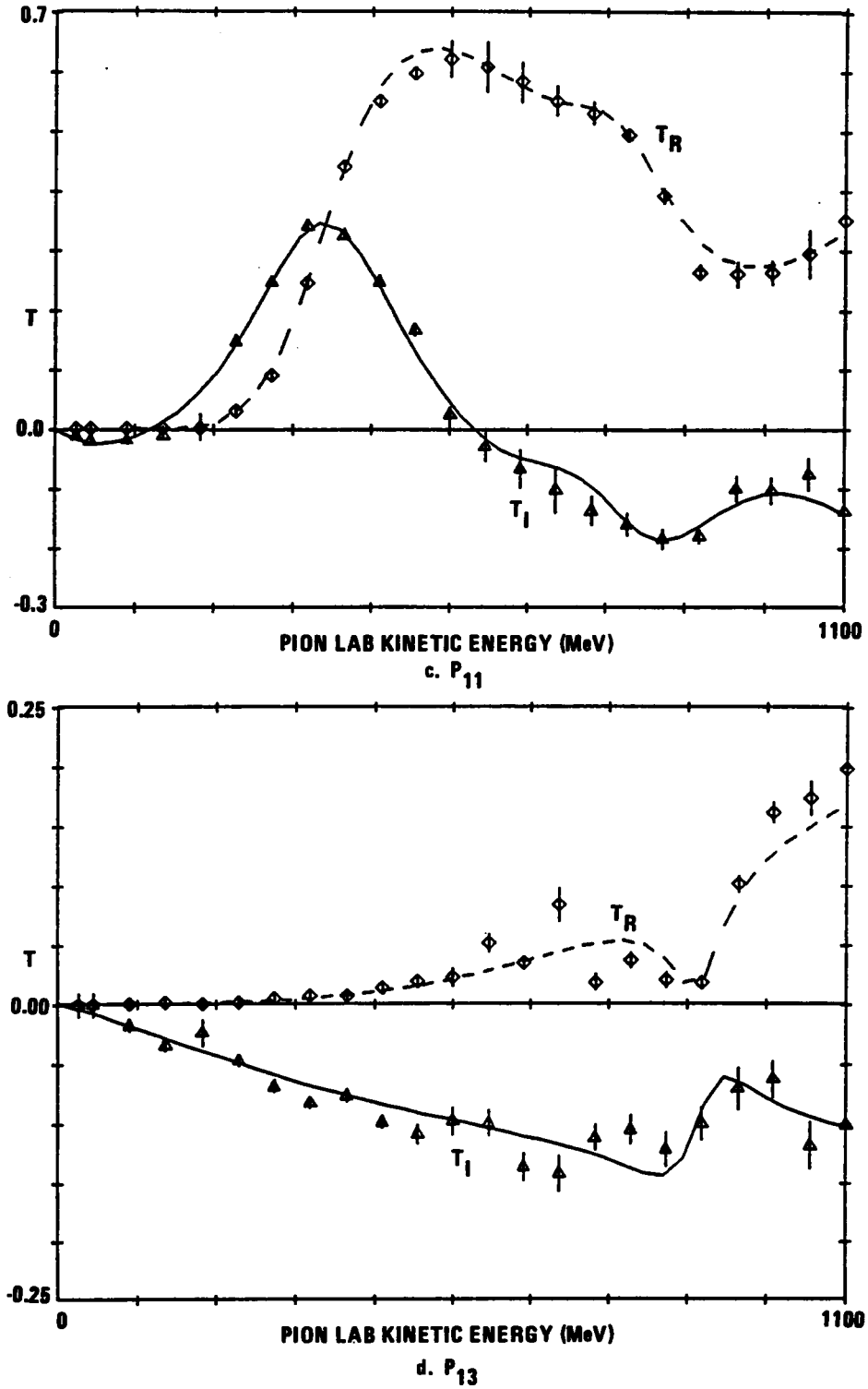

FIGURE 3-1. THE ENERGY-DEPENDENT SOLUTION COMPARED WITH THE ENERGY-INDEPENDENT SOLUTION. The imaginary part of the T-matrix is shown with triangles, the real part with diamonds. (Sheet 2 of 7)

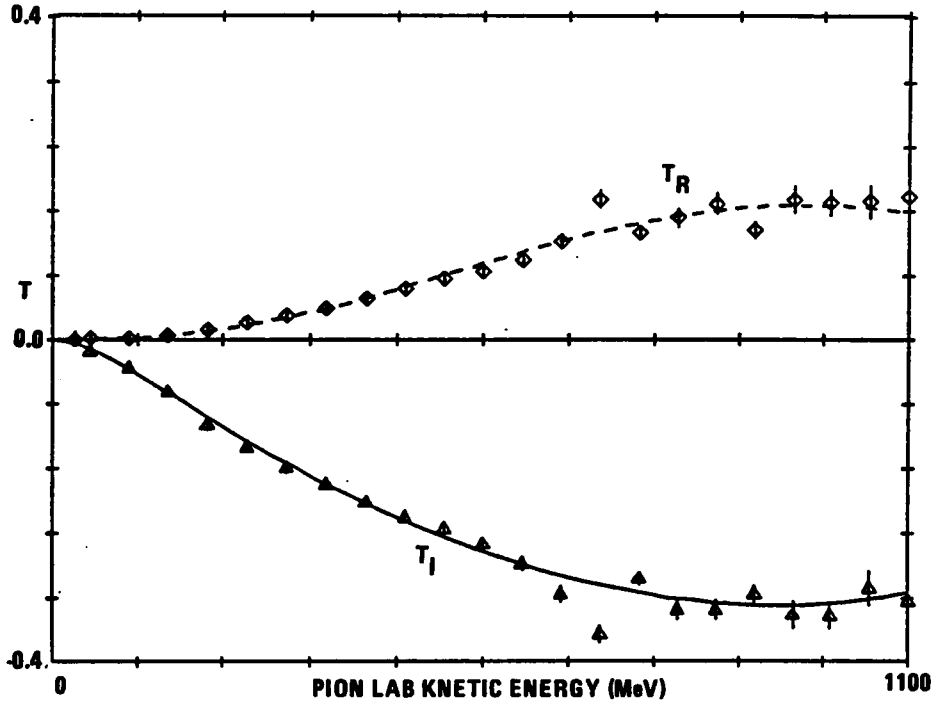

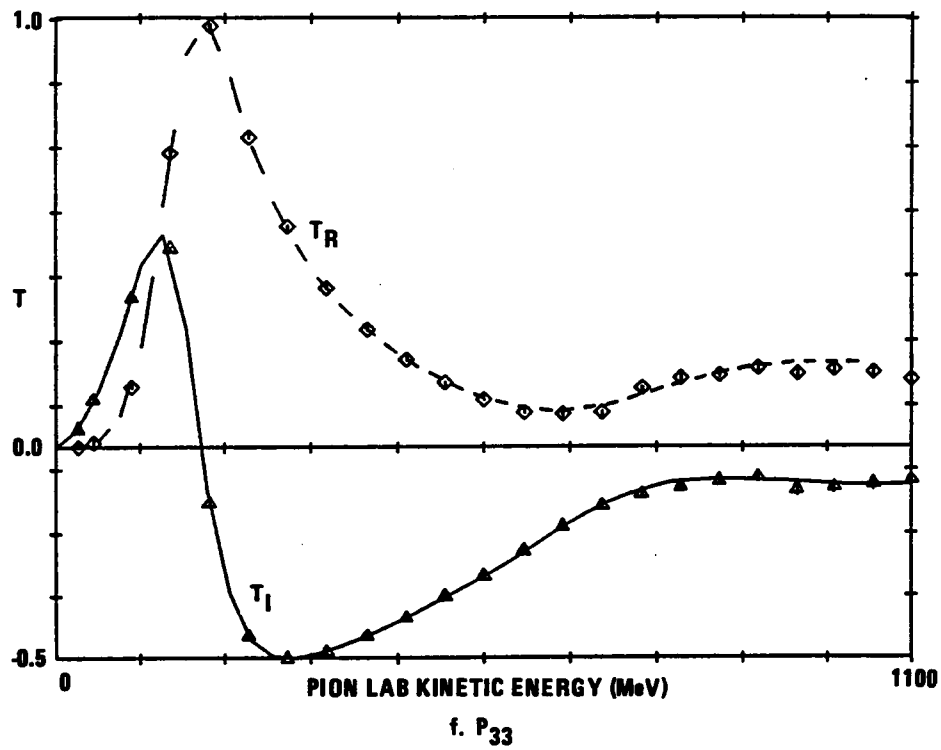

FIGURE 3-1. THE ENERGY-DEPENDENT SOLUTION COMPARED WITH THE ENERGY-INDEPENDENT SOLUTION. The imaginary part of the T-matrix is shown with triangles, the real part with diamonds. (Sheet 3 of 7)

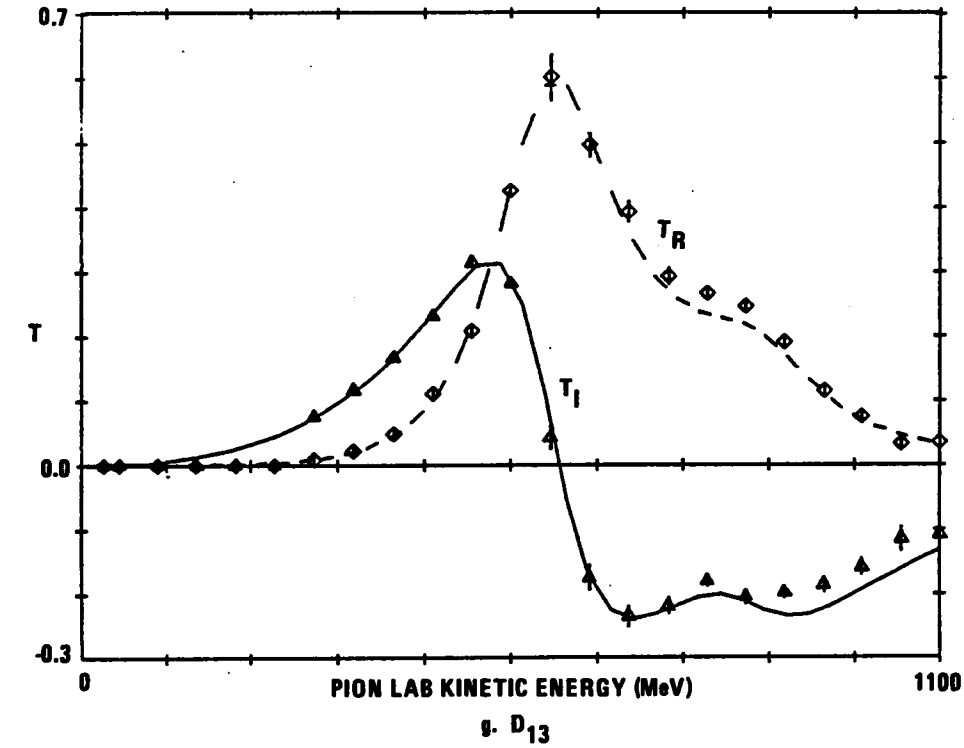

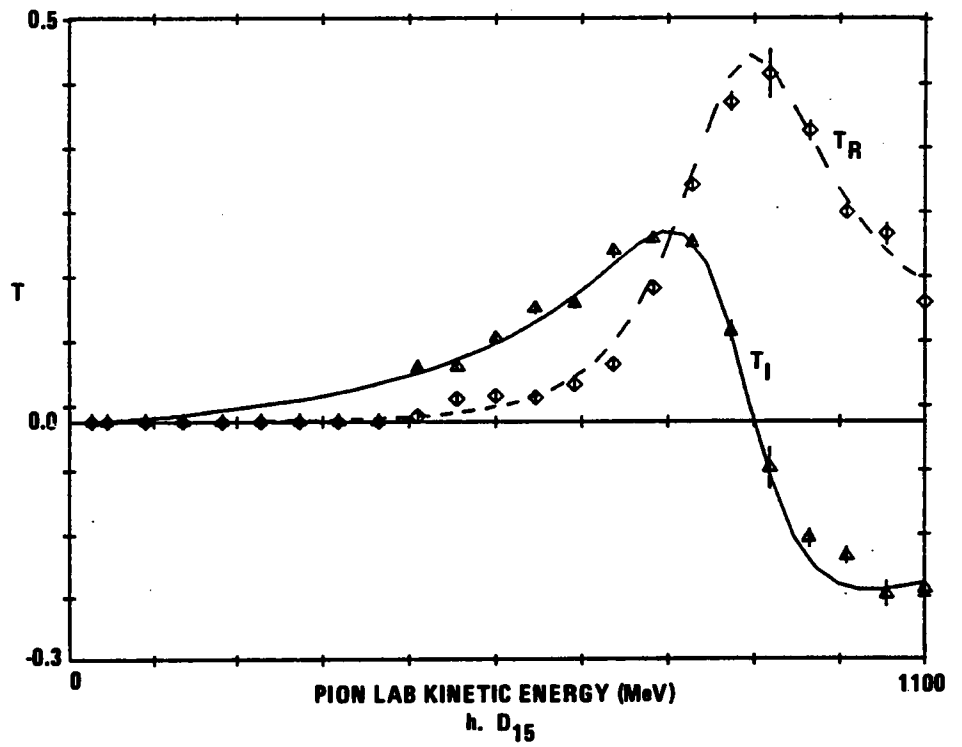

FIGURE 3-1. THE ENERGY-DEPENDENT SOLUTION COMPARED WITH THE ENERGY-INDEPENDENT SOLUTION. The imaginary part of the T-matrix is shown with triangles, the real part with diamonds. (Sheet 4 of 7)

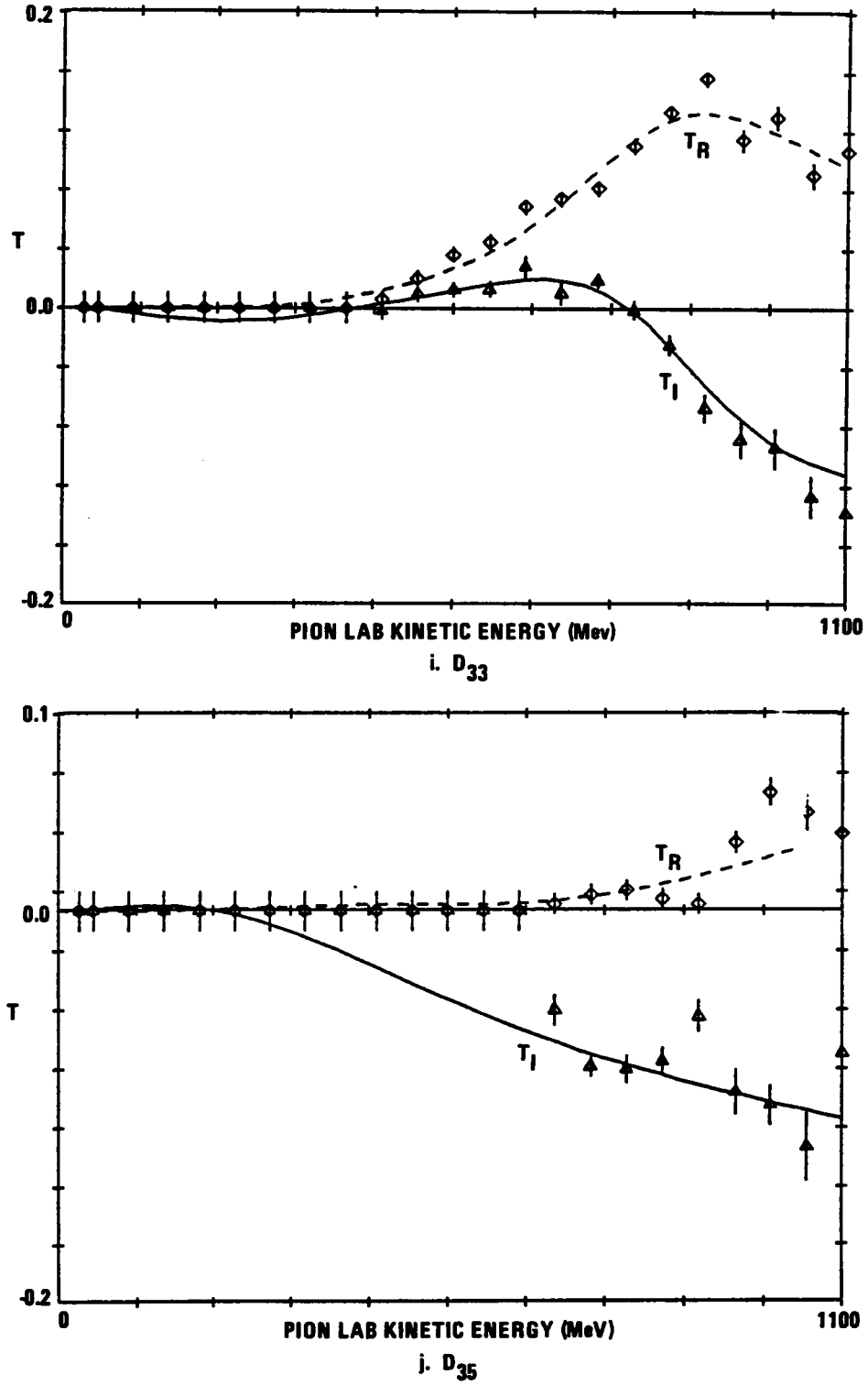

FIGURE 3-1. THE ENERGY-DEPENDENT SOLUTION COMPARED WITH THE ENERGY-INDEPENDENT SOLUTION. The imaginary part of the T-matrix is shown with triangles, the real part with diamonds. (Sheet 5 of 7)

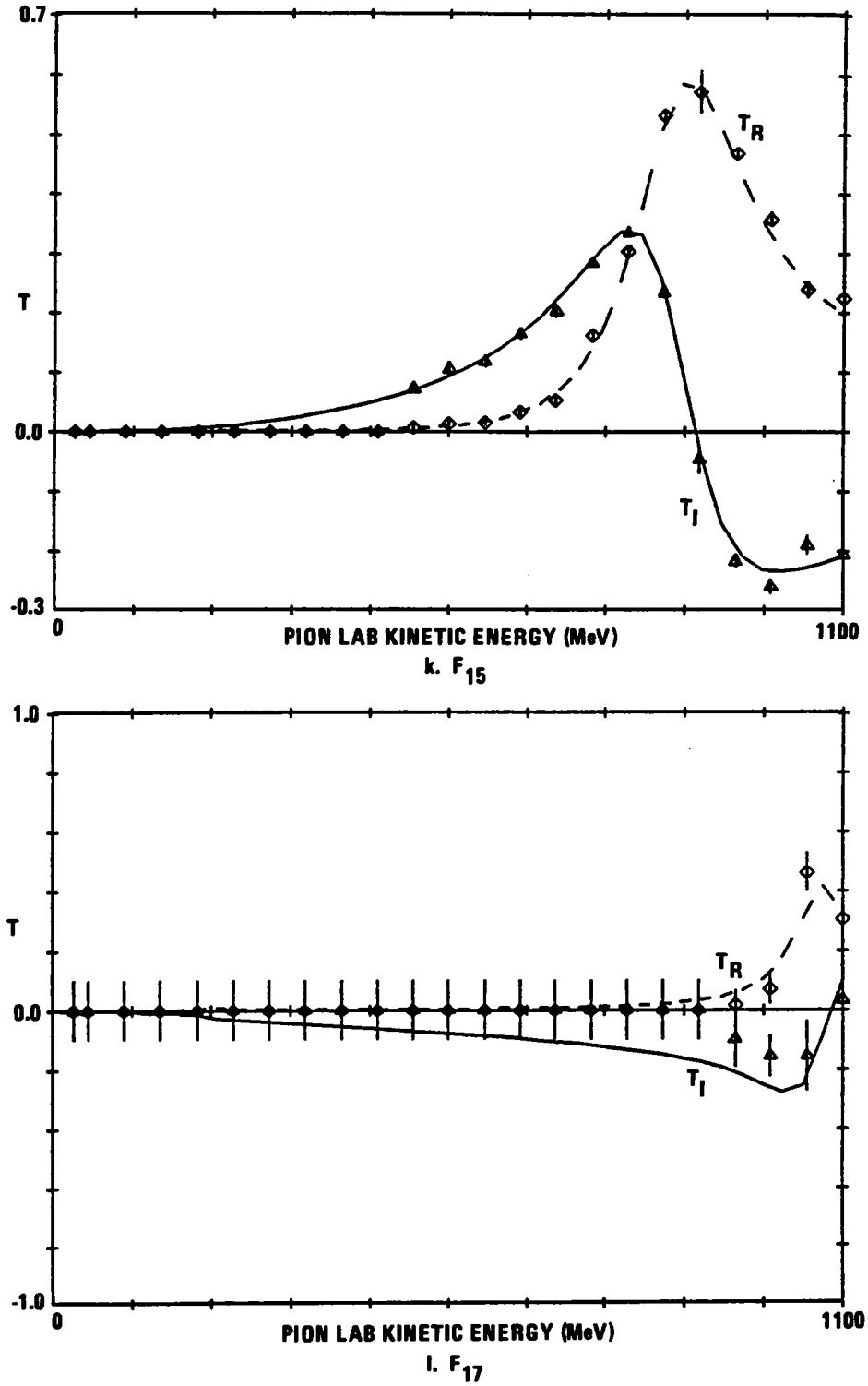

FIGURE 3-1. THE ENERGY-DEPENDENT SOLUTION COMPARED WITH THE ENERGY-INDEPENDENT SOLUTION. The imaginary part of the T-matrix is shown with triangles, the real part with diamonds. (Sheet 6 of 7)

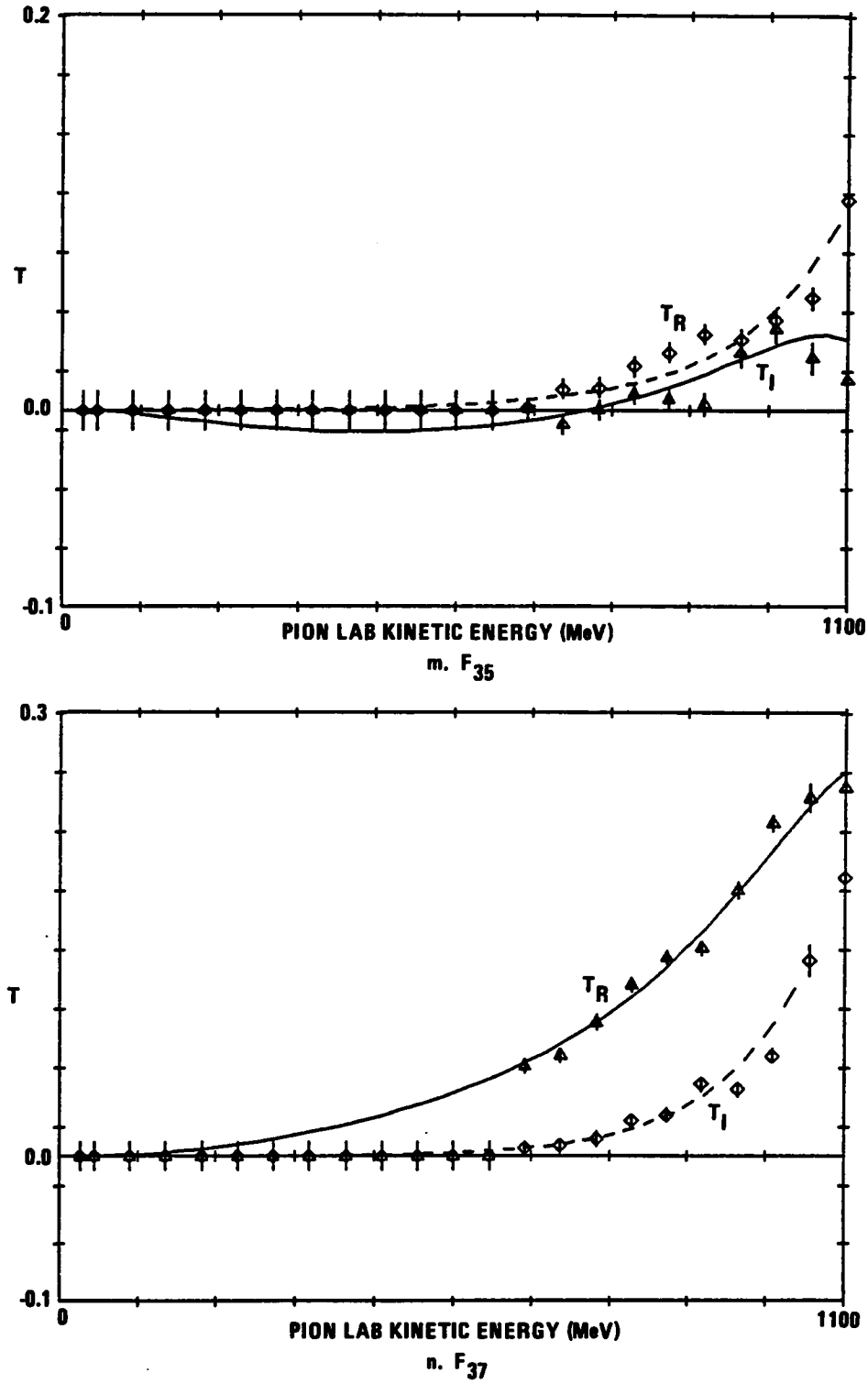

FIGURE 3-1. THE ENERGY-DEPENDENT SOLUTION COMPARED WITH THE ENERGY-INDEPENDENT SOLUTION. The imaginary part of the T-matrix is shown with triangles, the real part with diamonds. (Sheet 7 of 7)

slightly below this energy. This trend is apparently caused by a dearth of quality data in that energy region.

3.3 COULOMB CORRECTIONS TO NUCLEAR AMPLITUDES

In pion-nucleon scattering, the existence of charged initial and final states requires the inclusion of electromagnetic corrections to the pion-nucleon scattering amplitudes. Because it is presumed that the electromagnetic and strong interactions separately obey unitarity, the total phase shift will be a nonlinear function of the two interactions. The phase shifts caused by each interaction in the absence of the other cannot be simply added. The approach taken here to account for electromagnetic effects has been to use the direct or pure coulomb amplitudes developed by Tromberg *et al.*[8] and documented by Höhler *et al.*[7] The pion and proton form factors from Höhler are used. Rather than use the coulomb phase shifts (which some authors call coulomb rotation factors) and phase shift and inelasticity corrections given by these authors, the coulomb phase shift given by Zidell *et al.* and a coulomb barrier factor described below have been employed. In the analysis being reported here, charged-neutral pion and proton-neutron mass differences and the radiative capture process (π-P $\rightarrow \gamma$N) have been ignored. Also neglected are corrections to cross sections because of bremsstrahlung (soft photon emission).

The partial-wave T-matrices parametrized according to Subsections 3.1.2 and 3.2.2 must be charge-corrected for use in any of the three charge channels. The corrections to these nucleon partial waves are accomplished with coulomb barrier factors, B_ℓ:

$$B_\ell = B_o \prod_{j=1}^{\ell} [1 + (\eta/j)^2] \qquad (3\text{-}16)$$

with

B_0 = $2\pi\eta/(e^{2\pi\eta} - 1)$

v_r = (pion laboratory velocity)/c

α = fine structure constant

η = $\pm \alpha/v_r$, for $\pi^{\pm}P \rightarrow \pi^{\pm}P$. (3-17)

For charge-exchange scattering (π-P $\rightarrow \pi^0$N), the square root of the π-P barrier factor is used. These barrier factors are multiplied with a K-matrix computed from the nuclear T-matrices. The resulting modified K-matrix is then used to calculate the charge-corrected T-matrix. This recipe is documented further by Arndt *et al.*[9] and results in the following T-matrix:

$$T_{charge\ corrected} = \frac{B_\ell * T_{nuclear}}{1 + i * (1 - B_\ell) * T_{nuclear}} \quad . \qquad (3\text{-}18)$$

The coulomb phase shifts that multiply these charge-corrected T-matrices are given by Zidell[6] as follows

$$\sigma_\ell = \sum_{j=1}^{\ell} tan^{-1}(|\eta/j|)$$

$$\sigma_0 = 0.0 \cdot \qquad (3\text{-}19)$$

The comparison between energy-dependent solutions FP86, SPLT, PLUS, and MNUS reported in Subsection 3.1.3 showed that only the above charge corrections are required by the data. A similar conclusion can

be reached from single-energy analyses such as described by Arndt *et al.*[9]

3.4 REFERENCES

1. R. Koch and E. Pietarinen, *Nuclear Physics*, Vol. A336, 1980, p. 331

2. R. Koch and M. Hutt, *Zeitschrift für Physik*, Vol. C19, 1983, p. 110.

3. R. A. Arndt and M. H. MacGreggor, *Methods of Computational Physics*, Academic Press, New York, 1966, Vol. 6, p. 253

4. B. H. Bransdon and R. G. Moorhouse, *The Pion-Nuclean System*, Princeton University, Princeton, New Jersey, 1973, pp. 178-185

5. Particle Data Group, "Review of Particle Properties," *Physics Letters*, Vol. 170B, 10 April 1986, p. 245

6. V. S. Zidell, R. A. Arndt, and L. D. Roper, *Physical Review D*, Vol. 21, 1980, p. 1225; also preliminary unpublished results by R. A. Arndt and L. D. Roper

7. G. Höhler, F. Kaiser, R. Koch, and E. Pietarinen, *Handbook of Pion-Nucleon Scattering* (Fachinformation-szentrum, Karlsruhe, Germany) *Physics Data*, Vol. 12-1, 1979; R. Koch and E. Pietarinen, *ibid.*

8. B. Tromberg, S. Waldenstrom, and I. Overbo, *Physical Review D*, Vol. 15, 1977, p. 725

9. R. A. Arndt, J. M. Ford, and L. D. Roper, "Pion-Nucleon Partial-Wave Analysis to 1100 MeV," *Physical Review D*, Vol. 32, 1985, p. 1085

4. THE PARTIAL-WAVE RESONANCES

4.1 DEFINITION OF A RESONANCE

The energy dependence of the pion-nucleon elastic cross sections exhibits conspicuous bumps, manifesting the presence of the underlying partial-wave resonances. This structure in the cross sections of the energy-dependent solution FP86 is shown in the plots of Figure 4-1 for each of the three elastic charge channels. The most prominent peak seen here occurs near a lab kinetic energy of 190 MeV and is caused by the well-known delta P_{33} (1232) resonance.

The enhancement in scattering caused by the formation or production of meta-stable states having short lifetimes on the order of 10^{-23} seconds occurs in states with good quantum numbers of the strong interaction (angular momentum, isospin, parity, and spin), and these states are referred to as resonances. Because resonances have nonzero lifetimes, their formation or production during the scattering process results in a time delay of the emergence of the scattered particles with the resonance mass being identified as the center-of-mass energy at which the peak delay occurs.

Resonances are typically described in terms of a Breit-Wigner formula, where near the resonance energy of an elastic resonance,

$$T(W;I,J,L) \sim \frac{\Gamma/2}{M-W-i\Gamma/2} \quad . \tag{4-1}$$

A similar formula, which includes a background term, exists for nonideal and inelastic resonances. The mass and width of the

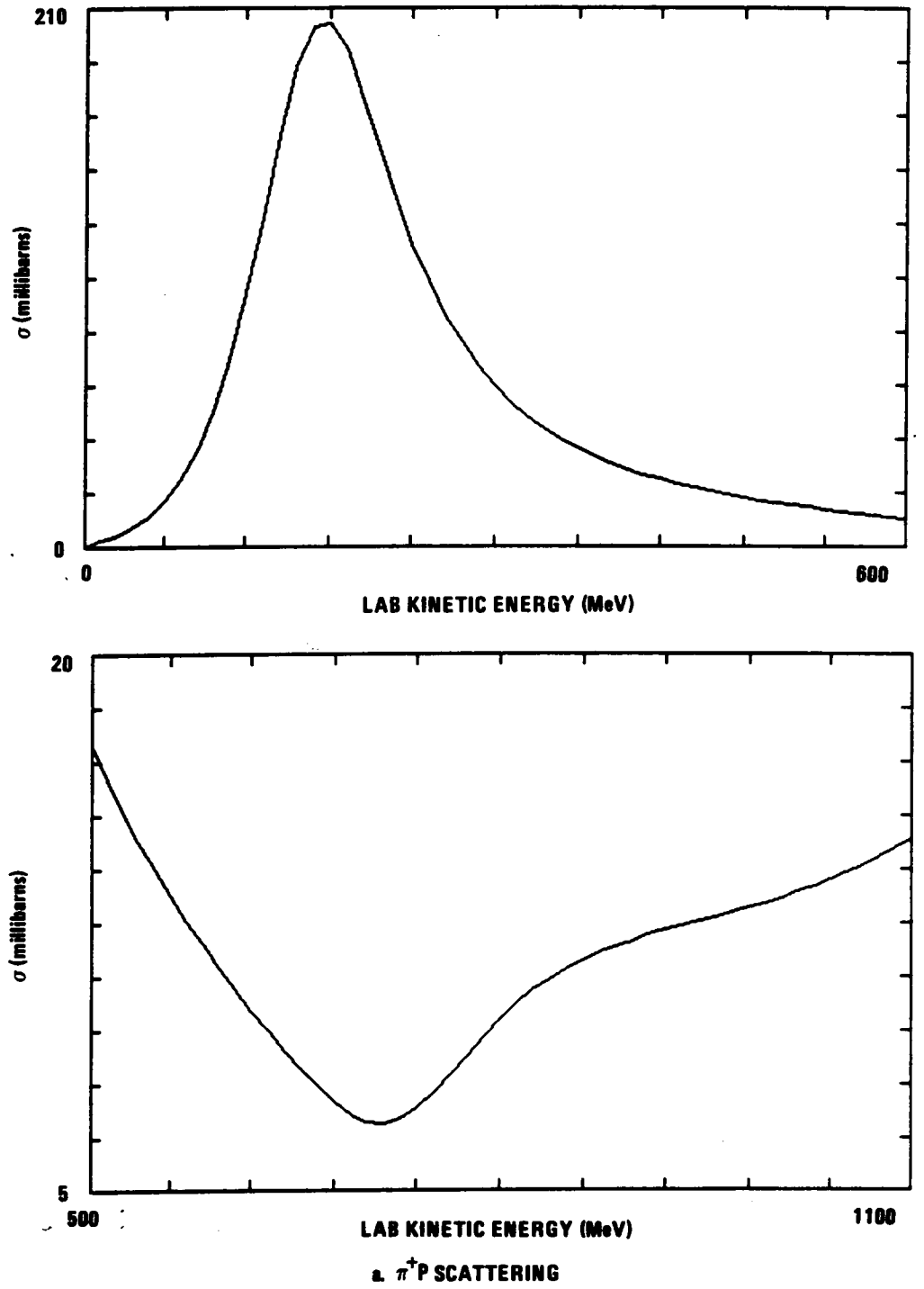

FIGURE 4-1. TOTAL CROSS SECTION FROM SOLUTION FP86 (Sheet 1 of 3)

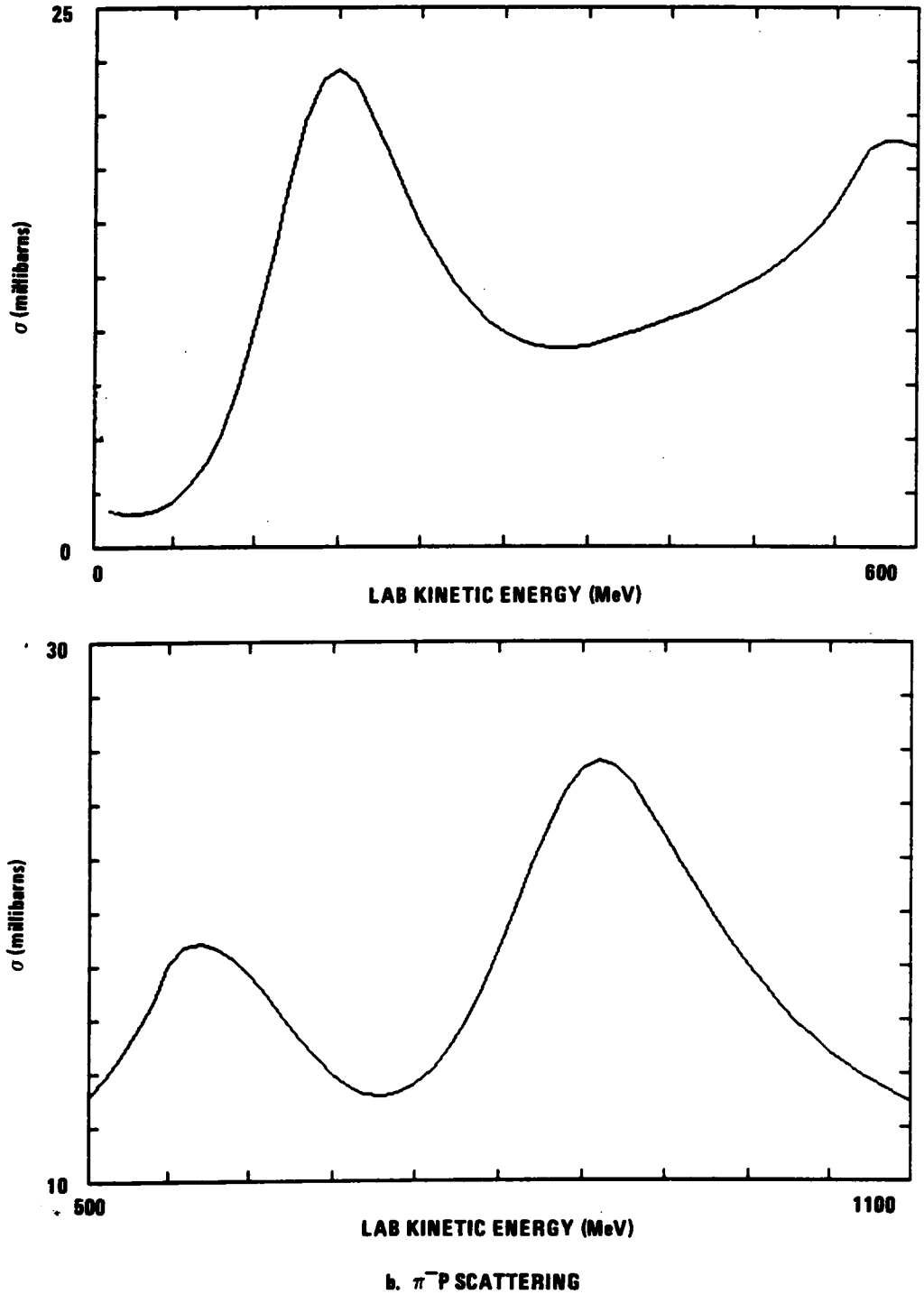

FIGURE 4-1. TOTAL CROSS SECTION FROM SOLUTION FP86 (Sheet 2 of 3)

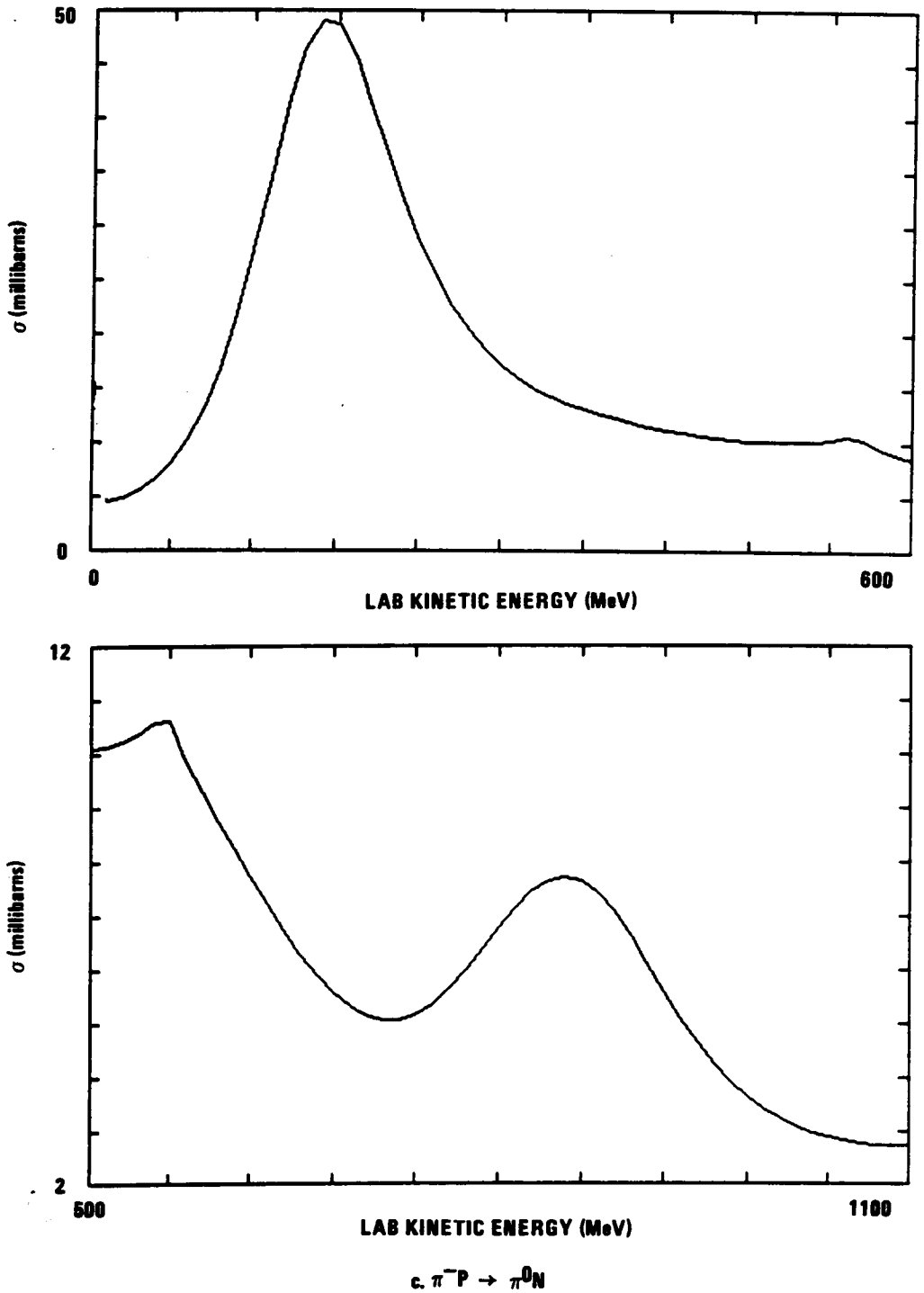

FIGURE 4-1. ELASTIC CROSS SECTION FROM SOLUTION FP86 (Sheet 3 of 3)

resonance are given by M and Γ, respectively. An elastic resonance can be identified by a phase shift rapidly increasing by an amount of order of π and by the counterclockwise movement of a partial-wave, T-matrix element along a deformed circle in an Argand diagram. There will also be a definite peak at the resonance mass in $|dT/dW|$. In the past, resonances have usually been reported by giving the Breit-Wigner resonance parameters, M and Γ; however, more recently, investigators have been reporting the location and residue of the poles of the T-matrix in the complex energy plane. This approach has the advantage of not necessarily depending on a Breit-Wigner-like parametrization and the disadvantage of requiring the analytic continuation of the amplitude into the second sheet of the complex-energy plane. The identification of a resonance with a pole in the T-matrix enables one to associate resonances with being new particles. According to S-matrix theory, both stable particles and unstable resonances are identified with poles in T or S in the second sheet of the complex-energy plane. For the stable particle, the pole is on the real axis below the threshold energy while a resonance pole is below the real axis and on the second or unphysical sheet determined by the physical branch cut in T(W) that begins at threshold. The presence of a T-matrix pole is surer criterion for the existence of a resonance than a rapidly varying phase shift or a loop in an Argand diagram because these latter can occur in the absence of a resonance.[1] It is the existence of a pole below the real axis on the second sheet in the

complex-energy plane that is being used to identify resonances in this work.

More detailed discussions about resonances are widely found in the literature with excellent discussions in Subsection 4.2 of Höhler[1] and in Chapter 5 of Bransden and Moorehouse.[2]

4.2 THE PION-NUCLEON RESULTS

The pion-nulceon system is well-known for its wealth of partial-wave resonances that include the first such resonance discovered, the P_{33}, $\Delta(1232)$. As described earlier, resonances can often be identified by a counterclockwise loop in an Argand diagram. Argand diagrams from the energy-dependent solution FP86 are given in Figure E-1 of Appendix E for each partial wave through $\ell = 3$ and for energies from threshold to a total center-of-mass energy of about 1800 MeV. Their behavior varies from the highly elastic P_{33} that remains near the unitarity circle as it loops through the $\Delta(1232)$ to the more inelastic partial waves, such as the D_{33}. Most of the waves show the counterclockwise looping behavior characteristic of resonant behavior. Indeed, partial waves S_{11} and D_{13} clearly show two such loops, which is strong evidence of two resonances in this energy range for each of those waves. Only partial waves D_{35} and F_{17} show no indication of resonant behavior. Although several waves (i.e., P_{13}, P_{31}, and D_{35}) begin by traveling along the unitarity circle in a clockwise direction, S_{31} has the unique behavior of then very sharply moving away from the unitarity circle and going into a counterclockwise resonance loop. Of the waves shown, the D_{35}, F_{17}, and F_{35} are the

smallest, with the smallness caused in part by the limited phase-space available to higher angular momentum states. Although Argand diagrams are useful for identifying resonances, they cannot serve as a rigorous test because of the possibility of loops occurring without other indications of resonances, such as a peak in the time delay, being present.

Another characteristic of many pion-nucleon resonances is the rapid rise in the phase shift by an amount of order π that results in a peak in the partial cross section at the resonance energy. The phase shifts from the energy-dependent solution are shown in Appendix E, Figure E-3. Of all the partial waves, only five, P_{11}, P_{33}, D_{13}, D_{35}, and F_{15}, show a rapid increase in the phase shift by an amount near 180 degrees, although many of the others also had a resonance loop in their Argand diagrams. These examples show that a rapid change in the phase shift cannot be used as an absolute criterion for the presence of a resonance. The four partial waves, whose Argand diagrams showed initial traversal of the unitarity circle in the clockwise direction, S_{31}, P_{13}, P_{31}, and D_{35}, also show a corresponding distinctive behavior in their phase-shift plots. They have negative phase shifts, which are caused by the existence of a repulsive potential acting in those channels. Positive phase shifts are correspondingly related to attractive potentials. Shown with the phase shifts in the plots of Figure E-3 are the inelasticity (or absorption) parameters, η. The actual quantity plotted is $1 - \eta^2$, which increases from zero for purely elastic scattering toward unity

as absorption increases. If the phase shift is given as a complex quantity, $\delta = \delta_R + i\delta_I$, then $\eta = e^{-2\delta_I}$. All the plots show an initial inelasticity parameter of unity since the inelastic threshold is not reached until a pion kinetic energy of 156 MeV (E_{cm} = 1290 MeV).

Descriptions of resonances in terms of phase-shift variation or even via Argand diagrams have been known to be unreliable tests for resonances. Here we use the existence of T-matrix poles near the real axis on the unphysical sheet in the complex energy plane as a precise test for the identification of a resonance. The results for each partial wave from solution FP86 are given in Table 4-1. Pole positions and residues are listed there for all three- and four-star resonances and the single two-star resonance identified by the Particle Data Tables[3] that are within or near the energy range of interest, below 2000 MeV. For each resonance, its status and the pole position and residue from both solution FP86 and the Carnegie-Mellon[4] (CM) analyses are given. The Carnegie-Mellon residue phases have been modified from their reported values by a uniform increase of 180 degrees to give agreement with the VPI&SU phase convention. The errors in the FP86 resonance parameters were computed from the errors in the fitting parameters and the variation of the resonance parameters with the fitting parameters. For fitting parameters pi with statistical error Δpi, the error, Δf, in a resonance parameter, f, is given by

$$(\Delta f)^2 = \sum_{ij} \left(\frac{\partial^2 f}{\partial p_i \, \partial p_j} * \Delta p_i * \Delta p_j \right)^2 . \qquad (4\text{-}2)$$

TABLE 4-1. PION-NUCLEON RESONANCE PARAMETERS (Sheet 1 of 2)

RESONANCE/STATUS	SOLUTION	POLE POSITION (MeV)		RESIDUE	
		Re {W}	-2*Im{W}	|r| (MeV)	θ (deg)
N1440 P_{11} ****	FP86	1351 ± 6	198 ± 2	66 ± 1	73 ± 1
	CM†	1375 ± 30	180 ± 40	52 ± 5	80 ± 35
N1520 D_{13}****	FP86	1508 ± 9	119 ± 2	38 ± 1	170 ± 1
	CM	1510 ± 5	114 ± 10	35 ± 2	168 ± 5
N1535 S_{11}****	FP86	1461 ± 14	205 ± 12	63 ± 9	152 ± 7
	CM	1510 ± 50	260 ± 80	120 ± 40	195 ± 45
N1650 S_{11}****	FP86	1655 ± 16	116 ± 6	41 ± 4	123 ± 3
	CM	1640 ± 20	150 ± 30	60 ± 10	105 ± 25
N1675 D_{15}****	FP86	1664 ± 12	134 ± 2	31 ± 1	164 ± 1
	CM	1660 ± 10	140 ± 10	31 ± 5	150 ± 10
N1680 F_{15}****	FP86	1669 ± 7	108 ± 2	32 ± 1	161 ± 1
	CM	1667 ± 5	110 ± 10	34 ± 2	155 ± 5
N1700 D_{13}***	FP86	1673 ± 9	114 ± 2	7 ± 1	-159 ± 7
	CM	1660 ± 30	90 ± 40	6 ± 3	180 ± 50
N1710 P_{11}***	FP86	1632 ± 15	158 ± 4	42 ± 2	-153 ± 7
	CM	1690 ± 20	80 ± 20	8 ± 2	-5 ± 35
N1720 P_{13}****	FP86	1687 ± 6	52 ± 2	2 ± 1	14 ± 1
	CM	1680 ± 30	120 ± 40	8 ± 2	20 ± 30

†CM = Carnegie-Mellon[4] solution with residue phases shifted uniformly by 180 degrees

TABLE 4-1. PION-NUCLEON RESONANCE PARAMETERS (Sheet 2 of 2)

RESONANCE/STATUS	SOLUTION	POLE POSITION (MeV)		RESIDUE	
		Re {W}	-2*Im{W}	|r| (MeV)	θ (deg)
Δ1232 P_{33}****	FP86	1212 ± 13	103 ± 2	56 ± 1	151 ± 1
	CM	1210 ± 1	100 ± 2	53 ± 2	133 ± 1
Δ1600 P_{33}**	FP86	1588 ± 15	309 ± 4	41 ± 1	71 ± 1
	CM	Not Reported			
Δ1620 S31****	FP86	1596 ± 8	114 ± 2	14 ± 1	65 ± 1
	CM	1600 ± 15	120 ± 20	15 ± 2	70 ± 20
Δ1700 D_{33}****	FP86	1657 ± 6	275 ± 20	19 ± 1	163 ± 2
	CM	1675 ± 25	270 ± 4	13 ± 3	160 ± 25
Δ1900 S_{31}***	FP86	Out of Energy Range			
	CM	1870 ± 40	180 ± 50	10 ± 3	20 ± 40
Δ1905 F_{35}****	FP86	1855 ± 5	191 ± 2	17 ± 1	170 ± 1
	CM	1830 ± 40	280 ± 60	25 ± 8	130 ± 20
Δ1910 P_{31}****	FP86	Out of Energy Range			
	CM	1880 ± 30	200 ± 40	20 ± 4	90 ± 30
Δ1920 P_{33}***	FP86	Out of Energy Range			
	CM	1900 ± 80	300 ± 100	24 ± 4	30 ± 30
Δ1930 D_{35}***	FP86	Out of Energy Range			
	CM	1890 ± 15	260 ± 40	18 ± 6	160 ± 40
Δ1950 F_{37}****	FP86	1879 ± 6	210 ± 2	54 ± 1	158 ± 1
	CM	1890 ± 15	260 ± 40	50 ± 7	147 ± 8

In the numerical differentiation, the variation in each parameter was taken at 1 percent of the corresponding error. The parameter errors were taken from the values given by the analysis program, SHSZSA, at each cycle of the fitting process, but are not identical to the diagonal elements of the error matrix. The large chi-squared second derivative matrix is nearly singular, so numerical difficulties require some massaging of the errors for the smaller parameters. Consequently, the smaller FP86 errors shown here in Table 4-1 and later in Table 4-2 are generally understated.

The resonance parameters presented in Table 4-1 show excellent agreement between the results of this analysis and the Carnegie-Mellon work. The only resonance for which major discrepancies exist is the P_{11} (1710) and is presumably caused by the complicated structure in this wave as described in the following section where each wave will be discussed in greater detail. Table 4-1 also shows that this analysis finds no resonances beyond those previously reported, and below the highest energy range of this analysis, 1800 MeV in the center of mass, all of the expected resonances are found except for the two questionable one-star resonances, N(1540) in P_{13} and Δ(1550) in P_{31}. In addition, the two-star Δ(1600) in the P_{33} wave is also seen, although with a large width. An explanation for its weak status will be presented in the next section. In the energy range between 1800 and 2000 MeV, just above the range of this analysis, two of the predicted six delta resonance poles are seen. The observance of the Δ(1905) and Δ(1950) poles is indicative that the effects of these two

resonances extend significantly into the energy range of FP86. The absence of the other four is not surprising; they just have little effect below 1800 MeV.

In a Briet-Wigner parametrization, the magnitude of a resonance pole residue is the elastic half-width, while the imaginary part of the pole position gives the total half-width of the state. The total width must obviously be greater than the elastic width, so it is therefore reassuring to observe that the reported residue magnitudes are all less than the magnitude of the imaginary parts of the pole position to within the reported errors.

4.3 TOPOLOGY OF THE PARTIAL-WAVE AMPLITUDES

One of the principal advantages in the decision to parametrize the partial waves, as described in Chapter 3, is the explicit analyticity of the partial amplitudes. Analytic continuation into the complex energy plane is straightforward with this parametrization and reveals a rich topological structure for solution FP86. Each channel threshold introduces a corresponding square root branch point, and hence an additional Riemann sheet of the amplitude. As discussed earlier, poles below but near the real axis on the second or unphysical sheet of the elastic branch cut are identified with resonances. Poles on other Riemann sheets of the complex amplitude also exist, but typically have little effect on the physical amplitude because of their long distance from the real axis. Zeros of the amplitude are also found in the complex energy plane and can influence the physical amplitude.

Details about the poles and zeros found in solution FP86 are summarized in Table 4-2. Features labeled as type "R" are resonance poles on the unphysical sheet of the elastic channel. For identification with specific resonances, the reader should refer back to Table 4-1. Other poles, those not identified with resonances and on the sheet introduced by the delta threshold, are labeled with a "P." Zeros of the amplitude are naturally labeled with a "Z." The errors in the positions of the features and in their residues shown in Table 4-2 were determined by the procedure described in the previous section and, for the reasons explained there, are generally understated. A pole residue has dimension of MeV and is given by,

$$Pole\,Residue = \lim_{W \to W_p} \left\{ T(W) * (W - W_p) \right\} \qquad (4\text{-}3)$$

where W_p is the pole (R or P) position in the complex energy plane. In order for the "residue" of a zero to have the same dimension as a pole residue, the zero "residue" is taken as,

$$Zero\,Residue = \lim_{W \to W_z} \left\{ \frac{T(W) * |W_z|^2}{(W - W_z)} \right\} \qquad (4\text{-}4)$$

with W_z being the position of the zero. Note that except for the S_{31} and the P_{13} waves, the zero residues are small in magnitude.

To aid in more detailed discussions of the topology of the partial waves, contour plots of the T-matrices in the complex energy plane for those waves exhibiting interesting poles and zeros are presented in Figure 4-2. On the contour plots, squares indicate resonance poles

TABLE 4-2. COMPLEX W-PLANE FEATURES FROM SOLUTION FP86

PARTIAL WAVE	TYPE*	POSITION (MeV)		RESIDUE*	
		Re {W}	-Im{W}	|r| (MeV)	θ (deg)
S_{11}	R	1461 ± 14	103 ± 6	63 ± 9	152 ± 7
	Z	1587 ± 17	55 ± 4	1 ± 4	-53 ± 18
	P	1654 ± 16	83 ± 4	84 ± 10	143 ± 4
	R	1655 ± 16	58 ± 3	41 ± 4	123 ± 3
S_{31}	Z	1587 ± 9	36 ± 1	33 ± 1	153 ± 3
	R	1596 ± 8	57 ± 1	14 ± 1	65 ± 1
P_{11}	R	1351 ± 6	99 ± 1	66 ± 1	73 ± 1
	P	1394 ± 14	114 ± 1	144 ± 3	108 ± 1
	Z	1587 ± 4	78 ± 1	11 ± 5	52 ± 13
	R	1611 ± 14	128 ± 2	86 ± 4	-8 ± 3
	R	1632 ± 15	79 ± 2	42 ± 2	-153 ± 7
	Z	1705 ± 7	74 ± 2	2 ± 1	22 ± 3
P_{13}	R	1687 ± 6	26 ± 1	2 ± 1	14 ± 1
	Z	1695 ± 3	13 ± 1	31 ± 4	-41 ± 3
P_{33}	R	1212 ± 13	51 ± 1	56 ± 1	151 ± 1
	R	1588 ± 15	154 ± 2	41 ± 1	71 ± 1
	Z	1588 ± 4	63 ± 1	0.40 ± 1	-109 ± 2
D_{13}	R	1508 ± 9	60 ± 1	38 ± 1	170 ± 1
	Z	1649 ± 15	64 ± 2	12 ± 17	-45 ± 23
	R	1673 ± 9	57 ± 1	7 ± 1	-159 ± 7
D_{15}	R	1664 ± 12	67 ± 1	31 ± 1	164 ± 1
D_{33}	Z	1325 ± 6	161 ± 5	0.00 ± 1	55 ± 8
	Z	1362 ± 8	31 ± 4	0.03 ± 1	-77 ± 30
	R	1657 ± 6	137 ± 2	19 ± 1	163 ± 2
D_{35}	Z	1312 ± 10	105 ± 2	0.02 ± 1	-55 ± 3
F_{15}	R	1669 ± 7	54 ± 1	32 ± 1	161 ± 1
F_{35}	Z	1576 ± 7	55 ± 2	0.01 ± 1	31 ± 1
	R	1855 ± 5	95 ± 1	17 ± 1	170 ± 1
F_{37}	R	1879 ± 6	105 ± 1	54 ± 1	158 ± 1

*See text for explanations.

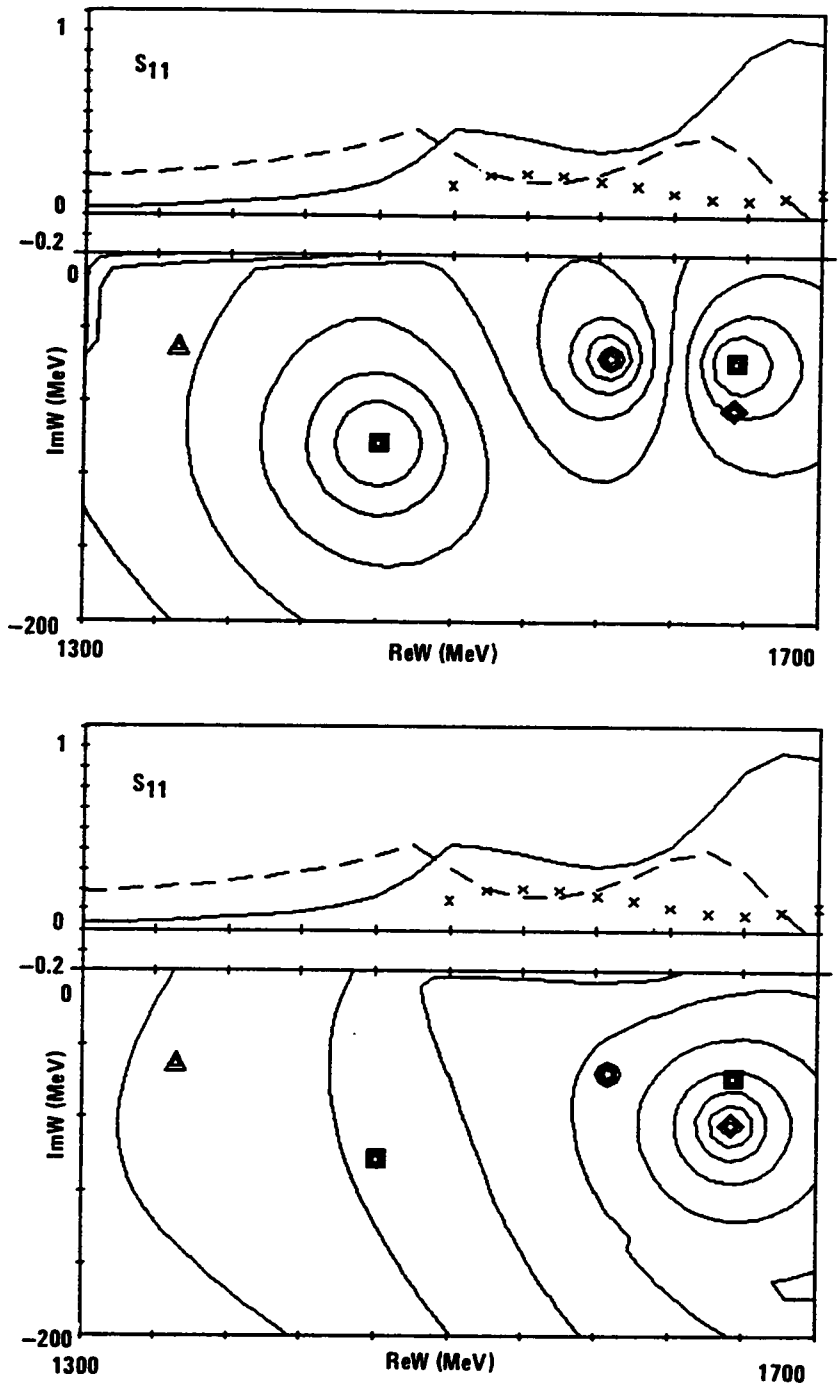

a. S_{11} PARTIAL WAVE

FIGURE 4-2. CONTOUR PLOTS OF log $|T|^2$ WITH LINEAR PLOTS OF T, SEE TEXT FOR EXPLANATION (Sheet 1 of 8)

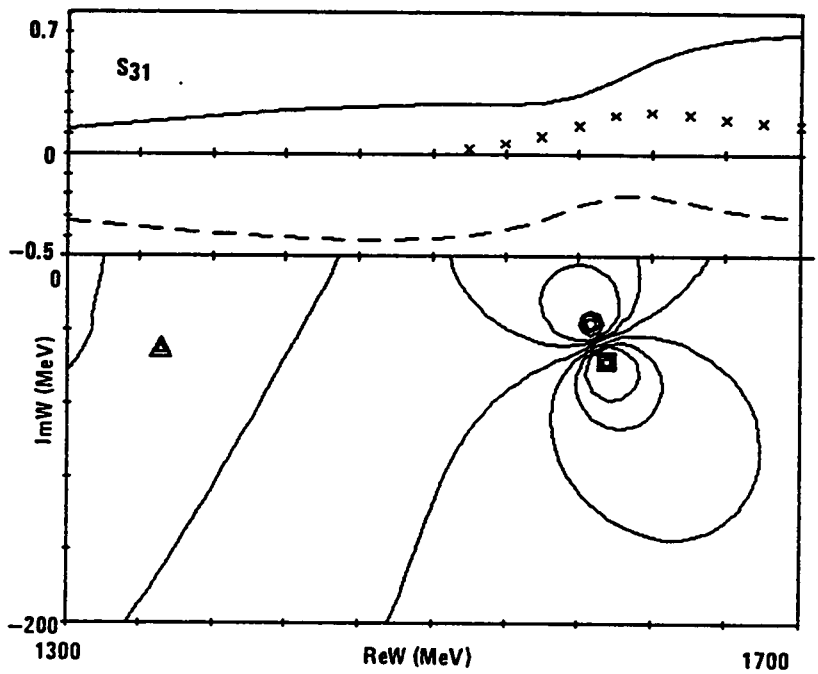

b. S_{31} PARTIAL WAVE

FIGURE 4-2. CONTOUR PLOTS OF log $|T|^2$ WITH LINEAR PLOTS OF T, SEE TEXT FOR EXPLANATION (Sheet 2 of 8)

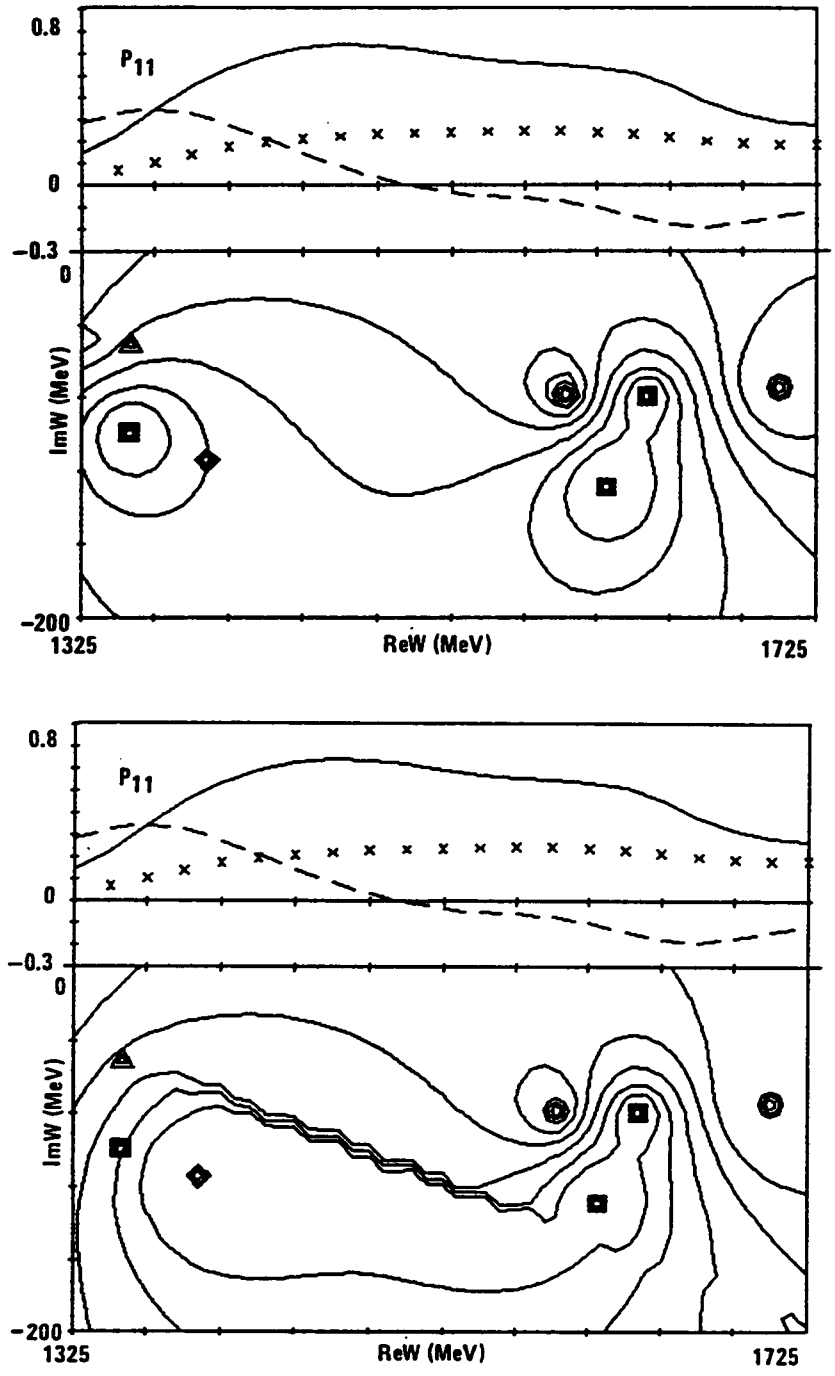

c. P_{11} PARTIAL WAVE

FIGURE 4-2. CONTOUR PLOTS OF log $|T|^2$ WITH LINEAR PLOTS OF T, SEE TEXT FOR EXPLANATION (Sheet 3 of 8)

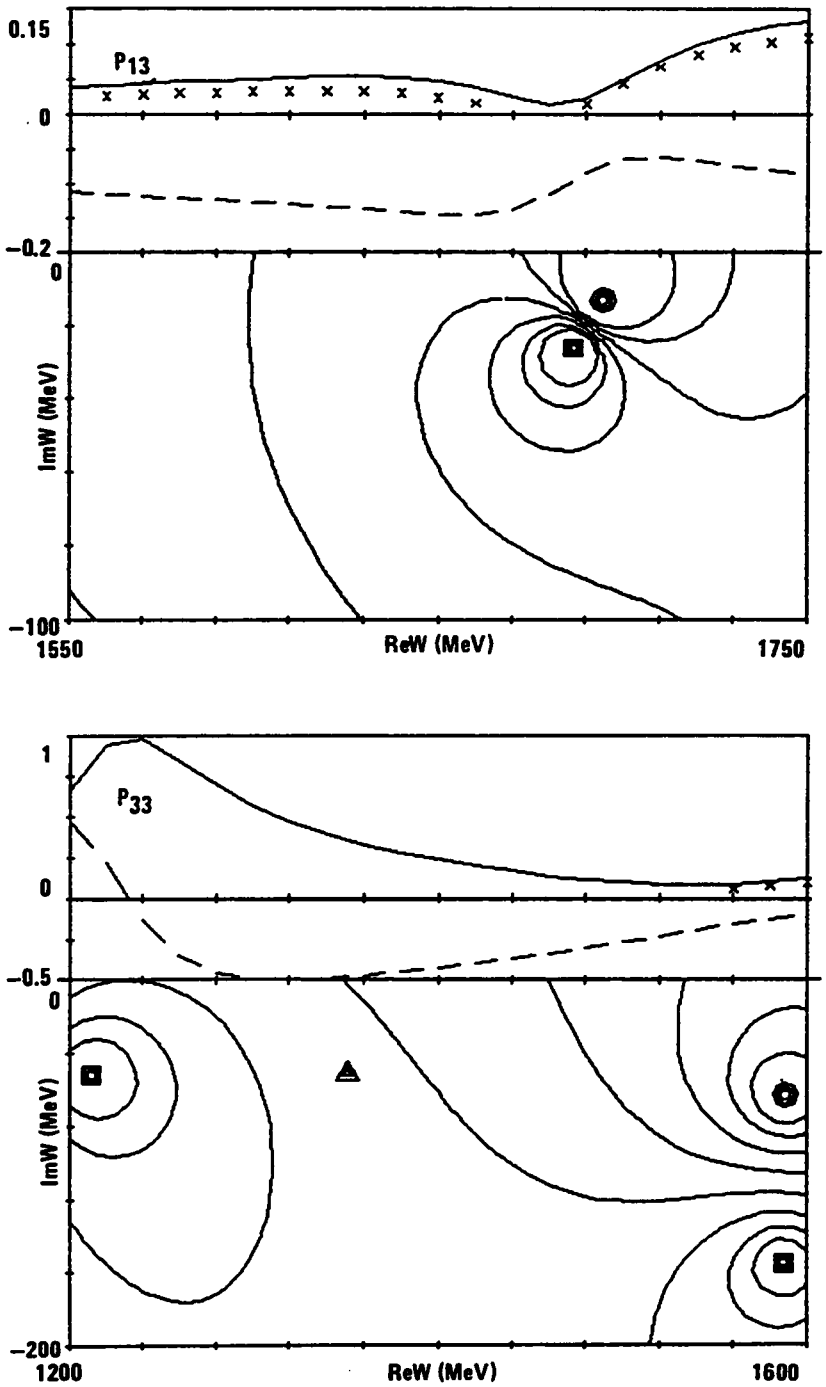

d. P_{13} AND P_{33} PARTIAL WAVES

FIGURE 4-2. CONTOUR PLOTS OF log $|T|^2$ WITH LINEAR PLOTS OF T, SEE TEXT FOR EXPLANATION (Sheet 4 of 8)

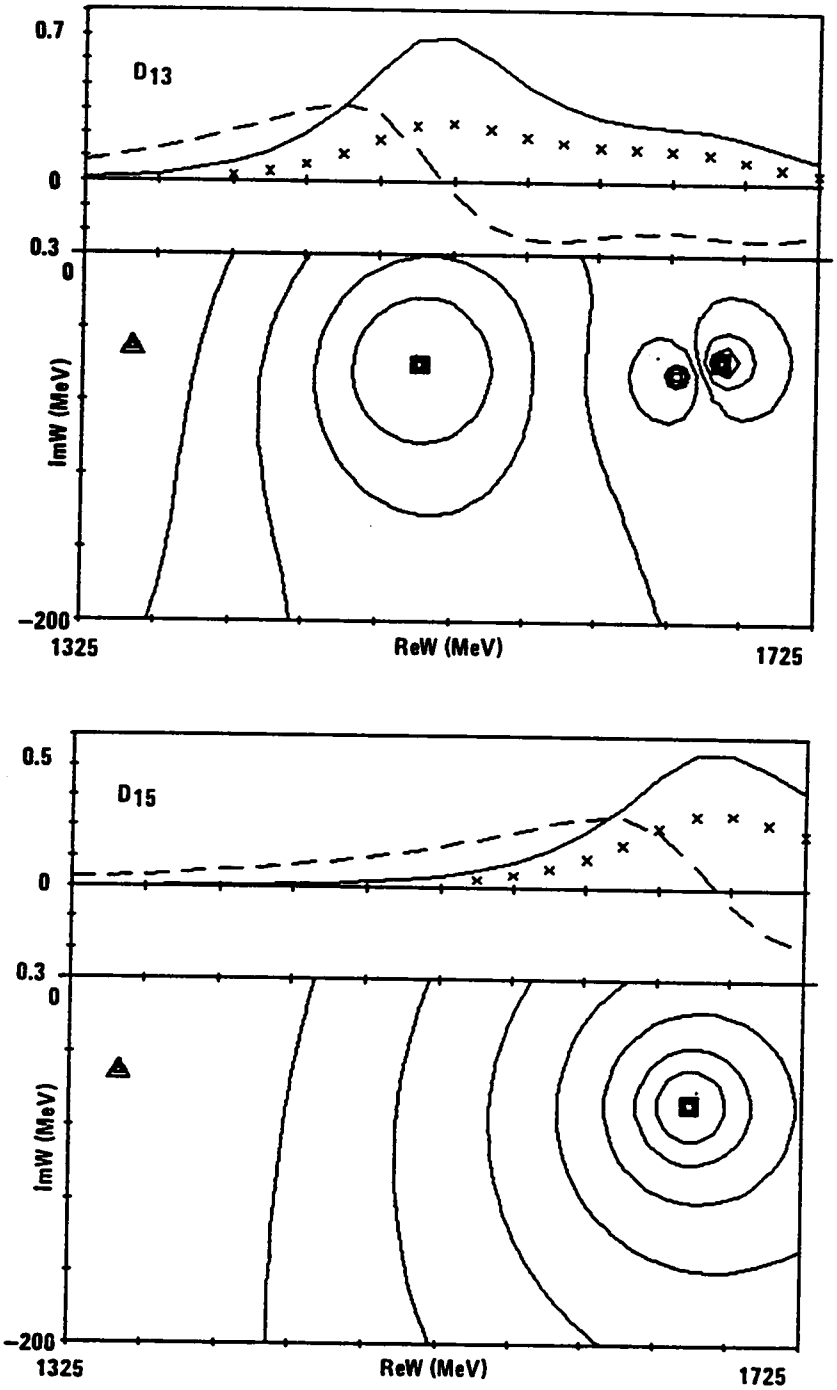

e. D_{13} AND D_{15} PARTIAL WAVES

FIGURE 4-2. CONTOUR PLOTS OF log $|T|^2$ WITH LINEAR PLOTS OF T, SEE TEXT FOR EXPLANATION (Sheet 5 of 8)

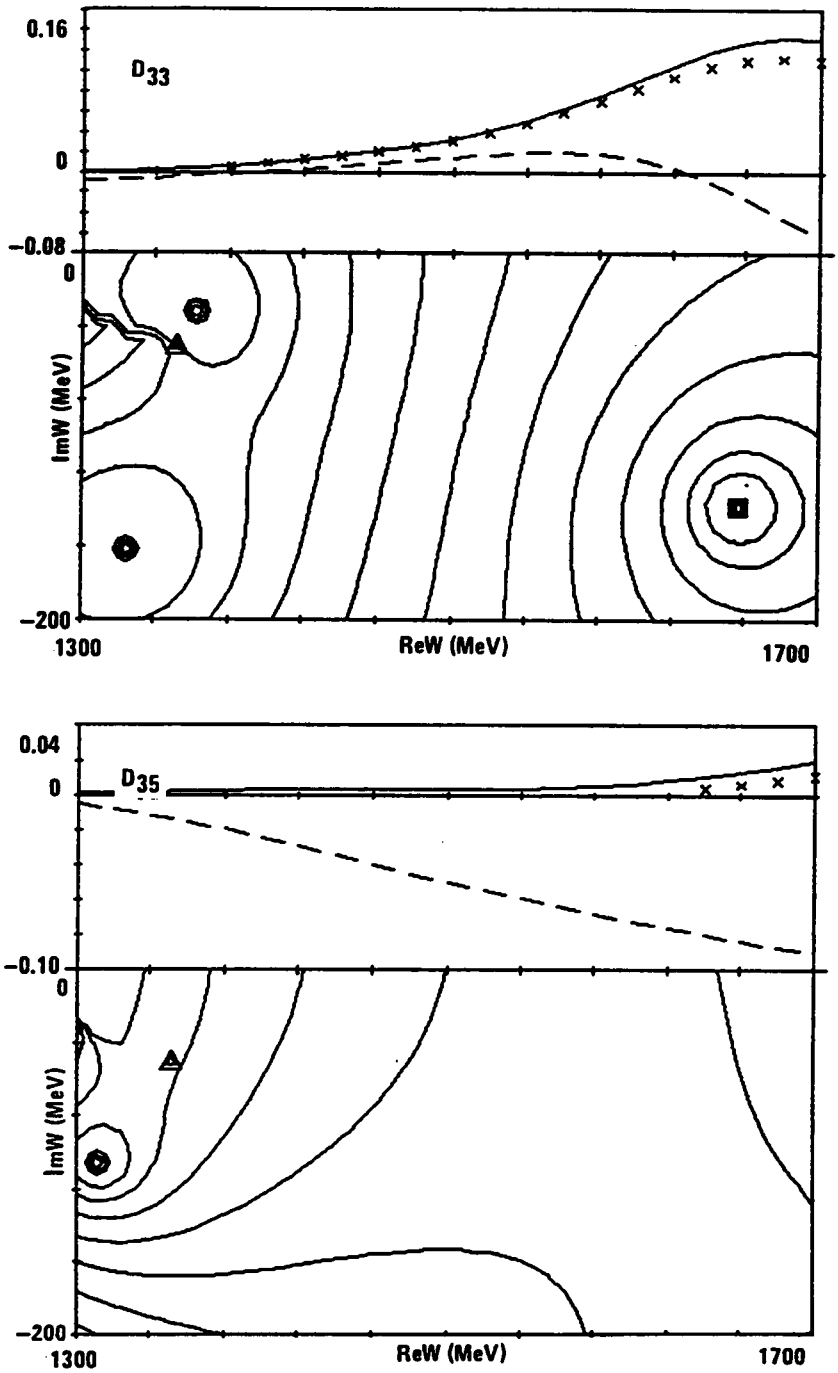

f. D_{33} AND D_{35} PARTIAL WAVES

FIGURE 4-2. CONTOUR PLOTS OF log $|T|^2$ WITH LINEAR PLOTS OF T, SEE TEXT FOR EXPLANATION (Sheet 6 of 8)

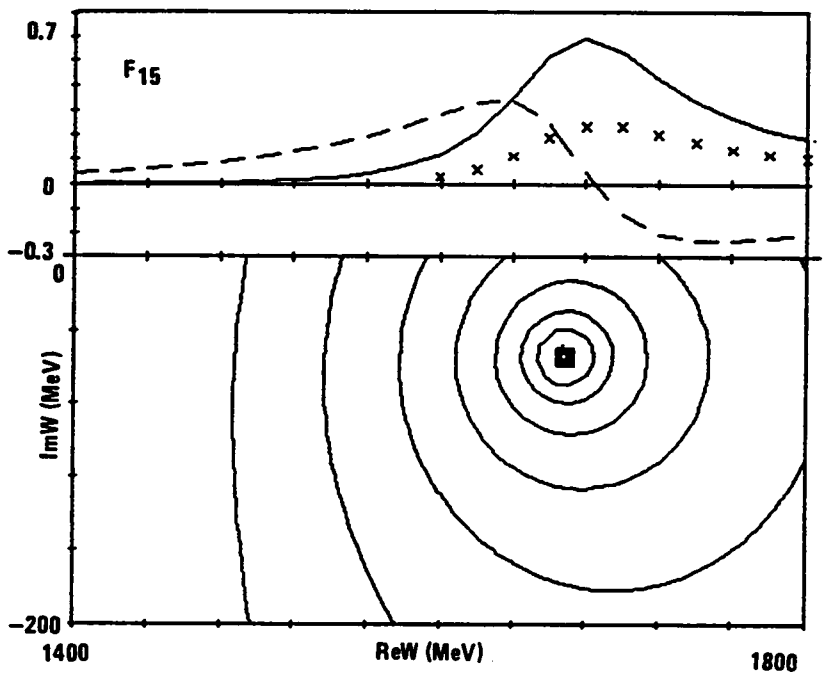

g. F_{15} PARTIAL WAVE

FIGURE 4-2. CONTOUR PLOTS OF log $|T|^2$ WITH LINEAR PLOTS OF T, SEE TEXT FOR EXPLANATION (Sheet 7 of 8)

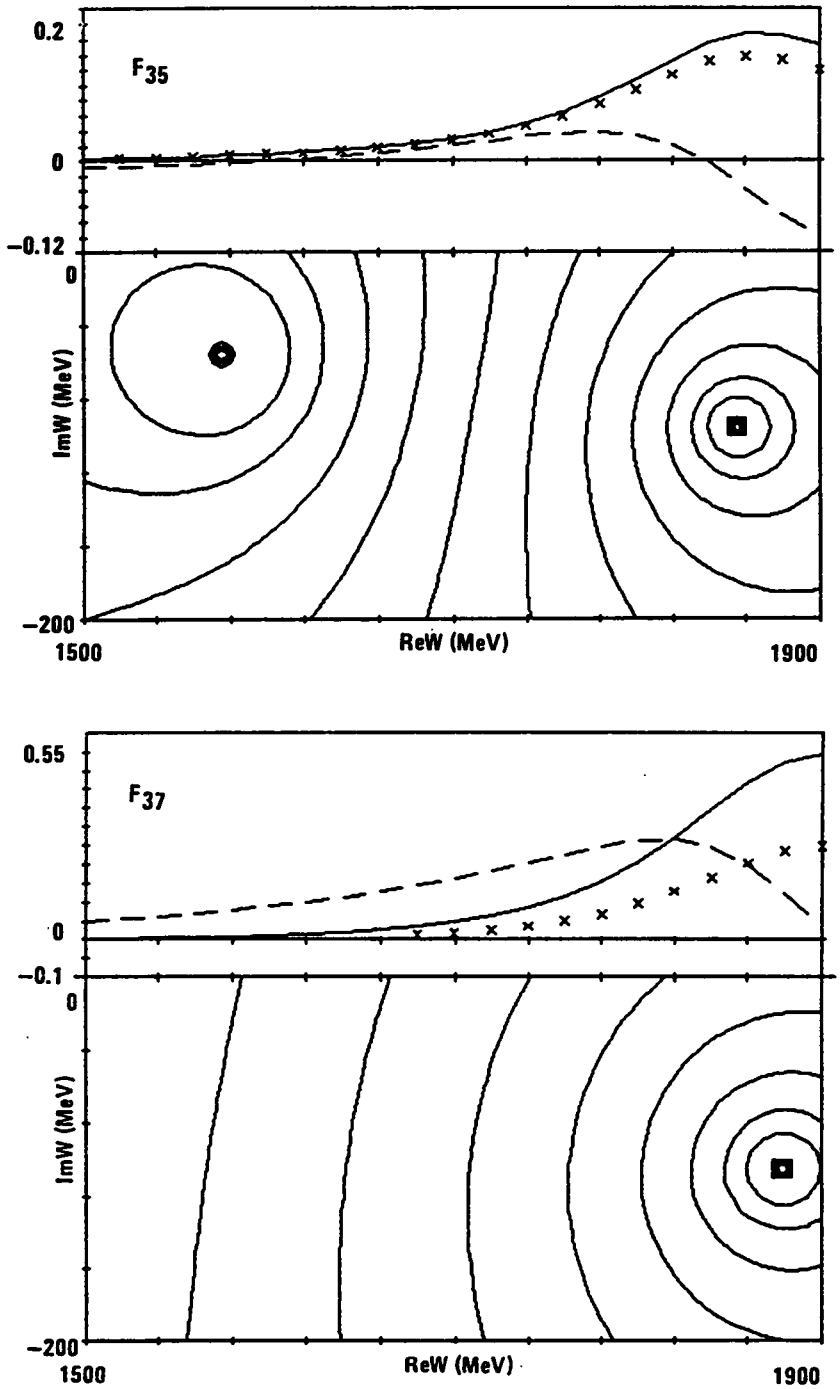

h. F_{35} AND F_{37} PARTIAL WAVES

FIGURE 4-2. CONTOUR PLOTS OF log $|T|^2$ WITH LINEAR PLOTS OF T, SEE TEXT FOR EXPLANATION (Sheet 8 of 8)

(R) on the unphysical sheet, diamonds mark poles (P) on the sheet introduced by the delta threshold, circles locate zeros (Z), and the triangles mark the delta branch point. Shown with the contour plots of log $|T|^2$ are linear plots of the T-matrices on the physical axis. The solid lines are Re {T} and the dashed lines are Im {T}. A measure of the inelasticity is shown by the "x's" that label Im {T} - $|T|^2$.

Figure 4-2a displays the two resonance poles of the S_{11} wave. The top contour plot shows the unphysical sheet and a zero between the two poles, with all three features influencing the physical amplitude. The structure in the other sheet of the pi-delta branch cut is displayed in the bottom plot. An additional pole is seen to exist on this sheet, but it is a long distance from the physical axis, having to go around the pi-delta branch point to reach the real axis. Consequently, it has negligible effect on the on-shell amplitude. Simpler structure is seen in the S_{31} wave shown in Figure 4-2b. Here a closely spaced zero and resonance pole are shown with both obviously influencing the real axis.

The most complicated structure of any of the waves is seen in the P_{11} wave as shown in Figure 4-2c. Again, the top plot displays the unphysical sheet of the elastic cut, and the bottom plot rotates the pi-delta branch cut to reveal the structure in the new sheet. The Roper resonance, N(1440), is seen to lie near, but below the pi-delta branch point. With the Roper is a nearby pole just around the pi-delta branch point from the real axis. Its proximity to the Roper, its relatively short distance to the real axis, and its significant

residue result in this extra pole having some effect on the physical amplitude. This second pole is relatively stable. Its presence was observed early in the analysis before the explicit K-matrix poles were introduced into the energy-dependent parametrization scheme. Although this extra pole cannot properly be called a resonance, its impact with the Roper on the on-shell amplitude is probably responsible for the split Roper proposed by the older results of Ayed *et al.*,[5] but discounted by other recent analyses.[1,4,6] The N(1710) resonance in the P_{11} wave also has a complicated structure: two poles and two zeros on the unphysical sheet. The bottom pole is shielded from the real axis by the upper pole and the two zeros. Its validity is questionable because of the lack of effect on the real axis, and it may be just an artifact of the parametrization for this wave. Because there is not just a simple pole for the N(1710), but rather the intertwined zeros and poles as shown, there are significant differences in the resonance parameters from FP86 and the Carnegie-Mellon results, as noted earlier.

To further investigate the structure of the Roper resonance, the sensitivity of the P_{11} pole positions to the coupling strength of the explicit K-matrix pole is examined. Recall from Chapter 3's energy-dependent parametrization that parameters 17 and 18 are the strengths of the coupling of the explicit K-matrix pole to the elastic and inelastic channels, respectively. Figure 4-3 shows the trajectories of the T-matrix poles as the elastic coupling constant, g_e, and the inelastic coupling constant, g_i, are varied between 0.1 and 1.0. The

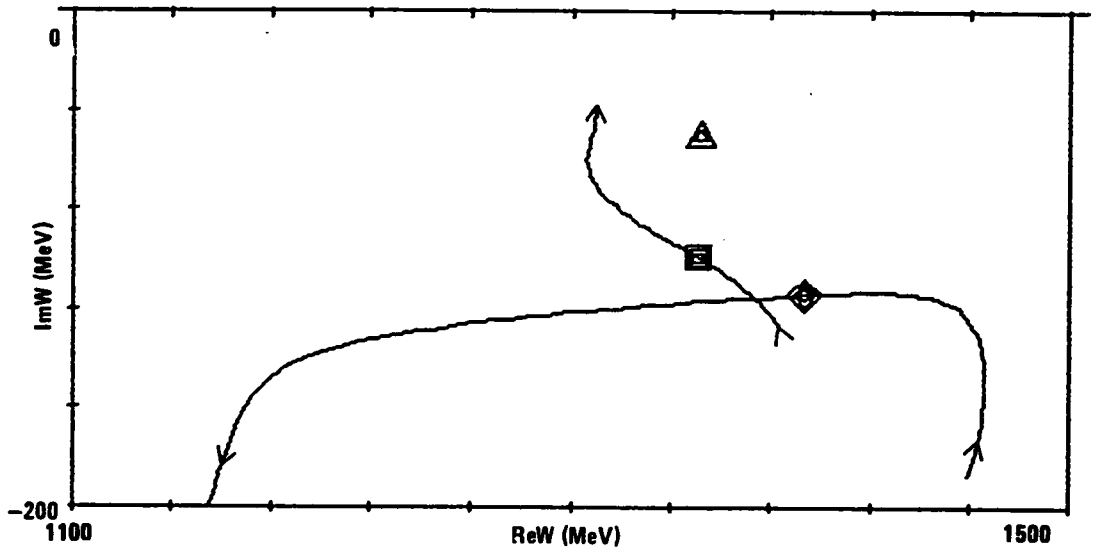

a. VARIATION WITH ELASTIC COUPLING, g_e

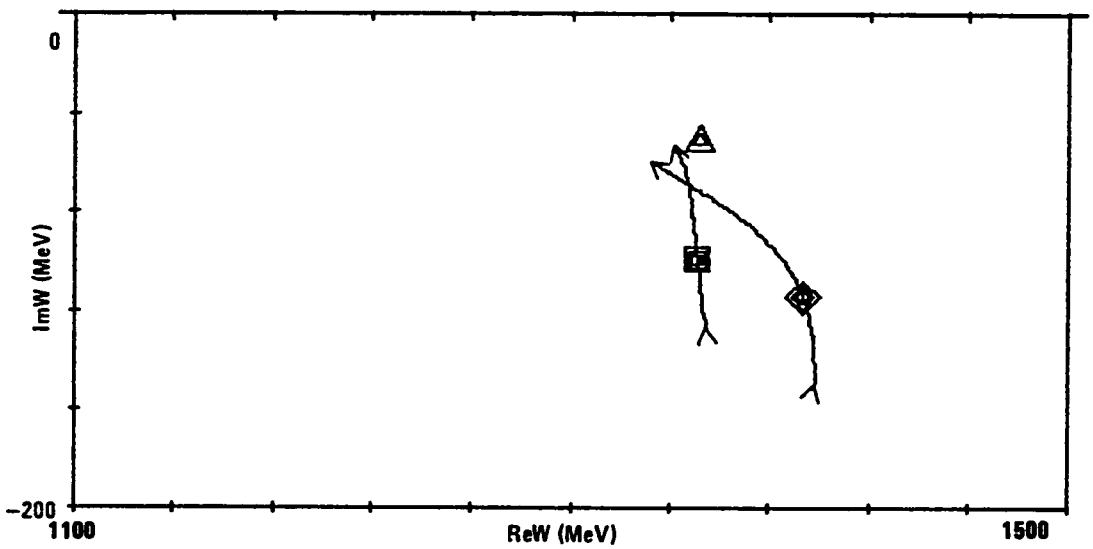

b. VARIATION WITHIN INELASTIC COUPLING, g_i

FIGURE 4-3. TRAJECTORY OF ROPER POLES AS COUPLING STRENGTH OF K-MATRIX POLE VARIES BETWEEN 0.1 AND 1.0

positions of the poles at the FP86 defined values of g_e = 0.3245 and g_i = 0.3569 are shown with the squares and diamonds described earlier. Arrows denote the direction of the movement as the indicated coupling increases. As expected, the Roper resonance pole moves about the delta branch point and closer to the real axis as the elastic coupling increases. As the non-resonant pole moves towards the second sheet, it also slides further away from the real axis. Although this pole continues to have some effect on the real axis for a range of coupling strengths, the true resonance pole dominates. When the inelastic coupling is increased, both poles move closer to the real axis and nearer to the delta branch point. The trajectories even cross, but the two poles never coalesce. As the inelastic coupling increases, the second pole moves to a position where it could be classified as a resonance. The interpretation of the movement of the T-matrix poles as the K-matrix pole coupling is varied is not conclusive. However, the movement is suggestive that the second pole might be related to a resonance that couples, at most, only weakly to the elastic channel.

The P_{13} and P_{33} partial waves displayed in Figure 4-2d show somewhat simpler structure. At the P_{13} N(1720) resonance is a pole-zero pair near the real axis. Other analyses[4] state a larger width for this resonance than observed here. The presence of the zero is responsible for this difference. Without it obscuring part of the effect of the pole, the pole would have to be farther from the real axis. It might be possible to reparametrize this wave to do away with the zero, but that investigation remains for the future. The delta

resonance is seen in the bottom plot as a strong pole near the real axis without any nearby zeros. The two-star resonance pole, P33 Δ1600, does have a zero between it and the real axis. Although it has a small residue, the zero blocks much of the effect this pole would otherwise have on the real axis, and this mitigation is presumably the reason the resonance is only weakly observed. Without the zero, the pole's presence would be obvious on the physical axis. With the zero, the pole has a reduced effect on the real axis and the resonance is difficult to observe.

The D-wave, pole-zero structures shown in Figures 4-2e and 4-2f are even simpler. The zeros do little to mitigate the effect on the real axis of any of the observed poles. All the D-waves except the D35 have isolated poles, and the D13 also has a pole-zero pair. Isolated zeros are seen near the pi-delta branch point in both the D33 and the D35 waves of Figure 4-2f, and this proximity renders their actual presence questionable.

The three F-waves shown in Figures 4-2g and 4-2h all have well isolated resonance poles, although more complicated structures could conceivably exist at higher energies. The F35-wave of Figure 4-2h exhibits, in addition, a relatively low-lying zero.

The presence of poles of $|T|^2$ in the complex energy plane is expected, and they can be identified with resonances if they are near the real axis. The interpretation of the zeros is more difficult. In nonrelativistic Schrödinger theory, Levinson's theorem for multiple bound states requires the existence of partial-wave zeros, as has been

demonstrated for the square well potential.[7] However, it is not clear how this aids the interpretation of the zeros seen here, other than to say that zeros are expected. If resonance poles are "sources" for the interaction, then the zeros are "sinks" that limit the poles' impact on the real axis, consistent with unitarity. The examination of solution FP86 has found both isolated poles and zeros and pole-zero pairs. In some cases such as the S_{31}, P_{13}, and P_{33} waves, the zero has a major impact on the effect the associated pole has on the real axis. It is conceivable that some of these zeros are not required to fit the data and could be removed by changing the position of the pole. This possibility should be pursued in future investigations, although preliminary efforts in that direction have not yet had any success.

4.4 Near-Axis Poles

In the nucleon-nucleon system, some analyses[8] report the presence of narrow poles in the partial-wave T-matrices near the real axis of the complex energy plane. It is interesting to investigate the possibility of the existence of such poles in the pion-nucleon system because none of the models described in the next chapter predict them and it would be useful to rule out their existence. That goal can be addressed by testing the impact on chi-squared when a narrow pole is imposed on a partial wave using a product S-matrix formulation,

$$S_{TOTAL} = S_{BACKGROUND} * S_{RESONANCE} . \qquad (4\text{-}5)$$

For the purpose of this investigation, the background S-matrix factor is taken explicitly from the energy-dependent parametrization

described in Chapter 3. The resonance S-matrix factor is given by a Breit-Wigner parametrization,

$$T_{RESONANCE} = \frac{1}{2i}\,(S_{RESONANCE} - 1) = \frac{a + i*b}{(c - WR) + i*(d - WI)} \qquad (4\text{-}6)$$

for real numbers a, b, c, and d and complex energy, W = WR + i*WI. For this investigation, the values of a, b, c, and d are fitted assuming an extra pole in only one partial wave. The initial values chosen for the Breit-Wigner residue parameters (a, b) were each about 0.1. The complex pole position parameters (c, d) were initialized at (1200, -1), (1500, -1), and (1700, -1) MeV for each of three separate sets of calculations. After the Breit-Wigner parameters are optimized for the partial wave being investigated, all the parameters including the K-matrix parameters are varied to minimize chi-square. This process was repeated for each S-, P-, D-, and F-wave and for each of the three initial near-axis resonance pole positions. All partial waves other than the one being examined are defined by solution FP86. The results of these investigations are given in Table 4-3, showing the change in chi-square after optimizing the Breit-Wigner parameters, and also after varying all the parameters for that wave.

For most of the cases considered, chi-square changes by an insignificant amount to justify the possibility of the extra pole. For those waves where the decrease in chi-square was greater than 10, the Breit-Wigner parameters are shown in Table 4-4. The residues' magnitudes ($\sqrt{a^2 + b^2}$) for these are all small compared to the pole

TABLE 4-3. CHANGE IN CHI-SQUARE WITH INCLUSION OF NEAR-AXIS POLE COMPARED TO SOLUTION FP86

PARTIAL WAVE	INITIAL VALUE OF REAL PART OF RESONANCE POLE		
	1200	1500	1700
S_{11}	+1.,* 0.**	-0.9,* -0.9**	-0.2,* -1.**
S31	-4., -4	-3., -8.	-0.2, -0.8
P_{11}	+3., +0.5	-5., -6.	-0.7, -6.
P_{13}	-3., -3.	-27., -27.	-8., -29.
P_{31}	-7., -7.	-5., -6.	-17, -19.
P_{33}	-6., -6.	-8., -9.	-12., -12.
D_{13}	-1., -1.	-8., -9.	-2., -2.
D_{15}	+0.5, -0.5	-2., -2.	-2., -0.3
D_{33}	-5., -18.	-3., -7.	-2., -13.
D_{35}	-5., -5.	-3., -3.	-14., -18.
F_{15}	+2., -19.	-9., -12.	-2., -2.
F_{17}	-3., -3	-21., -21.	-3., -3.
F_{35}	-4., -4.	-12., -12.	-9., -9.
F_{37}	-2., -4.	-14, -14.	-25., -27.

*After fitting resonance parameters

**After refitting all parameters for the searched wave

TABLE 4-4. NEAR-AXIS BREIT-WIGNER POLE PARAMETERS

WAVE	POLE POSITION (c + id)		RESIDUE (a + ib)	
	c	d	100*a	100*b
P_{13}^{*}	1502.6	-7.6087	6.9143	0.12222
P_{31}^{*}	1705.1	-3.9313	2.7161	5.6324
P_{33}^{*}	1702.2	-0.93372	-2.0196	1.498
D_{35}^{*}	1711.6	-2.493	1.2844	1.4073
F_{17}^{*}	1498.1	-3.4236	1.5562	2.2023
F_{35}^{*}	1500.5	-3.8956	1.4469	1.7365
F_{37}^{**}	1502.7	-3.5666	0.61382	2.9028
F_{37}^{**}	1714.0	-4.0284	0.37903	1.9888
P_{13}^{**}	1511.8	-2.4855	5.5175	3.5079
D_{33}^{**}	1703.2	-1.3354	-2.1832	1.9353
D_{33}^{**}	1195.2	-1.3413	-1.9954	1.6074
F_{15}^{**}	1283.0	-32.445	5.5005	-3.2483
F_{15}^{**}	1502.1	-3.4115	0.69244	-1.4424

*Wave where chi-square decreased by more than 10 after fitting only Breit-Wigner parameters

**Wave where chi-square decreased by more than 10, only after refitting entire wave.

half-width (|d|), typically 1 percent, and thus the near-axis poles are highly inelastic.

For a more in-depth examination of these partial waves, the partial T-matrices for those four cases with a chi-squared reduction of greater than 20 are shown in Figure 4-4. The differential cross sections, polarizations, and spin rotation parameters were calculated for each of these waves at the pole energy and compared with results for solution FP86. The differential cross sections seldom changed by more than 0.1 millibarn/steradian, and then only slightly. The polarization values never differed by more than 0.05 and the rotation values by more than 0.03. Although these differences are small, it is difficult, but possible, to measure differential cross sections and polarizations to within these accuracies. Calculating chi-square for the experimental data base in a 30-MeV neighborhood of each Breit-Wigner pole and comparing with solution FP86 show that the decrease in chi-square for these waves is primarily caused by differential cross-section data. In only one of the four cases, F_{37} with a pole at 1714 MeV, is the decrease primarily caused by polarization data. In conclusion, these results show that the data do not preclude the existence of near-axis poles, but neither are they required by the data. To completely disprove their existence requires the measurement of differential cross sections and polarizations to better than the accuracies stated above over a wide range of angles and at small steps in energy. The needed energy step size is illustrated by the close spacings of the pole positions in Table 4-4, on the order of 1 MeV.

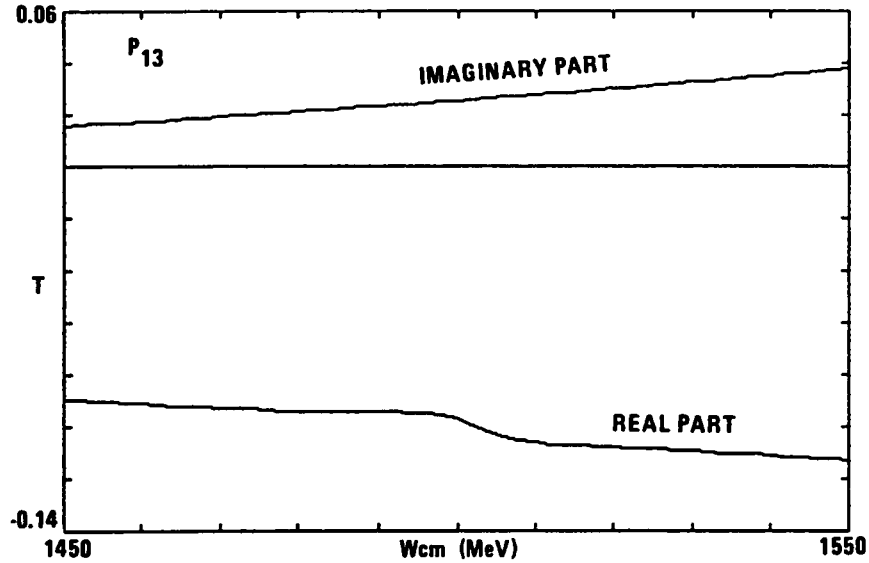

a. P_{13}, CHI-SQUARED REDUCTION OF 27

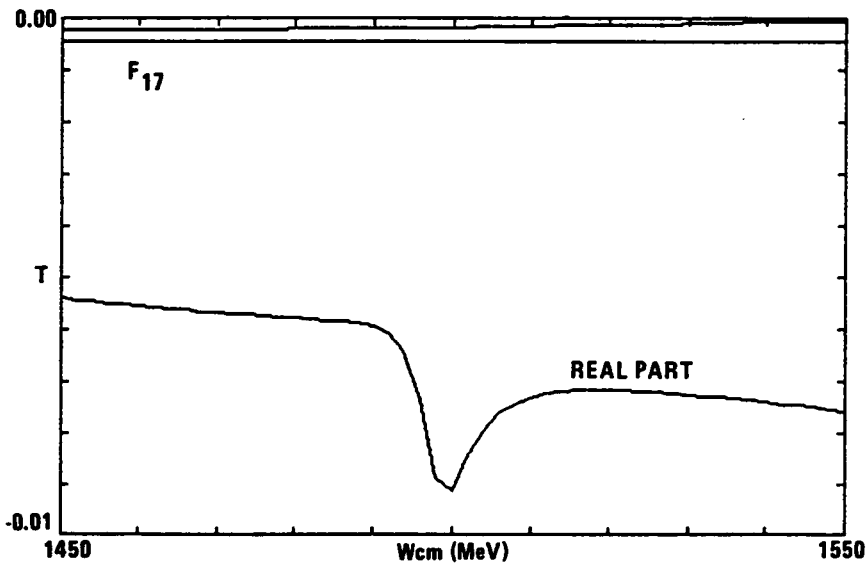

b. F_{17}, CHI-SQUARED REDUCTION OF 21

FIGURE 4-4. PARTIAL WAVES MODIFIED WITH NEAR-AXIS BREIT-WIGNER POLE (Sheet 1 of 2)

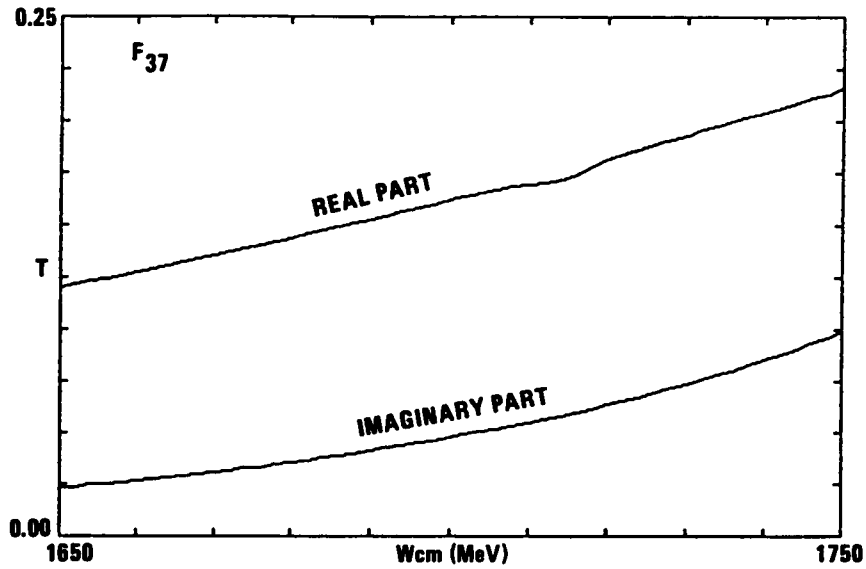

c. F_{37}, CHI-SQUARED REDUCTION OF 25

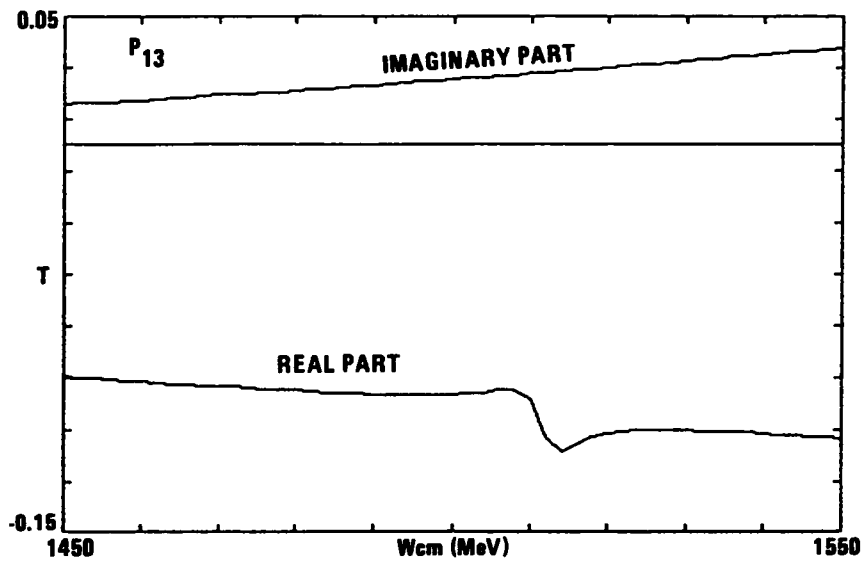

d. P_{13}, CHI-SQUARED REDUCTION OF 29

FIGURE 4-4. PARTIAL WAVES MODIFIED WITH NEAR-AXIS BREIT-WIGNER POLE (Sheet 2 of 2)

4.5 REFERENCES

1. G. Höhler, Landolt-Börnstein, Vol. I/9b: *Pion-Nucleon Scattering*, ed. H. Schopper (1983).

2. B. H. Bransden and R. G. Moorhouse, "Pion-Nucleon Scattering," Princeton University Press (1973).

3. Particle Data Group, *Physics Letters*, Volume 170B, 10 April 1986, Review of Particle Properties, p. 245, ff.

4. R. E. Cutkosky *et al.*, *Physical Review*, Vol. 20 (1979), pp. 2804, 2839; and in Proceedings of the IVth International Conference on Baryon Resonances (Toronto, 1980), ed. N. Isgur, p. 19; and in Proceedings of the 3rd LAMPFII Workshop, Vol. II (1983), p. 785.

5. Ayed, Unpublished Thesis from the Saclay Group as Reported in Particle Data Group, *Reviews of Modern Physics*, Vol. 48, 1976, p. S147

6. R. Koch, *Zeitschrift für Physik C*, Vol. 29 (1985), p. 597.

7. R. A. Arndt, L. D. Roper, "Scattering in a Spherical Potential Motion of Complex Plane Poles and Zeros," Unpublished.

8. B. Tatischeff *et al.*, *Physical Review C*, Vol. 36, November 1987, p. 1995

5. THEORETICAL MODELS

The current theory of the strong interaction is, of course, quantum chromodynamics (QCD). QCD is analogous to the theory of the electromagnetic interaction, quantum electrodynamics (QED), but, whereas there exists only one type of electromagnetic charge, there are three types (colors) of color charge. Also, whereas the QED exchange boson, the photon is uncharged, the carrier of the strong force, the gluon does carry color charge. Presumably these differences are responsible for the experimentally observed facts that quarks are confined into the color singlet combinations of mesons and baryons (quark confinement) and that within hadrons, the quarks are nearly free (asymptotic freedom). The differences also result in a theory so complicated that no exact solution has been (can be?) found, and it has been necessary to develop models that are approximations to the full theory. Consequently, the models only contain part of physics needed to fully explain the experimental results. Indeed, with the current state of knowledge, the experimental data are used to improve the models rather than the models used to make precise quantitative predictions. The models cannot be expected to agree completely with the phase-shift results presented here, but they can provide useful and important insight into the physics of the strong pion-nucleon interaction.

In this chapter, three classes of the most popular and successful of such models are described and their specific applications to the pion-nucleon problem are discussed. The three model types presented

here are the constituent quark models, the bag models, and the Skyrme soliton models. The approach used in this chapter is largely tutorial with only previously published results discussed. Particular emphasis is given to using the results of these models to "explain" the phase-shift results. No new theoretical calculations have been performed and, indeed, would be outside the scope of this effort.

5.1 THE CONSTITUENT QUARK MODEL

5.1.1 Overview

The first class of models to be examined here is the non-relativistic quark potential models, or constituent quark models in which baryons are composed of three valence quarks that define the baryon quantum numbers. Although these models suffer from the liability that the quarks are treated in a nonrelativistic fashion, they benefit from the ease in which center-of-mass motion can usually be separated from the internal degrees of freedom. Baryon wave functions must exhibit the permutation symmetry appropriate to their three quark composition and also must have total angular momentum as a good quantum number. Appendix F describes the ensuing baryon spectroscopy, showing how the baryon states may be classified according to standard group-theoretic language. Good summaries of this class of models are found in References 1 and 2.

A variety of quark-quark potentials have been used in these models to account for the observed quark confinement. Included among them are logarithmic,[3] linear,[4,5] and power law[6] forms for the confining potential's dependence on quark-quark separation. One of the most

useful and successful forms is the quadratic or harmonic oscillator model made popular by Isgur and Karl.[7-10] In all cases, the confining long-range potential is flavor- and spin-independent, except for possible constituent quark mass dependence. DéRujula *et al.*[11] have shown how QCD can give rise to short-range, spin-dependent forces that might account for much of the splitting within supermultiplets. They argue that in analogy to QED, one-gluon exchange (OGE) results in a short-range force between quarks of the same form as the two-body Fermi-Breit interaction. For quarks labeled by i and j, the baryon Hamiltonian that they propose is:

$$H = L(r_1, r_2, r_3, \ldots) + \sum_i \left(m_i + \frac{p_i^2}{2m_i} + \ldots\right) + \sum_{i>j} \left(\alpha q_i q_j - \frac{2}{3}\alpha_s\right) S_{ij} \,. \quad (5\text{-}1)$$

The constants α and α_s are the electromagnetic fine structure and strong coupling constants, respectively, for quarks of charge, effective mass, position and momentum, q_i, m_i, r_i, and p_i. The interaction responsible for binding the quarks is denoted by L. It could include any of the potentials described earlier. The three dots denote any missing relativistic corrections to this Hamiltonian. The two-body Fermi-Breit interaction for $r = r_i - r_j$ is given by S_{ij}:

$$S_{ij} = \frac{1}{r}\,, \textit{ coulomb} \quad (5\text{-}2)$$

$$-\frac{\pi}{2}\left[\left(\frac{1}{m_i^2} + \frac{1}{m_j^2}\right)\delta^3(r)\right], \textit{ Darwin}$$

$$- \frac{2\pi}{3m_i m_j} [\vec{\sigma}_i \cdot \vec{\sigma}_j \delta^3(\vec{r})], \textit{Fermi contact term hyperfine interaction}$$

$$- \frac{1}{4r^3 m_i m_j} [3(\vec{\sigma}_i \cdot \hat{r})(\vec{\sigma}_j \cdot \hat{r}) - \vec{\sigma}_i \cdot \vec{\sigma}_j], \textit{tensor term hyperfine interaction}$$

$$- \frac{1}{4r^3} \left\{ \frac{1}{m_j^2} (\vec{r} \times \vec{p}_i) \cdot \vec{\sigma}_i - \frac{1}{m_j^2} (\vec{r} \times \vec{p}_j) \cdot \vec{\sigma}_j \right.$$

$$\left. + \frac{2}{m_i m_j} \left[(\vec{r} \times \vec{p}_i) \cdot \vec{\sigma}_j - (\vec{r} \times \vec{p}_j) \cdot \vec{\sigma}_i \right] \right\} \textit{spin orbit } (\vec{L} \cdot \vec{S})$$

$$- \frac{1}{2m_i m_j r} [\vec{p}_i \cdot \vec{p}_j + \hat{r} \cdot (\hat{r} \cdot \vec{p}_j)\vec{p}_j] . \qquad (5\text{-}2)$$

Identification of the various terms is indicated as shown where σ_i's are the usual Pauli spin matrices. DéRujula rewrites equation 5-1 as $H = H_0 + H'$ with:

$$H_o = L + \sum_i (m + p_i^2/2m) \qquad (5\text{-}3)$$

and H' including everything else with m being the effective (constituent, as opposed to current) and assumed equal mass up-and-down quarks. The spin-dependent potential, H', splits the degenerate supermultiplet, eigenstates of H_0. DéRujula *et al.* also show how the Fermi term causes the nearly degenerate quark spin 3/2 nucleon (8,4) and quark spin 1/2 delta (10,2) members of the {70, $L=1^-$} supermultiplet to lie above the quark spin 1/2 nucleon (8,2) members of the multiplet.

5.1.2 The Harmonic Oscillator Model

Although, as described above, a variety of forms has been used for the long-range quark binding interaction, the emphasis is on the quadratic form in this chapter. In their first works, Isgur and Karl[7,8] extended the work of DéRujula by explicitly calculating the Breit contribution to {70, $L=1^-$} supermultiplet splitting by using harmonic oscillator wavefunctions as a zero-order approximation to the true spatial wavefunction. The harmonic oscillator model has the advantage that the spatial wavefunction reduces to the product of two independent spherically symmetric oscillator wavefunctions of the identical spring constant with center-of-mass motion separating completely out. For the nonstrange sector of interest here, we define

$$\vec{R}_{c.m.} = \frac{1}{3}(\vec{r}_1 + \vec{r}_2 + \vec{r}_3)$$

$$\vec{\rho} = \sqrt{\frac{1}{2}}(\vec{r}_1 - \vec{r}_2)$$

$$\vec{\lambda} = \sqrt{\frac{1}{6}}(\vec{r}_1 + \vec{r}_2 - 2\vec{r}_3)\,. \qquad (5\text{-}4)$$

They obtain the harmonic confining Hamiltonian as follows:

$$H_{HO} = \frac{1}{2m}(p_\rho^2 + p_\lambda^2) + \frac{3}{2}K(\rho^2 + \lambda^2) \qquad (5\text{-}5)$$

that they use as their unperturbed Hamiltonian. In comparison with DéRujula, they include the effects of the nonspin-dependent part of the Fermi-Breit interaction in the unperturbed energy and they omit

the spin-orbit term. The splitting was found to be one-half of the nucleon-delta mass difference, in good agreement with experiment.[7] In fact, they used the nucleon-delta mass difference to fit the one parameter in their model, the overall strength of the color magnetic hyperfine interaction. Isgur and Karl also explicitly calculated the contribution caused by the tensor part of the hyperfine interactions.[8] They found weak mixing within the two $J^P = 1/2^-$ nucleon states and strong mixing within the two $J^P = 3/2^-$ nucleon states, again in good agreement with the empirical results of Hey *et al.*[12] The splitting caused by the tensor term is caused by the mixing between states of different quark spin that it produces. The operators have S = L = 2. On the other hand, the Fermi term has S = L = 0 and only connects quark pairs of zero orbital angular momentum. The resulting predicted masses for the low-lying, negative-parity baryons are compared in Table 5-1 and later in Table 5-4 with the results of the reported phase-shift analysis. The higher lying negative-parity states are presumably caused by N = 3 excitations that Isgur and Karl do not address.

The successes of this model[8] as shown with the low-lying, negative-parity baryons demonstrate the importance of the hyperfine interaction in breaking the $\{70,1^-\}$ degeneracy. The Fermi-Breit interaction also apparently gives the correct relative strength between the Fermi and tensor terms of the observed hyperfine interaction. Conversely, there appears to be little evidence for the presence of the expected spin-orbit force. Isgur and Karl estimate that

TABLE 5-1. HARMONIC OSCILLATOR MODEL PREDICTIONS OF LOW-LYING, NEGATIVE-PARITY NONSTRANGE BARYON MASSES

STATE $L_{2I,2J}$ (MeV)	ISGUR AND KARL PREDICTIONS[8] (MeV)	PHASE SHIFT* (MeV)
S_{11} (1535)	1490	1461
S_{11} (1650)	1655	1655
D_{13} (1520)	1535	1508
D_{13} (1700)	1745	1673
D_{15} (1675)	1670	1664
S_{31} (1620)	1685	1596
D_{33} (1700)	1685	1657

*Mass as given by pole from Table 4-1

the spin-orbit force can be present with at most 10 percent of its expected strength, speculating that the dominance of the spin-spin force over the spin-orbit force may be caused by a highly anomalous quark-gluon color magnetic moment. They also suggest and prefer an alternative explanation that the spin-orbit contribution from OGE is largely canceled by the spin-orbit contribution of the confining potential through Thomas precision.

Isgur's and Karl's analysis of the positive-parity, excited, nonstrange baryons[9] illustrates the added complication in these states as mentioned in Appendix F. For purely harmonic SU(6) invariant quark confining forces, the positive-parity N = 2 states will lie in the degenerate multiplets of (56*, $L^P = 0^+$), (56, $L^P = 2^+$), (70, $L^P = 0^+$), (70, $L^P = 2^+$), and (20, $L = 1^+$). Unlike the negative-parity states where a purely harmonic confining interaction with hyperfine splitting agrees well with experiment, the observed positive-parity states do not lie in the degenerate multiplets listed above and predicted by the harmonic confining interaction. There must be an anharmonic contribution to the confining force, and, for these analyses, Isgur and Karl add an undetermined anharmonic term, $U(r_{ij})$, to the confining potential:

$$H = \sum_i m_i + H_o + H_{hyp}$$

$$H_o = H_{HO} + \sum_{i>j} U(r_{ij}) \,. \qquad (5\text{-}6)$$

Because $U(r_{ij})$ is unknown, it is not possible to obtain exact solutions to the eigenstates of H_o as it was in the negative-parity states where the presence of $U(r_{ij})$ is not needed. In the harmonic oscillator model, lack of knowledge of $U(r_{ij})$ is not fatal to the analysis because first-order perturbation theory shows in a straightforward fashion that the zero-order energies of the five multiplets with N = 2 reduce to functions of two parameters, E_o and ε, that can be roughly fitted by the observed states with E_o = 2,020 MeV and ε = 420 MeV. The five multiplets - (56*, $L^P = 0^+$), (56, $L^P = 2^+$), (70, $P = 0^+$), (70, $L^P = 2^+$), and (20, $L^P = 1^+$) then have eigenmasses of $E_o - \varepsilon$ = 1,600 MeV, $E_o - 2/5\ \varepsilon \simeq$ 1,850 MeV, $E_o - 1/2\ \varepsilon \simeq$ 1,800 MeV, $E_o - 1/5\ \varepsilon \simeq$ 1,935, and $E_o \simeq$ 2,020 MeV, respectively. The excited, nonstrange, positive baryons in the N = 2 oscillator model, as predicted by Isgur and Karl, along with their zero-order masses are given in Table 5-2. As the authors note, the (56*, 0^+) naturally emerges as low-lying and can be identified with the Roper resonance. The unobserved (20, $L^P = 1^+$) is pushed up high in energy.

Once the zero-order eigenmasses have been established, Isgur and Karl use the hyperfine interaction and harmonic oscillator wave-functions to mix the states within each of the SU(6) multiplets and also to mix states of the same J^P and isospin between the various multiplets. A summary of their mass predictions and suggested identification with states from the Particle Data Table[13] is given in Table 5-3. For the states that can be identified, the agreement is again very good. The major apparent problem is the prediction of many

TABLE 5-2. HARMONIC OSCILLATOR MODEL PREDICTIONS FOR POSITIVE, NONSTRANGE BARYON STATES AND ZERO-ORDER MASSES (MeV)

J^P	FLAVOR MULTIPLET, QUARK SPIN			
	(8,2)N	(8,4)N	(10,2)Δ	(8,4)Δ
$1/2^+$	(56, L = 0), 1600 (70, L = 0), 1810 (20, L = 1), 2020	(70, L = 2), 1935	(70, L = 0), 1810	(56, L = 2), 1850
$3/2^+$	(56, L = 2), 1850 (70, L = 2), 1935 (20, L = 1), 2020	(70, L = 0), 1810 (70, L = 2), 1935	(70, L = 2), 1935	(56, L = 0), 1600 (56, L = 2), 1850
$5/2^+$	(56, L = 2), 1850 (70, L =2), 1935	(70, L = 0), 1810 (70, L = 2), 1935	(70, L = 2), 1935	(56, L = 2), 1850
$7/2^+$	--	(70, L = 2), 1935	--	(56, L = 2), 1850

TABLE 5-3. ISGUR AND KARL[9] HARMONIC OSCILLATOR MODEL WITH HYPERFINE SPLITTING PREDICTIONS FOR POSITIVE-PARITY, NONSTRANGE BARYON STATES

STATE L_{2I2J}	PREDICTED MASS (MeV)	OBSERVED STATE L_{2I2J} (MeV)	PHASE SHIFT (MeV)
P_{11}	1405	P_{11} (1440)	1351
	1705	P_{11} (1710)	1632
	1890	--	--
	2055	--	--
P_{13}	1710	P_{13} (1720)	1687
	1870	--	--
	1955	--	--
	1980	--	--
	2060	--	--
P_{31}	1875	P_{31} (1910)	**
	1925	--	--
P_{33}	1780	P_{33} (1600)	1588
	1925	P_{33} (1920)	**
	1975	--	--
F_{15}	1715	F_{15} (1680)	1669
	1955	F_{15} (2000)	**
	2025	--	--
F_{17}	1955	F_{17} (1990)	**
F_{35}	1940	F_{35} (1905)	1855
	1975*	--	--
F_{37}	1915	F_{37} (1950)	1879

*Isgur and Karl claim that this state should largely decouple from the elastic πN channel.

**Beyond range of phase-shift analysis

states, including both of the high predicted mass (20, $L^P = 1^+$) states, that cannot be matched with observed pion-nucleon resonances. The two low-lying resonances of questionable validity, the one-star P_{13} (1540) and P_{31} (1550), are not predicted in Isgur's and Karl's model. Again, the success of this model indicates little evidence for the presence of any spin-orbit contribution to the baryon spectroscopy. Flavor-independent quark confinement forces split by hyperfine forces produce a good match to the low-lying nucleon and delta states.

In their next major work,[10] Isgur and Karl re-examine the masses of the ground-state baryons. The major impact in the nonstrange sector including some second-order effects in the hyperfine interaction is to allow mixing between the ground state (56, $L^P = 0^+$) multiplet and the excited N = 2 positive-parity states described above. Since the nucleon and delta masses were used to fit the masses of all members in the ground-state multiplet, the ground-state masses for the nonstrange baryons obviously are not influenced, but the masses reported above for the excited postive-parity baryons should be adjusted slightly.

The problem with the excess of positive-parity states over those seen in pion-nucleon phase-shift analyses is reconciled by Isgur and his new collaborator, Koniuk,[14,15] when they show that the unobserved states couple only weakly to the elastic channel. Using the same harmonic oscillator model of quark confinement with hyperfine splitting, as discussed above, to describe baryon structure and a

simple nonrelativistic model of baryon decay, they compute the baryon decay amplitudes for pseudoscalar-meson and photon emission. Their baryon decays proceed by a single-quark transition, and the nonrelativistic model for decay was chosen to be consistent with the nonrelativistic nature of the constituent quark oscillator model. Koniuk's and Isgur's analysis showed that the "missing" states are, in general, too inelastic to be easily seen in partial-wave analysis. The observed states that remain are in good agreement in mass (as was shown earlier) and in the size and magnitude of the decay amplitudes considering the crudeness of the decay model. The authors also demonstrated the necessity of the hyperfine interaction in inducing the appropriate mixing responsible for the decoupling of the unseen states.

The oscillator model is extended to the N = 3 excitations in the work of Forsyth and Cutkosky[16] to include the next set of negative-parity states. Only the nonstrange baryons are considered. This work differs from that of Isgur and Karl[7-10] in allowing the relative strength of the Fermi contact and tensor terms of the hyperfine interaction to vary independently. Unlike Isgur and Karl, these authors conclude that the tensor contribution to the spin-spin interaction is small enough to not be needed to fit the data and that the strength of Fermi term varies with parity. Although Forsyth and Cutkosky omit the two-body, spin-orbit force as do Isgur and Karl, they do include a small three-body contribution. Ten parameters were fitted in constructing their Hamiltonian, four from the anharmonic,

two-body, spin-independent, confining potential. The baryon decay model they use is more sophisticated than is Koniuk's and Isgur's[14,15] in that the model included dependence of the elastic width on the spin and orbital state of the so-called "spectator" quarks. Forsyth's and Cutkosky's predictions for the masses and group composition of the nonstrange baryons are shown in Table 5-4 for states up to about 1800 MeV for comparison with the phase-shift analysis reported here. Also shown are similar results from Isgur and Karl. The most obvious difference in composition for the two oscillator models occurs in the S_{11} (1535), S_{11} (1650), and the troublesome Roper P_{11} (1440). The two one-star resonances in this energy range, P_{13} (1540) and P_{31} (1550), are neither predicted by the oscillator model nor seen in this work. Two predicted N = 3 states at 1809 MeV, an S_{11}, and a D_{13} are not seen. In agreement with Koniuk and Isgur,[14,15] Forsyth and Cutkosky[16] observe that these two and many higher lying N = 2 and N = 3 states are largely decoupled from the elastic pion-nucleon channel and are expected to be difficult to observe.

5.1.3 Deformation in the Harmonic Oscillator Model

The limitation to spherically symmetric oscillators in Isgur's and Karl's model is relaxed in the work of Bhaduri and his collaborators.[17-20] Although their ground states remain nearly spherical, they assume that in the excited states the valence quarks should no longer be modeled with spherical oscillators, but instead with a deformed oscillator potential. In their first paper on the subject,[17] the authors examine qualitatively the positive-party,

TABLE 5-4. NUCLEON AND DELTA STATES IN THE HARMONIC OSCILLATOR MODEL (Sheet 1 of 3)

STATE	MASS	COMPOSITION(d)
S_{11} (1535)****	(a) 1530 (b) 1490 (c) 1461	0.91 (70^2, 1^-) + 0.40 (56^2, 1^-) 0.87 (70^2, 1^-) + 0.53 (70^4, 1^-)
S_{11} (1650)****	1643 1655 1655	0.99 (70^4, 1^-) -0.85 (70^4, 1^-) + 0.53 (70^2, 1^-)
S_{11}	1809 - -	0.90 (56^2, 1^-) - 0.41 (70^2, 1^-) N = 3 excitation not examined by Isgur and Karl Beyond energy range
S_{31} (1620)****	1643 1685 1596	(70^2, 1^-) (70^2, 1^-)
P_{11} (938)****	938 940 938	0.93 (56^2, 0^+) + 0.27 (56^2, 0^{+*}) + 0.23 (70^2, 0^+) 0.93 (56^2, 0^+) - 0.29 (56^2, 0^+) - 0.04 (70^4, 2^+)
P_{11} (1440)****	1383 1405 1351	0.96 (56^2, 0^{+*}) - 0.28 (56^2, 0^+) 0.99 (56^2, 0^+) + 0.17 (70^2, 0^+) + 0.01 (70^4, 2^+)

(a) Results of Forsyth and Cutkosky[16]

(b) Results of Isgur and Karl[7-10]

(c) Results from the present phase-shift analysis, the real part of the pole position

(d) Spectroscopic notation is (M^S, L^p) where M is the SU(6) multiplet, s is the quark spin, L is the quark orbital angular momentum, and p is the parity.

TABLE 5-4. NUCLEON AND DELTA STATES IN THE HARMONIC OSCILLATOR MODEL (Sheet 2 of 3)

STATE	MASS	COMPOSITION
P_{11} (1710)***	1714 1705 1632	0.95 (70^2, 0^+) - 0.22 (56^2, 0^+) + 0.2 (20^2, 1^+) 0.94 (70^2, 0^+) - 0.31 (70^4, 2^+) - 0.15 (56^2, 0^+) - 0.07 (20^2, 1^+)
P_{13} (1540)*	-	Neither predicted by oscillator model nor seen by this analysis
P_{13} (1720)****	1768 1710 1687	0.93 (56^1, 2^+) + 0.3 (70^2, 2^+) 0.84 (56^2, 2^+) - 0.52 (70^2, 2^+) - 0.17 (70^4, 0^+) + 0.03 (70^4, 2^+)
P_{31} (1550)*	-	Neither predicted by oscillator model nor seen by this analysis
P_{33} (1232)****	1232 1240 1212	0.97 (56^4, 0^+) - 0.24 (56^4, 0^{+*}) 0.97 (56^4, 0^+) + 0.2 (56^4, 0^{+*}) - 0.1 (56^4, 2^+) + 0.07 (70^2, 2^+)
P_{33} (1600)**	1787 1780 1588	0.97 (56^4, 0^{+*}) + 0.24 (56^4, 0^+) 0.98 (56^4, 0^{+*}) + 0.18 (56^4, 2^+) - 0.1 (70^2, 2^+)
D_{13} (1520)****	1529 1535 1508	0.9 (70^2, 1^-) - 0.14 (70^4, 1^-) + 0.39 (56^2, 1^-) 0.99 (70^2, 1^-) - 0.11 (70^4, 1^-)
D_{13} (1700)***	1682 1745 1673	0.98 (70^4, 1^-) + 0.15 (56^2, 1^-) 0.99 (70^4, 1^-) + 0.11 (70^2, 1^-)
D_{13}	1809 - -	0.89 (56^2, 1^-) - 0.42 (70^2, 1^-) + 0.13 (70^2, 1^{-3}) N = 3 excitation not examined by Isgur and Karl Beyond energy range

TABLE 5-4. NUCLEON AND DELTA STATES IN THE HARMONIC OSCILLATOR MODEL (Sheet 3 of 3)

STATE	MASS	COMPOSITION
D_{15} (1675)****	1661 1670 1664	$(70^4, 1^-)$ $(70^4, 1^-)$
D_{33} (1700)****	1676 1685 1657	$(70^2, 1^-)$ $(70^2, 1^-)$
D_{35}	-	None in this energy range
F_{15} (1680)****	1684 1715 1669	$0.83\ (56^2, 2^+) + 0.53\ (70^2, 2^+) + 0.14\ (70^4, 2^+)$ $0.88\ (56^2, 2^+) - 0.48\ (70^2, 2^+) + 0.01\ (70^4, 2^+)$
F_{17}	-	None in this energy range
F35	-	None in this energy range
F37	-	None in this energy range

excited, nonstrange baryons and show how the resulting strong deformation is responsible for the low-lying P_{11} (1440). The more excitation quanta a state has, the more deformed it will be and, hence, the lower in energy it will be with respect to the spherical model.

In their more quantitative paper,[18] Bhaduri *et al.* explicitly examine the nonstrange baryons for states up to the lowest N = 3 levels. By initially assuming the quarks to be noninteracting and then separating out the center of mass, they obtain the unperturbed Hamiltonian, H_o, for the deformed oscillator

$$H_o = \frac{1}{2m}\left(p_\rho^2 + p_\lambda^2\right) + \frac{m}{2}\sum \omega_i^2\left(\rho_i^2 + \lambda_i^2\right) \qquad (5\text{-}8)$$

as compared to equation 5-5. They then borrow from nuclear physics the concept of volume conservation, which they implement through the condition,

$$\omega_o^3 = \omega_x\ \omega_y\ \omega_z$$

to obtain the eigenenergies after minimization;

$$E = h\omega_o\left[e^{\alpha}(N_x + 1) + e^{\beta}(N_y + 1) + e^{-(\alpha+\beta)}(N_z + 1)\right]$$

$$\alpha = \frac{1}{3}\ln\left[\frac{(N_y + 1)(N_z + 1)}{(N_y + 1)^2}\right]$$

$$\beta = \frac{1}{3}\ln\left[\frac{(N_x + 1)(N_z + 1)}{(N_y + 1)^2}\right] , \qquad (5\text{-}9)$$

where the total number of excitations N = Nx + Ny + Nz. The intrinsic states of proper permutation symmetry are produced from the ensuing deformed oscillators in which the ground states remain spherical and the N = 1, N = 2, and lowest N = 3 state are all prolate except for the completely antisymmetric (spatially) N = 2 state with $N_x = N_y = 1$ and $N_z = 0$. These intrinsic states no longer have quark orbital angular momentum, L, as a good quantum number, but instead states of good total angular momentum, J, must be formed by projecting out states of good L and coupling to quark spin 1/2 or 3/2. In addition to the lowering of a states energy because of deformation, the projecting out of states with L = 0 reduces the energies even further as seen by the low energy of the P_{11} (1440). Those states of a given SU(6) multiplet with the lowest value of L then become a band head for a series of rotational bands with L = 0, 2, 4, ... for the positive-parity prolate states and L = 1, 3, 5, ... for the negative-parity prolate and the positive-parity oblate band.

The intrinsic unperturbed eigenstates are then used to diagonalize the full Hamiltonian that they choose as

$$H = K + H_o + H_c + \sum U(r_{ij}) \ , \qquad (5\text{-}10)$$

where K is a constant (-286 MeV), H_c is the Fermi contact term of the hyperfine interaction, and U accounts for any missing short-range interaction. U is about half the strength of Isgur's and Karl's similar term. Bhaduri *et al.* ignore the tensor term of the hyperfine interaction because they believe it to be small. They also show that

the spin-orbit force has little effect in their deformed model, so they omit it too. They do need to retain the Fermi contact term to obtain the proper mixing of the {56, N = 2} and {70, N = 2} states needed to explain the radiative decay amplitude of the P_{11} (1440) and P_{11} (1710). Diagonalizing H then gives the intrinsic energies and properly mixed wavefunctions that form the bandheads for the rotational spectra having energies:

$$E(L) = E_{intrinsic} - \frac{\hbar^2}{2I} <L^2> + \frac{\hbar^2}{2I} L(L+1) \qquad (5\text{-}11a)$$

for the positive-parity prolate bands with L = 0, 2, 4, ... and for the negative parity and oblate bands with L = 1, 3, 5, ...:

$$E(L) = E_{intrinsic} - \frac{\hbar^2}{2I} [<L^2> - 2] + \frac{\hbar^2}{2I} L(L+1) \quad . \qquad (5\text{-}11b)$$

The moment of inertia, I, and the expectation value, $<L^2>$, for these states are functions of the rotational band through their dependence on N_x, N_y, and N_z.

The resulting spectroscopy is in good agreement with the observed states although there are some differences in detail with the predictions of Isgur and Karl. Again, they predict a number of the positive-parity states couple only weakly to the elastic π-N channel. Bhaduri's deformed oscillator model naturally brings down, in energy, the N = 2 and N = 3 states. He does not need the very strong spin-independent central interaction, $U(r_{ij})$, required, but treated perturbatively by Isgur and Karl. Perturbative treatment of Bhadrui's weaker anharmonic term is much less objectionable.

Bhaduri *et al.* next addressed, in more detail, the issue of the lack of significant spin-orbit splitting in the low-lying baryon states.[19-20] One-gluon exchange as expected from QCD would seem to require a stronger spin-orbit force than is seen experimentally. The suggestion by Isgur and Karl[8] that Thomas precession from the confining potential might cancel the OGE spin-orbit force is only a partial solution since it is applicable only to the nucleon states. The two spin-orbit forces would reinforce in the delta states, and there must be an alternate solution. Gromes[21] has suggested that the scalar confining potential might be nonlocal, leading to a spin-orbit force that can compensate for the OGE spin-orbit team. Bhadrui *et al.* propose a different answer. They consider quarks coupling to pions in addition to the gluon coupling resulting in a one-pion-exchange (OPE) potential similar to the OGE interaction. Their revised Hamiltonian is, therefore,

$$H = H_o + V_{OGE} + V_{OPE} + V_{SO} \quad , \tag{5-12}$$

where

$V_{OGE} = V_c^G$ coulomb plus Darwin terms

$+ V_s^G$ Fermi spin-spin term

$+ V_T^G$ tensor hyperfine term

$+ V_{SO}^G$ gluon-exchange spin-orbit

$V_{OPE} = V_s^\pi$ central spin-spin term

$= V_T^\pi$ tensor hyperfine term

V_{SO} = phenomonelogical Thomas one-body, spin-orbit term.

They diagonalize the Hamiltonian without the various spin-orbit and tensor spin-spin terms using the deformed oscillator wavefunctions described earlier, and they project out the states of good L to generate the rotational spectra. They then diagonalize the remaining terms after constructing the states of good J to completely specify the splittings and mixings. The additional OPE contribution to the spin-spin force allowed the use of a strong coupling constant one third of the value in the original analysis and, therefore, correspondingly reducing the strength of the OGE spin-orbit force. Deformation in the N = 1 states further reduces the spin-orbit contribution in these states. The one-body, spin-orbit force cancels the remaining OGE spin-orbit force. Thus, Bhaduri claims that including OPE interactions account for the lack of significant spin-orbit splittings.

5.2 THE BAG MODEL

5.2.1 The MIT Bag

One of the most successful extended models of hadrons has been the bag model in which the quarks are explicitly confined to a region of space, the bag, having a constant postive potential energy density. As originally developed by Chodes, Jaffe *et al.*[22] the so-called MIT Bag Model was motivated by two important features of the quark theory of the strong interaction, QCD: 1) asymptotic freedom and 2) quark confinement. Although it has not yet been possible to demonstrate a mechanism for quark confinement based on a proof using QCD field theory, no quarks have been isolated experimentally. With the

confined quarks forming a fundamental triplet representation of SU(3) color, the bag model ensures[22] that only color singlet combinations of quarks exist as physically realizable states. Asymptotic freedom results from the free or nearly free behavior of the quark fields inside the bag. The colored quarks are, at most, weakly coupled through quark-gluon interactions that account for the quantum numbers of the observed hadrons. It is only near the bag boundary that the quarks experience the strong force of the confining pressure.

The bag model is described by the MIT[22,23] group through the action for a Dirac field (without quark-gluon interactions),

$$W = \int_V d^4x \left[\frac{1}{2}\, i\,(\bar{\psi}\not{\partial}\psi) - m\bar{\psi}\psi - B\right], \tag{5-13}$$

where

B - constant energy density that provides the confining pressure

V - volume of the spatial region referred to as the bag.

For colored quarks having a flavor-color index, α, varying this action results in the following equations of motion inside the bag and linear boundary conditions on the bag surface for each field degree of freedom

$$i\not{\partial}\psi_\alpha = m_\alpha\,\psi_\alpha \ (\textit{inside bag}) \tag{5-14}$$

$$i\,n_\mu\gamma^\mu\,\psi_\alpha = \psi_\alpha \ (\textit{on bag surface}), \tag{5-15}$$

where n_μ is the covariant four-normal to the boundary surface of the bag. In addition, there is a quadratic boundary condition that guarantees that the phenomenological pressure, B, is balanced at each point on the surface by the pressure of the constituent quark fields,

$$\sum_a n_\mu \partial^\mu \bar{\Psi}_a \Psi_a = 2B. \qquad (5\text{-}16)$$

The equations of motion and boundary conditions are obviously Lorentz. invariant as well as causal and local. In this version of the bag model, B is the only parameter of the model and should be uniform for all hadrons with the size of the bag scaling as $(1/B)^{\frac{1}{4}}$.

Even the physically simple model, as given by equations 5-13 through 5-16, is not amenable to an exact solution. Several approximations are possible, such as treating the bag as a static spherical bag and assuming that the quarks are massless. The first calculations[23] made with the bag model used both of these assumptions, resulting in a bag radius of 1.37 fermis. Reasonable values for the gyromagnetic ratio, axial-vector charge, and charge radius for the nucleon were determined in this calculation. Golowich[24,25] first investigated the effect of finite quark mass using the nucleon axial vector coupling constant to calculate an effective up/down quark mass of 122 MeV. His ground-state bag radius was 1.63 fermis. DeGrand[26] *et al.* expanded on the MIT model by including the effects of colored-gluon exchange to lowest order, zero-point energy as well as quark mass to calculate the masses and static parameters of the light hadrons. The color-magnetic interaction split the nucleon and delta, which are

degenerate in the original MIT model. For the proton and delta, the bag radii ranged from 0.99 to 1.10 and 1.08 to 1.26 fermis, respectively, as the quark mass varied from 0 to 108 MeV. More recent and sophisticated adaptations of the MIT model[27,28] have resulted in even smaller nucleons with bag radii on the order of 0.5 fermi.

For the simple, static, spherical approximation to the bag, only j = 1/2 quarks are allowed by the quadratic boundary condition (equation 5-16). Consequently, for a three-quark baryon, only j = 1/2 and j = 3/2 states are allowed by the spherical bag. Higher angular momentum states can arise only in bags that are not static spheres. For the spherical bag, there will, therefore, be two types of quark states in the bag, $S_{1/2}$ and $P_{1/2}$, according to the two possible states of parity. The energy or mass of a bag state will then be given by

$$E = \sum_i N_i (m_i^2 + x_i^2/R^2)^{\frac{1}{2}} + \frac{4}{3} \pi R^3 B, \tag{5-17}$$

where the sum is over the quarks in the bag of mass m_i and momentum x_i. R is the bag radius and is related to the pressure, B, by minimizing the energy. In turn, the parameter B is typically found by fitting to the nucleon-delta mass. The various baryons with $j \leq 3/2$ are described by the set of possible quark modes given by the quark momentum eigenvalues of the transcendental equation,

$$tan(x) = \frac{x}{1 - mR + k\sqrt{x^2 + (mR)^2}}, \tag{5-18}$$

where $k = \pm 1$ distinguishes the two possible parity states. The lowest solution to this equation increases from 2.04 for a massless quark to a maximum of π as the quark mass approaches infinity.

The first author to go beyond the static sphere approximation and address nonspherical deformations of the bag was Rebbi.[29,30] He allowed the bag to perform small oscillations about the static spherical boundary S-wave configuration but kept the assumptions of massless and noninteracting quarks as he investigated nonstrange baryons having orbital angular momentum L = 1, allowing one quark to be excited to a P state. Allowing the bag boundary to oscillate resulted in a proper treatment of the translational degrees of freedom and caused only the states of the {70, L = 1}, representation of $SU(6) \times O(3)_L$ to remain at low energy, agreeing with experimental observation. The states of the other low-energy representation, {$\underline{56}$, L = 1}, separate into translation modes of the L = 0 multiplet and into excited states of higher energy. DeGrand and Rebbi[30,31] also similarly investigated the effects of small oscillations on the spectroscopy of low-energy-excited baryons. Using the j-j coupling required for relativistic quarks, their $(1S_{1/2})^2$ $(1P_{1/2})$ and $(1S_{1/2})^2$ $(1P_{3/2})$ states resulted in the qualitatively correct number of states and splitting but a spectrum that was too low in energy.

An alternative to exciting one of the three quarks to a P-state is to radially excite the quark to the second S-state, resulting in $(1S_{1/2})^2$ $(2S_{1/2})$ baryons. Bowler and Hey[32] first considered this possibility and used a color magnetic gluon interaction to split and

mix the two otherwise degenerate nucleon P_{11} states at 1543 and 1646 MeV compared to the 1410 and 1780 MeV states seen in experiments. DeGrand and Rebbi[33] also examined the radial excited states of the quark, but, in addition, included the coupling of radial "breathing" oscillations of the bag to these excited quark fields. Unfortunately, they were able to only examine bosonic bags and then by analog apply their results to the fermionic bag. Their results were, however, in good qualitative agreement with experiment as shown in Table 5-5.

5.2.2 Chiral Bags

The MIT Lagrangian (equation 5-13) has some fundamental problems. The confinement of quarks to the interior of bags with the associated required reflection of the quarks at the bag surface violates the chiral invariance of the QCD Lagrangian. In the limit of massless quarks, the axial-vector current is not conserved at the bag boundary. It has, therefore, been difficult to reconcile the pion of partial conservation of axial-vector current (PCAC) with the quark-bag-model pion,[22,23,25,26] although Donoghue's[35] effort to include the effects of spatial localization of the pion in the bag model has shown some improvement. Also, the MIT bag generally has a radius of at least 1 fermi, which makes it difficult to picture how there could be room in a nucleus[36] for the pion exchange mechanism that dominates the N-N interaction. Although the MIT Bag Model has had considerable success with fitting or predicting static hadronic properties, it has not been as successful with dynamic processes such as scattering and decay of excited states.

TABLE 5-5. SPECTRUM OF N AND Δ STATES ACCORDING TO RADIAL EXCITED BAG MODEL OF DeGRAND AND REBBI[33] COMPARED WITH RESULTS OF PHASE-SHIFT ANALYSIS DESCRIBED IN CHAPTERS 3 AND 4

STATE	BAG MODEL MASS PREDICTION (MeV)	PHASE-SHIFT MASS (MeV)
N P_{11}	1410	1351
N P_{11}	1603	1632
N P_{13}	1756	1687
Δ P_{33}	1572	1588
Δ P_{31}	1652	Not seen
Δ P_{31}	1910	Not seen

The above difficulties are related and have been mitigated with the inclusion into the bag Lagrangian of the pion as an explicit and fundamentally independent field.[37] The pion contribution to the total axial-vector current restores PCAC (for massive quarks) and chiral symmetry is re-established. The actual incorporation of the pion field into the bag Lagrangain has been accomplished in a number of ways. In Chodos' original chiral model,[38] chiral symmetry has been built into the Lagrangian using a linear sigma model with $\bar{\psi}\ \psi \rightarrow \bar{\psi}\ (\sigma + i\ \vec{\tau} \cdot \vec{\pi}\gamma_5)\ \psi$ as the chirally invariant combination. He assumed unconfined and massless pion and sigma fields coupling to the quarks only at the bag surface. Other authors[39,40] have used nonlinear sigma models with $\bar{\psi}\ \psi \rightarrow \bar{\psi}\ \exp\ (i\ \vec{\tau} .\ \pi\vec{\gamma_5}/f)\ \psi$.

In the Little Bag Model,[31,41-43] Brown and Rho have restricted the pions to the exterior of the bag with coupling again at the bag surface resulting in an increased pressure and much smaller bag, less than 0.5 fermi. Outside the bag where pions exist, chiral symmetry is realized in the Goldstone mode while inside the bag the chiral symmetry is via the Wigner mode. Other models, most notably, the Cloudy Bag Model,[44-46] do not confine the pion field at all. There are even models that confine the pions interior to the bag[47] and "skin" models,[48,49] which allow the pion field to penetrate part way into the bag!

In most chiral bags, the pion is allowed to couple to the bag quarks only at the bag surface, but there are some references[45-53] that employ pion-quark coupling throughout the bag volume. In these

models, the volume coupling is obtained from the surface coupling via a unitary transformation of the quark fields and results in a Lagrangian that gives the desired isovector S-wave scattering length at threshold.[50]

5.2.3 Bags and πN Scattering

One of the main practical advantages of the chiral bags is their ability to provide a natural means for πN interactions. Since the delta P33 resonance dominates the low-energy, pion-nucleon interaction, it is reasonable to ask how well the chiral bags are able to duplicate the P33 partial wave. The answer to this question enables one to attempt to reconcile the two distinct pictures of the physical resonance as a dynamic pion-nucleon state and as a bare three-quark delta bag state. Several authors[44,54,55] have addressed this problem and are in agreement in concluding that the physical resonance is mostly (approximately 80 percent) a delta bag, but that pionic effects are not negligible. Gross and Hunter[56] also examined the delta resonance but were primarily interested in assessing deformations of the chiral bag. They concluded that the nonlinear boundary condition gives a spherical nucleon but an oblate bag shape for deltas with spin projection of 3/2 and a prolate delta for spin projection of 1/2.

Scattering in the S-wave was first investigated by Thomas.[50] He used the volume-coupling version of the Cloudy Bag Model to obtain a generalization of the Weinberg effective Lagrangian[57] and, hence, was able to derive the well-known result of a purely isovector S-wave

scattering length at threshold. Subsequent analyses[58,59] attempted to extend this work to calculate S- and P-wave phase shifts. The authors were not able to match the S-wave phase shifts very well except close to threshold and concluded that some physics was lacking in their approach. On the other hand, the small P-waves (P_{13} and P_{31}) and the dominant P_{33} wave were in good agreement with experiment. Just as the Roper was difficult to explain with the MIT bag (see Subsection 5.1.1), the P_{11} wave was also poorly described by these authors.

The P_{11} (1440) Roper resonance has consistently been difficult to fully explain in quark models,[60,61] seemingly appearing at too low an energy. As discussed earlier, the MIT Bag Model describes the Roper as the lowest lying radial [$(1S)^2$ (2S)] excitation of the nucleon. It is unclear whether there are two nearly degenerate Ropers, N*(70) and N*(56), split and mixed by direct gluon exchange as predicted by Bowler and Hey[32] or whether surface oscillations eliminate mixing, giving two widely separated states identified as the P_{11} (1440) and P_{11} (1700) by Close and Horgan[34] and by DeGrand and Rebbi.[33] Since it is expected that the Chiral Bag Model should describe hadronic properties better than the MIT Bag Model, it is instructive to investigate the troublesome P_{11} states with a chiral model. Umland and Duck[62,63] have done this; they studied the two low-lying radial excitations, the symmetric N*(56), and the mixed symmetric N*(70), using the Cloudy Bag Model, correcting for spurious center-of-mass motion, and including pionic self-energy effects. Surprisingly they obtained two adjacent Ropers with masses of 1418 and 1533 MeV.

According to their results, the lower mass state is predominately N*(56) and couples more strongly to the πN channel than does the higher state. Consequently, the 1533-MeV state may be difficult to observe in experiments. Further supporting confidence in these results is the author's calculation of N^* decay rates that are in good agreement with experiment. If the two radial states are nearly degenerate, as determined by Umland and Duck, what is the explanation of the observed P_{11} (1710) that some authors[33,64] claim to be the higher of the radial excitations? Umland and Duck also examine this state and suggest that the P_{11} (1710) is a $(1S)^3$ + TE gluon state.

5.3 THE SKYRME MODEL

Another model of the strong interaction that has experienced considerable recent interest is the Skyrme model, based on ideas that he originally proposed over 25 years ago.[65] At that time, Skyrme proposed a unified, but nonlinear field theory of mesons and baryons in which the fundamental pion fields are represented as angular variables. In this nonlinear sigma model, the baryons appear as solitons with a topological charge that is identified as the baryon number.

5.3.1 Static Properties in the Skyrme Model

Skyrme's work has remained largely dormant until recently. In 1974 't Hooft showed that when the number of colors, N_c, becomes large, QCD reduces to an effective field theory of mesons.[66] In 1979, Witten applied this idea to show how baryons can emerge as solitons whose masses diverge as the inverse of the coupling constant, $1/N_c$, in

this weakly coupled field theory.[67] Then, in 1983, Guadagnini and he explicity showed that these solitons have exactly the quantum numbers of baryons of QCD.[68,69] The solitons were shown to have baryon number B = 1 and to be fermions if the effects of the Wess-Zumino coupling, which takes into account the anomalies,[70] are included. Adkins and Nappi together with Witten then used the Skyrme model to investigate the static properties of nucleons for SU(N_f) with the number of flavors, $N_f = 2$.[71] The Skyrme model Lagrangian for massless pions and exact chiral symmetry is

$$L = \frac{1}{16} F_\pi^2 \, Tr\,(\partial_\mu U \, \partial_\mu U^\dagger)$$

$$+ \frac{1}{32e^2} \, Tr\,[(\partial_\mu U)U^\dagger, (\partial_\mu U)U^\dagger]^2 + n\,\Gamma, \qquad (5\text{-}19)$$

where U is an SU(2) matrix.

The first term here is the nonlinear, sigma Lagrangian, and the second is a nonminimal term used to prevent the solitons from vanishing. The dimensionless parameter, e, is free for fitting. The last term is the Wess-Zumino term that actually vanishes for the two-flavor, SU(2), case considered by Adkins *et al.*[71] The soliton solution for this Lagrangian is the hedgehog,

$$U_o = e^{iF(r)\vec{\tau}\cdot\hat{x}} \qquad (5\text{-}20)$$

that can be seen to interweave angular momentum (or spin) and isospin because of its dependence on the spatial coordinate r and the isospin

bases τ. Indeed, the correlation between spin and isospin results in the hedgehog having a new quantum number, K, the vector sum of spin and isospin. Spin and isospin are no longer separately good quantum numbers, but rather the hedgehog configuration becomes invariant under global rotations in physical and isospin space. Physical baryons must be constructed from the hedgehog by projecting out states of appropriate spin and isospin. The Skyrme angle F(r) was computed numerically from the differential equation of motion resulting from inserting equation 5-20 into equation 5-19. Solutions other than equation 5-20 are obtained from

$$U = A(t)\, U_o\, A^{-1}(t)\,, \tag{5-21}$$

where A(t) is an arbitrary, but time-dependent SU(2) matrix. Treating A as a quantum mechanical variable, the authors were able to calculate the static properties of the nucleon by using the nucleon and delta masses to fit Fπ and e. Among the computed properties were the nucleon magnetic moments, isoscalar charge radii, and pion-baryon coupling constants. With the exception of the axial coupling, g_A, all these properties were determined within about 30 percent of their known experimental values. Adkins and Nappi later extended this work by examining the effects of explicitly breaking the chiral symmetry.[72] They added to the SU(2) Skyrme Lagrangian of equation 5-19 the mass term,

$$\frac{1}{8}\, M_\pi^2\, F_\pi^2\, [Tr\,(U) - 2]\,. \tag{5-22}$$

As expected, the earlier results were not modified much because chiral symmetry is typically valid in experiments to within 10 percent. They were, however, able to calculate several additional quantities, the isovector charge radii and the sigma term.

5.3.2 Skyrmion-Skrymion Interactions

Now that it has been shown that nucleons, baryons with B = 1, can be considered to be solitons in the Skyrme model and reasonable static properties computed it is useful to go one step further and examine how Skyrmions might interact with one another in a model of the nucleon-nucleon interaction. Jackson and Rho[73] were the first to investigate this aspect of the Skyrme model. They computed the Skyrmion energy for B = 1, 2, and 3, obtaining the values shown here in Table 5-6, using the Goldberger-Treimann relation to establish the asymptotic form of the chiral angle. They were then able to make an estimate of the interaction between nucleons by comparing the energy of a B = 2 Skyrmion with that of two coincident nucleons:

$$V_2\,(r_{12} = 0) = E(2) - 2\,E(1) \approx E(1) \quad , \tag{5-23}$$

where V_2 is a measure of the two-body, nucleon-nucleon interaction energy. It is seen to be equal about 1.4 GeV. This value can be compared with a similar estimate of the three-body interaction energy,

$$V_3(r_{12} = 0, r_{13} = 0) = E(3) + 3E(1) - 3E(2) \approx -\,0.025\,E(1) \; . \tag{5-24}$$

Hence, because V_3 is small compared to V_2, the Skyrme model implies the expected dominance of two-body forces over three-body forces.

TABLE 5-6. SCALED SKYRMION MASSES

B	E(B)/E(B = 1)
1	1.000
2	2.983
3	5.926

Jackson and Rho were also able to compute the baryon number density, obtaining a reasonable rms radius of 0.48 fm for the baryon (e.g., nucleon.)

Later, Jackson *et al.* expanded this analysis to deduce the main features of the nucleon-nucleon potential.[74] The only two parameters in the theory were fit with the experimental values of the pion decay constant and the πN-coupling constant, so the ability of the Skyrme model in predicting a short-range repulsion of order 1 GeV and a long-range potential equivalent to one-boson exchange can be considered a notable success. Their adiabatic calculation included some of the obvious effects of the finite size of N_c suggested by quark chiral-bag models and resulted in agreement with semiphenomenological potentials to about 30 percent.

5.3.3 Skyrmion Monopole Resonances

The next logical test for the Skyrme model is its application to the fundamental pion-nucleon problem. Several authors have examined monopole excitations of the Skyrmion in order to identify nucleon and delta resonances. Hajduk and Schwesinger[75] investigated breathing mode excitations of the Skyrmion by scaling the radial coordinate of the meson fields with a time-dependent factor, $r \rightarrow \lambda(t) \cdot r$. They used the usual Skyrme Lagrangian (equation 5-19) and hedgehog *ansatz* and allowed the Skyrmion to rotate so that states of definite spin and isospin could be projected out from the Skyrmion. For the breathing mode of the nucleon, they obtained an excitation energy of about

250 MeV, over 200 MeV less than that needed for the Roper resonance, which is expected to be a radial excitation of the nucleon.

Breit and Nappi[76] also examined the breathing mode of the Skyrmion, but their Lagrangian included the explicit pion mass term of equation 5-22. They investigated the breathing mode by allowing time-dependent radial fluctuations of the Skyrme angle about the classical solution:

$$F(r) \rightarrow F(r) + e\delta F(r,t) .$$

Expanding to second order in δF, they calculated Skyrmion phase shifts and used phase shifts passing through 90 deg as the criteria for a resonance. The ensuing resonance occurs at a pion energy of 330 MeV and produces breathing mode resonances for the nucleon at 1270 MeV and the delta at 1560 MeV. Again, the resonance masses are considerably lower than the experimental values of 1440 and 1600 MeV, respectively.

The work of Liu *et al.*[77] followed the same approach very closely except that they also examined the case of considering the rotational degrees of freedom before the pion scattering; that is, they examined small oscillations about a rotating soliton. Naturally, their results were similar to Breit's and Nappi's.

These results were contradicted by Zahed *et al.*,[78] who explicitly constructed a quantization scheme within the framework of the Skyrme model. In the $K^P = 0^+$ sector (recall that $K = J_{spin} + I_{isospin}$), their approach also reduced to examining fluctuations about the static solution. Although the resulting phase shift rose to a peak near

90 deg, it did not indicate a Roper resonance. In the odd parity $K^{\pi} = 1^{-}$ sector, the phase shift does show a clear cut indication of a resonance, passing through 90 deg.

5.3.4 The Siegen Analysis

An early attempt, more systematic than the work quoted in the previous section, has been made of the investigation of baryon resonances within the Skyrme model by the group at Siegen University.[79-82] They have examined isovector fluctuations of the pionic field about the static Skyrme hedgehog within chiral SU(2). The small amplitude vibrations of the rotating soliton are interpreted in terms of normal mode vibrations, phonons that carry orbital angular momentum. The orbital angular momentum, ℓ, is added to the isospin fluctuation to obtain the phonon spin, K.

In the group's first paper on the subject,[79] Hayashi and Holzwarth showed how the nucleon and delta resonances can be interpreted in terms of an underlying phonon spectrum with a rotation-vibration coupling of the $\vec{\ell} \cdot \vec{S}$ form and a coupling coefficient of about 30 MeV. They then derived a similar phonon spectrum (energies and coupling coefficients) from the Skyrme model having energies roughly consistent with the experimental data. The approximation used here to estimate the phonon spectrum was a simple, time-dependent scaling of the coordinates. A subsequent calculation of the restoring force and vibrational inertia was used to estimate resonance energies.

The scaling approximation was removed in a second paper[80] in which the normal modes of the fluctuations about the static solution are

quantized. The eigenvalue problem they obtained has solutions that decouple into both magnetic modes of phonon parity $(-1)^{\ell}$ and into electric modes with phonon parity $(-1)^{\ell+1}$. The authors recognized that this eigenvalue problem (see their equations 12 and 13) contained modes of zero frequency (translations, and rotations) that must be handled carefully. The translational modes do not effect level-spacing and were ignored. Because the intrinsic frame of the Skyrmion is rotating in isospin space, the rotational modes are important in obtaining states of definite spin and isospin. The authors made a so-called adiabatic approximation by decoupling the rotation and the vibration of the Skyrmion. The Lagrangian that they obtained includes a sum over the normal modes. By quantizing this Lagrangian, they determined the energy eigenvalues:

$$E_{\{N_n\}} = M + \frac{S(S+1)}{\lambda} + \sum_n (N_n + \frac{1}{2}) \omega_n \quad , \qquad (5\text{-}25)$$

where

M - classical Skyrmion mass

N_n - number of phonons for the nth mode

ω_n - 1-phonon excitation energy

S - spin (or isospin) = 1/2 for nucleon, 3/2 for delta

λ - moment of inertia of rotating Skyrmion.

Interestingly enough, the asymptotic forms of their quantized normal mode solutions decay into pions just as physical baryons do.

Numerically solving the Lagrangian equations of motion enabled the authors to determine the normal mode phase shifts. These phase shifts

cannot be directly identified with the pion-nucleon phase shifts because the rotating Skyrmion does not have definite isospin and spin but are useful in identifying approximate resonance energies and widths. Agreeing with the results of the previous section, they found an electric monopole (K = spin plus isospin = 0) resonance at a low-excitation energy of about 200 MeV, several hundred MeV below the 500 MeV expected for the Roper. For both the electric and magnetic modes, states with K = 1 have no resonances but instead have zero-energy bound states because of infinitesimal rotations (magnetic dipole) or translations (electric dipole). The absence of any dipole resonance was conjectured to be caused by their improper treatment of the zero-energy modes. Phase shifts for the higher multipole states, K > 1, all showed resonances.

In a manner similar to Hayashi's and Holzwarth's classification scheme, Walliser and Eckert in this paper[80] were able to classify, according to phonon spin, most of the well-established nucleon and delta resonances having excitation energies less than about 1200 MeV. The only exceptions were the S_{11} (1650) and the S_{31} (1900). They found the states of different phonon spin to clearly separate in energy, having a well-defined band structure. For the nucleon resonances, the average experimental excitation energies are 500, 590, 760, and 1150 MeV for K = 0, 1, 2, and 3, respectively. Therefore, the classification according to underlying phonon spin is a possible explanation for the energy-grouping of the pion-nucleon resonances noticed by many including Höhler.[83]

In the next paper,[81] the Siegen group was able to derive the actual physical π-N scattering phase shifts from the normal mode phase shifts computed in the adiabatic approximation for which coupling between rotation and vibration of the Skyrmion is neglected. Because the phonon spin, vector sum of the vibration's orbital momentum (ℓ) and isospin, is conserved in the scattering process, states of vibration with different values of ℓ will couple in the scattering. Physically, this means that pion-nucleon phase shifts, necessarily having definite values of orbital momentum, will consist of a mixture of phonons of electric and magnetic modes. There is no direct one-to-one correspondence between the normal modes and the physical pion-nucleon states, but rather the pion-nucleon partial waves are constructed by a recoupling of the normal modes. The geometrical coupling scheme that the authors propose is given by the triangle rules:

$$\begin{aligned}
\vec{L} &= \vec{\ell} + \vec{t} \\
\vec{J} &= \vec{L} + \vec{S} \\
\vec{J} &= \vec{\ell} + \vec{s} \\
\vec{T} &= \vec{t} + \vec{\tau},
\end{aligned} \tag{5-26}$$

where

$\vec{L}$ - phonon spin

$\vec{\ell}$ - orbital angular momentum of asymptotic pion field (the fluctuation)

$\vec{t}$ - isospin (t = 1) of asymptotic pion field

$\vec{J}$ - total angular momentum in intrinsic frame

$\vec{S}$ - total spin (S = T, total isospin) in intrinsic frame

$\vec{s}$ - target spin (s = τ, target isospin) in intrinsic frame.

This geometrical recoupling scheme allowed them to obtain linear relations between different S-matrix elements, $S_{\ell,2T,2J}$:

$$2(2\ell+1)S_{\ell,3,2\ell+1} = 3\ell S_{\ell,1,2\ell-1} + (\ell+2)S_{\ell,1,2\ell+1}$$

$$2(2\ell+1)S_{\ell,3,2\ell+1} = (\ell-1)S_{\ell,1,2\ell-1} + 3(\ell+1)S_{\ell,1,2\ell+1}\,. \qquad (5\text{-}27)$$

The authors showed phase-shift predictions for the pion-nucleon F-waves as an example of their procedure, and there was surprising agreement with the experimental results. They did, however, admit that serious difficulties exist with the S- and P-waves, which they blame on their approximations in the treatment of zero-energy modes and the adiabatic approximation.

The work of the Siegen group has been documented most completely in their latest paper.[82] Here, they describe, in more detail, the work outlined in the earlier papers.[79-81] Although they still were not able to avoid the adiabatic approximation, they made a start in that direction by reformulating the analysis directly in the physically relevant isospin-space-fixed frame. This is in contrast to the previous work for which results were obtained from a unitary transformation of the isospin-space-rotating S-matrix. The adiabatic approximation, which consists of a decoupling of the rotating Skyrmion from its vibrations, results in an improper treatment of the zero-energy modes and an exclusion of all rotational energies. The zero-energy translational modes affect the S- and D-waves, while the zero-energy rotational modes affect the P-waves. The authors also

investigated both the effect of allowing a nonzero pion mass and the effect of including a term in the Lagrangian of sixth order in the fields, but only second order in time derivatives. In each case, the results were not significantly improved.

5.3.5 The Stanford Linear Accelerator Analysis

Following soon after the initial reports from the Siegen group were similar results from the group at Stanford Linear Accelerator Center (SLAC).[84-88] They too examined the two-flavor Skyrme Lagrangian of equation 5-19 to lowest order in $1/N_c$. In particular, Mattis and his co-workers, Karliner and Peskin, elucidated the nature of the adiabatic approximation, especially its relation to the $1/N_c$ expansion.[84-85] They omitted the effects of soliton (baryon) deformation and recoil caused by the scattering and also ignored the rotation of the soliton during scattering, a $1/N_c$ effect. The scattering amplitudes were derived based on a bare pion propagator,[85] again a result of the lowest order expansion. This approximation results in amplitudes that do not include multiple-pion production and, hence, are only appropriate to scattering with two-particle final states.

As Mattis and Karliner reported in the group's first paper,[84] they were able to obtain the pion-nucleon resonance masses to an average of 8 percent of their experimental values. Their resonance masses were defined by the position of peaks in the speed, $|dT/dW|$, obtained from their numerical calculation of the phase shifts. The phase-shift calculations resulted in a systematic ordering of the sizes of the

partial amplitudes that is well followed by the results from experiments, including the results reported in Chapter 3 of this work. For L > 2, amplitudes $L_{1,2\ell-1}$ and $L_{3,2\ell+1}$ move further in the unitarity circle than do $L_{1,2\ell+1}$ and $L_{3,2\ell-1}$, respectively. In general, the amplitudes they computed agree well with experiment for L > 2 except for the inelasticities. A poor prediction of the inelasticity was expected because of a lack of coupling to many inelastic channels as noted earlier. They also make the claim that the Roper P_{11} is not a pure-breathing mode excitation. In addition, their best fit to the resonance masses resulted in improved predictions for some of the static properties of the Skyrme model, including predictions of the proton and neutron magnetic moments, the axial-vector coupling constant, and isoscalar charge radii. Mattis and Peskin[85] were also able to derive the same linear relations between the pion-nucleon elastic partial waves, equation 5-27. In addition, they derived similar formulas relating $\pi N \rightarrow \pi\Delta$ S-matrix elements and one other relating πN elastic S-matrix element to the $\pi N \rightarrow \pi\Delta$ S-matrices.

As did the Siegen group, the SLAC group also found much poorer agreement with the S-, P-, and D-waves. Again, they attribute this discrepancy largely to the lowest order expansion used here that produces translational-zero and rotational-zero modes of the soliton.[85] These modes are then manifested as zero-energy bound states that directly couple to the S-, P-, and D-waves. The P-waves couple to the rotational-zero mode while the S- and D-waves couple to the translational-zero mode. Therefore, they could not predict the

S_{11} (1650), S_{31} (1900), or the D_{13} (1700).[84] The biggest failure was the lack of finding the two most important resonances, the Delta and Roper resonances. They claim that the resonance pole and the rotational mode zero coincide at the elastic threshold, preventing these resonances from appearing. However, with the next order in the $1/N_c$ expansion, the poles and zeros are perturbed away from the origin. For the P_{11} and P_{33}, the pole should move into the fourth quadrant of the complex energy plane, producing the expected resonances. For the P_{13}, P_{31}, and also S_{31}, the poles should move into the first or second quadrant resulting in the observed repulsive behavior.

In their most recent papers,[86-88] the SLAC group has progressed beyond the Siegen group in considering the Skyrme model for the case of three light flavors [unbroken SU(3)]. They used the same Skyrme Lagrangian, equation 5-19, but had to include the Wess-Zumino term that no longer vanishes for SU(3). They retained the approximations of expanding to lowest order in $1/N_c$ and using exact chiral symmetry. Going to SU(3) allowed Karliner and Mattis[86] to consider pseudoscalar octet meson (pion, eta, kaon) scattering from unrotated Skyrmions. They saw modest improvement in the agreement between the Skyrme model and experiment, primarily because of the increase in inelasticity that the additional degrees of freedom allows. Because they kept only the leading order in $1/N_c$ approximation, they saw no reconciliation of the disagreements in the P_{11}, P_{33}, and S_{31} channels.

With the SU(3) version of the Skyrme model, Karliner[87] and Mattis[88] were able to examine KN and $\bar{K}N$ scattering in addition to πN. The approach used here is very similar to that used earlier for the πN problem. They were able to derive linear formula relating the partial-wave amplitudes for these reactions. The last paper[88] is their comprehensive work on πN, KN, $\bar{K}N \rightarrow \phi_{ps}B$ in the three-flavor Skyrme model, where ϕ_{ps} is an arbitrary pseudoscaler meson and B is a baryon, either a $1/2^+$ octet or a $3/2^+$ decuplet. No new additional results relating to elastic pion-nucleon scattering were reported, however.

The Skyrme model has shown some spectacular successes in its agreement with much of the dynamics of pion-nucleon scattering. It will be very interesting to see whether future work on this problem is able to include the next term in the $1/N_c$ expansion and resolve the discrepancies noted in the S-, D-, and, especially, the P-waves.

5.4 REFERENCES

1. R. K. Bhaduri, *Spectroscopy of N-Δ Excited States and the Quark-Model*, NATO ASI Lectures, Banff, Alberta, Canada, August 1985

2. F. E. Close, *An Introduction to Quarks and Partons*, Academic Press, Inc., London, Ltd., 1979

3. C. Quigg and L. Rosner, *Physics Letters*, Vol. 71B, 1977, p. 153

4. E. Eichten, K. Gottfried, T. Kinoshita, K. D. Lane, and T. M. Yan, *Physical Review D*, Vol. 21, 1980, p. 203

5. W. Celmaster, *Physical Review D*, Vol. 15, 1977, p. 1391

6. A. Martin, CERN Report No. TH 2980, 1980

7. N. Isgur and G. Karl, *Physics Letters*, Vol. 72B, 1977, p. 109

8. N. Isgur and G. Karl, *Physical Review* D, Vol. 18, 1978, p. 4187

9. N. Isgur and G. Karl, *Physical Review* D, Vol. 19, 1979, p. 2653

10. N. Isgur and G. Karl, *Physical Review* D, Vol. 20, 1979, p. 1191 and N. Isgur, G. Karl, R. Koniuk, *Physical Review D*, Vol. 25, 1982, p. 2394

11. A. DéRujula, H. Georgi, and S. L. Glashow, *Physical Review D*, Vol. 12, 1975, p. 147

12. A. J. G. Hey, P. J. Litchfield, and R. J. Cashmore, *Nuclear Physics*, Vol. B95, 1975, p. 516

13. Particle Data Group, "Review of Particle Properties," *Physics Letters*, Vol. 170B, 10 April 1986, p. 245

14. R. Koniuk and N. Isgur, *Physical Review Letters* , Vol. 44, 1980, p. 845

15. R. Koniuk and N. Isgur, *Physical Review D*, Vol. 21, 1980, p. 1868

16. C. P. Forsyth and R. E. Cutkosky, *Zeitschrift für, Physik C*, Vol. 18, 1983 p. 219 and *Physical Review Letters*, Vol. 46, 1981, p. 576

17. R. K. Bhaduri, B. K. Jennings, and J. C. Waddington, *Physical Review D*, Vol. 29, 1984, p. 2051

18. M. V. N. Murthy, M. Dey, J. Dey, and R. K. Bhaduri, *Physical Review D*, Vol. 30, 1984, p. 152

19. M. V. N. Murthy and R. K. Bhaduri, *Physical Review Letters*, Vol. 54, 1985, p. 745

20. M. V. N. Murthy, M. Brack, R. K. Bhaduri, and B. K. Jennings, *Zeitschrift für Physik C*, Vol. 29, 1985, p. 385

21. D. Gromes, *Zeitschrift für Physik C*, Vol. 18, 1983, p. 249

22. A. Chodos, R. L. Jaffe *et al.*, *Physical Review D*, Vol. 9, 1974, p. 3471

23. A. Chodos, R. L. Jaffe *et al.*, *Physical Review D*, Vol. 10, 1974, p. 2599

24. E. Golowich, *Physical Review D*, Vol. 12, 1975, p. 2108

25. J. F. Donoghue, E. Golowich, and B. R. Holstein, *Physical Review D*, Vol. 12, 1975, p. 2875

26. T. DeGrand, R. L. Jaffe *et al.*, *Physical Review D*, Vol. 12, 1975, p. 2060

27. C. E. Carlson, T. H. Hansson, and C. Peterson, *Physical Review D*, Vol. 27, 1983, p. 1556 and *Physical Review D*, Vol. 28, 1983, p. 2895-E

28. W. Y. P. Hwang, *Physical Review D*, Vol. 31, 1985, p. 2826

29. C. Rebbi, *Physical Review D*, Vol. 12, 1975, p. 2407 and *Physical Review D*, Vol. 14, 1976, p. 2362

30. T. A. DeGrand and R. L. Jaffe, *Annals of Physics*, Vol. 100, 1976, p. 425

31. T. A. DeGrand, *Annals of Physics*, Vol. 101, 1976, p. 496

32. K. C. Bowler and A. J. G. Hey, *Physics Letters*, Vol. 69B, 1977, p. 469

33. T. DeGrand and C. Rebbi, *Physical Review D*, Vol. 17, 1978, p. 2358

34. F. E. Close and R. R. Horgan, *Nuclear Physics*, Vol. B164, 1980, p. 413

35. J. F. Donoghue and K. Johnson, *Physical Review D*, Vol. 21, 1980, p. 1975

36. G. E. Brown and M. Rho, *Physics Letter*, Vol. 82B, 1979, p. 177

37. A. W. Thomas, *Nuclear Physics*, Vol. 416B, 1984, p. 69c

38. A. Chodos and C. Thorn, *Physical Review D*, Vol. 12, 1975, p. 2733

39. R. L. Jaffe, *Proceedings of the 1979 Summer School, "Ettore Majorana" on Subnuclear Physics* (Unpublished)

40. C. E. DeTar, *Physical Review D*, Vol. 24, 1981, pp. 752, 762

41. G. E. Brown, M. Rho, and V. Vento, *Physics Letters*, Vol. 84B, 1979, p. 383

42. G. A. Miller, A. W. Thomas, and S. Theberge, *Physics Letters*, Vol. 91B, 1980, p. 192

43. V. Vento, M. Rho *et al.*, *Nuclear Physics*, Vol. 345A, 1980, p. 413

44. S. Theberge, A. W. Thomas, and G. A. Miller, *Physical Review D*, Vol. 22, 1980, p. 2838

45. A. W. Thomas, S. Theberge, and G. A. Miller, *Physical Review D*, Vol. 22, 1981, p. 216

46. L. R. Dodd, A. W. Thomas, and R. Alvarez-Estroda, *Physical Review D*, Vol. 24, 1981, p. 1961

47. A. Chodos and H. Nadeau, *Physical Review D*, Vol. 33, 1986, p. 1450

48. S. A. Chin and G. A. Miller, *Physics Letters*, Vol. 121B, 1983, p. 232

49. V. Vento, *Physics Letters*, Vol. 121B, 1983, p. 370

50. A. W. Thomas, *Journal of Physics G: Nuclear Physics*, Vol. 7, 1981, p. L283

51. G. Kalbermann and J. M. Eisenberg, *Physical Review D*, Vol. 28, 1983, p. 66

52. E. Veit, B. K. Jennings *et al.*, *Physical Review D*, Vol. 33, 1986, p. 1859

53. E. Veit, B. K. Jennings *et al.*, *Physical Review D*, Vol. 31, 1985, p. 1033

54. C. Y. Cheung, *Physical Review D*, Vol. 29, 1984, p. 1417

55. R. J. McLeod and D. J. Ernst, *Physical Review C*, Vol. 29, 1984, p. 906

56. F. Gross and J. Hunter, *Physical Review D*, Vol. 28, 1983, p. 2266

57. S. Weinberg, *Physical Review Letters*, Vol. 17, 1966, p. 616 and *Physical Review Letters*, Vol. 18, 1967, p. 188

58. B. K. Jennings, E. Veit, and A. W. Thomas, *Physical Review D*, Vol. 31, 1985, p. 1033

59. F. A. Veit, B. K. Jennings, and A. W. Thomas, *Physical Review D*, Vol. 33, 1986, p. 1859

60. M. B. Gavela, A. LeYaouanc *et al.*, *Physical Review D*, Vol. 21, 1980, p. 182

61. A. S. Rinat, *Nuclear Physics*, Vol. 377A, 1982, p. 341

62. E. Umland, I. Duck, and W. von Witsh, *Physical Review D*, Vol. 27, 1983, p. 2678

63. E. Umland and I. Duck, *Physics Letters*, Vol. 124B, 1983, p. 284

64. T. Barnes and F. E. Close, *Physics Letters*, Vol. 123B, 1983, p. 89

65. T. H. R. Skyrme, *Proceedings of the Royal Society*, Vol. A260, 1961, p. 127

66. G. 't Hooft, *Nuclear Physics*, Vol. B72, 1974, p. 461

67. E. Witten, *Nuclear Physics*, Vol. B160, 1979, p. 57

68. E. Witten, *Nuclear Physics*, Vol. B223, 1983, pp. 422 and 433

69. E. Guadagnini, *Nuclear Physics*, Vol. B236, 1984, p. 35

70. J. Wess and B. Zumino, *Physics Letters*, Vol. 37B, 1971, p. 95

71. G. S. Adkins, C. R. Nappi, and E. Witten, *Nuclear Physics*, Vol. B228, 1983, p. 552

72. G. S. Adkins and C. R. Nappi, *Nuclear Physics*, Vol. B233, 1984, p. 109

73. A. D. Jackson and M. Rho, *Physical Review Letters*, Vol. 51, 1983, p. 751

74. A. Jackson, A. D. Jackson, and V. Pasquier, *Nuclear Physics*, Vol. A432 1985, p. 567

75. C. Hajduk and B. Schwesinger, *Physics Letters*, Vol. 140B, 1984, p. 172

76. J. D. Breit and C. R. Nappi, *Physical Review Letters*, Vol. 53, 1984, p. 889

77. K. F. Liu, J. S. Zhang, and G. R. E. Black, *Physical Review D*, Vol. 30, 1984, p. 2015

78. I. Zahed, U. Meissner, and U. B. Kaulfuss, *Nuclear Physics*, Vol. A426, 1984, p. 525

79. A. Hayashi and G. Holzwarth, *Physics Letters*, Vol. 140B, 1984, p. 175

80. H. Walliser and G. Eckart, *Nuclear Physics*, Vol. A429, 1984, p. 514

81. A. Hayashi, G. Eckart *et al.*, *Physics Letters*, Vol. 147B, 1984, p. 5

82. G. Eckart, A. Hayashi, and G. Holzwarth, *Nuclear Physics*, Vol. A448, 1986, p. 732

83. G. Höhler, *Pion-Nucleon Scattering*, *Landolt-Bornstein*, Vol. I/9b, Part 2, Springer-Verlag: Berlin 1983

84. M. P. Mattis and M. Karliner, *Physical Review D*, Vol. 31, 1985, p. 2833

85. M. P. Mattis and M. E. Peskin, *Physical Review D*, Vol. 32, 1985, p. 58

86. M. Karliner and M. P. Mattis, *Physical Review Letters*, Vol. 56, 1986, p. 428

87. M. Karliner, SLAC preprint, SLAC-PUB-3958, 1986

88. M. Karliner and M. P. Mattis, SLAC preprint, SLAC-PUB-3901, 1986

6. SUMMARY AND CONCLUSIONS

A comprehensive phase-shift analysis of elastic pion-nucleon scattering from threshold to a pion kinetic energy of 1100 MeV has been performed. The foundation for this analysis is the data base of worldwide pion-nucleon experimental results assembled by the author and described in Chapter 2 and Appendix A. The phase-shift analysis is explained in great detail in Chapter 3, where both the energy-dependent and energy-independent parametrizations and methodology have been described. The analysis process resulted in seven energy-dependent solutions and a single final set of energy-independent solutions. The first of the seven solutions to be developed consisted of a fit to all active experiments using waves S through I and was named FA86 for Fall 1986. Because a small number of the data were responsible for unnecessarily inflating chi-square, a second solution based on removing (pruning) these data from the data base was developed by iterating the process of removing those data and experiments with a chi-square per data point greater than 16 and refitting the partial-wave parameters. The resulting solution, named FP86 (P for prune), provides an excellent fit to 9493 data with a chi-square of 15,646 using 131 parameters.

The seven energy-dependent solutions summarized in Tables 3-2 and 3-3 were used to address several issues. Solutions HP86, FP86, and FP86 tested the sensitivity of the analysis to the number of peripheral waves included in the calculation of the scattering amplitudes. It was concluded that J and higher partial waves are not

needed to fit the data in this energy region or to uniquely determine the important (S through F) waves. The charge independence of the I = 3/2 waves was verified by solutions FP86, MNUS, PLUS, and SPLT to within the accuracy of the data. These same solutions also demonstrated the adequacy of the prescription (see Subsection 3.3) used to correct the partial waves for the electromagnetic interaction. Solution FP86, together with the complementary energy-independent solutions described in Subsection 3.2.3, is presented here as the most economical and best representation to date of pion-nucleon scattering experiments below 1100 MeV.

6.1 INTERPRETATION

Having completed an in-depth phase-shift analysis, it is necessary to interpret the results to understand their significance. Chapter 4 presents the results from solution FP86 and describes its important features. The basis for understanding these results is the insight obtained from the three classes of theoretical models described in Chapter 5.

In Chapter 4, the rich topological structure of the partial-wave amplitudes in the complex energy plane is displayed, showing a variety of poles and zeros. Poles on the second sheet are interpreted as resonances in the elastic channel, and all of the states cited by the Particle Data Tables are seen here except for the two questionable on-star resonances, the P_{13} (1540) and the P_{31} (1550). Because the models discussed in Chapter 5 do not predict these two states, they are probably not valid. The resonance pole parameters for the other

waves agree well with the determination of other analyses as reported in Chapter 4 with the exception of the second P_{11} and P_{33} resonances. The two-star P_{33} (1600) is confirmed by this analysis, and the reason for its weak effect on the physical axis was discovered. A zero in the amplitude between the pole and the real axis masks much of its impact, disguising its presence. The models of Chapter 5 predict this state and the two recalcitrant P_{11} resonances to be predominantly radial (breathing modes) excitations. The P_{11} wave has been difficult to explain in any of the models, and the complicated structure shown in Subsection 4.3 is indicative of these difficulties. Approximations made in the Skyrme model, particularly in the treatment of rotational zero modes, prevent the model from adequately addressing the P-waves until another term in the $1/N_{color}$ expansion is added. The bag models, however, have provided useful insight here. Solution FP86 showed a second pole near the Roper resonance, but around the delta branch point. As the coupling to the explicit K-matrix pole is varied, the motion of both of these poles is consistent with the interpretation given in Subsection 5.2.3 and obtained from a calculation of the cloudy bag model that this second pole is a manifestion of a radial excitation in an inelastic channel, presumably the $n\Delta$ channel. This suggestion is hardly conclusive, and further analysis would definitely be needed to validate the presence of both poles in the inelastic channel. If this interpretation is indeed verified, then the P_{11} (1710) would not be a radial excitation but might be a gluon-quark hybrid.

All three classes of quark models reasonably match most of the pion-nucleon states. Some of this success is simply because of the underlying SU(6) group structure present in the models and obvious in the data. Both the constituent quark and the bag models agree that the color magnetic hyperfine interaction as obtained from one-gluon exchange is responsible for much of the observed splitting between nearby states but that the spin-orbit interaction has a negligible effect. It is obvious that the resonances tend to fall in groups according to their energy. According to the Skyrme model, this grouping is caused by an underlying phonon spin spectrum. The Skyrme model has also had great success in "explaining" the linear relationship observed between various partial waves as described in Subsections 5.3.4 and 5.3.5.

In addition to the resonance poles observed in solution FP86, another obvious characteristic of the solution is the presence of zeros in the amplitudes. A few isolated zeros were observed, but generally the zeros are found paired with poles, sometimes beside a pole and sometimes between the pole and the real axis. The models of Chapter 5, however, have not been able to provide any insight into these zeros. No analyses outside of the VPI and SU group have reported such zeros, and it would be useful to provide some interpretation of their significance beyond their necessity to satisfy unitarity.

6.2 RECOMMENDATIONS

The analysis presented herein still does not completely solve the pion-nucleon problem, although it has resulted in significant progress in our understanding of this important interaction. There is additional experimental and theoretical work that should be performed. As discussed in Chapter 2, the data base is incomplete, lacking data at some energies and especially at the extreme angles. The discussion there indicated where data are lacking and what experiments are needed to fill out the data base. Data in the charge exchange channel are particularly sparse. Of greatest significance, however, is the complete lack of any measurements in this energy region of any of the spin rotation observables. Such data are required to ensure confidence in any phase-shift analysis including this one. In addition, high-precision measurements are needed over much of the energy range to conclusively address the possibility of the narrow poles as examined in Subsection 4.4. Such poles are not expected but cannot be ruled out by the present analysis.

Further phase-shift analyses are also appropriate, particularly as new experiments are performed to reduce some of the deficiencies given in the preceeding paragraph. As discussed in Subsection 4.3, effort is certainly justified in attempting to reparametrize several of the partial waves to validate the pole and zero structure observed in solution FP86. It may be possible that the observed zeros are not all required to fit the data, and their presence needs to be confirmed. Particular care should be given to reexamining the P-waves and the S_{31}

wave, whose zeros significantly impact the effect nearby poles have on the real axis. This investigation would also serve to validate the complicated multiple pole structure seen with the two P_{11} resonances as shown in Figure 4-2c. The author has suggested that the additional pole seen in solution FP86's P_{11} wave just around the delta branch point from the Roper pole might be a manifestation of an additional resonance in the inelastic $\pi\Delta$ channel. This possibility would be best investigated in an inelastic phase-shift analysis and, in particular, a new analysis of the $\pi N \rightarrow \pi\pi N$ reaction is recommended.

Further theoretical investigation on the subject of partial-wave zeros is also warranted. With the goal of providing a physical interpretation of their existence, the author plans to continue to examine the subject, initially by continuing to study the exactly solvable square well potential. If the sqaure well zeros can be understood, it is hoped that their signficance can be applied to the pion-nucleon problem.

APPENDIX A. DATA REFERENCES

Presented here are the journal references of all the experiments in the data base. All references noted in Table 2-1 are included in this alphabetical listing.

1. K. Abe *et al.*, *Physical Review D*, Vol. 10, 1974, p. 3556
2. J. M. Abillon *et al.*, *Physics Letters*, Vol. 32B, 1970, p. 712
3. J. M. Abillon *et al.*, *Nuclear Physics B*, Vol. 46, 1972, p. 630
4. M. G. Albrow *et al.*, *Nuclear Physics B*, Vol. 25, 1970, p. 9
5. M. G. Albrow *et al.*, *Nuclear Physics B*, Vol. 37, 1972, p. 594
6. J. C. Alder *et al.*, *Lettre Nuovo Cimento*, Vol. 23, 1978, p. 381
7. J. C. Alder *et al.*, *Physical Review D*, Vol 27, 1983, p. 1040
8. C. Amsler *et al.*, *Physics Letters*, Vol. B57, 1975, p. 289
9. C. Amsler *et al.*, *Lettre Nuovo Cimento*, Vol. 15, 1976, p. 209
10. P. S. Aplin *et al.*, *Nuclear Physics B*, Vol. 32, 1971, p. 253
11. F. F. Arens *et al.*, *Physical Review*, Vol. 167, 1968, p. 1261
12. E. G. Auld *et al.*, *Canadian Journal of Physics*, Vol. 57, 1979, p. 73
13. T. C. Bacon *et al.*, *Physical Review*, Vol. 157, 1967, p. 1263
14. P. Baillon *et al.*, *Nuclear Physics B*, Vol. 105, 1976, p. 365
15. S. L. Baker *et al.*, *Nuclear Physics B*, Vol. 18, 1970, p. 29
16. S. L. Baker *et al.*, *Nuclear Physics B*, Vol. 41, 1972, p. 91
17. M. Banner *et al.*, *Nuovo Cimento*, Vol. 50A, 1967, p. 431
18. P. C. Barber *et al.*, *Nuclear Physics B*, Vol. 84, 1975, p. 109
19. P. Bareyre *et al.*, *Physics Review Letters*, Vol. 14, 1965, p. 198
20. P. Bareyre *et al.*, *Physics Review Letters*, Vol. 14, 1965, p. 878
21. E. Barrelet *et al.*, *Physics Reviews D*, Vol. 15, 1977, p. 2435

22. W. Bayer *et al.*, *Nuclear Instruments and Methods*, Vol. 134, 1976, p. 449

23. V. S. Bekrenev *et al.*, *Journal of Experimental and Theoretical Physics*, Vol. 21, 1975, p. 282

24. V. S. Bekrenev *et al.*, *Nuclear Physics A*, Vol. 364, 1981, p. 515

25. V. S. Bekrenev *et al.*, *Soviet Journal of Nuclear Physics*, Vol. 31, 1980, p. 92

26. V. S. Bekrenev, V. V. Abaev *et al.*, *Zeitschrift für Physik A*, Vol. 311, 1983, p. 217

27. V. S. Bekrenev *et al.*, *Journal of Experimental and Theoretical Physics Letters*, Vol. 34, 1981, p. 145

28. V. S. Bekrenev *et al.*, *Journal of Experimental and Theoretical Physics Letters*, Vol. 35, 1982

29. P. A. Berardo *et al.*, *Physical Review D*, Vol. 6, 1972, p. 756

30. L. Bertanza *et al.*, *Nuovo Cimento*, Vol. 44A, 1966, p. 712

31. L. Bertanza *et al.*, CERN Preprint Number 8990, 1968

32. A. Berthon *et al.*, CEA Preprint Number R3401, 1967

33. A. Berthon *et al.*, *Nuclear Physics B*, Vol. 81, 1974, p. 431

34. P. Y. Bertin *et al.*, *Nuclear Physics B*, Vol. 106, 1976, p. 341

35. G. Bizard *et al.*, *Nuovo Cimento*, Vol. 144A, 1966, p. 999

36. G. Bizard *et al.*, *Nuclear Physics B*, Vol. 5, 1968, p. 515

37. G. Bizard *et al.*, *Physics Letters*, Vol. 31B, 1970, p. 481

38. D. J. Blasberg *et al.*, UCLA Preprint Number UCLA-10-P25-6, 1971

39. M. Blecher *et al.*, VPI and SU Private Communication, 1978

40. P. Borgeaud *et al.*, *Physics Letters*, Vol. 10, 1964, p. 134

41. M. G. Bowler *et al.*, *Nuclear Physics B*, Vol. 17, 1970, p. 331

42. M. G. Bowler *et al.*, *Nuclear Physics B*, Vol. 37, 1972, p. 133

43. A. D. Brady *et al.*, *Physical Review D*, Vol. 3, 1971, p. 2619

44. A. D. Brady *et al.*, *Physical Review D*, Vol. 4, 1971, p. 2693

45. R. M. Brown *et al.*, *Nuclear Physics B*, Vol. 117, 1976, p. 12

46. R. M. Brown, Kiev Conference, 1977

47. R. M. Brown *et al.*, *Nuclear Physics B*, Vol. 137, 1978, p. 542

48. R. M. Brown *et al.*, *Nuclear Physics B*, Vol. 144, 1978, p. 287

49. P. V. Bugg *et al.*, *Nuclear Physics B*, Vol. 26, 1971, p. 588

50. F. Bulos *et al.*, *Physical Review Letters*, Vol. 13, 1964, p. 558

51. F. Bulos *et al.*, *Physical Review*, Vol. 187, 1969, p. 1827

52. R. A. Burnstein *et al.*, *Physical Review*, Vol. 137, 1965, p. 1044

53. P. J. Bussey *et al.*, *Nuclear Physics B*, Vol. 58, 1973, p. 363

54. A. A. Carter *et al.*, *Physical Review*, Vol. 168, 1968, p. 1457

55. A. A. Carter *et al.*, *Nuclear Physics B*, Vol. 26, 1971, p. 445

56. A. A. Carter and J. R. Carter, Rutherford Laboratory, Report Number RL-73-024, 1973 (Unpublished)

57. N. M. Cason *et al.*, *Physical Review*, Vol. 150, 1966, p. 1134

58. J. B. Cheze *et al.*, *Nuclear Physics B*, Vol. 72, 1974, p. 365

59. C. B. Chiu *et al.*, *Physical Review*, Vol. 156, 1967, p. 1415

60. J. C. Comiso *et al.*, *Physical Review D*, Vol. 12, 1975, p. 738

61. C. R. Cox *et al.*, *Physical Review*, Vol. 184, 1969, p. 1453

62. Crowe, University of California Research Laboratory, Report No. UCRL-18473, 1968

63. D. C. Cundy *et al.*, *Proceedings of the Physical Society of London*, Vol. 85, 1965, p. 275

64. D. Davidson *et al.*, *Physical Review D*, Vol. 6, 1972, p. 1199

65. J. Debaisieux *et al.*, *Nuclear Physics B*, Vol. 63, 1965, p. 273

66. J. Debaisieux *et al.*, *Nuclear Physics B*, Vol. 147, 1968, p. 147

67. M. DeBeer *et al.*, *Nuclear Phyiscs B*, Vol. 12, 1969, p. 599

68. M. DeBeer *et al.*, *Nuclear Physics B*, Vol. 12, 1969, p. 617

69. N. C. Debenham *et al.*, *Physical Review D*, Vol. 12, 1975, p. 2545

70. Deler, University of Saclay, CEA-3579, 1967

71. Derre, University of Orsay Thesis, 1969

72. T. J. Devlin *et al.*, *Physical Review Letters*, Vol. 14, 1965, p. 1031

73. D. F. Dickinson *et al.*, *Physics Letters*, Vol. 20, 1966, p. 549

74. J. Dolbeau *et al.*, University of Karlsruhe, 1973

75. J. Dolbeau *et al.*, *Nuclear Physics B*, Vol. 78, 1974, p. 233

76. R. A. Donald *et al.*, *Proceedings of the Physical Society of London*, Vol. 87, 1966, p. 445

77. L. Dubal *et al.*, *Helvitica Physica Acta*, Vol. 50, 1977, p. 569

78. L. Dubal *et al.*, *Helvitica Physica Acta*, Vol. 50, 1977, p. 815

79. J. Duclos *et al.*, *Physics Letters*, Vol. 43B, 1973, p. 245

80. P. J. Duke *et al.*, *Physical Review*, Vol. 149, 1966, p. 1077

81. P. J. Duke *et al.*, *Physical Review*, Vol. 166, 1968, p. 1448

82. R. D. Eandi *et al.*, *Physical Review*, Vol. 136, 1964, p. 536

83. D. N. Edwards *et al.*, *Proceedings of the Physical Society of London*, Vol. 92, 1967, p. 602

84. S. Femino *et al.*, *Nuovo Cimento*, Vol. 52A, 1967, p. 892

85. D. H. Fitzgerald *et al.*, *Physical Review C*, Vol. 34, 1980, p. 619

86. J. S. Frank *et al.*, *Physical Review D*, Vol. 28, 1983, p. 1569

87. F. C. Gaille *et al.*, Preprint, 1984

88. V. A. Gordeev *et al.*, *Nuclear Physics A*, Vol. 364, 1981, p. 408

89. W. Gorn *et al.*, *Bulletin of the American Physical Society*, Vol. 12, 1967, p. 469

90. W. Gorn *et al.*, Lawrence-Berkley Laboratory Report No. LBL-1320, 1973

91. M. Greenburg *et al.*, Lawrence-Berkley Laboratory Report No. UCRL-1563, 1973

92. Hansroul, University of California Research Laboratory Report No. UCRL-17263, 1967

93. M. G. Hauser *et al.*, *Physics Letters*, Vol. 35B, 1971, p. 252

94. J. A. Helland *et al.*, *Physical Review*, Vol. 134, 1964, p. 1062

95. J. A. Helland *et al.*, *Physical Review*, Vol. 134, 1964, p. 1079

96. R. E. Hill *et al.*, *Physical Reivew D*, Vol. 1, 1970, p. 729

97. R. E. Hill *et al.*, *Physical Review D*, Vol. 2, 1970, p. 1199

98. G. Höhler, F. Kaiser, R. Koch, and E. Pietarinen, "Handbook of Pion-Nucleon Scattering," Fachinformation-Szentrum, Karlsruhe, Germany, *Physics Data*, Vol. 12-1, 1979

99. E. Hyman *et al.*, *Physical Review*, Vol. 165, 1968, p. 1437

100. F. Irom, personal communication

101. R. F. Jenefsky *et al.*, *Helvitica Physica Acta*, Vol. 47, 1974, p. 80

102. R. F. Jenefsky *et al.*, *Nuclear Physics A*, Vol. 290, 1977, p. 407

103. Johnson, Preprint UCRL-17683, 1968

104. G. E. Kalmus *et al.*, *Physical Review D*, Vol. 4, 1971, P. 676

105. H. Karami *et al.*, *Nuclear Physics B*, Vol. 154, 1979, p. 503

106. G. J. Kim, personal communication

107. A. V. Kravtsov *et al.*, *Nuclear Physics B*, Vol. 140, 1978, p. 279

108. D. L. Lind *et al.*, *Physical Review*, Vol. 138, 1965, p. 1509

109. Malos, Unpublished, University of Karlsruhe Tape

110. J. F. Martin *et al.*, *Nuclear Physics B*, Vol. 89, 1975, p. 253

111. D. F. Measday *et al.*, *Nuclear Physics A*, Vol. 414, 1984, p. 493

112. W. J. Metzger *et al.*, *Physical Review*, Vol. 164, 1967, p. 1680

113. A. Mokhatari *et al.*, *Physical Review D*, Vol. 33, 1986, p. 286 and *Physical Review Letters*, Vol. 55, 1985, p. 359

114. A. Muller *et al.*, *Physics Letters*, Vol. 10, 1964, p. 349

115. B. M. K. Nefkins *et al.*, *Physical Review D*, Vol. 18, 1978, p. 3911

116. J. E. Nelson *et al.*, *Physics Letters*, Vol. 47B, 1973, p. 281

117. P. M. Ogden *et al.*, *Physical Review*, Vol. 137, 1965, p. 1115

118. J. D. Olner *et al.*, *Physical Review*, Vol. 147, 1966, p. 932

119 R. J. Ott *et al.*, *Physical Review D*, Vol. 16, 1977, p. 2699

120. E. Pedroni *et al.*, *Nuclear Physics A*, Vol. 300, 1978, p. 321

121. T. J. Richards *et al.*, *Physical Review D*, Vol. 10, 1974, p. 45

122. W. S. Risk *et al.*, *Bulletin of the American Physical Society*, Vol. 11, 1966, p. 36

123. W. S. Risk *et al.*, *Physical Review*, Vol. 167, 1968, p. 1249

124. B. G. Ritchie *et al.*, *Physics Letters*, Vol. 125B, 1983, p. 128

125. R. E. Rothschild *et al.*, *Physical Review D*, Vol. 5, 1972, p. 499

126. M. E. Sadler *et al.*, *Physics Letters*, Vol. 119B, 1982, p. 69

127. M. E. Sadler, personal communication

128. H. N. K. Sarma *et al.*, *Nuclear Physics B*, Vol. 161, 1979, p. 1

129. S. R. Shannon *et al.*, *Physical Review Letters*, Vol. 33, 1974, p. 237

130. Sleeman, Oxford University, RHEL, 1971

131. Sterling, Preprint CEA-R2838, 1966

132. C. A. Tilger *et al.*, *Physical Review*, Vol. 142, 1966, p. 972

133. W. Troka *et al.*, *Physical Review*, Vol. 144, 1966, p. 1115

134. R. T. Van de Walle *et al.*, *Nuovo Cimento*, Vol. A53, 1968, p. 745

135. I. M. Vasilevsky *et al.*, *Physics Letters*, Vol. 23, 1966, p. 174

136. J. Vavra *et al.*, *Physical Review D*, Vol. 16, 1977, p. 2687

137. C. N. Vittitoe *et al.*, *Physical Review*, Vol. 135, 1964, p. 232

138. J. A. Wightman, personal communication

APPENDIX B. AMPLITUDE CONVENTIONS

The analysis being reported in this paper has used the usual no-spin-flip amplitude, f(θ), and the spin-flip amplitude, g(θ), where in the center-of-mass system,

$$f(\theta) = \frac{\hbar}{q} \sum_{\ell=0}^{\infty} \left[(\ell + 1) T_{\ell^+} + \ell T_{\ell^-} \right] P_\ell (\cos\theta) \ ,$$

and

$$g(\theta) = \frac{\hbar}{q} \sum_{\ell=0}^{\infty} \left(T_{\ell^+} - T_{\ell^-} \right) P_\ell^1 (\cos\theta) \ , \qquad \text{(B-1)}$$

with

q = barycentric momentum

θ = center-of-mass scattering angle

P_ℓ = ordinary Legendre function

P_ℓ^1 = associated Legendre function = $\sin\theta \, dP_\ell (\cos\theta)/d\cos\theta$

ℓ = orbital angular momentum index

$T_{\ell\pm}$ = partial-wave amplitude for total angular momentum $j = \ell \pm \frac{1}{2}$.

The usual assumption of isospin invariance allows the following isospin decomposition of the partial-wave amplitudes:

$$T_{\ell^\pm} \rightarrow T^{3/2}_{\ell^\pm} \quad \text{for positive-pion scattering,}$$

$$T_{\ell^\pm} \rightarrow 1/3 \, (T^{3/2}_{\ell^\pm} + 2T^{1/2}_{\ell^\pm}) \quad \text{for negative-pion scattering,} \qquad \text{(B-2)}$$

and

$$T_{\ell^\pm} \rightarrow \sqrt{2}/3 \, (T^{3/2}_{\ell^\pm} - T^{1/2}_{\ell^\pm}) \quad \text{for charge-exchange scattering state.}$$

with the superscript labeling the isospin state.

The four complex, partial-wave, T-matrix elements for a given value of ℓ, $T^{1/2}{}_{\ell\pm}$ and $T^{3/2}{}_{\ell\pm}$ are labeled according to the standard spectroscopic notation; L_{2I2J}, with $J = \ell \pm 1/2$, $I = 1/2$ or $3/2$, and L = S, P, D ... for ℓ = 0, 1, 2, ..., respectively. The nuclear phase shifts, $\delta^I{}_{\ell\pm}$, inelasticities, $\eta^I{}_{\ell\pm}$ are then given by

$$T^I_{\ell\pm} = \frac{1}{2i}\left[\eta^I_{\ell\pm}\ exp\left(2i\ \delta^I_{\ell\pm}\right) - 1\right], \tag{B-3}$$

and, hence, for each ℓ greater than zero, there are eight real numbers to be determined.

The amplitudes used to compute the experimental observables must include the electromagnetic corrections described in Subsection 3.3. According to equations 3-17 and 3-18, the charge-corrected, partial-wave amplitude is a function of the scattering reaction being examined. Modifying the nuclear amplitudes of equations B-2 and B-3 according to this prescription then gives the charge-corrected amplitudes $(T_{\ell\pm})^x_{cc}$ for positive exchange (x = 0) scattering. Using the coulomb phase shift of equation 3-19 and Tromberg's direct positive pion coulomb amplitudes, f_c and g_c, the total amplitudes for each reaction can then be written as follows:

For positive-pion scattering,

$$F^{(+)} = f_c + \frac{\hbar}{q}\sum_{\ell=0}^{\infty} e^{2i\sigma_\ell}\left[(\ell+1)\left(T^{3/2}_{\ell^+}\right)^+_{cc} + \ell\left(T^{1/2}_{\ell^+}\right)^+_{cc}\right] P_\ell\,(\cos\theta)\,,$$

and

$$G^{(+)} = g_c + \frac{\hbar}{q} \sum_{\ell=0}^{\infty} e^{2i\sigma_\ell} \left[\left(T^{3/2}_{\ell^+} \right)^{+}_{cc} - \ell \left(T^{3/2}_{\ell^-} \right)^{+}_{cc} \right] P^1_\ell (\cos\theta) . \tag{B-4}$$

For negative-pion scattering,

$$F^{(-)} = -f_c^* + \frac{\hbar}{q} \sum_{\ell=0}^{\infty} \frac{1}{3} e^{-2i\sigma_\ell} \left\{ (\ell+1) \left[\left(T^{3/2}_{\ell^+} \right)^{-}_{cc} + 2 \left(T^{1/2}_{\ell^+} \right)^{-}_{cc} \right] \right.$$

$$\left. + \ell \left[\left(T^{3/2}_{\ell^-} \right)^{-}_{cc} + 2 \left(T^{1/2}_{\ell^-} \right)^{-}_{cc} \right] \right\} P_\ell (\cos\theta) ,$$

and

$$G^{(-)} = -g_c + \frac{\hbar}{q} \sum_{\ell=0}^{\infty} \frac{1}{3} e^{-2i\sigma_\ell} \left\{ \left[\left(T^{3/2}_{\ell^+} \right)^{-}_{cc} + 2 \left(T^{1/2}_{\ell^-} \right)^{-}_{cc} \right] \right.$$

$$\left. - \left[\left(T^{3/2}_{\ell^-} \right)^{-}_{cc} + 2 \left(T^{1/2}_{\ell^-} \right)^{-}_{cc} \right] \right\} P^1_\ell (\cos\theta) . \tag{B-5}$$

For charge-exchange scattering,

$$F^{(0)} = \frac{\hbar}{q} \sum_{\ell=0}^{\infty} \frac{\sqrt{2}}{3} e^{-i\sigma_\ell} \left\{ (\ell+1) \left[\left(T^{3/2}_{\ell^+} \right)^{0}_{cc} - \left(T^{1/2}_{\ell^+} \right)^{0}_{cc} \right] \right.$$

$$\left. + \ell \left(T^{3/2}_{\ell^-} \right)^{0}_{cc} - \left(T^{1/2}_{\ell^-} \right)^{0}_{cc} \right] \right\} P_\ell (\cos\theta),$$

and

$$G^{(0)} = \frac{\hbar}{q} \sum_{\ell=0}^{\infty} \frac{\sqrt{2}}{3} e^{-i\sigma_\ell} \left\{ \left[\left(T^{3/2}_{\ell^+} \right)^{0}_{cc} - \left(T^{1/2}_{\ell^+} \right)^{0}_{cc} \right] \right\}$$

$$- \left[\left(T^{3/2}_{\ell^-} \right)^{0}_{cc} - \left(T^{1/2}_{\ell^-} \right)^{0}_{cc} \right\} P^1_\ell (\cos\theta) . \tag{B-6}$$

The observables are calculated from the full amplitudes of equations B-4 through B-6 or from the "nuclear" amplitudes of equations B-1 and B-2 where the T-matrix elements have also have been charge-corrected according to the prescription of equations 3-17 and 3-18, but the coulomb amplitudes and phases have not been included. This latter set of amplitudes is used to compute all forward scattered quantities such as the quasi-data of Carter and Höhler discussed in Subsection 2.1 and Chapter 3 as well as the total, inelastic, and elastic cross sections. The explicit formulas used to calculate the observables follow below where all the T-matrices shown are the charge-corrected ones as described earlier.

According to the Optical Theorem, the total cross sections for positive- and negative-pion scattering are computed with

$$\sigma_t = 4\pi \frac{\hbar}{q} Im\,[f(\theta = 0)]\,. \tag{B-7}$$

The total elastic cross sections are calculated with the charge-corrected T-matrices appropriate for each reaction as follows:

$$\sigma_e^{(+)} = 4\pi\left(\frac{\hbar}{q}\right)^2 \sum_{\ell=0}^{\infty} \left[(\ell+1)\,|T_{\ell^+}^{3/2}|^2 + \ell|T_{\ell^-}^{3/2}|^2\right],$$

$$\sigma_e^{(-)} = 4\pi\left(\frac{\hbar}{q}\right)^2 \sum_{\ell=0}^{\infty} \left[(\ell+1)\,|\frac{1}{3}\,T_{\ell^+}^{3/2} + \frac{2}{3}\,T_{\ell^+}^{3/2}|^2 + \ell|\frac{1}{3}\,T_{\ell^-}^{3/2} + \frac{2}{3}\,T_{\ell^-}^{1/2}|^2\right],$$

and

$$\sigma_e^{(0)} = 4\pi\left(\frac{\hbar}{q}\right)^2 \sum_{\ell=0}^{\infty} \left[(\ell+1)\left|\frac{\sqrt{2}}{3} T_{\ell^+}^{3/2} - \frac{\sqrt{2}}{3} T_{\ell^+}^{1/2}\right|^2 \right.$$

$$\left. + \ell\left|\frac{\sqrt{2}}{3} T_{\ell^-}^{3/2} - \frac{\sqrt{2}}{3} T_{\ell^-}^{1/2}\right|^2 \right] . \qquad \text{(B-8)}$$

The inelastic cross sections for positive- and negative-pion scattering are then given by

$$\sigma_{in}^{(+)} = \sigma_t^{(+)} - \sigma_e^{(+)}$$

and

$$\sigma_{in}^{(-)} = \sigma_t^{(-)} - \sigma_e^{(-)} - \sigma_e^{(0)} \quad . \qquad \text{(B-9)}$$

The inelastic cross section for charge-exchange scattering obviously does not exist.

The differential cross section for scattering by an unpolarized target is given by

$$\frac{d\sigma}{d\Omega}(\theta) = |F(\theta)|^2 + |G(\theta)|^2 \ . \qquad \text{(B-10)}$$

For an unpolarized target, the polarization of the outgoing nucleon in a direction perpendicular to the scattering plane is calculated with:

$$P(\theta)\frac{d\sigma}{d\Omega} = 2\,Im\{F(\theta)\,G^*(\theta)\} \ . \qquad \text{(B-11)}$$

This polarization is often determined from the asymmetry of the scattering cross section for scattering from a transversely polarized target

$$P(\theta)P_i = \frac{\frac{d\sigma}{d\Omega}(\theta) - \frac{d\sigma}{d\Omega}(-\theta)}{\frac{d\sigma}{d\Omega}(\theta) + \frac{d\sigma}{d\Omega}(-\theta)} \quad , \tag{B-12}$$

where P_i is the initial polarization of the target.

For a target polarized in the beam direction, the spin rotation parameters, R and A, give the components of the recoil nucleon polarization in the direction of the outgoing nucleon and perpendicular to the nucleon but still in the scattering plane, respectively. R and A are computed as follows:

$$R(\theta)\frac{d\sigma}{d\Omega} = (|F|^2 - |G|^2)\cos\theta - 2\,Re\{FG^*\}\sin\theta \ , \tag{B-13}$$

and

$$A(\theta)\frac{d\sigma}{d\Omega} = (|G|^2 - |F|^2)\cos\theta - 2\,Re\{FG^*\}\sin\theta \ , \tag{B-14}$$

where θ is the center of mass-scattering angle. The three spin observables are related by $P^2 + A^2 + R^2 = 1$.

Other experimental observables exist but are not independent of those shown above. One such example is the Wolfenstein spin-rotation angle, β, which is given by

$$\tan(\beta) = 2\,Re(FG^*)/(|G|^2 - |G|^2) = (R\sin\theta + A\cos\theta)/R\cos\theta - A\sin\theta) \ . \tag{B-15}$$

APPENDIX C. THE ANALYSIS PROGRAM SHSZSA

The fitting process described in Chapter 3 was accomplished with the FORTRAN program SHSZSA (Spin-Half Spin-Zero Scattering Analysis) developed over the last 20 years by Drs. R. A. Arndt and L. D. Roper. SHSZSA was used for both the energy-dependent and the single-energy analyses. The logic flow in SHSZSA is illustrated in the flow chart of Figure C-1. The diamond figures indicate a decision process where alternate pathways are given for yes (Y) and no (N) answers to the posed question. The bold line marks the path taken by the program in a simple-energy-dependent analysis. The dashed line shows the modification to this path for when the data are pruned before the search. The second pass through PINDTA and PINSOL is required by the obvious need to read the data base and initial solution parameter set before the pruning, while the pruning option flag is set in PINDTA. The variable, M, shown in the flow chart is used by SHSZSA to select among many optional logic paths by controlling transfers between different sections of the code. It is defined whenever input data are requested. A more complete hierarchy of the major routines in SHSZSA is shown in Figure C-2, while Table C-1 provides a brief description of each of these subroutines.

The heart of the analysis is the chi-squared reduction process performed by SCHPIN. Using initial parameter increments (DPZ(K) = Δp_k) provided by DDPPIN, it varies the parameters to decrease chi-square for a number of user-specified cycles or until chi-square is minimized. After first randomly reordering the set of parameters to

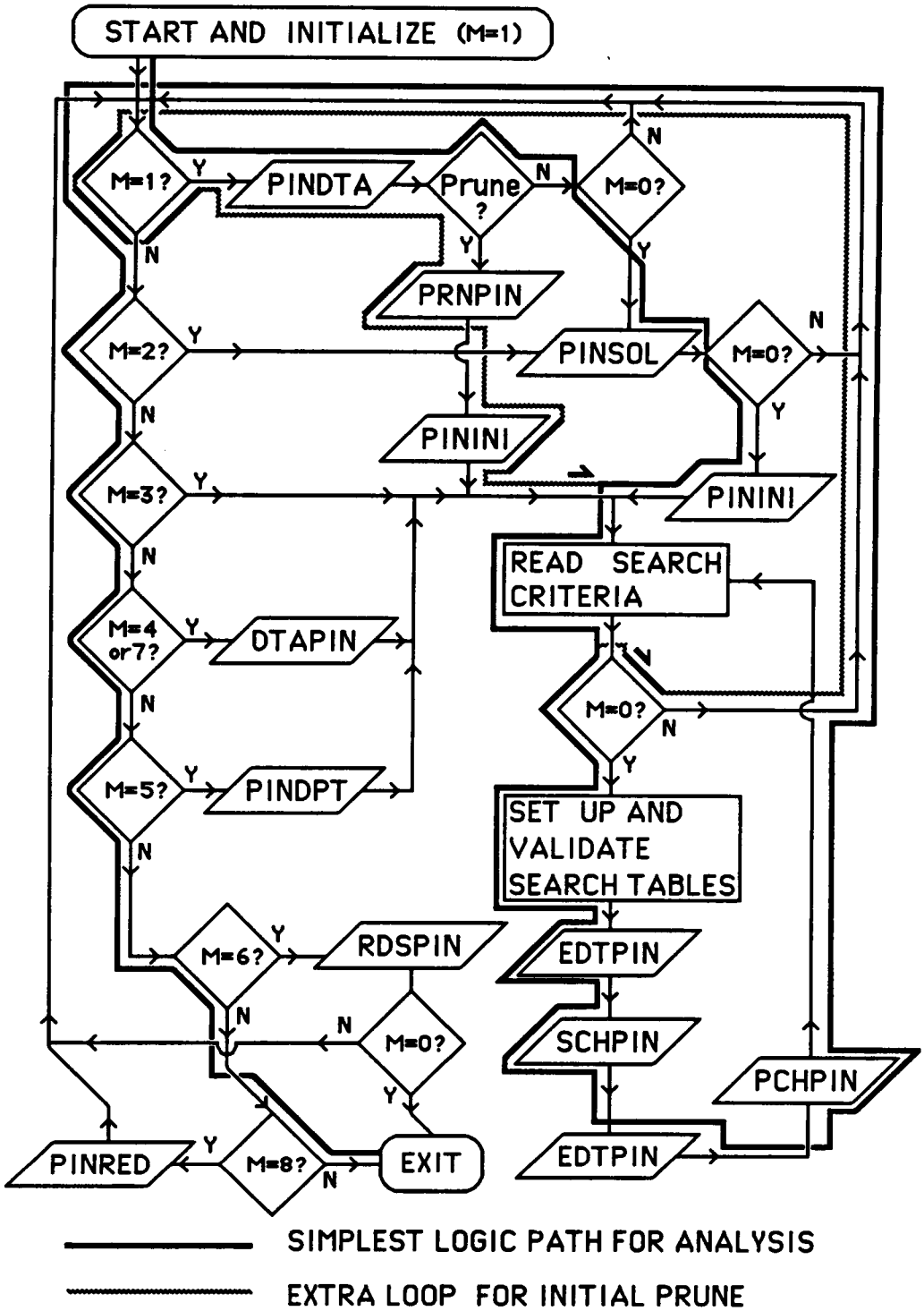

FIGURE C-1. SHSZSA FLOWCHART

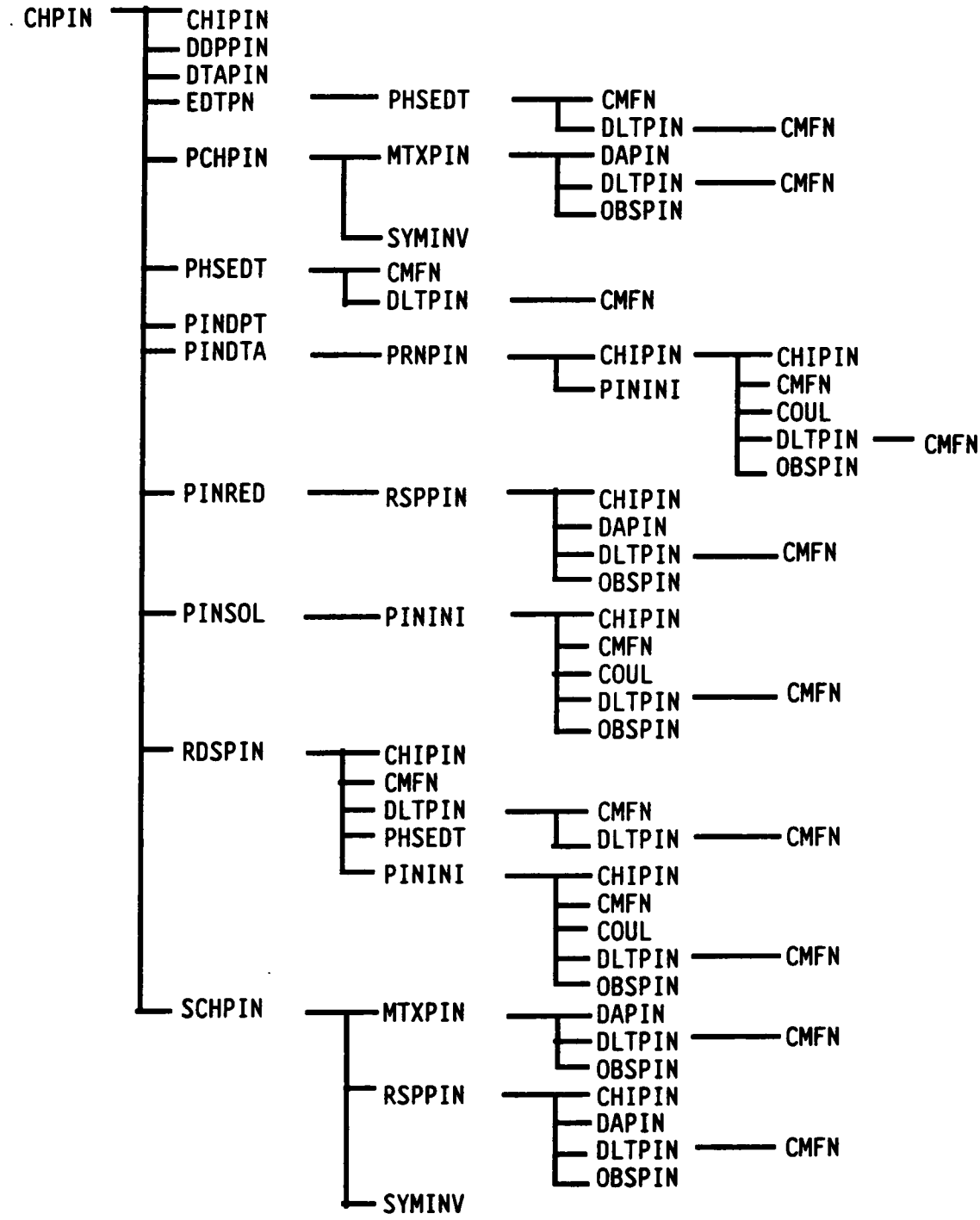

FIGURE C-2. SUBROUTINE CALLING HIERARCHY

TABLE C-1. SHSZSA SUBROUTINE DESCRIPTION (Sheet 1 of 2)

NAME	DESCRIPTION
SHSZSA	Top-level program that controls logic of the analysis and sets up and validates the search tables.
CHIPIN	Calculates chi-square of data set and when specified, renormalizes all angular observables
CMFN	Calculates the Chew-Mandelstom dispersion functions used in the energy-dependent analysis and described in Appendix D
COUL	Calculates the direct coulomb amplitudes as developed by Tromberg *et al.* and documented by Höhler[1]
DAPIN	Resets the total amplitude (f and g) after a partial wave has been changed because of parameter variation in the process of chi-squared reduction.
DDPPIN	Sets the initial parameter increments during the setup of search tables and before the fitting process
DLTPIN	Calculates the partial-wave T-matrix according to the user-specified parametrization (see Subsections 3.1.1 and 3.2.1)
DTAPIN	Prints out a summary of data, including the experimental and theoretical values and chi-square of each datum plus the normalization and total chi-squares for each experiment. If specified, also will print total amplitudes (f and g) for each datum.
EDTPIN	Prints out various quantities describing the search, including the parameters that were varied, the number of search steps and final chi-square. Prints out the parameter values for each partial wave.
MTXPIN	Calculates the gradient and second derivative of chi-square with respect to the parameters being varied.
OBSPIN	Calculates each of the possible experimental observables from the total amplitudes (see Appendix B).

TABLE C-1. SHSZSA SUBROUTINE DESCRIPTION (Sheet 2 of 2)

NAME	DESCRIPTION
PCHPIN	Writes onto an external file the solution (parameter set) of an energy-dependent analysis after a search, and, if specified, also writes the error matrix. For single-energy analyses, prints out parameter errors.
PHSEDT	Prints out phase-shift and absorption coefficients and elastic T-matrix element for a set of user-specified energies.
PINDPT	Prints histogram of chi-square per data point for each experiment.
PINDTA	Reads data selection criteria from input and then reads selected data from input and/or data files.
PININI	Calculates initial partial-wave amplitudes, Legendre polynomials, and observables for each datum, as well as initial total chi-square.
PINRED	Reduces the number of parameters available to be searched by zeroing out small parameters.
PINSOL	Reads solution parameters from input or a data file or keeps current solution as directed.
PRNPIN	Prunes data if option is selected by removing from the analysis any single data points or entire experiments with excessive chi-square. Then prints out details of deleted data.
RDSPIN	Sets up parametrization for single-energy analysis
RSPPIN	Resets partial-wave amplitudes to new values after parameters have changed.
SCHPIN	Searches for new parameter set to reduce chi-square, using the square-error-matrix search method.
SYMINV	Inverts a real symmetric matrix and checks for positive definiteness.

be varied, MTXPIN is called to calculate the gradient and second derivative of chi square with respect to the parameters. For chi-square given by equation 3-1, we have:

$$YZ(K) = -\frac{1}{2}\frac{\partial \chi^2}{\partial p_k} = \sum_{i=1}^{N_D}\left[\frac{\theta^i_{exp} - a^n\,\theta^i(p)}{\sigma^i_{exp}}\right]\left[\frac{a^n}{\sigma^i_{exp}}\frac{\partial\theta^i(p)}{\partial p_k}\right], \quad \text{(C-1)}$$

and

$$AZ(JK) = \frac{1}{2}\frac{\partial^2\chi^2}{\partial p_j \partial p_k} \simeq \sum_{i-1}^{N_D}\left[\frac{a^n}{\sigma^i_{exp}}\frac{\partial\theta^i(p)}{\partial p_j}\right]\left[\frac{a^n}{\sigma^i_{exp}}\frac{\partial\theta^i(p)}{\partial p_k}\right]. \quad \text{(C-2)}$$

AZ is also called the curvature matrix and is manifestly real symmetric. Its inverse is the error matrix. Because the derivatives are calculated by numerical differencing, the integrity of the second derivative matrix, AZ, is checked by looking for nonpositive diagonal elements, since these elements are related to the error in the respective parameters.[2] If necessary, any "bad" rows and columns are fixed and a message printed. Next, elements in AZ are scaled with the corresponding diagonal error when the error in a parameter is large while its value is small. After computing the inverse of the second derivative matrix,

$$AZI = (AZ)^{-1}, \quad \text{(C-3)}$$

and establishing its integrity, a revised set of parameter increments is calculated from which a new parameter set is obtained,

$$(p_k)_{new} = (p_k)_{old} + \Delta p_k \,. \quad \text{(C-4)}$$

According to Arndt and MacGregor,[2] the optimum parameter set, p, can be determined independently of the determination of the normalization parameters, a^n. Using the notation shown above, they show that the new set of parameter increments can be calculated from

$$(AZ) \cdot (DPZ) = YZ$$

or

$$\Delta p = DPZ = (AZI) \cdot (YZ) \quad . \tag{C-5}$$

The normalization parameters are calculated and revised by CHIPIN, while MTXPIN includes corrections to AZ required by this revision.

REFERENCES

1. G. Höhler, F. Kaiser, R. Koch, and E. Pietarinen, "Handbook of Pion-Nucleon Scattering," *Physics Data*, Vol. 12-1, 1979

2. R. A. Arndt and M. H. MacGregor, *Methods of Computational Physics*, Academic Press, New York, 1966, Vol. 6, p. 253

APPENDIX D. ANALYTIC STRUCTURE OF THE DISPERSION INTEGRAL

The dispersion function given by equation 3-5 and used in the energy-dependent parametrization can readily be evaluated and its analytic properties investigated as follows:

$$\pi C_\ell = \int_0^1 \frac{x^{\ell+1/2}}{x-z}\, dx \tag{D-1}$$

$$z = (W-W_t)/(W-W_s) \ . \tag{3-5}$$

First, a recursion relation is obtained:

$$\pi C_\ell = \int_0^1 \frac{x^{\ell+1/2}}{x-z}\, dx = \int_0^1 \frac{x^{\ell-1/2}}{x-z}\, [z + (x-z)]\, dx$$

$$= z \int_0^1 \frac{x^{\ell-1/2}}{x-z}\, dx + \int_0^1 x^{\ell-1/2}\, dx$$

$$\pi C_\ell = z\, \pi C_{\ell-1} + \frac{2}{2\ell+1} \tag{D-2}$$

that gives

$$\pi C_\ell = z^\ell\, \pi C_o + \sum_{j=1}^{\ell} \frac{2}{2j+1}\, z^{\ell-j}, \text{ for } \ell \neq 0 \ . \tag{D-3}$$

Next, the lowest order integral is evaluated:

$$\pi C_0 = \int_0^1 \frac{x^{1/2}}{x-z}\, dx$$

$$= \left[2\sqrt{x} + \sqrt{z}\, ln \left(\frac{\sqrt{x}-\sqrt{z}}{\sqrt{x}+\sqrt{z}} \right) \right]_0^1$$

$$= 2 + \sqrt{z}\left[ln\left(\frac{1-\sqrt{z}}{1+\sqrt{z}}\right) - i\pi(1+2n)\right]$$

$$\pi C_o = 2 + \sqrt{z}\left[ln\left(\frac{1-\sqrt{z}}{1+\sqrt{z}}\right) - i\pi\right] \qquad \text{(D-4)}$$

when the principal value (n = 0) is taken.

Because $\sqrt{z}$ may be complex, we expand the logarithm function to facilitate its evaluation and elucidate its structure.

$$ln(a+ib) = ln\left(\sqrt{a^2+b^2}\right) + i\left(tan^{-1}\frac{a}{b} + 2\pi n\right) .$$

Upon continuing to use the principal value,

$$\pi C_o = 2 + \sqrt{z}\left(ln\left|\frac{1-\sqrt{z}}{1+\sqrt{z}}\right| - i\pi\right) + i\sqrt{z}\ tan^{-1}\ \frac{Im\left(\frac{1-\sqrt{z}}{1+\sqrt{z}}\right)}{Re\left(\frac{1-\sqrt{z}}{1+\sqrt{z}}\right)} . \qquad \text{(D-5)}$$

For real $\sqrt{z}$ with $-1 < \sqrt{z} < 1$, the inverse tangent vanishes; while for $\sqrt{z} < -1$ or $\sqrt{z} > 1$, it contributes "$-\pi$." Together, equations D-3 and D-5 constitute an explicit evaluation of the dispersion integral, equation 3-5. Although we have chosen to take the principal value of the logarithm, there still remains an ambiguity in the choice of sign for the square root function. This ambiguity will be used to reveal different sheets of the scattering amplitude in the complex W-plane.

Now, we will examine C_ℓ more closely. For each of the three channels being utilized in this work (equation 3-5 ff), W_s is real. For the elastic channel, W_t is also real, but the imaginary components

in the masses of the unstable delta and eta result in complex values of W_t and, hence, also of z for each of the two inelastic channels.

Below a channel's subtraction point, we have $W \leq W_s < \mathrm{Re}(W_t)$, and z lies in the first quadrant of the complex z-plane with $\mathrm{Re}\ z \geq 1$, $\mathrm{Im}(z) \geq 0$. For the elastic channel with real W_t ($\mathrm{Im}\ z = 0$), we have

$$\pi C_o = 2 + \sqrt{z}\left(ln\left|\frac{1-\sqrt{z}}{1+\sqrt{z}}\right| - 2\pi i\right)$$

$$\pi C_\ell = 2z^\ell + \sum_{j=1}^{\ell} \frac{2}{2j+1} z^{\ell-j} + z^{\ell+1/2}\left(ln\left|\frac{1-\sqrt{z}}{1+\sqrt{z}}\right| - 2\pi i\right). \tag{D-6}$$

Therefore, in the elastic channel for $W \leq W_s$,

$$Im(C_\ell) = -2z^{\ell+1/2}. \tag{D-7}$$

For the two inelastic channels, z is complex, and there is no simple reduction. Equations D-3 and D-4 must be used in their entirety.

Between the subtraction point and threshold, $W_s < W < \mathrm{Re}(W_t)$, and z will lie in the second quadrant with $\mathrm{Re}(z) \leq 0$, $\mathrm{Im}(z) \geq 0$. For the elastic channel, there is a simple reduction because z is strictly negative. If we write $z = -\gamma^2$ for real γ, then $\sqrt{z} = \pm i\gamma$ where the sign ambiguity in the square root is explicitly shown, and

$$\left(\frac{1-\sqrt{z}}{1+\sqrt{z}}\right) = \frac{1 \mp i\gamma}{1 \pm i\gamma} = \frac{1-\gamma^2 \mp 2i\gamma}{1+\gamma^2}$$

$$\pi C_o = 2 + \sqrt{z}\left(ln\left|\frac{1-\gamma^2 \mp 2i\gamma}{1+\gamma^2}\right| - i\pi\right) \mp i\sqrt{z}\ tan^{-1}\left(\frac{\mp 2\gamma}{1-\gamma^2}\right)$$

$$\pi C_o = 2 \pm \gamma \left[\pi + tan^{-1} \left(\frac{\pm 2\gamma}{1-\gamma^2} \right) \right] . \qquad \text{(D-8)}$$

Therefore, C_o and hence all C_ℓ's are real for $W_s < W < Re(W_t)$ in the elastic channel. The inelastic channels are again more complicated with $Im(C_\ell)$ nonvanishing.

Above channel threshold, $W > Re(W_t) > W_s$, and z will be in the fourth quadrant with $0 \leq Re(z) < 1$ and $Im(z) \leq 0$. For the elastic channel, there is again a simplification because $\sqrt{z}$ is real, and we have:

$$\pi C_o = 2 + \sqrt{z} \left(ln \left| \frac{1-\sqrt{z}}{1+\sqrt{z}} \right| - i\pi \right)$$

$$\pi C_\ell = 2z^\ell + z^{\ell+1/2} \left(ln \left| \frac{1-\sqrt{z}}{1+\sqrt{z}} \right| - i\pi \right) + \sum_{j=1}^{\ell} \frac{2}{2j+1} z^{\ell-j} \qquad \text{(D-9)}$$

and for the elastic channel with $W > Re(W_t)$ gives

$$Im(C_\ell) = -z^{\ell+1/2} . \qquad \text{(D-10)}$$

Let us now examine the threshold dependence of the dispersion integral. For a generalized, two-particle channel with masses M_1 and M_2 and center-of-mass momentum, q, we have $W_t = M_1 + M_2$. Just above the channel's threshold, q^2 will be small, and

$$\begin{aligned} W - W_t &= (\sqrt{M_1^2 + q^2} + \sqrt{M_2^2 + q^2}) - (M_1 + M_2) \\ &\approx q^2 (M_1 + M_2)/2M_1M_2 \\ W - W_s &= (W_t - W_s) + (W - W_t) \\ &\approx (W_t - W_s) + q^2(M_1 + M_2)/2M_1M_2 \quad . \end{aligned} \qquad \text{(D-11)}$$

These approximations give:

$$z = (W - W_t)/(W - W_s)$$

$$\approx q^2(M_1 + M_2)/[2M_1M_2(W_t - W_s) + q^2(M_1 + M_2)]$$

$$z \approx q^2(M_1 + M_2)/2M_1M_2(W_t - W_s) \quad . \qquad \text{(D-12)}$$

Using the masses following equation 3-5, we obtain $z = q^2A^2e^{2i\phi}$, where A and ϕ are given below.

CHANNEL	A (c/MeV)	ϕ (deg)
Elastic	5.25×10^{-3}	0.000
π-Δ	4.65×10^{-3}	-17.00
η-N	2.31×10^{-3}	-0.695

For the elastic channel with real M_1 and M_2 and, hence, small real $z(0 \leq z << 1)$, equation D-10 gives

$$Im(C_\ell) = -\sqrt{z}\, z^\ell \quad . \qquad \text{(D-13)}$$

If the negative sign of the square root is chosen, then just above threshold we have:

$$Im(C_\ell) = |z^{\ell+1/2}| = [q^2 (5.25 \times 10^{-3})^2]^{\ell+1/2}$$

$$Im(C_\ell) \propto q^{2\ell+1} \quad . \qquad \text{(D-14)}$$

That this is the threshold dependence needed to identify $Im(C_\ell)$ as the phase space factor for the elastic channel, providing the T-matrix with its proper threshold dependence, will follow from equation 3-4. For the two-channel K-matrix appropriate for all waves except S_{11},

equation 3-4 yields:

$$T_e = Im(C_e)\left[\frac{K_{ee} - C_i(K_{ee}K_{11} - K_{e1}^2)}{(1 - C_1K_{11}) - C_eK_{ee} + C_eC_i(K_{ee}K_{11} - K_{e1}^2)}\right] . \qquad \text{(D-15)}$$

Since the expression in the brackets does not vanish at threshold, both $Im(C_e)$ and T_e have an identical threshold dependence of $q^{2\ell+1}$. Similar arguments will hold for the S_{11} wave.

For the inelastic channels, the situation is very different because z is complex. To find the threshold dependence, we need only to find the terms having the lowest powers of $\sqrt{z}$. With small q, equations D-3 and D-5 give:

$$\pi C_o \simeq 2 - i\pi\sqrt{z}$$

$$\approx 2 - i\pi(qA\cos\phi)$$

$$\pi C_\ell \simeq \frac{2}{2\ell+1} + \frac{2}{2\ell-1}\, z$$

$$\approx \frac{2}{2\ell+1} + i\,\frac{2}{2\ell-1}\,(q^2A^2 \sin 2\phi) . \qquad \text{(D-16)}$$

If the negative sign of the square root is again taken,

$$Im(C_o) \simeq (qA\cos\phi) \propto q$$

$$Im(C_\ell) \simeq \frac{2q^2A^2}{\pi(2\ell+1)} \sin 2\phi \propto q^2 , \qquad \text{(D-17)}$$

and the inelastic channel has a threshold dependence of $q^{2\ell+1}$ only for S-waves.

When examining the complex topology of the scattering amplitudes, W is continued analytically off the real axis resulting in complex z. The best manner to understand the structure of C_ℓ is by examining the contour plots shown in Figures D-1 through D-8. The real and imaginary parts of C_0 and C_1 are displayed for both the elastic π-N and the inelastic π-Δ channels. C_0 is also shown in Figures D-7 and D-8 for the inelastic η-N channel. For the elastic channel, only the physical sheet of complex W is shown, while for the two inelastic channels, both the physical and unphysical sheets are shown. For convenience, each contour plot is shown covering the same size region of the complex W-plane with the zero contour identified by a "Z." The sign of the dispersion functions in each region of the plot is also identified.

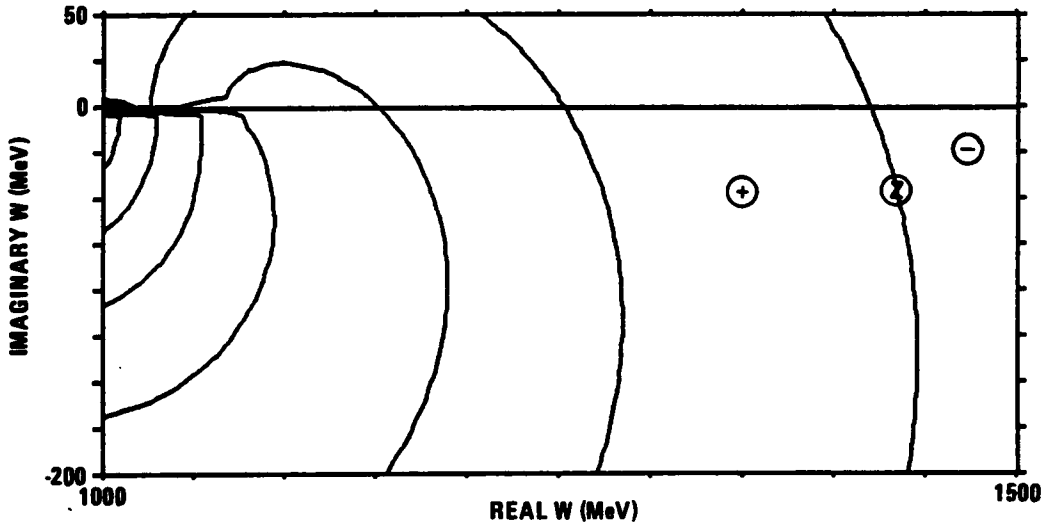

a. $\ell = 0$

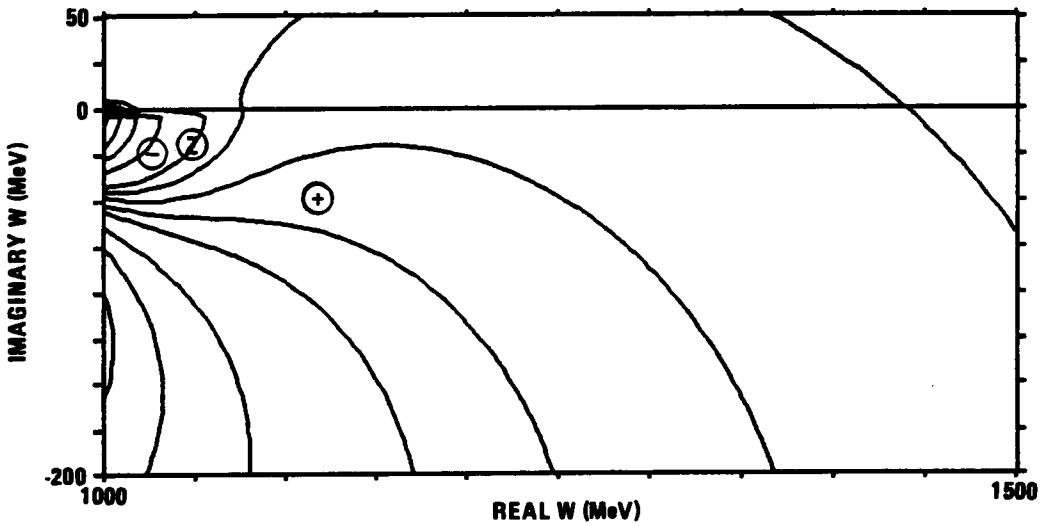

b. $\ell = 1$

FIGURE D-1. THE REAL PART OF ELASTIC CHANNEL DISPERSION FUNCTION (C_e) FOR THE PHYSICAL SHEET

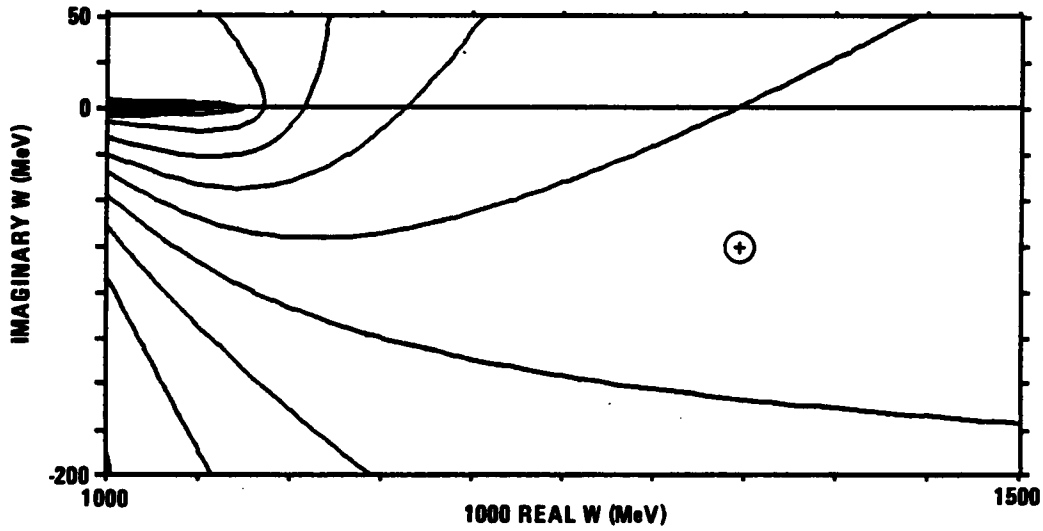

a. $\ell = 0$

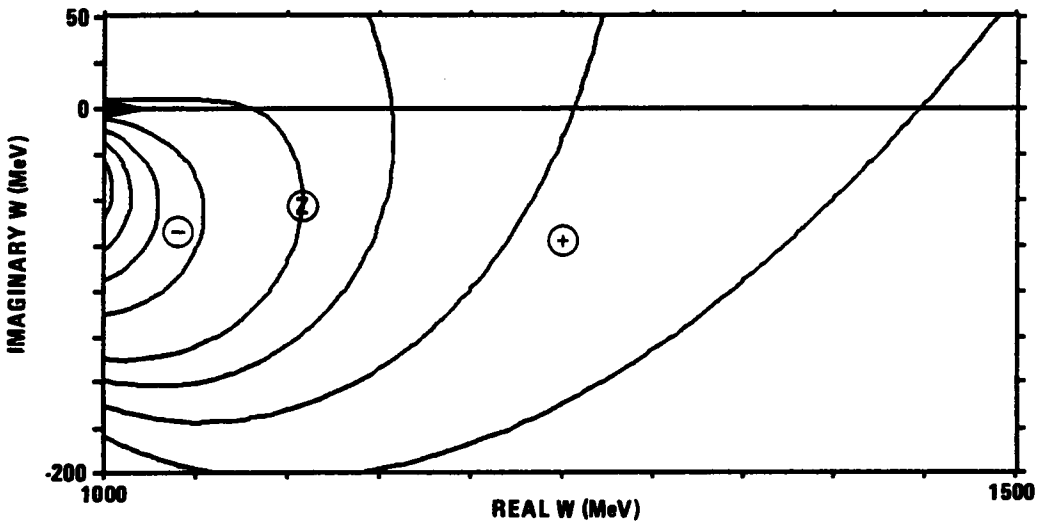

b. $\ell = 1$

FIGURE D-2. IMAGINARY PART OF ELASTIC CHANNEL DISPERSION FUNCTION (C_e) FOR THE PHYSICAL SHEET

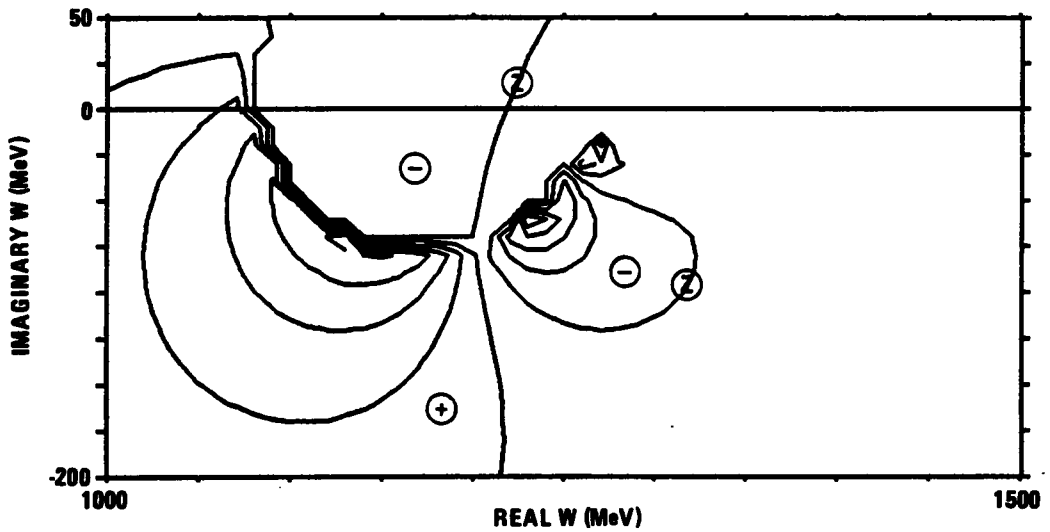

a. $\ell = 0$

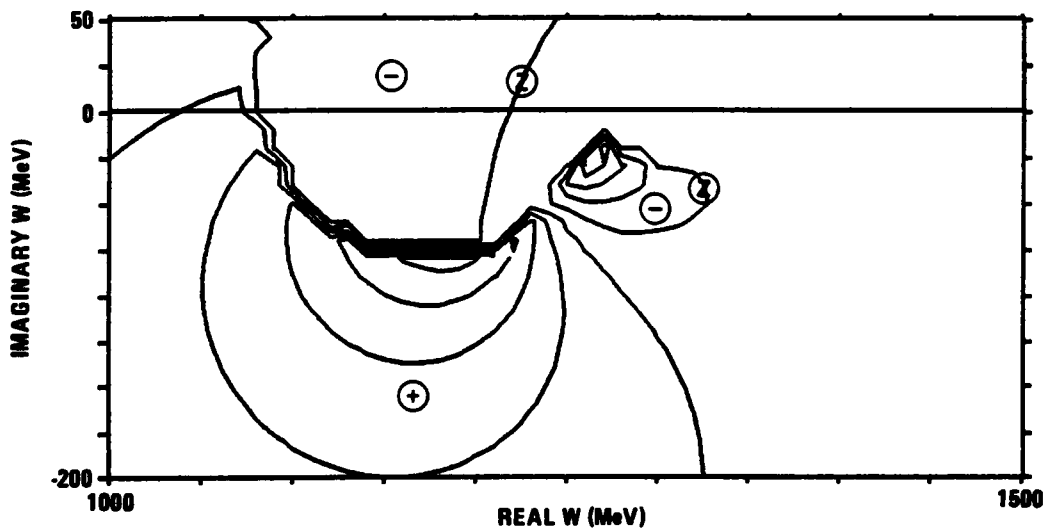

b. $\ell = 1$

FIGURE D-3. THE REAL PART OF π-Δ DISPERSION FUNCTION (C_I) FOR THE PHYSICAL SHEET

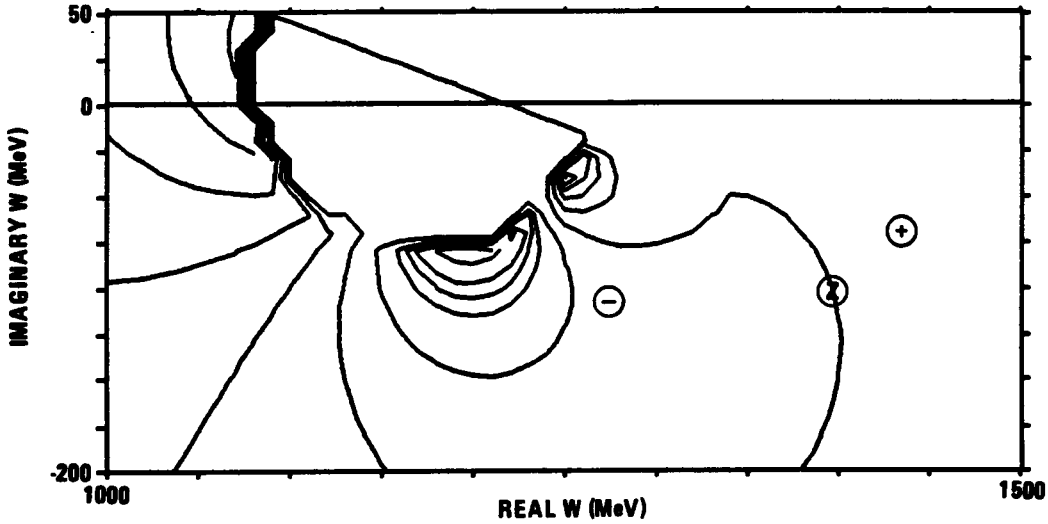

a. $\ell = 0$

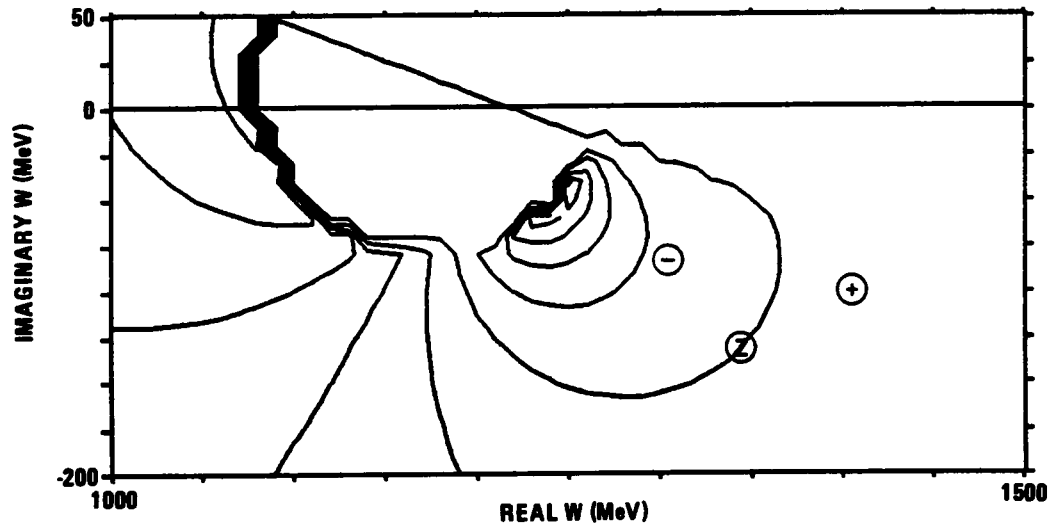

b. $\ell = 1$

FIGURE D-4. THE IMAGINARY PART OF π-Δ DISPERSION FUNCTION (C_j) FOR THE PHYSICAL SHEET

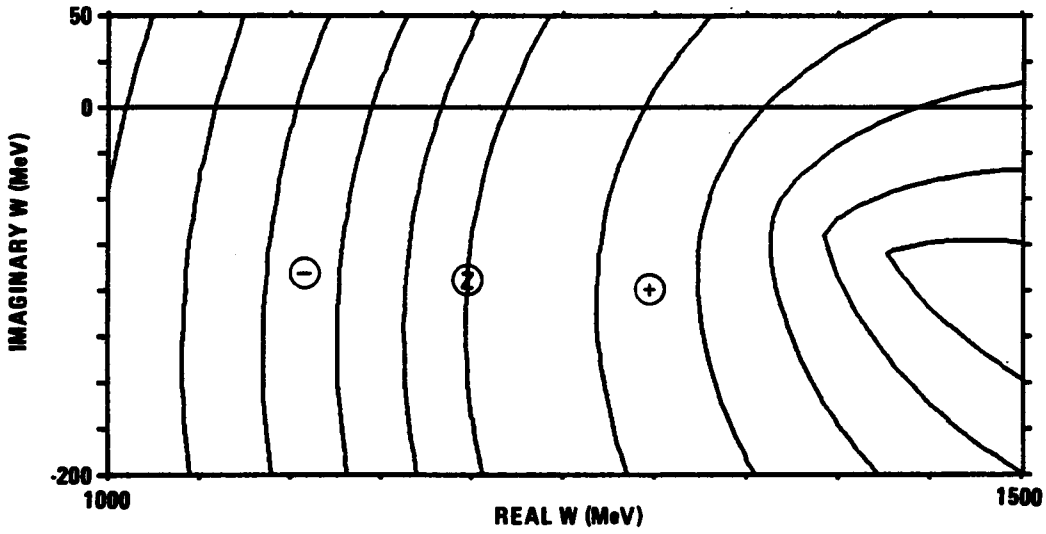

a. $\ell = 0$

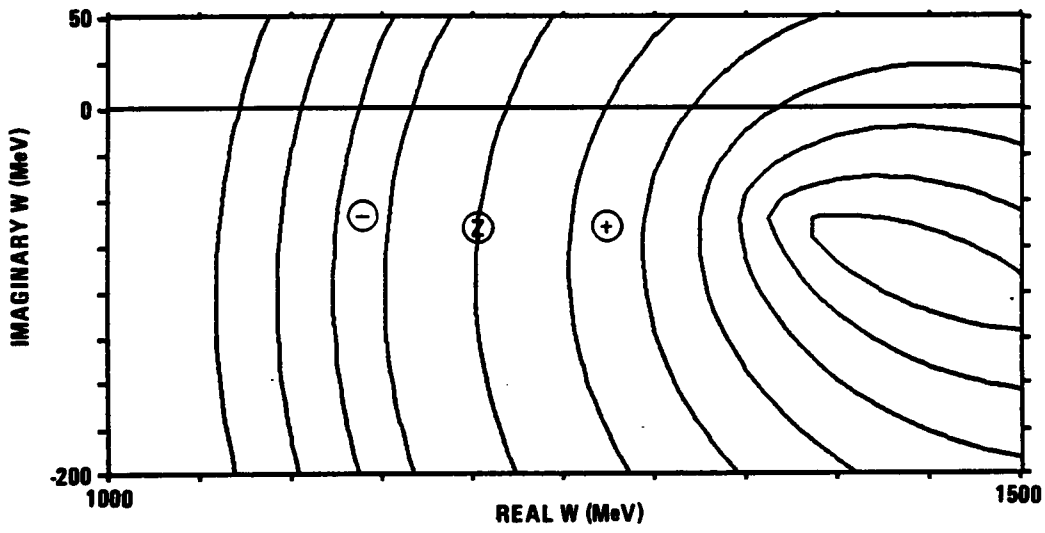

b. $\ell = 1$

FIGURE D-5. THE REAL PART OF π-Δ DISPERSION FUNCTION (C_1) FOR THE UNPHYSICAL SHEET

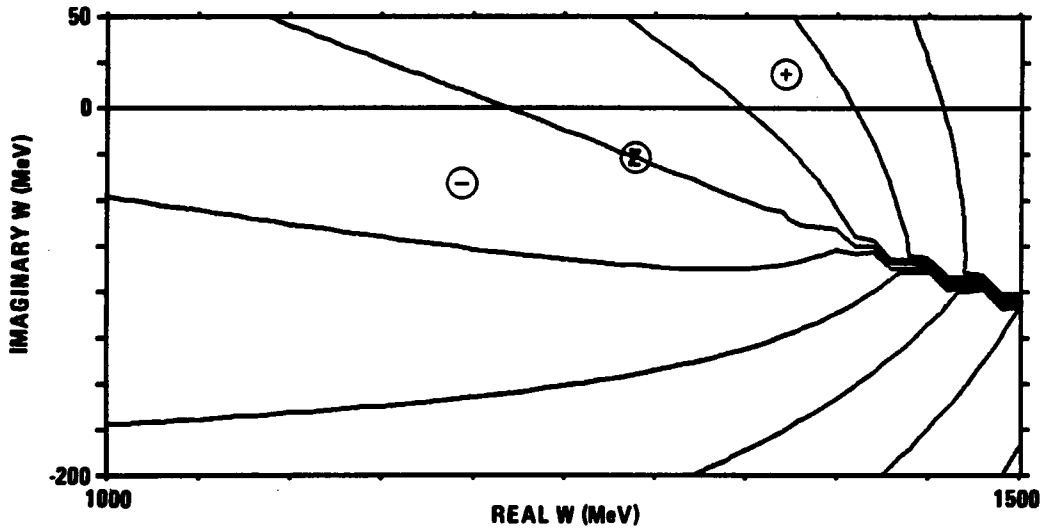

a. $\ell = 0$

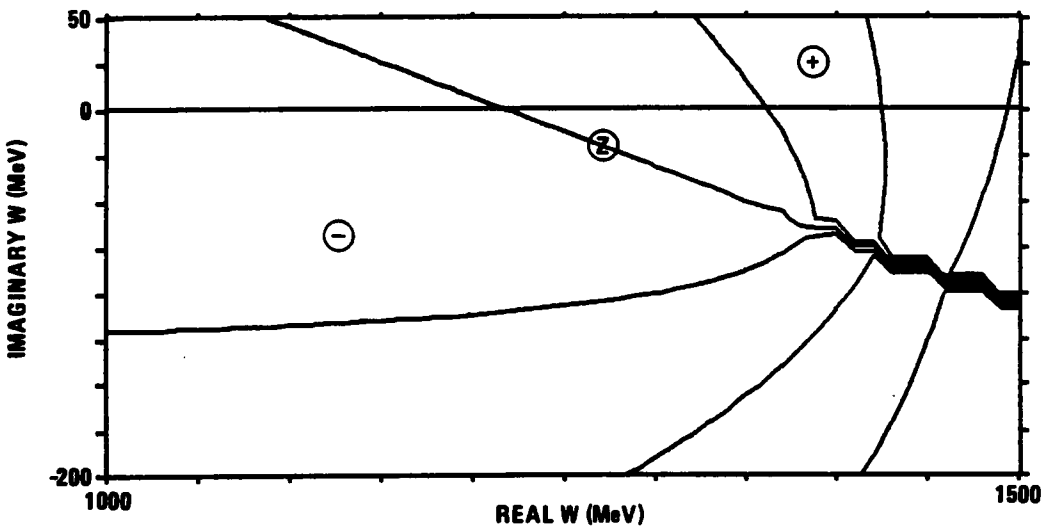

b. $\ell = 1$

FIGURE D-6. THE IMAGINARY PART OF THE π-Δ DISPERSION FUNCTION (C_1) FOR THE UNPHYSICAL SHEET

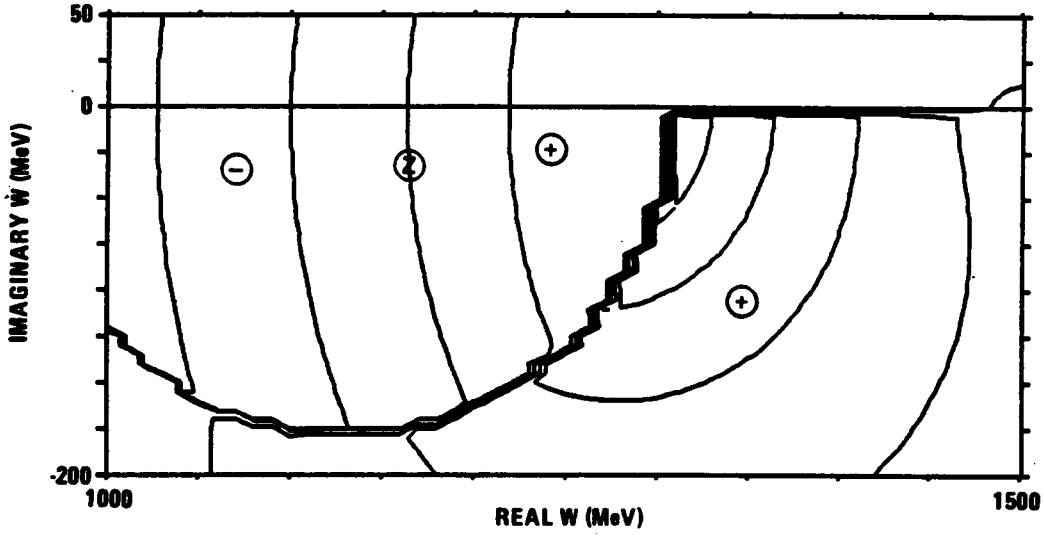

a. REAL PART

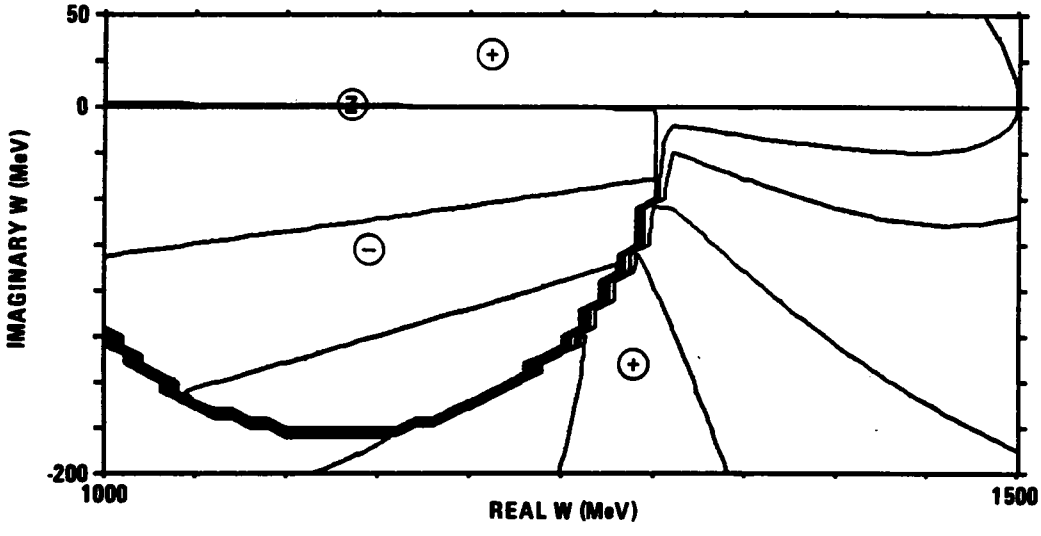

b. IMAGINARY PART

FIGURE D-7. S-WAVE DISPERSION FUNCTION FOR THE η-N CHANNEL ON THE PHYSICAL SHEET

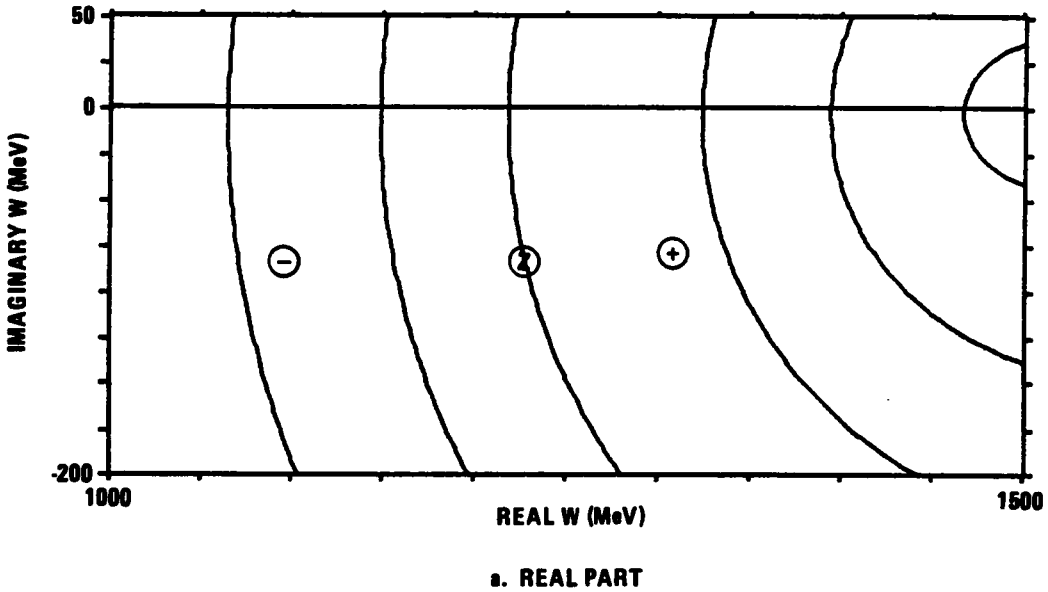

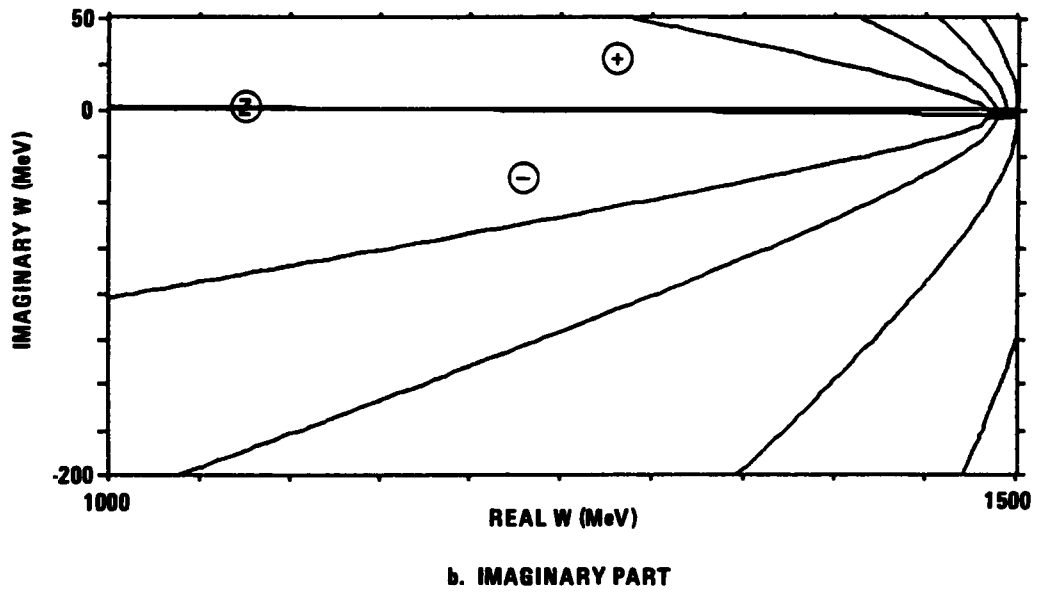

FIGURE D-8. S-WAVE DISPERSION FUNCTION FOR THE η-N CHANNEL ON THE UNPHYSICAL SHEET

APPENDIX E. PARTIAL-WAVE AMPLITUDES

The partial-wave amplitudes obtained from solution FP86 can be displayed in a variety of formats beyond the partial-wave T-matrices shown in Chapter 3. Figure E-1 provides Argand diagrams for each of the partial waves of interest here, S- through F-wave. Shown in Figure E-2 are the partial-wave cross sections,

$$\sigma_{total}^{\ell IJ} = \frac{4\pi\hbar^2}{q^2}\left(j+\frac{1}{2}\right) Im\left\{T_{IJ}^{\ell}\right\}$$

$$\sigma_{inelastic}^{\ell IJ} = \frac{4\pi\hbar^2}{q^2}\left(j+\frac{1}{2}\right)\left[Im\left\{T_{IJ}^{\ell}\right\} - |\,T_{IJ}^{\ell}\,|^2\right] ,$$

where q is the center-of-mass momentum. The energy dependence of the phase shift and the inelasticity or actually one minus the inelasticity squared are provided in the plots of Figure E-3. For all the plots in this appendix, the energy runs from 1080 to 1780 MeV in the center of mass.

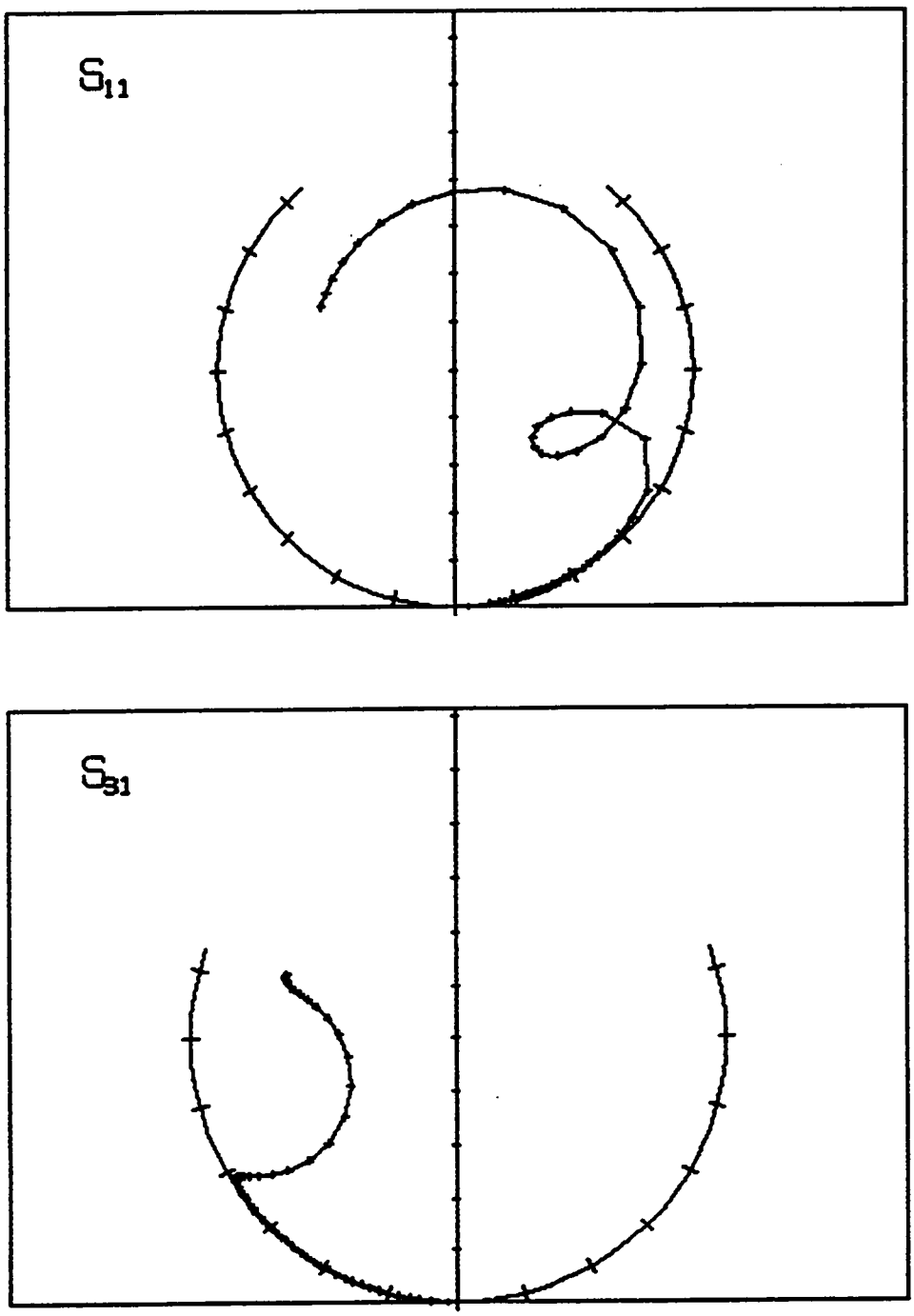

FIGURE E-1. PARTIAL-WAVE ARGAND DIAGRAM FOR CENTER-OF-MASS ENERGY FROM 1080 TO 1780 MeV (Sheet 1 of 7)

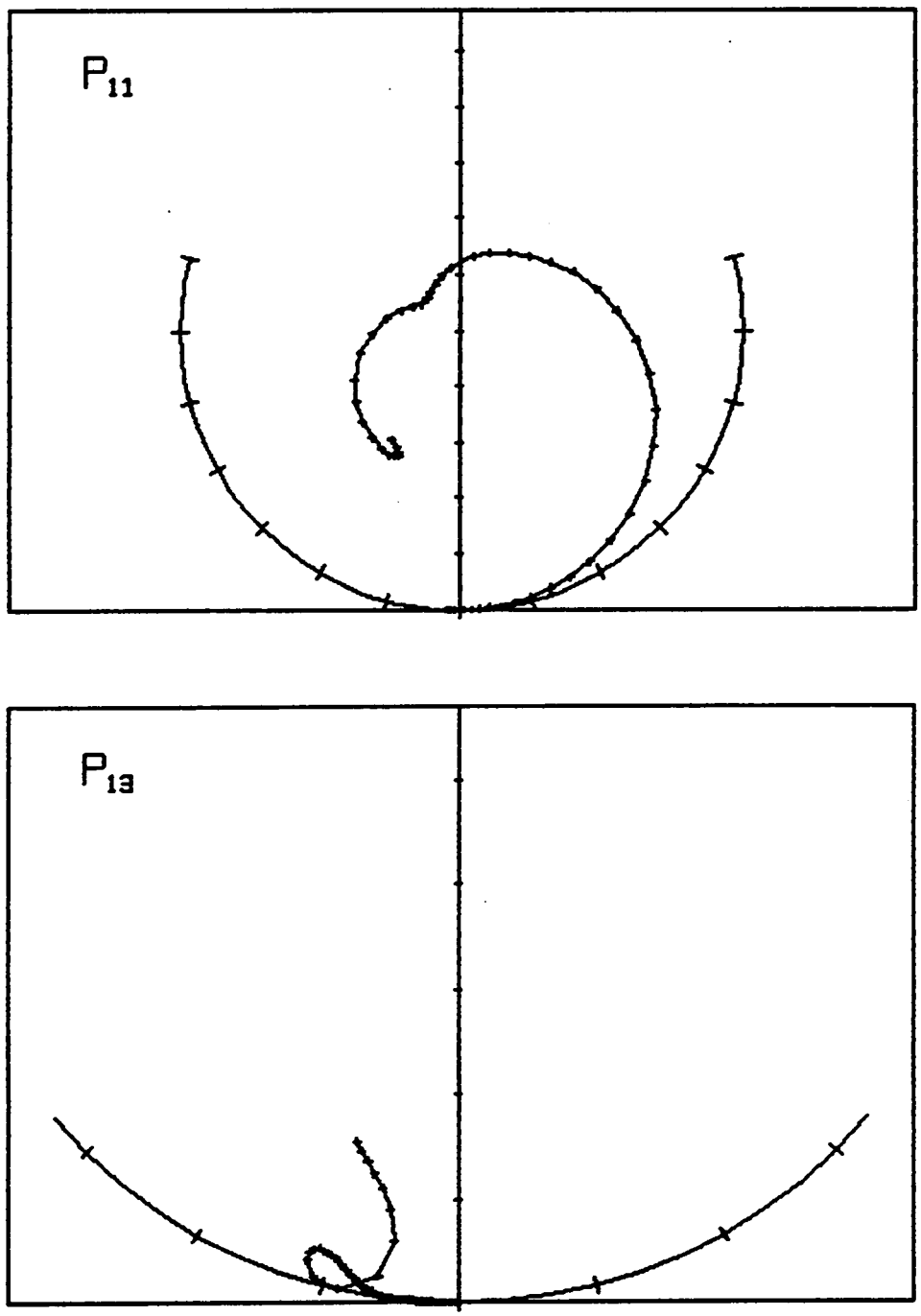

FIGURE E-1. PARTIAL-WAVE ARGAND DIAGRAM FOR CENTER-OF-MASS ENERGY FROM 1080 TO 1780 MeV (Sheet 2 of 7)

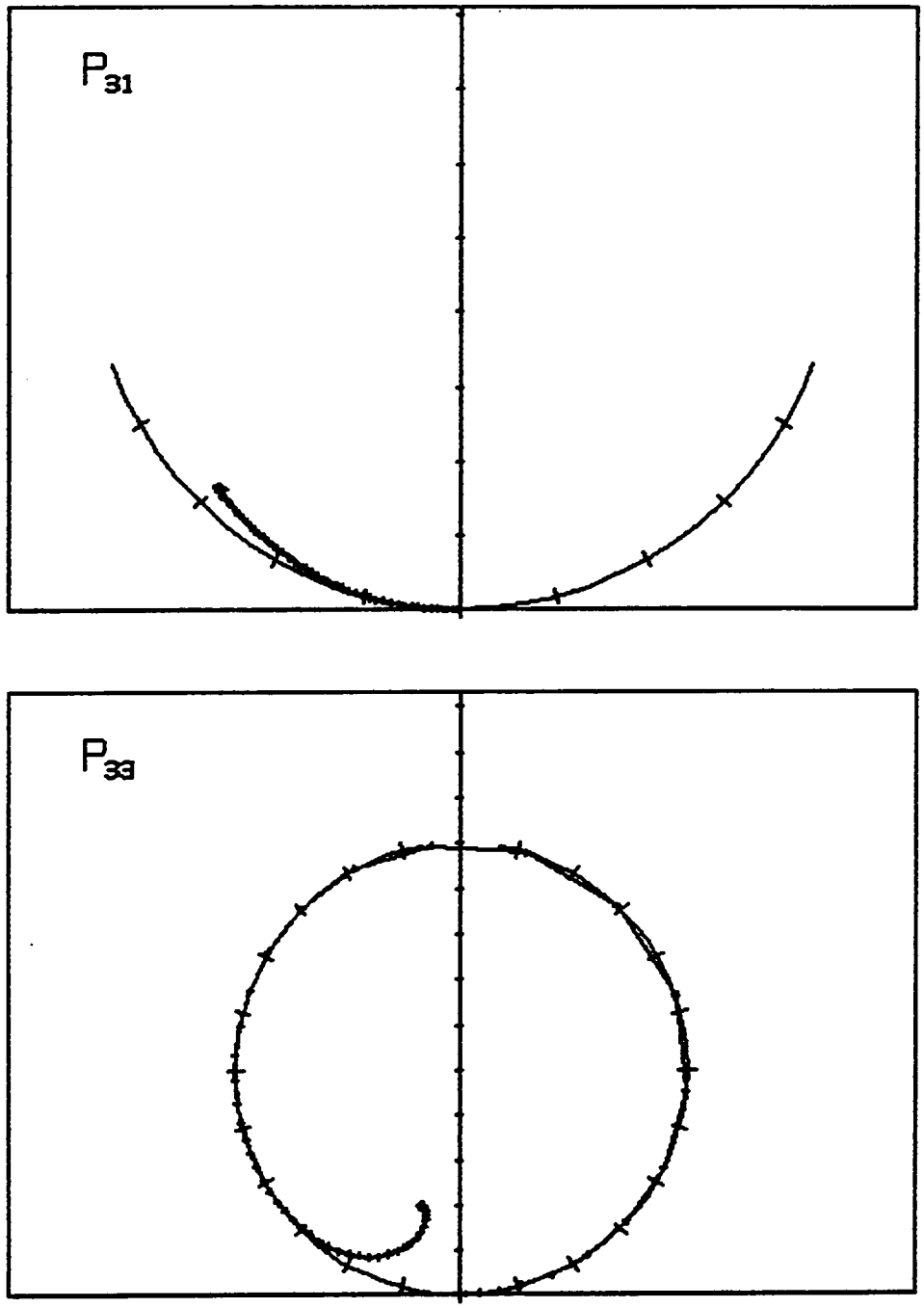

FIGURE E-1. PARTIAL-WAVE ARGAND DIAGRAM FOR CENTER-OF-MASS ENERGY FROM 1080 TO 1780 MeV (Sheet 3 of 7)

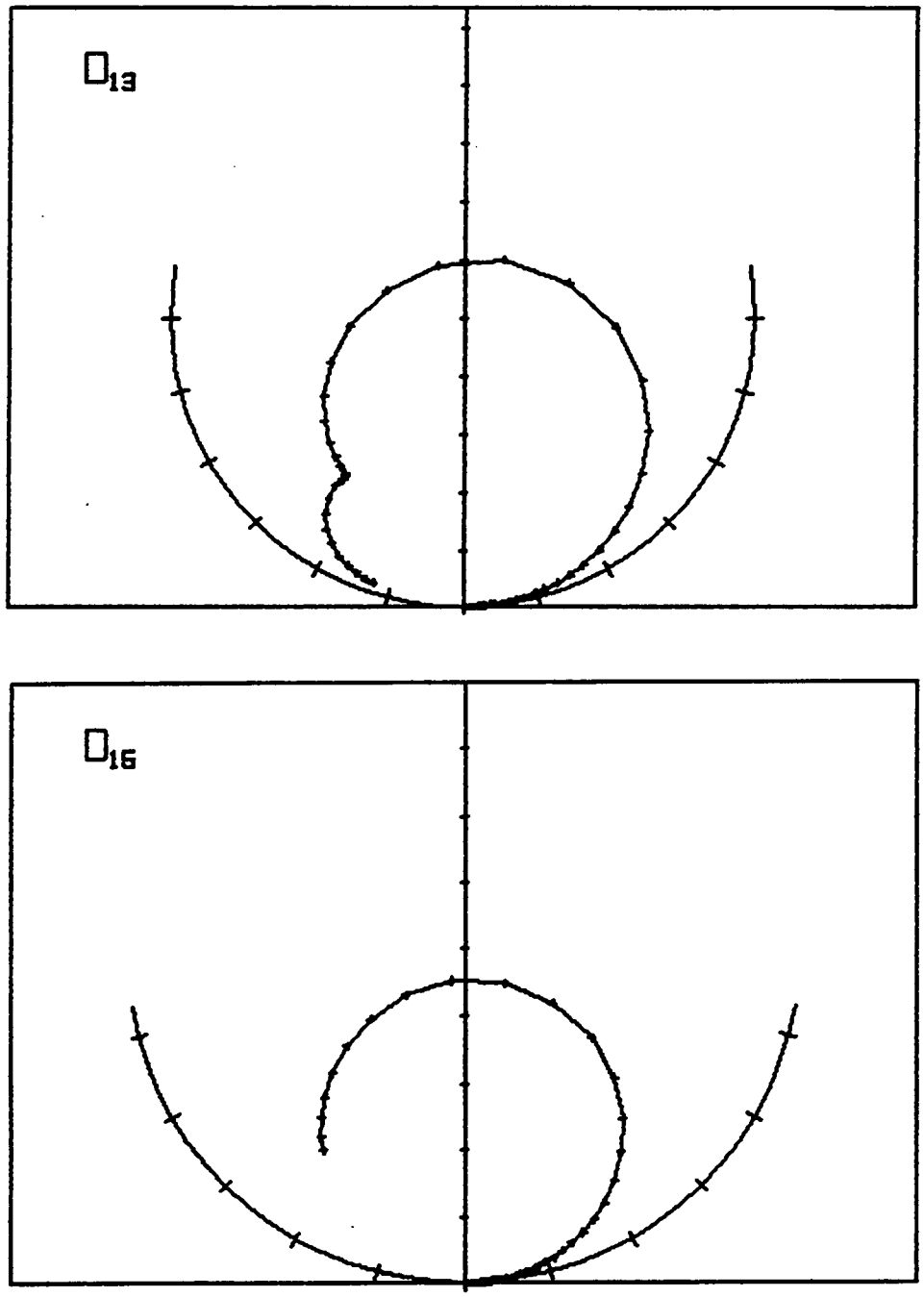

FIGURE E-1. PARTIAL-WAVE ARGAND DIAGRAM FOR CENTER-OF-MASS ENERGY FROM 1080 TO 1780 MeV (Sheet 4 of 7)

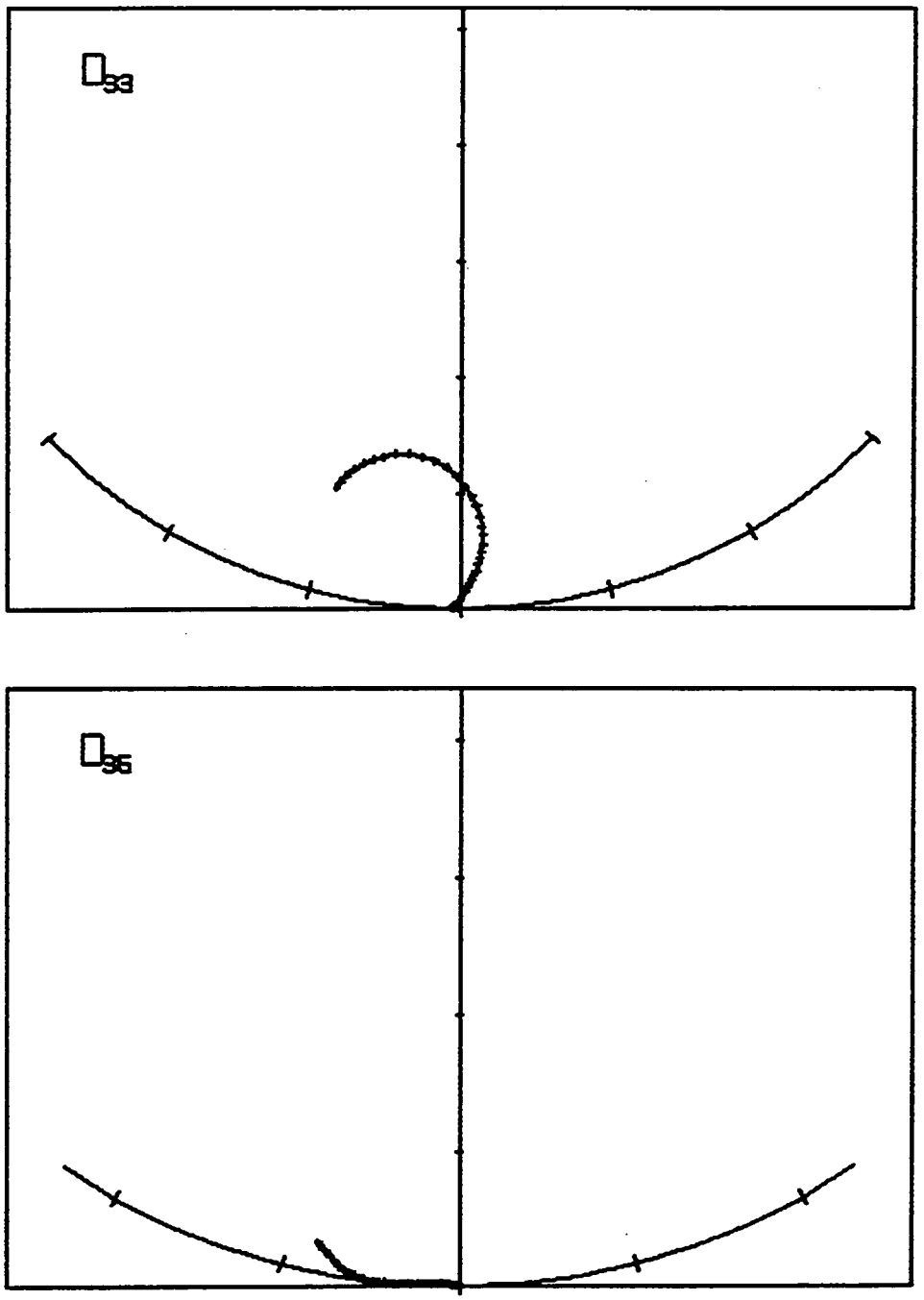

FIGURE E-1. PARTIAL-WAVE ARGAND DIAGRAM FOR CENTER-OF-MASS ENERGY FROM 1080 TO 1780 MeV (Sheet 5 of 7)

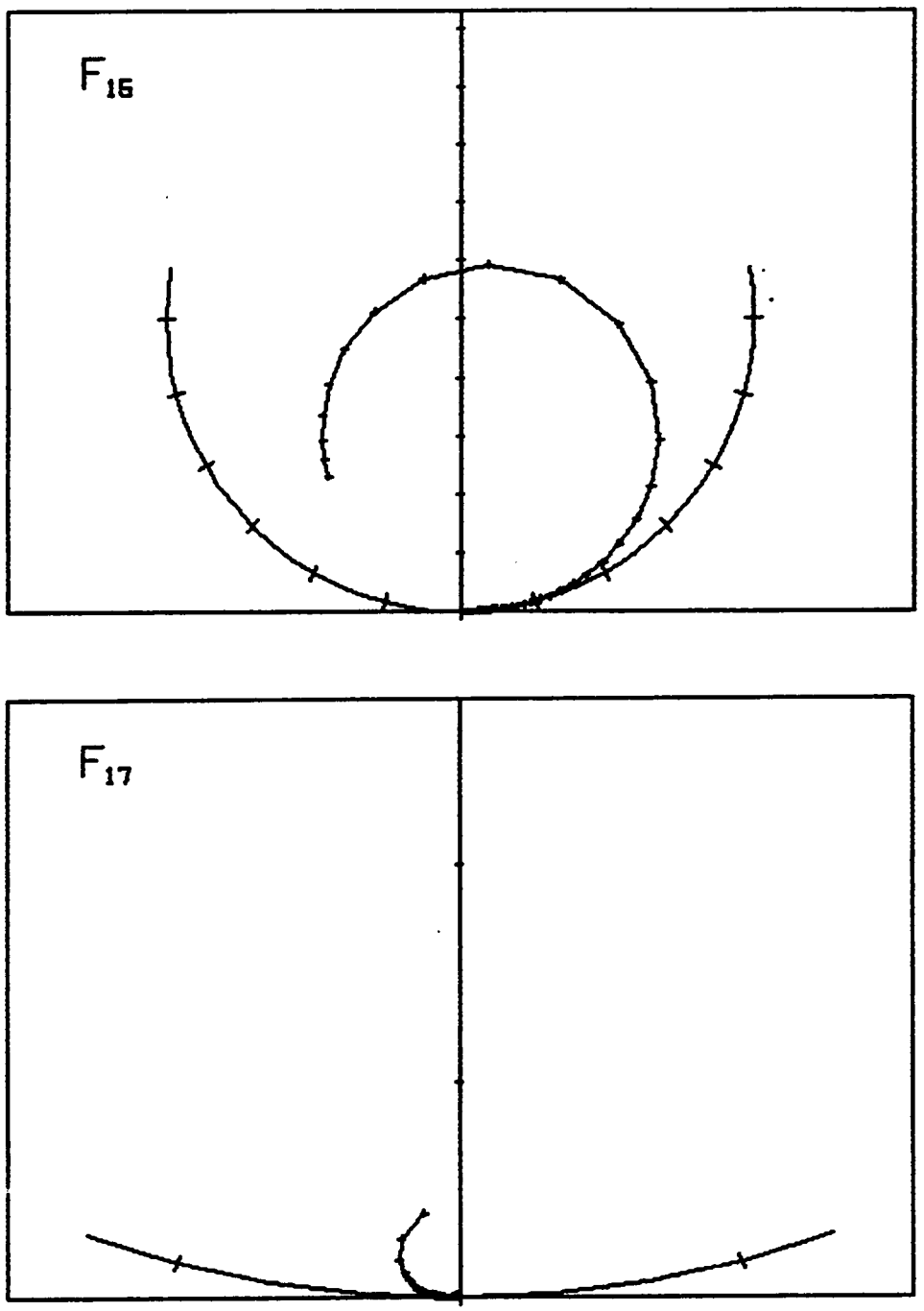

FIGURE E-1. PARTIAL-WAVE ARGAND DIAGRAM FOR CENTER-OF-MASS ENERGY FROM 1080 TO 1780 MeV (Sheet 6 of 7)

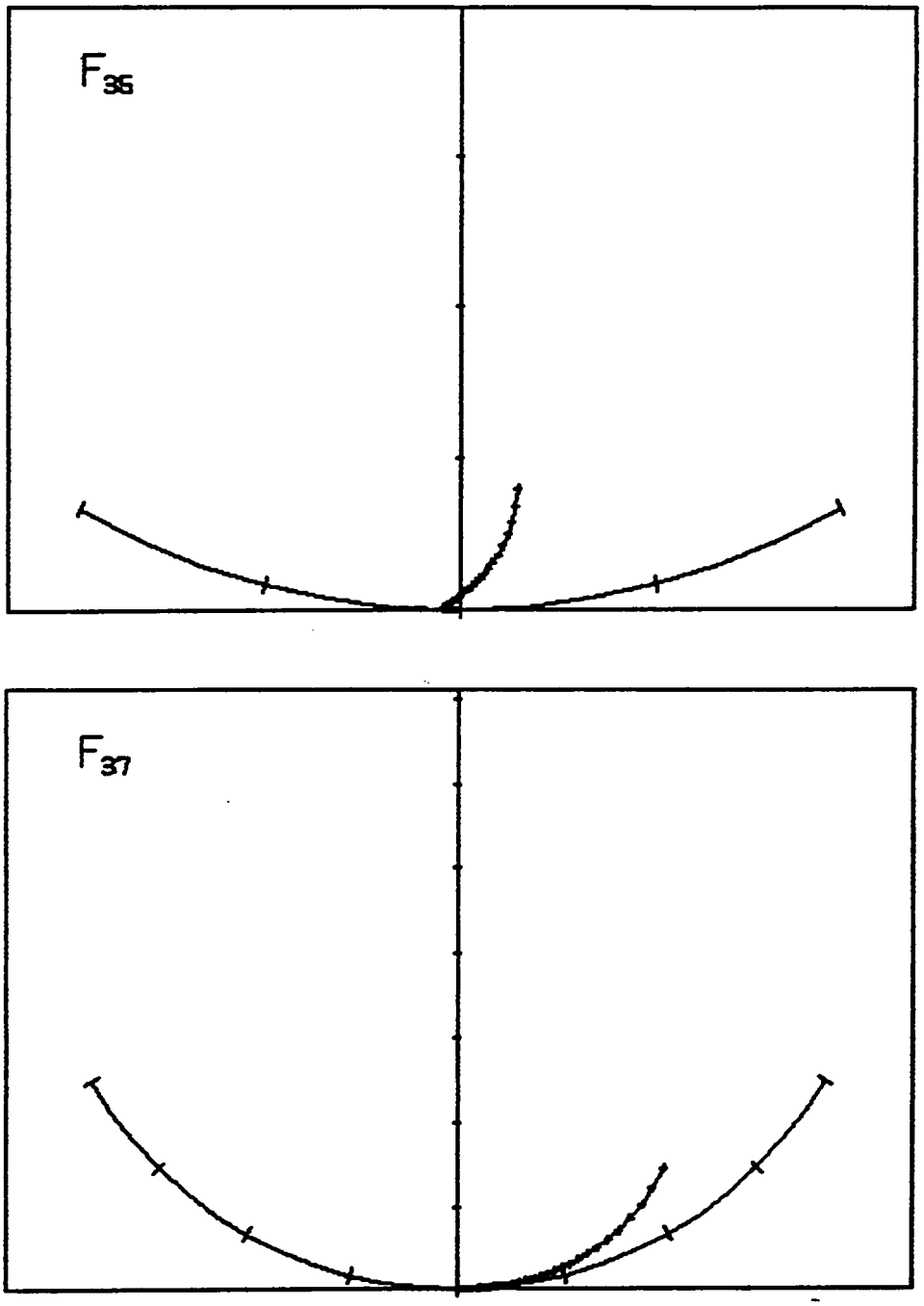

FIGURE E-1. PARTIAL-WAVE ARGAND DIAGRAM FOR CENTER-OF-MASS ENERGY FROM 1080 TO 1780 MeV (Sheet 7 of 7)

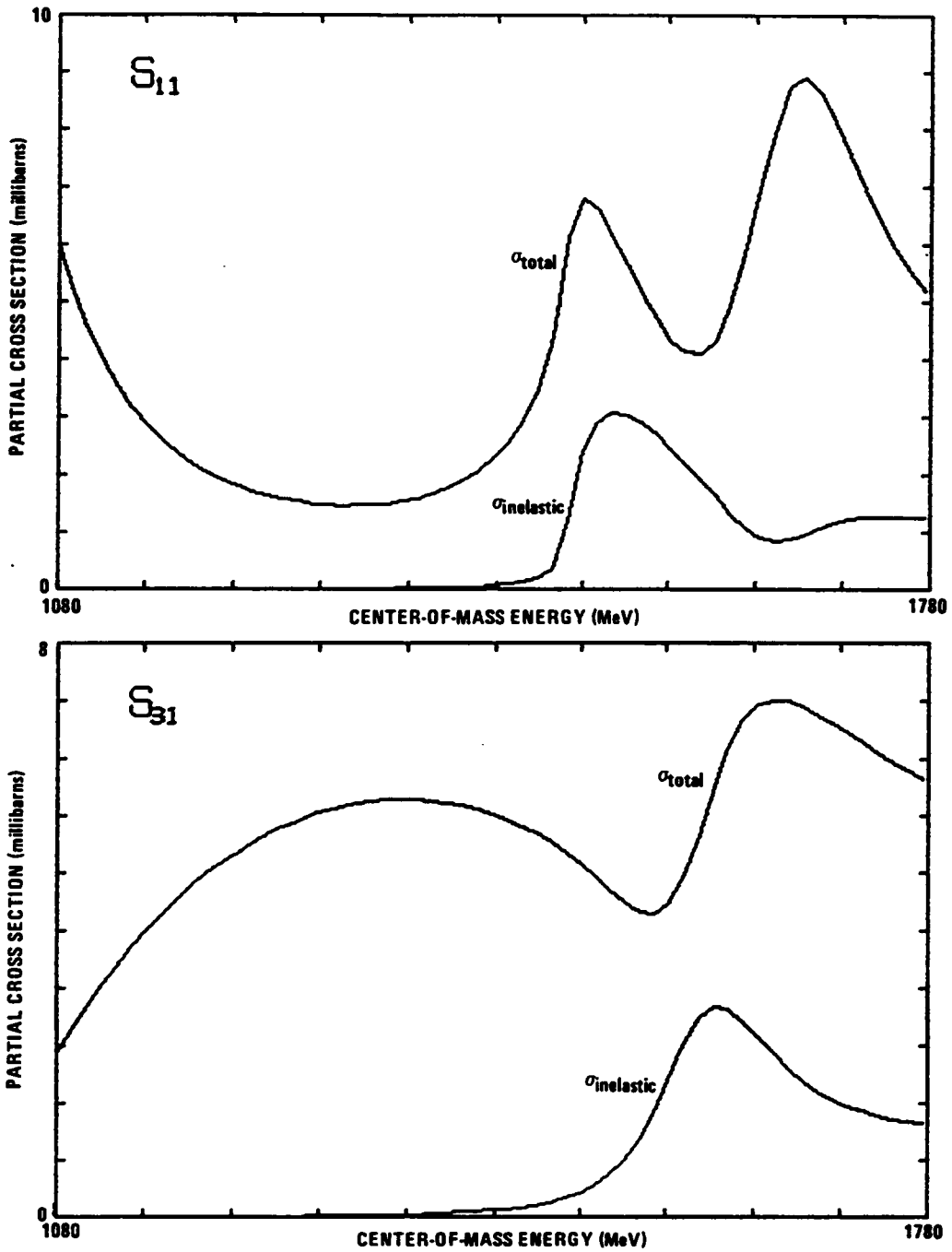

FIGURE E-2. PARTIAL-WAVE CROSS SECTION FOR CENTER-OF-MASS ENERGY FROM 1080 TO 1780 MeV (Sheet 1 of 7)

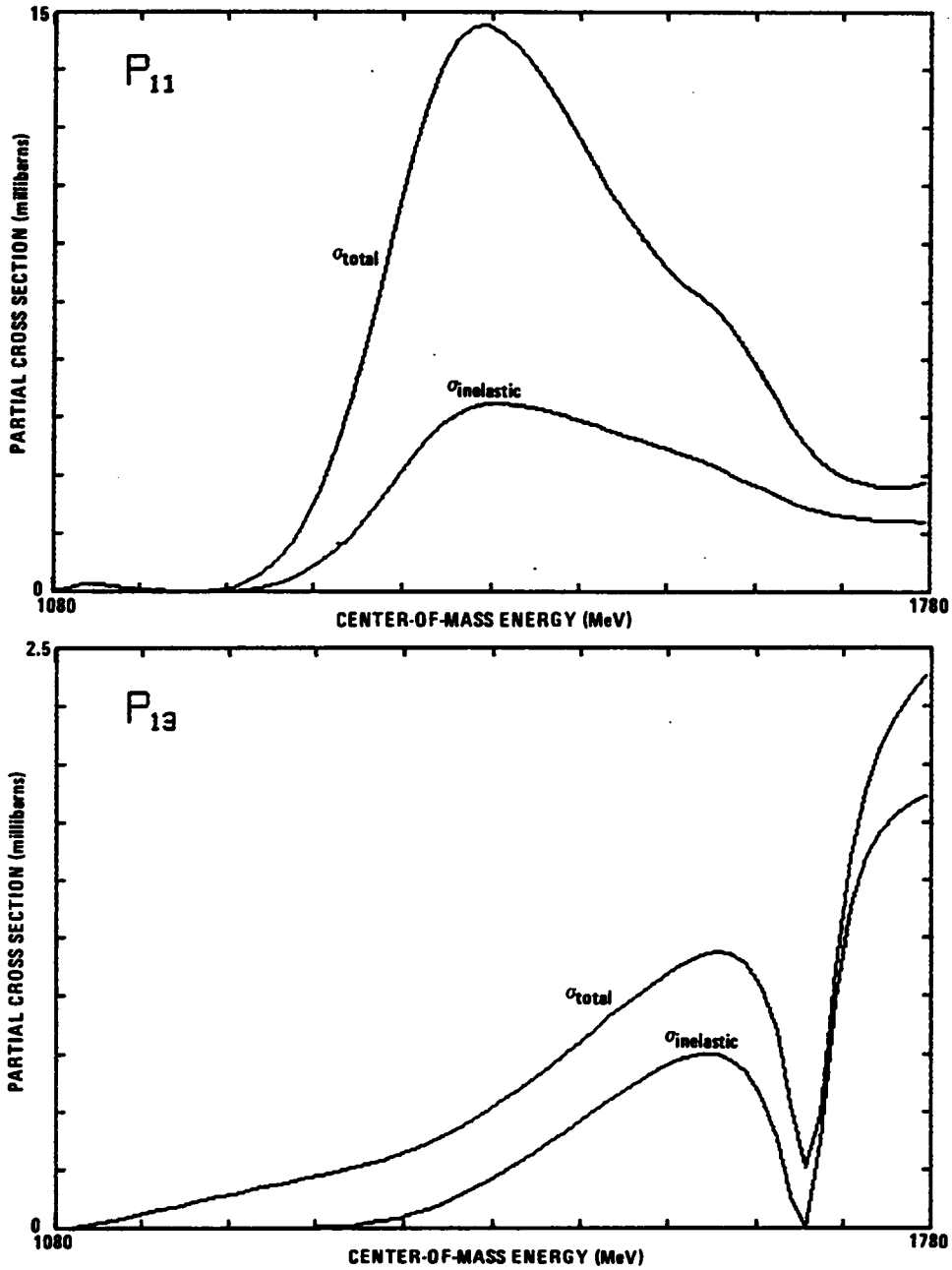

FIGURE E-2. PARTIAL-WAVE CROSS SECTION FOR CENTER-OF-MASS ENERGY FROM 1080 TO 1780 MeV (Sheet 2 of 7)

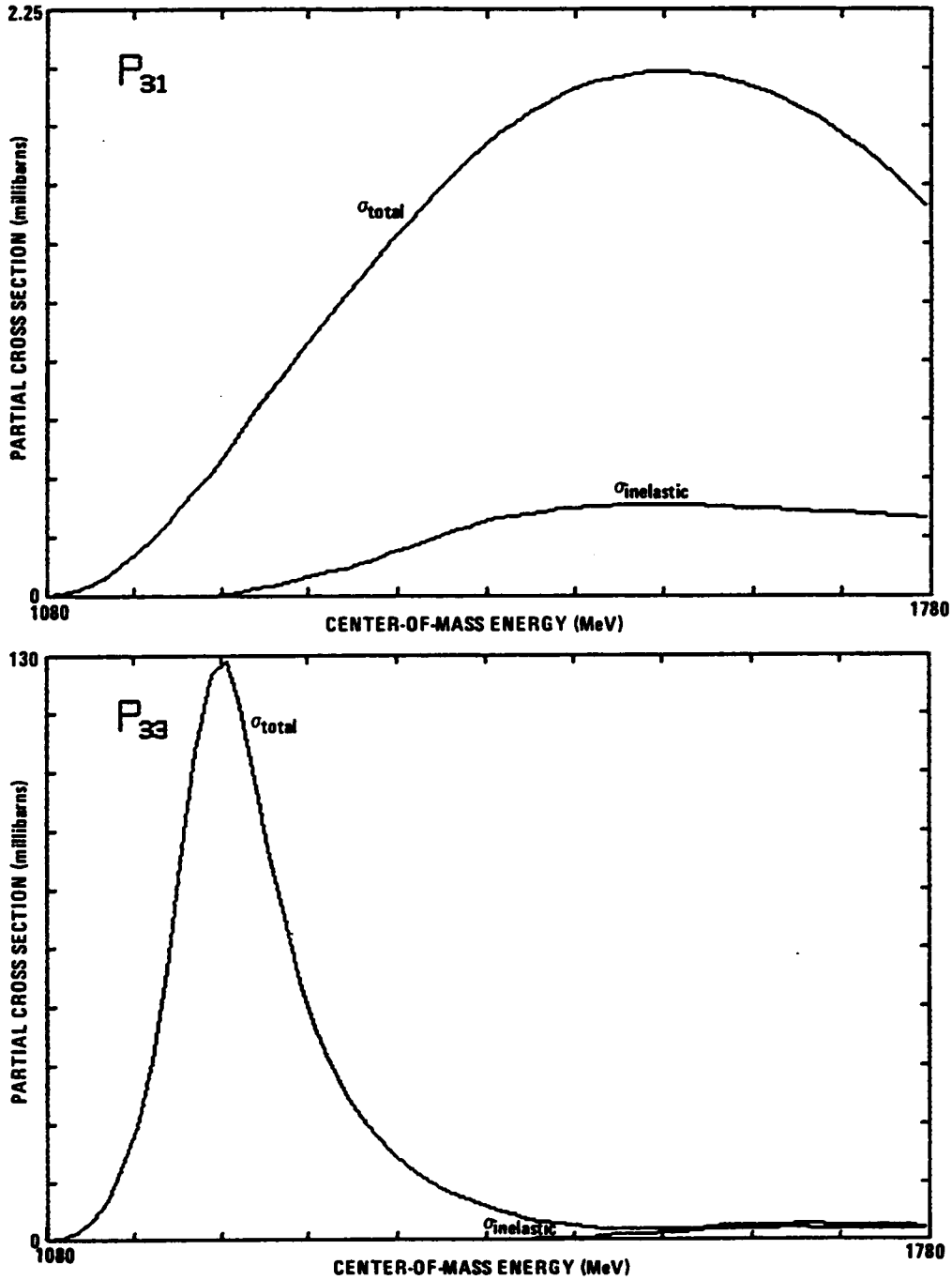

FIGURE E-2. PARTIAL-WAVE CROSS SECTION FOR CENTER-OF-MASS ENERGY FROM 1080 TO 1780 MeV (Sheet 3 of 7)

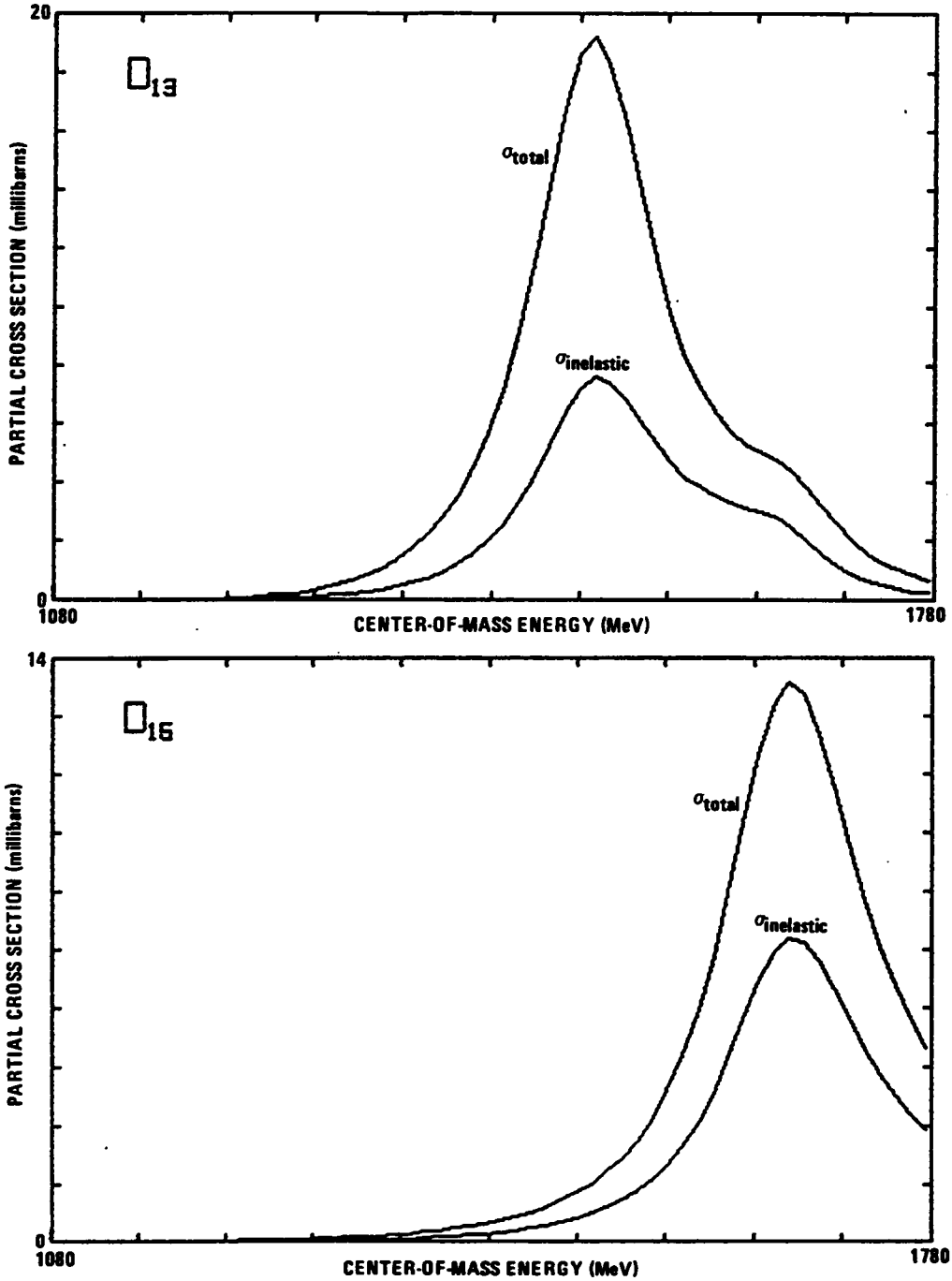

FIGURE E-2. PARTIAL-WAVE CROSS SECTION FOR CENTER-OF-MASS ENERGY FROM 1080 TO 1780 MeV (Sheet 4 of 7)

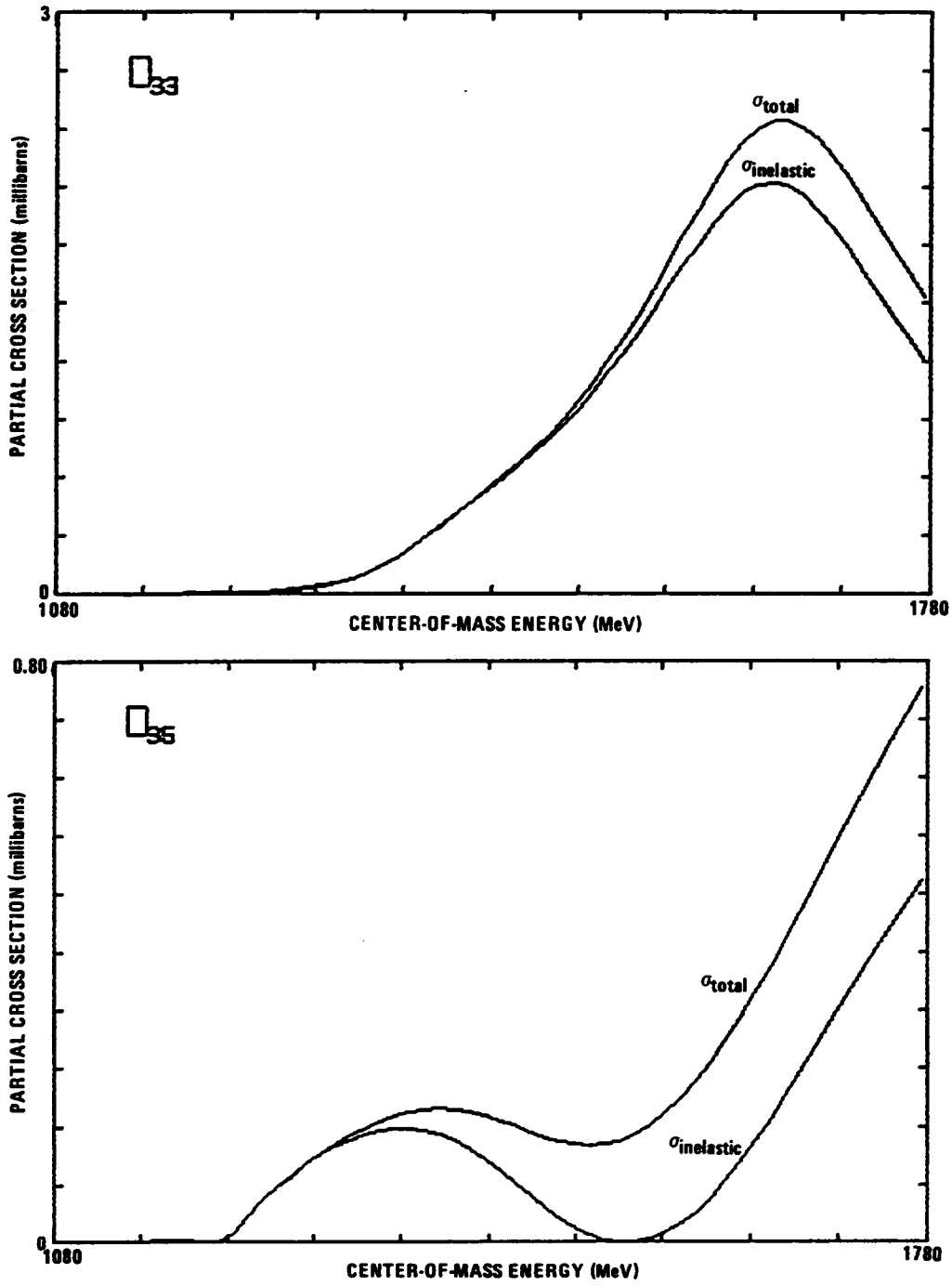

FIGURE E-2. PARTIAL-WAVE CROSS SECTION FOR CENTER-OF-MASS ENERGY FROM 1080 TO 1780 MeV (Sheet 5 of 7)

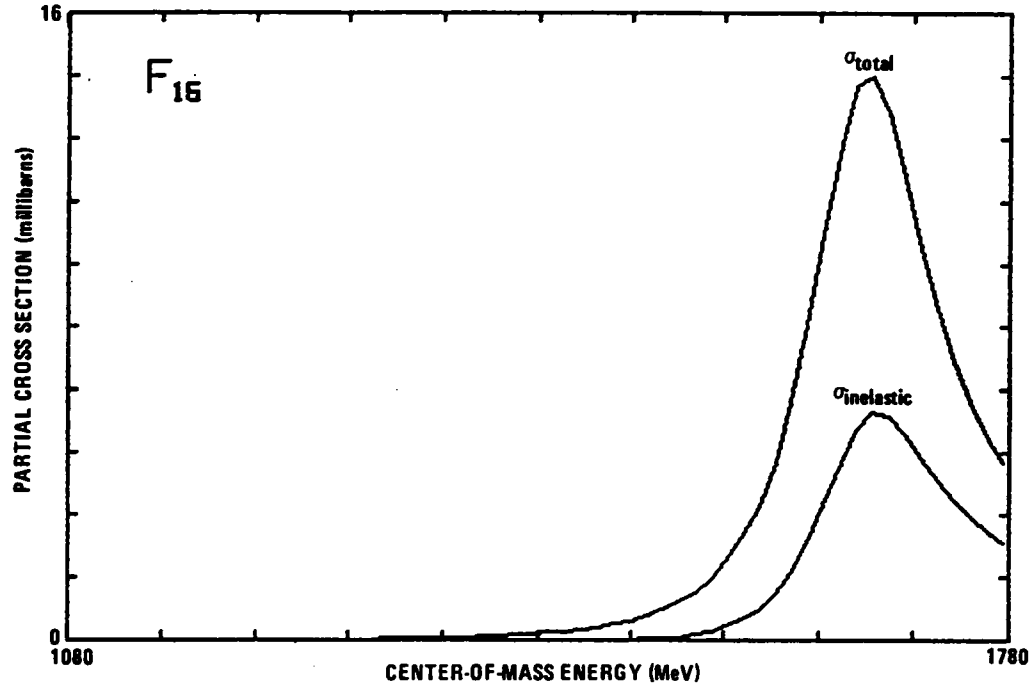

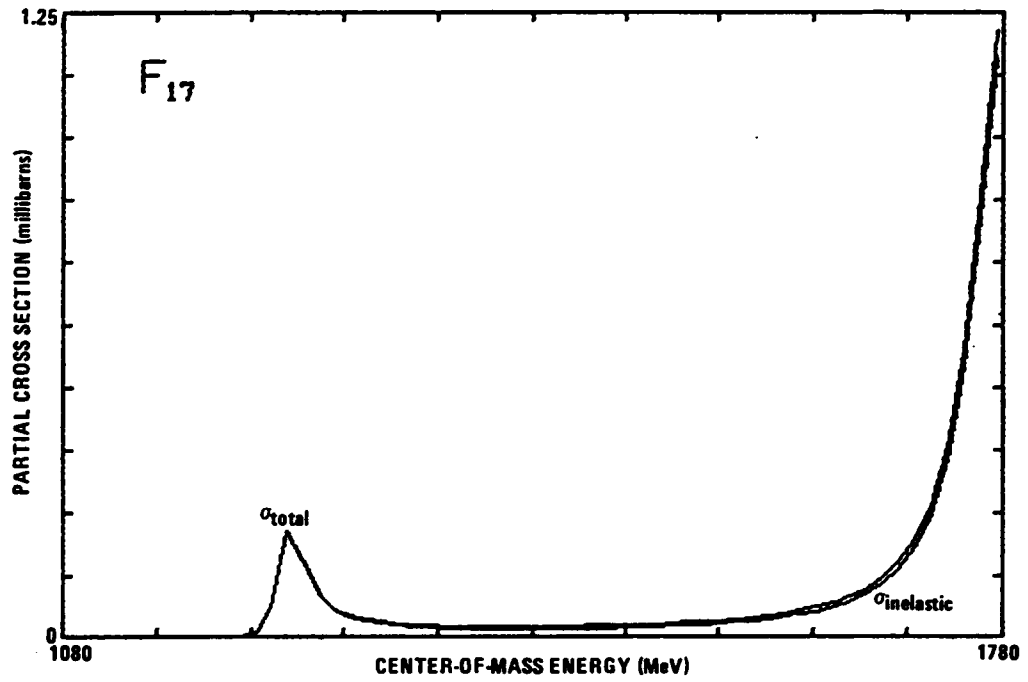

FIGURE E-2. PARTIAL-WAVE CROSS SECTION FOR CENTER-OF-MASS ENERGY FROM 1080 TO 1780 MeV (Sheet 6 of 7)

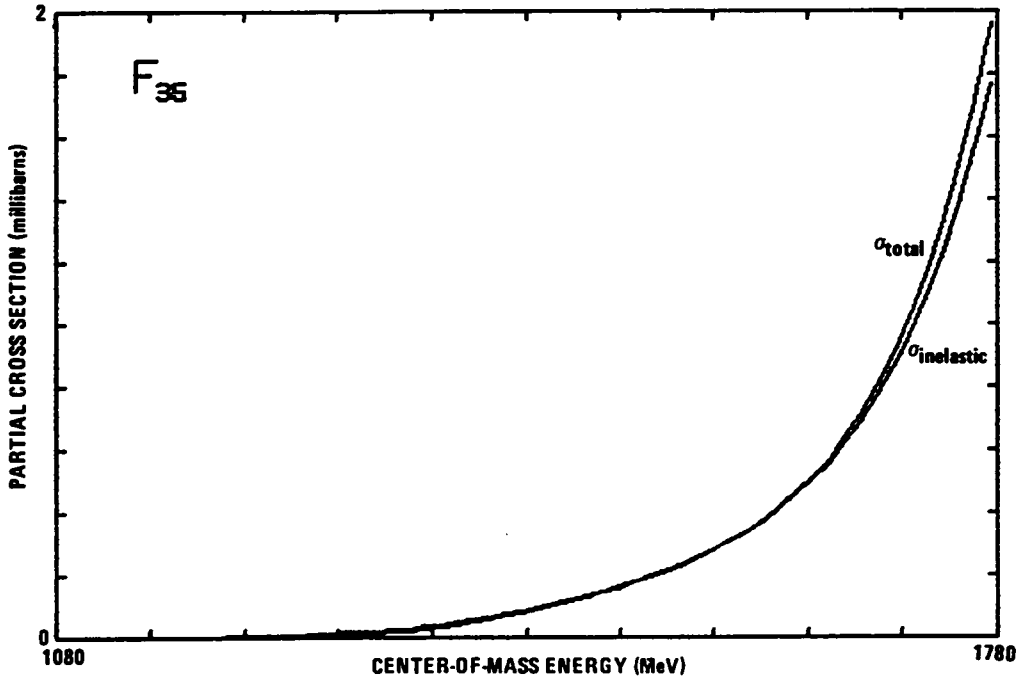

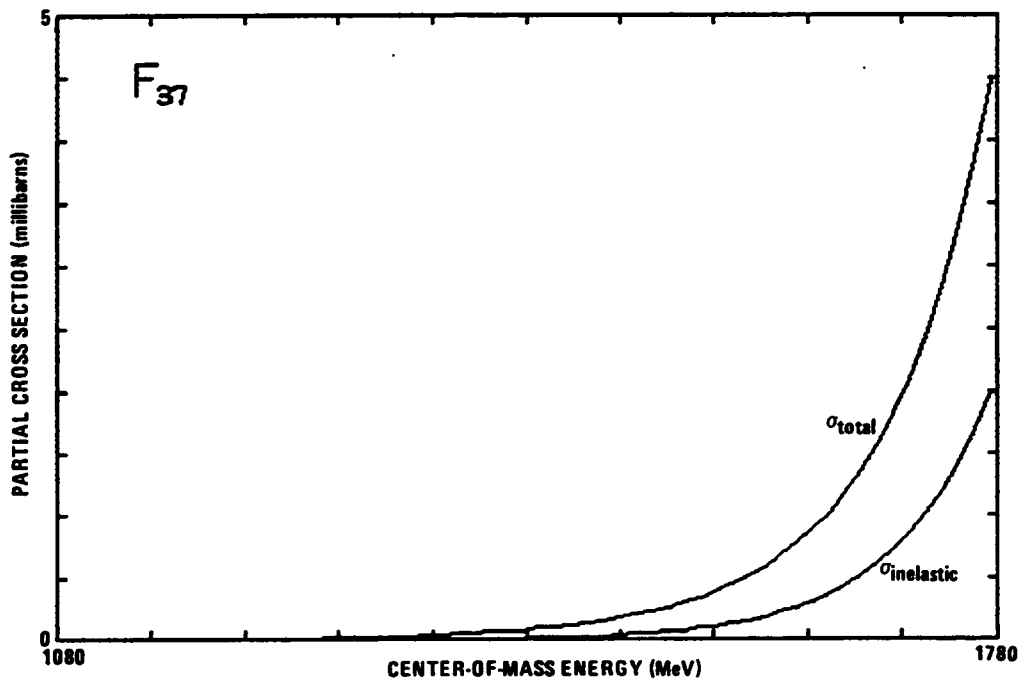

FIGURE E-2. PARTIAL-WAVE CROSS SECTION FOR CENTER-OF-MASS ENERGY FROM 1080 TO 1780 MeV (Sheet 7 of 7)

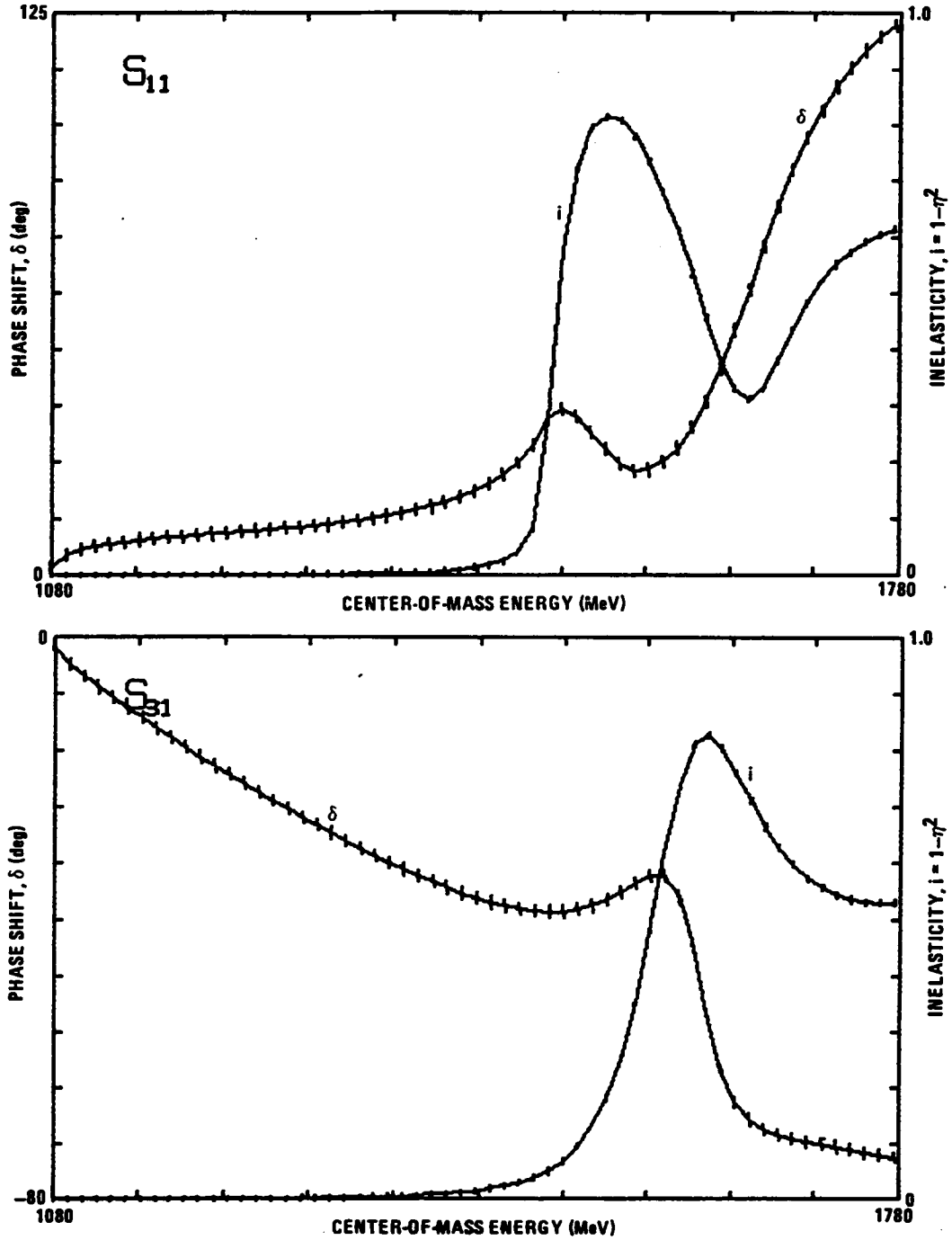

FIGURE E-3. PARTIAL-WAVE PHASE SHIFTS AND INELASTICITIES FOR CENTER-OF-MASS ENERGY FROM 1080 TO 1780 MeV (Sheet 1 of 7)

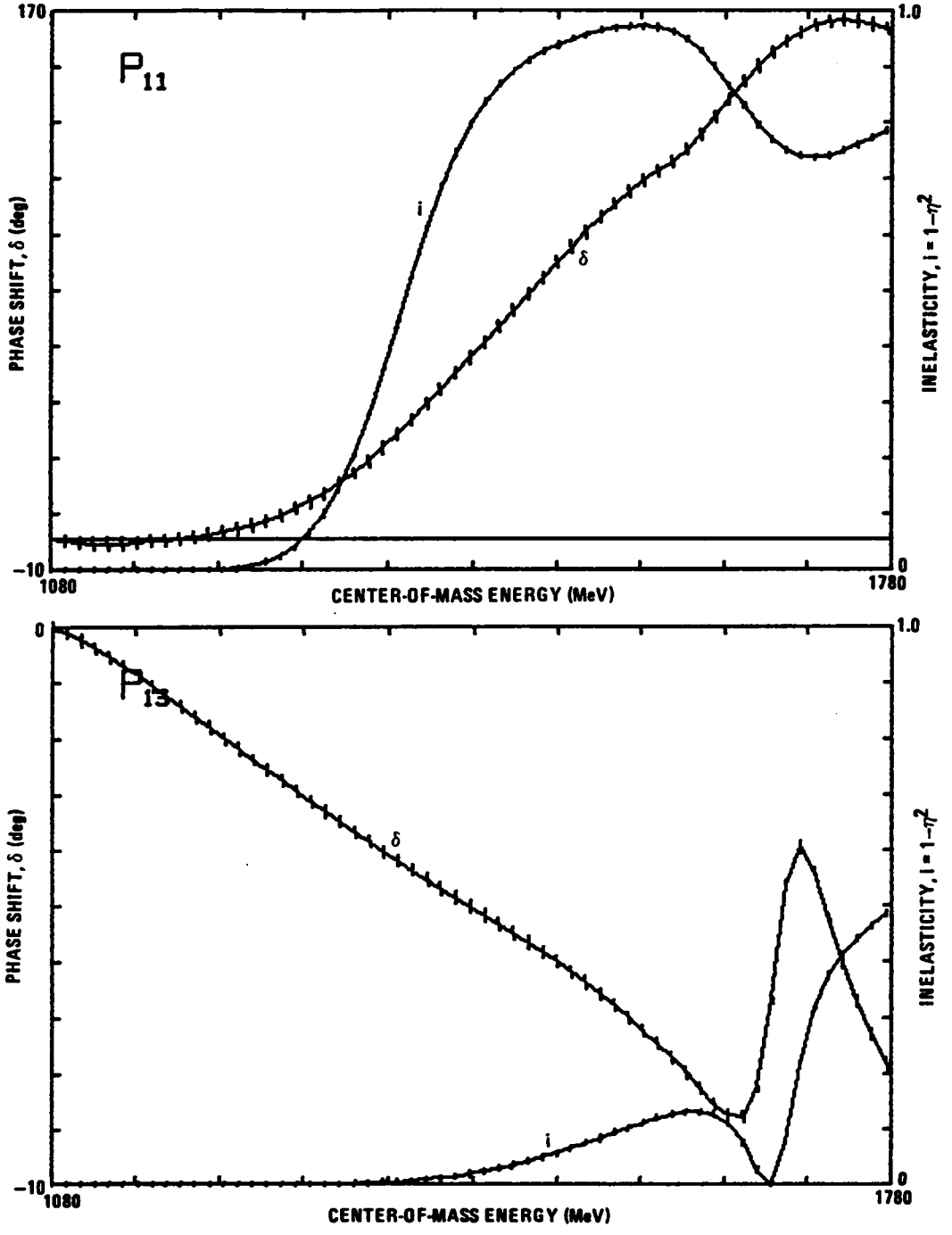

FIGURE E-3. PARTIAL-WAVE PHASE SHIFTS AND INELASTICITIES FOR CENTER-OF-MASS ENERGY FROM 1080 TO 1780 MeV (Sheet 2 of 7)

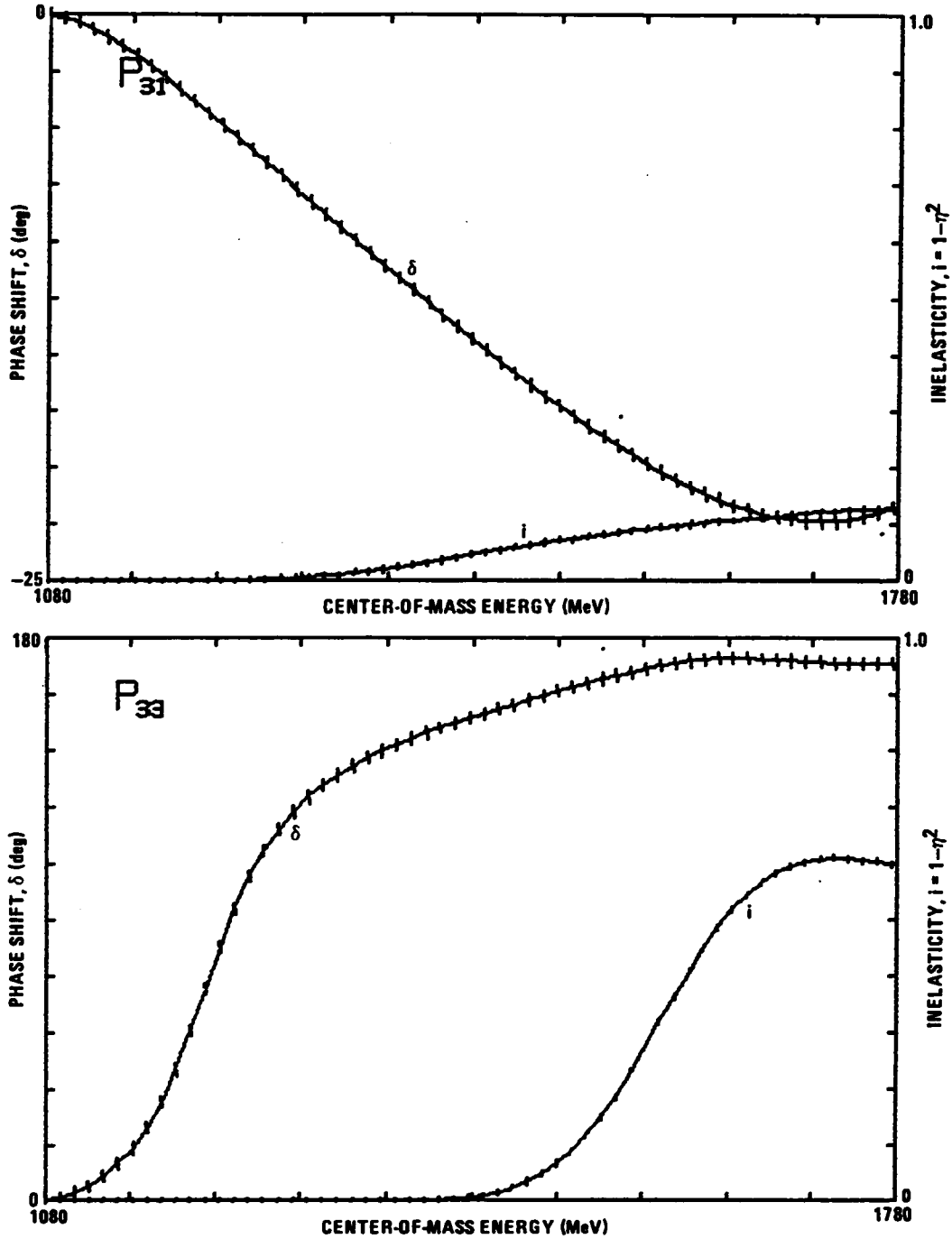

FIGURE E-3. PARTIAL-WAVE PHASE SHIFTS AND INELASTICITIES FOR CENTER-OF-MASS ENERGY FROM 1080 TO 1780 MeV (Sheet 3 of 7)

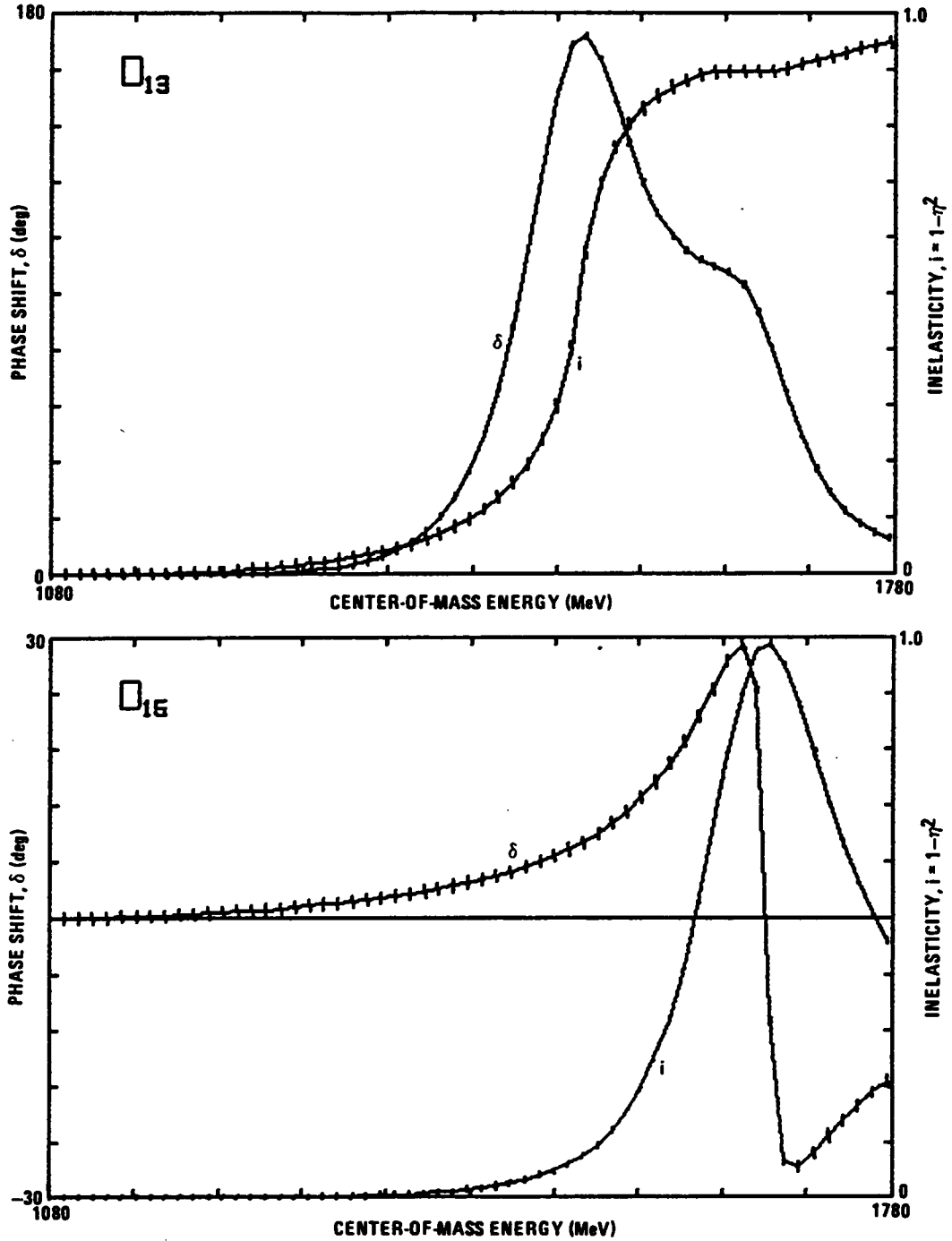

FIGURE E-3. PARTIAL-WAVE PHASE SHIFTS AND INELASTICITIES FOR CENTER-OF-MASS ENERGY FROM 1080 TO 1780 MeV (Sheet 4 of 7)

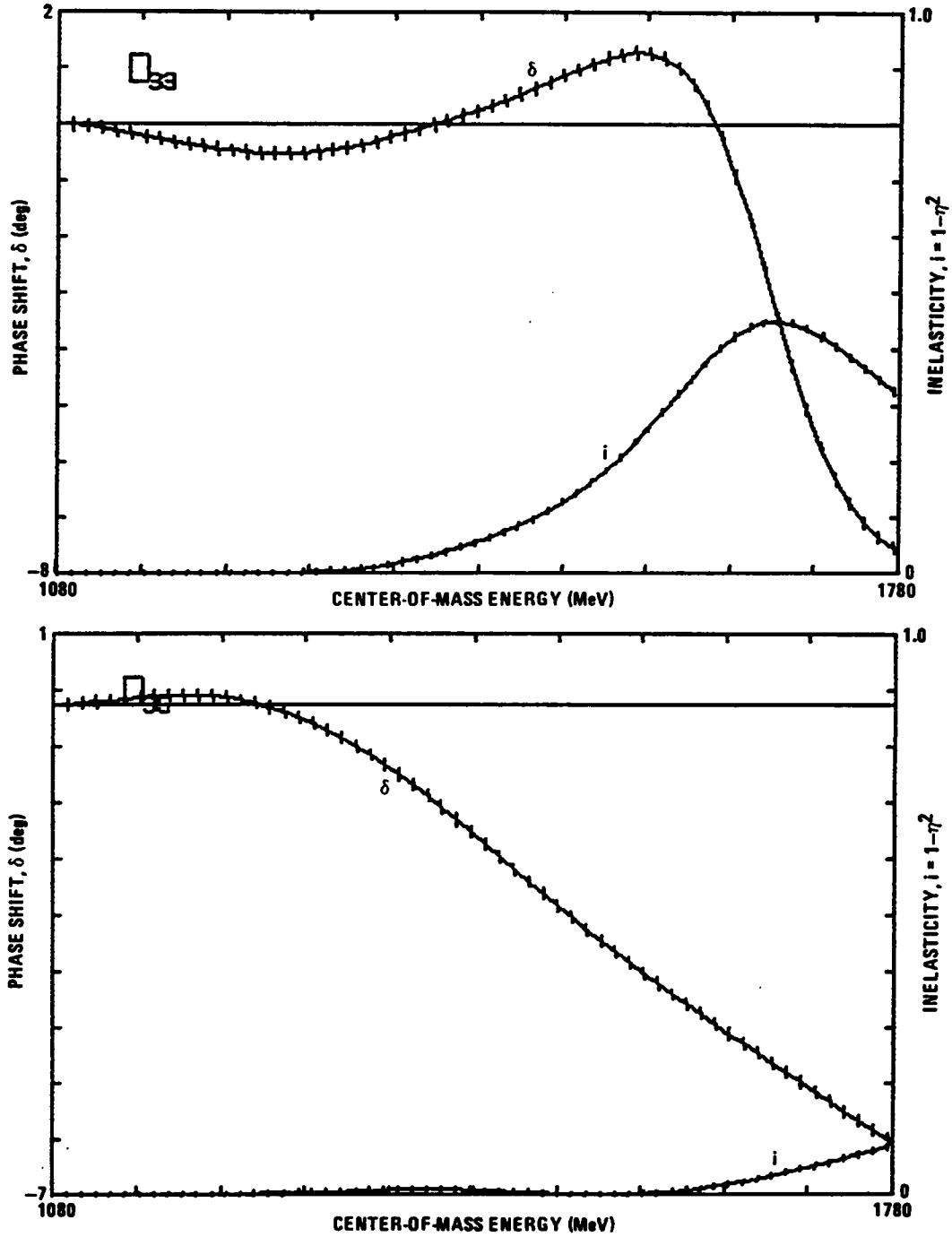

FIGURE E-3. PARTIAL-WAVE PHASE SHIFTS AND INELASTICITIES FOR CENTER-OF-MASS ENERGY FROM 1080 TO 1780 MeV (Sheet 5 of 7)

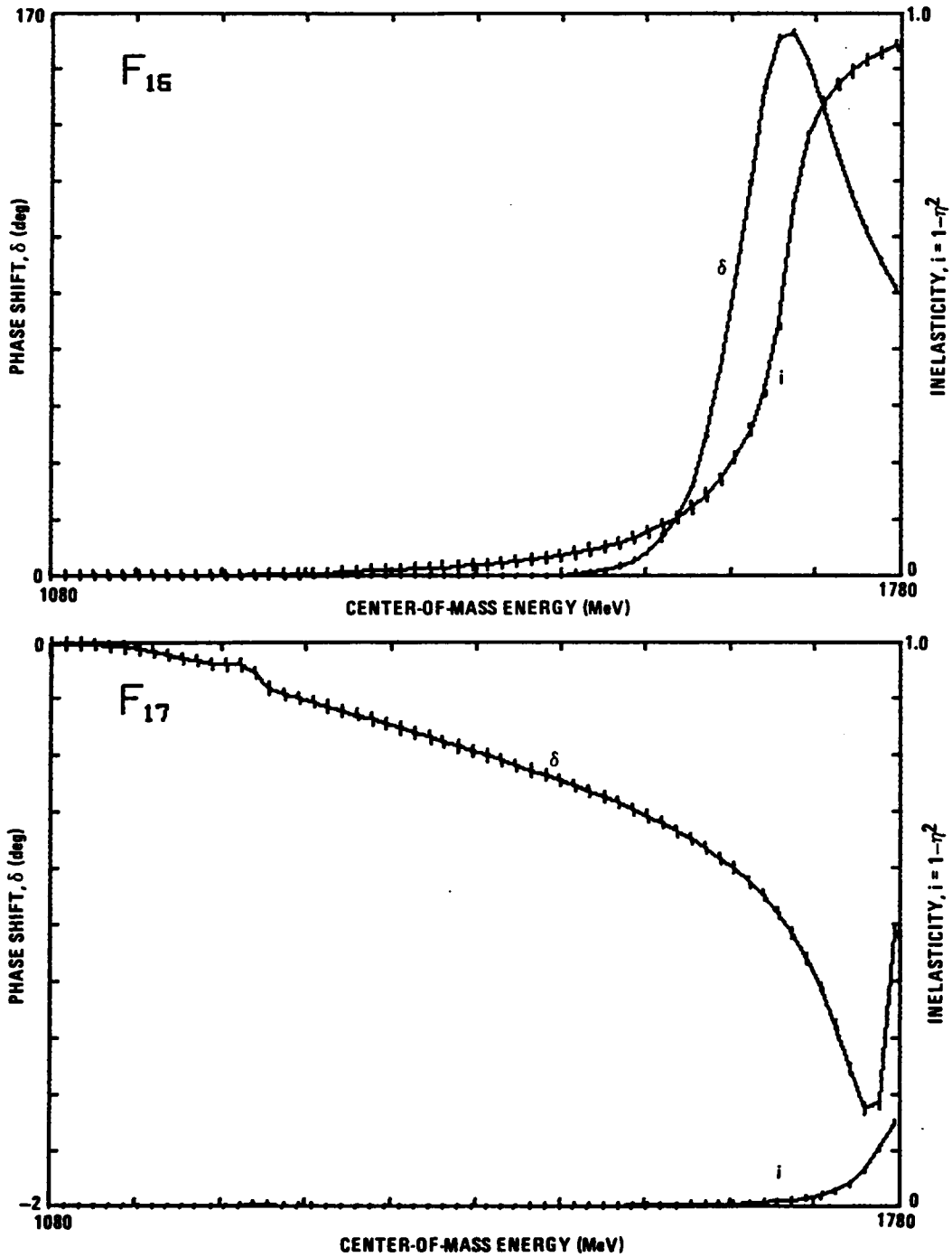

FIGURE E-3. PARTIAL-WAVE PHASE SHIFTS AND INELASTICITIES FOR CENTER-OF-MASS ENERGY FROM 1080 TO 1780 MeV (Sheet 6 of 7)

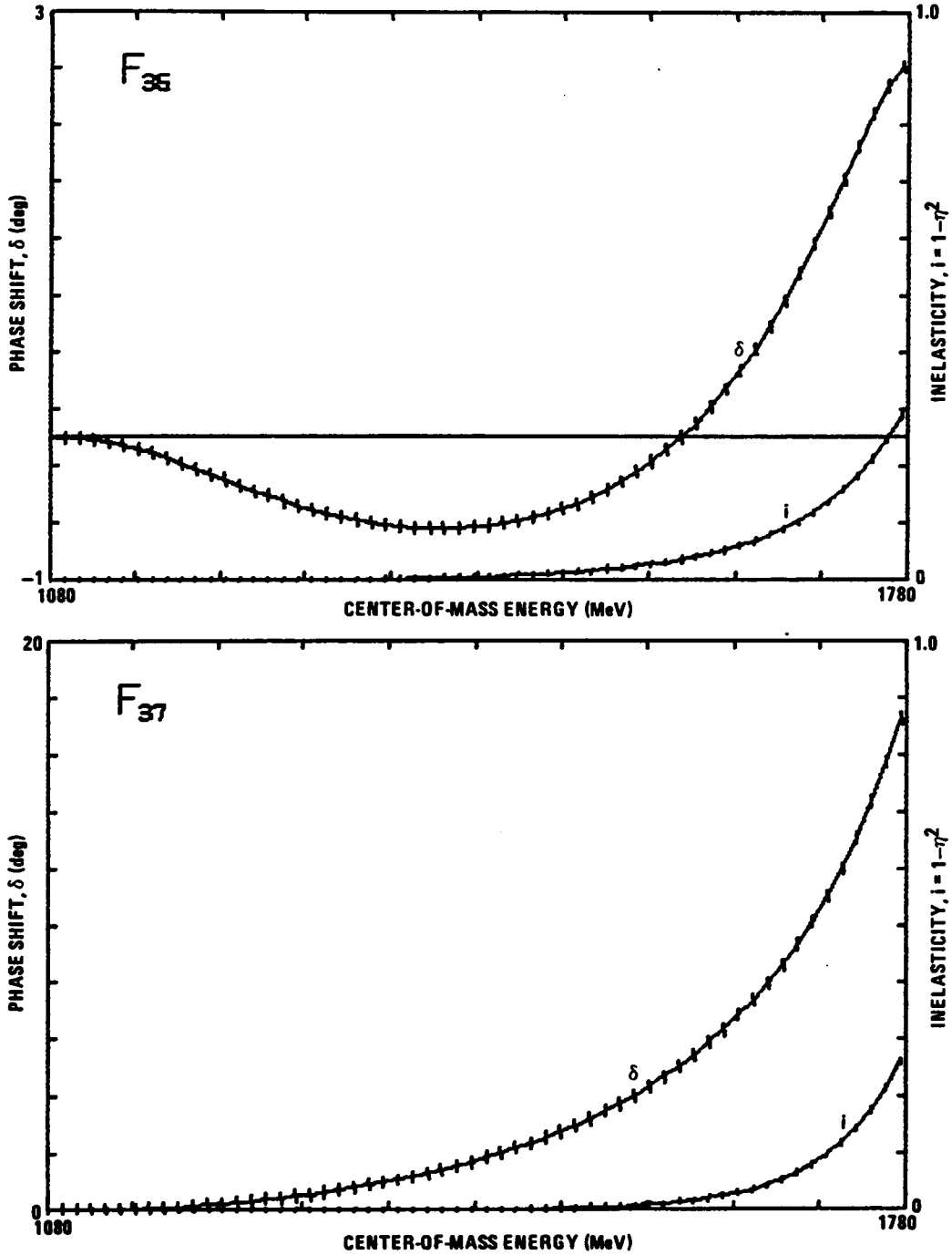

FIGURE E-3. PARTIAL-WAVE PHASE SHIFTS AND INELASTICITIES FOR CENTER-OF-MASS ENERGY FROM 1080 TO 1780 MeV (Sheet 7 of 7)

APPENDIX F. BARYON WAVEFUNCTIONS

Baryons are presumed to consist of three spin 1/2 quarks. Considering here three light flavors of quarks: up (u), down (d), and strange (s), the flavor content of the baryon wavefunction, ϕ_{flavor}, will be a three-dimensional representation of the group $SU(3)_{flavor}$. These flavor wavefunctions with appropriate permutation symmetry are shown in Table F-1 along with the baryons that they constitute. The phase conventions used are those of Close.[1] The corresponding three-dimensional representation of the SU(2) spin wavefunctions are given in Table F-2. The flavor and spin wavefunctions combine to form the SU(6) wavefunctions shown in Table F-3.

The baryon total wavefunction will then consist of a product of the flavor-spin, spatial, and color wavefunctions as follows:

$$\Psi_{baryon} = (\Phi_{flavor}\, X_{spin})\, R_{space}\, C_{color}\,. \qquad \text{(F-1)}$$

The baryon wavefunction, ψ, is totally antisymmetric as proper for fermi statistics, while C is antisymmetric. The color wavefunction is an antisymmetric, three-dimensional representation of SU(3) for the three possible colors that compose the quark color singlet baryons. The spatial wavefunction, R, has the group structure of O(3) required by rotational invariance. The actual form of R depends on the inter-quark forces and how they are modeled.

The ground-state baryons are in the lowest possible spatial state with each quark in an S-wave = $(1s)^3$ and $L^P = 0^+$, therefore, the ground-state spatial wavefunctions are spatially symmetric. The

TABLE F-1. SU(3) FLAVOR BARYON WAVEFUNCTIONS SHOWING EXPLICIT PERMULATION SYMMETRY ($3 \otimes 2 \otimes 3 = 10 \oplus 8 \oplus 8 \oplus 1$)

GROUP CONTENT	FLAVOR WAVEFUNCTION	BARYON
$\Phi_{symmetric}$ = 10 (Φ_s)	uuu	Δ^{++}
	$(uud + udu + duu)/\sqrt{3}$	Δ^{+}
	$(ddu + dud + udd)/\sqrt{3}$	Δ^{o}
	ddd	Δ^{-}
	sss	Ω^{-}
	$(ssd + sds + dss)/\sqrt{3}$	Ξ^{-*}
	$(ssu + sus + uss)/\sqrt{3}$	Ξ^{o*}
	$(dds + dsd + sdd)/\sqrt{3}$	Σ^{-*}
	$(uus + usu + suu)/\sqrt{3}$	Σ^{+*}
	$(sud + sdu + uds + usd + dsu + dus)/\sqrt{6}$	Σ^{+*}
$\Phi_{mixed\ symmetric}$ = 8 (Φ_{ms})	$(udu + duu - 2\ uud)/\sqrt{6}$	P
	$(2\ ddu - udd - dud)/\sqrt{6}$	N
	$(usu + suu - 2\ UUs)/\sqrt{6}$	Σ^{+}
	$(s[du + ud] + [dsu - usd] - 2[du + ud]s)/\sqrt{12}$	Σ^{o}
	$(dsd + sdd - 2\ dds)$	Σ^{-}
	$(dsu - usd + s[du - ud])/2$	Λ^{o}
	$(2\ ssd - [ds + sd]s)/\sqrt{6}$	Ξ^{-}
	$(2\ ssu - [us + su]s)/\sqrt{6}$	Ξ^{o}
$\Phi_{mixed\ antisymmetric}$ = 8 (Φ_{ma})	$(ud - du)u/\sqrt{2}$	P
	$(ud - du)d/\sqrt{2}$	N
	$(us - su)u/\sqrt{2}$	Σ^{+}
	$([dsu + usd] - s\ [ud + du])/2$	Σ^{o}
	$(ds - sd)d\sqrt{2}$	Σ^{-}
	$(s[du + ud] + [usd - dsu] - 2[du+ud]s)/\sqrt{12}$	Λ^{o}
	$(ds - sd)s/\sqrt{2}$	Ξ^{-}
	$(us - su)s/\sqrt{2}$	Ξ^{o}
$\Phi_{antisymmetric}$ = 1 (Φ_a)	$(s[du - ud] + [usd - dsu] + [du - ud]s)\sqrt{6}$	Λ^{o}

TABLE F-2. SU(2) SPIN BARYON WAVEFUNCTIONS
$(2 \otimes 2 \otimes 2 = 4 \oplus 2 + \oplus 2)$

GROUP CONTENT	SPIN WAVEFUNCTION ($\uparrow$ = SPIN UP, $\downarrow$ = SPIN DOWN)
$\chi_{\text{symmetric}}$ = 4 (χ_s)	$\uparrow\uparrow\uparrow$ $(\uparrow\uparrow\downarrow + \uparrow\downarrow\uparrow + \downarrow\uparrow\uparrow)/\sqrt{3}$ $(\downarrow\downarrow\uparrow + \downarrow\uparrow\downarrow + \uparrow\downarrow\downarrow)/\sqrt{3}$ $\downarrow\downarrow\downarrow$
$\chi_{\text{mixed symmetric}}$ = 2 (χ_{ms})	$(\uparrow\downarrow\uparrow + \downarrow\uparrow\uparrow - 2\uparrow\uparrow\downarrow)/\sqrt{6}$ $(2\downarrow\downarrow\uparrow - \uparrow\downarrow\downarrow + \downarrow\uparrow\downarrow)/\sqrt{6}$
$\chi_{\text{mixed antisymmetric}}$ = 2 (χ_{ma})	$(\uparrow\downarrow\uparrow + \downarrow\uparrow\uparrow)/\sqrt{2}$ $(\uparrow\downarrow\downarrow - \downarrow\uparrow\downarrow)/\sqrt{2}$

TABLE F-3. SU(6) FLAVOR-SPIN WAVEFUNCTIONS FOR THREE-QUARK BARYONS
$(6 \otimes 6 \otimes 6 = 56 \oplus 70 \oplus 70 \oplus 20)$

SYMMETRY REPRESENTATION	FLAVOR-SPIN GROUP STRUCTURE CONTENT	FLAVOR-SPIN WAVEFUNCTION
Symmetric 56S	(10,4)* (8,2)*	$\Phi_S\ x_S$ $(\Phi_{ms}\ x_{ms} + \Phi_{ma}\ x_{ma})/\sqrt{2}$
Mixed Symmetric 70MS	(10,2)* (8,4)* (8,2)* (1,2)	$\Phi_S\ x_{ms}$ $\Phi_{ms}\ x_S$ $(\Phi_{ma}\ x_{ma} - \Phi_{ms}\ x_{ms})/\sqrt{2}$ $\Phi_a\ x_{ma}$
Mixed Antisymmetric 70MA	(10,2)* (8,4)* (8,2)* (1,2)	$\Phi_s\ x_{ma}$ $\Phi_{ms}\ x_S$ $(\Phi_{ma}\ x_{ma} - \Phi_{ms}\ x_{ms})/\sqrt{2}$ $\Phi_a\ x_{ms}$
Antisymmetric 20A	(1,4) (8,2)*	$\Phi_a\ x_S$ $(\Phi_{ms}\ x_{ms} - \Phi_{ma}\ x_{ms})/\sqrt{2}$

*Representation containing nucleon and delta states

ground-state flavor-spin wavefunctions are then required to be a symmetric representation of SU(6), namely 56S from Table F-3. From Table F-1, it then follows that ground-state nucleons are members of octet $J^P = 1/2^+$, (8,2), and ground-state deltas are members of decuplet $J^P = 3/2^+$, (10,4).

In a baryon shell model, the first excited (N = 1) state has a single quark excited to a relative P-state $(1s)^2(1p)$ and, therefore, $L^P = 1^-$ with only mixed-symmetric and mixed-antisymmetric spatial states possible. The flavor-spin wavefunction must also have mixed symmetry in order to have a symmetric combination of flavor, spin, and spatial dependence,

$$\Phi_{first\ excited\ state} = (70\,MS\,R_{ms} + 70\,MA\,R_{ma})/\sqrt{2} \ . \qquad \text{(F-2)}$$

The first excited states of the nucleons are then (8,4) x 1^- with J^P = $1/2^-$, $3/2^-$, $5/2^-$ or (8,2) x 1^- with $J^P = 1/2,^- 3/2^-$. The first excited states of the delta are (10,2) x 1^- with $J^P = 1/2^-$, $3/2^-$. There are five nucleon and two delta low-lying (mass less than about 1700 MeV), negative-parity, pion-nucleon states seen experimentally that can be matched with these seven $L^P = 1^-$, three-quark states. Assuming that the spin 1/2 (8,2) states lie lower in energy than do the spin 3/2 (8,4) states, the assignment is given in Table F-4. An assignment of the odd-parity and higher energy negative-parity states (N > 2) is not as direct, but is instead model-dependent.

Within a supermultiplet, the ground state $(56,0^+)$ or the excited multiplets (70, 1^-), (56*, 0^+), (70, 0^+), (56, 2^+), etc., the

TABLE F-4. GROUP ASSIGNMENT OF LOW-LYING, NEGATIVE-PARITY, PION-NUCLEON STATES

GROUP ASSIGNMENT	J^P	PION-NUCLEON STATE
(8,2) ⊗ 1⁻	$1/2^-$ $3/2^-$	S_{11} (1535) D_{13} (1520)
(8,4) ⊗ 1⁻	$1/2^-$ $3/2^-$ $5/2^-$	S_{11} (1650) D_{13} (1700) D_{15} (1675)
(10,2) ⊗ 1⁻	$1/2^-$ $3/2^-$	S_{31} (1620) D_{33} (1700)

degenerate states are broken by mass differences between quarks and by dynamic effects such as caused by spin. Although nonequal quark masses break SU(6) in the nonstrange sector where the up and down constitutent quark masses are nearly equal, it remains convenient to use SU(6) multiplet nomenclature.

REFERENCES

1. F. E. Close, *An Introduction to Quarks and Partons*, Academic Press, Inc., London, Ltd., 1979

The vita has been removed from the scanned document